

May 2016

Effects of Surface Topography and Vibrations on Wetting: Superhydrophobicity, Icephobicity and Corrosion Resistance

Rahul Ramachandran
University of Wisconsin-Milwaukee

Follow this and additional works at: <https://dc.uwm.edu/etd>

 Part of the [Materials Science and Engineering Commons](#), [Mechanical Engineering Commons](#), and the [Nanoscience and Nanotechnology Commons](#)

Recommended Citation

Ramachandran, Rahul, "Effects of Surface Topography and Vibrations on Wetting: Superhydrophobicity, Icephobicity and Corrosion Resistance" (2016). *Theses and Dissertations*. 1192.
<https://dc.uwm.edu/etd/1192>

This Dissertation is brought to you for free and open access by UWM Digital Commons. It has been accepted for inclusion in Theses and Dissertations by an authorized administrator of UWM Digital Commons. For more information, please contact open-access@uwm.edu.

EFFECTS OF SURFACE TOPOGRAPHY
AND VIBRATIONS ON WETTING:
SUPERHYDROPHOBICITY, ICEPHOBICITY AND CORROSION RESISTANCE

by

Rahul Ramachandran

A Dissertation Submitted in

Partial Fulfillment of the

Requirements for the Degree of

Doctor of Philosophy

in Engineering

at

The University of Wisconsin-Milwaukee

May 2016

ABSTRACT

EFFECTS OF SURFACE TOPOGRAPHY AND VIBRATIONS ON WETTING: SUPERHYDROPHOBICITY, ICEPHOBICITY AND CORROSION RESISTANCE

by

Rahul Ramachandran

The University of Wisconsin-Milwaukee, 2016
Under the Supervision of Professor Michael Nosonovsky

Concrete and metallic materials are widely used in construction and water industry. The interactions of both these materials with water and ice (or snow) produce undesirable results and are therefore of interest. Water that gets absorbed into the pores of dry concrete expands on freezing and can lead to crack formation. Also, the ice accretion on concrete surfaces such as roadways can have disastrous consequences. Metallic components used in the water industry undergo corrosion due to contact with aqueous corrosive solutions. Therefore, it is desirable to make concrete water/ice-repellent, and to make metallic surfaces corrosion-resistant.

Recent advances in micro/nanotechnology have made it possible to design functional micro/nanostructured surfaces with micro/nanotopography providing low adhesion. Some examples of such surfaces are superhydrophobic surfaces, which are extremely water repellent, and icephobic surfaces, which have low ice adhesion, repel incoming water droplets before freezing, or delay ice nucleation. This dissertation investigates the effects of surface micro/nanotopography and small amplitude fast vibrations on the wetting and adhesion of concrete with the goal of producing hydrophobic and icephobic concrete, and on the wetting of metallic surfaces to prevent corrosion.

The relationship between surface micro/nanotopography and small fast vibrations is established using the method of separation of motions. Both these small scale effects can be substituted by an effective force or energy. The structure-property relationships in materials and surfaces are established. Both vibrations as well as surface micro/nanopatterns can affect wetting properties such as contact angle and surface free energy.

Hydrophobic engineered cementitious composite samples are produced by controlling their surface topography and surface free energy. The surface topography is controlled by varying the concrete mixture composition. The surface free energy of concrete is lowered using a hydrophobic emulsion. The hydrophobic concrete samples were able to repel incoming water droplets as well as resist droplet pinning.

Corrosion resistance is achieved in cast iron samples by rendering them superhydrophobic. The corrosion resistance of superhydrophobic surfaces with micro/nanotopography may be explained by the low effective contact area with the electrolyte. The experimental results matched the theoretical predictions based on surface roughness and wettability.

The icephobicity of engineered cementitious composite samples is achieved by hydrophobization, by using coatings containing dielectric material (such as polyvinyl alcohol fibers), and by controlling the surface topography. Two aspects of the icephobicity of concrete, namely, the repulsion of incoming water droplets before freezing and the ice adhesion strength, are investigated experimentally. It is found that icephobic performance of concrete depends on these parameters – the hydrophobic emulsion concentration, the polyvinyl alcohol fiber content, the water to cement ratio, and the sand to cement ratio.

The potential for biomimetic icephobicity of thermogenic skunk cabbage plant is investigated, and it is found that the surface topography of its leaves can affect the heat transfer from the plant to the surrounding snow. The hierarchical microstructure of the leaf surface coupled with its high adhesion to water suggests the presence of an impregnated wetting state, which can minimize the heat loss.

Thus functional materials and surfaces, such as hydrophobic and icephobic engineered cementitious composites and corrosion resistant metallic surfaces, can be produced by controlling the surface micro/nanotopography.

© Copyright by Rahul Ramachandran, 2016
All Rights Reserved

*To
my grandmother
and
my parents*

TABLE OF CONTENTS

ABSTRACT.....	ii
TABLE OF CONTENTS.....	vii
LIST OF FIGURES	xii
LIST OF TABLES	xvii
LIST OF ABBREVIATIONS.....	xviii
ACKNOWLEDGMENTS	xix
CHAPTER 1: INTRODUCTION	1
1.1 Objectives of the Dissertation.....	3
1.2 Organization of the Dissertation	5
CHAPTER 2: CONCEPTS OF WETTING AND VIBRATIONAL MECHANICS	8
2.1 Contact Angle and Models of Wetting	8
2.2 Contact Angle Hysteresis.....	11
2.3 Superhydrophobicity and Biomimetic Self-Cleaning Surfaces	14
2.4 Geometric Interpretation of the Surface Tension at Equilibrium	16
2.5 Separation of Motions and Effective Forces.....	20
2.6 Vibrational Mechanics	24
2.7 Conclusion	25
2.8 References.....	25
CHAPTER 3: EFFECTS OF VIBRATIONS AND SPATIAL MICRO/NANO PATTERNS ON EQUILIBRIUM, WETTING, FLOW AND PHASE TRANSITION	30
3.1 Effective Force Corresponding to Small Fast Vibrations.....	30
3.1.1 Inverted pendulum and vibro-levitation.....	31
3.1.2 Mathieu equation method	34

3.1.3 Multiple pendulums and the so-called “Indian rope trick”	36
3.1.4 Experimental	41
3.1.5 Results and discussion	41
3.2 Vibro-Levitation of Droplets	44
3.2.1 Vibro-levitating droplets and inverted pendulum	46
3.2.2 Experimental	49
3.2.3 Results.....	50
3.3 Vibration-Induced Phase Transition and Locomotion	51
3.3.1 Effective freezing	52
3.3.2 Cornstarch monsters.....	52
3.3.3 Effective liquid properties and surface tension of granular materials	54
3.3.4 Locomotion in viscous liquid.....	56
3.4 Effect of the Surface Texture on Stability and Phase Transitions	57
3.4.1 Kirchhoff’s analogy between spatial and temporal patterns.....	57
3.4.2 Surface patterns leading to the superhydrophobicity, phase transition and propulsion.....	62
3.5 Effect of the Patterns on Fluid Flow Through Membranes	66
3.5.1 Water penetration through a hole in a vibrating vessel.....	66
3.5.2 Liquid penetration through pores in vibrating or patterned membranes.....	69
3.6 Conclusion	76
3.7 References.....	78
CHAPTER 4: DYNAMICS OF INCOMING DROPLETS ON TEXTURED HYDROPHOBIC CONCRETE	83
4.1 Introduction.....	83
4.2 Experimental.....	85
4.2.1 Materials	85

4.2.2 Contact angle and surface roughness measurement.....	87
4.2.3 Droplet impact test.....	87
4.3 Results.....	88
4.3.1 Contact angle and surface roughness.....	88
4.3.2 Analysis of vertical impacts.....	89
4.3.3 Analysis of oblique impacts.....	91
4.4 Discussion.....	95
4.5 Conclusion	98
4.6 References.....	99
CHAPTER 5: CORROSION RESISTANT SUPERHYDROPHOBIC METALLIC SURFACES	102
5.1 Introduction.....	102
5.2 Electrochemical Foundations of Corrosion and Wetting.....	107
5.3 Theoretical Model.....	111
5.3.1 Ohm’s law and the wetting states	112
5.3.2 Faraday’s law of electrolysis and wetting properties.....	113
5.3.3 Rate of corrosion and the surface free energy	113
5.4 Experimental.....	114
5.4.1 Surface roughening	114
5.4.2 Hydrophobic coating.....	115
5.4.3 Contact angle and surface roughness measurements	115
5.4.4 Potentiodynamic polarization test.....	116
5.5 Results and Discussion	116
5.6 Conclusion	125
5.7 References.....	126

CHAPTER 6: ANTI-ICING SUPERHYDROPHOBIC SURFACES.....	129
6.1 Introduction.....	129
6.2 Hydrophobic Interactions Essential for Ice Repulsion	132
6.2.1 Entropic and hydrophobic forces	132
6.2.2 Self-organized criticality and hysteresis of the contact angle.....	136
6.2.3 Ice crystal formation	139
6.3 Three Approaches to Synthesizing Icephobic Surfaces.....	144
6.3.1 Ice adhesion to solids	144
6.3.2 Decreasing contact time for droplets approaching the solid surface	146
6.3.3 Suppression of frost formation.....	147
6.4 Experimental	149
6.4.1 Materials	149
6.4.2 Contact angle and roll-off angle	150
6.4.3 Ice adhesion strength.....	150
6.4.4 Interaction of incoming droplets	151
6.4.5 Sample preparation	152
6.4.6 Surface roughness	153
6.5 Results and Discussion	153
6.5.1 Surface roughness results.....	153
6.5.2 Ice adhesion strength results	156
6.5.3 Interaction of incoming droplets	160
6.6 Optimization of Icephobic Surfaces.....	161
6.6.1 Ice adhesion to solids	162
6.6.2 Suppression of frost formation.....	163
6.6.3 Minimizing contact time for incoming droplets	166

6.7 Conclusion	168
6.8 References.....	169
CHAPTER 7: BIOMIMETIC POTENTIAL OF THE ICEPHOBICITY OF SKUNK CABBAGE	176
7.1 Introduction.....	176
7.2 <i>Symplocarpus foetidus</i> and the Icephobicity	178
7.3 Experimental.....	180
7.3.1 Contact angle measurement	180
7.3.2 Surface topography using SEM	180
7.4 Results.....	181
7.5 Discussion.....	184
7.6 Conclusion	188
7.7 References.....	189
CHAPTER 8: CONCLUSION	192
APPENDIX.....	198
CURRICULUM VITAE.....	202

LIST OF FIGURES

Figure 2.1. (a) Surface tension forces at the three-phase line on a non-deformable solid surface. The vertical components of the forces remain unbalanced. (b) The equilibrium of surface tensions at the three-phase line of liquid phases A, B and C. Note the deformation of the interface between A and C. 9

Figure 2.2. (a) A liquid droplet in Wenzel state, with a homogenous solid-liquid interface below the droplet. (b) A liquid droplet in Cassie-Baxter state, with a composite solid-liquid-vapor interface below the droplet. (c) Contact angle hysteresis (CAH) measurement by tilting the droplet. The maximum or advancing (θ_{adv}) and minimum or receding (θ_{rec}) contact angles are measured at the front and rear of a moving droplet respectively. 11

Figure 2.3. (a) When the interface between A and B is displaced along the vector dr , the surface tension force acts on the three-phase line l in the direction of the normal n . (b) Equilibrium of surface tension vectors at the three-phase line. (c) The Neumann's triangle for a three-phase system. (d) The Neumann's triangle for a three-phase system in the Wenzel state. 17

Figure 2.4. The Neumann's triangles for the three-phase systems (a) S1AW, and (b) S2AW respectively. (c) The Neumann's triangle for a three-phase Cassie-Baxter state. (d) Contact angle hysteresis represented using Neumann's triangle as a rotation of the vector γ_{wa} . A range of contact angles are possible under a constraint that γ_{wa} remains constant. 19

Figure 2.5. (a) A four-phase system. The pockets of air trapped on the solid surface constitutes the fourth phase [31]. (b) Tetrahedron of surface tension vectors in 3D space for a four-phase system. 20

Figure 2.6. (a) Unstable equilibrium corresponding to the maximum potential energy (b) A metastable equilibrium due to the stabilizing effect of the external force. 23

Figure 3.1. The potential energy Π of a pendulum as a function of its angular displacement ψ . 32

Figure 3.2. The figure on the left shows an inverted pendulum stabilized by a foundation vibrating with a periodic displacement $A\cos\Omega t$. The same system can be represented as shown in the figure on the right with the pendulum being stabilized by a spring of effective spring constant k 33

Figure 3.3. The region of stability for an inverted pendulum as seen in the Ince-Strutt diagram. 35

Figure 3.4. An inverted double pendulum whose foundation is subjected to a sinusoidal vibration $A\cos\Omega t$ 37

Figure 3.5. A multiple pendulum which is being stabilized by vibrating its foundation is equivalent to a multiple pendulum which is stabilized by a system of generalized vibro-levitation forces $V_1, V_2 \dots V_n$ 39

Figure 3.6. (a) Experimental setup (b) Instabilities in the plastic rope with the foundation vibrating at 130 Hz.....	42
Figure 3.7. (a) A rope which is under no vibration, buckles under its own weight (b) Vertical vibrations results in an increased effective stiffness which prevents buckling (c) For any beam there is a critical force (F_{cr}) that depends on the beam material and geometry. Any load (F) greater than this will cause the beam to buckle (d) Vibrating the foundation leads to an increase in the effective stiffness of the beam, and the beam is able to resist buckling.	43
Figure 3.8. (a) and (b) The droplet as it spreads from a full sphere to a spherical cap of radius R , (c) Energy of a droplet (corn oil, $R_o = 0.25\text{mm}$, $\gamma = 0.032\text{N/m}$) as it coalesces with the bulk liquid, and the similarity of this energy function to that of an inverted pendulum.	47
Figure 3.9. (a) Experimental setup (b) A droplet of corn oil levitating on the surface of corn oil vibrating at 150 Hz.....	49
Figure 3.10. Cornstarch monsters in sample A at 30 Hz.	53
Figure 3.11. Vibrations can result in flow of granular material. This vibration-induced effective liquid-like behavior is similar to melting phase change.	55
Figure 3.12. Kirchhoff's analogy between a pendulum and a beam. Deflection of the beam due to a (a) compressive load (corresponding to the stable equilibrium of the regular pendulum) and (b) tensile (buckled configuration corresponding to the unstable equilibrium of an inverted pendulum) force F . The waviness in the case (c) would promote stable (unbuckled) equilibrium similarly to the vibrations stabilizing an inverted pendulum.....	58
Figure 3.13. Ince-Strutt stability diagram for a beam.	61
Figure 3.14. A Surface can be made hydrophobic or hydrophilic by controlling the surface texture.	63
Figure 3.15. (a) Levitating liquid droplet over a sufficiently hot surface due to the Leidenfrost effect. (b) Self-propelled Leidenfrost droplets on an asymmetric saw-tooth surface. The temperature of the surface is usually much greater than the boiling point of the liquid.....	64
Figure 3.16. (a) Fluid flow through a pipe where the pressure difference ΔP_0 is a nonlinear function of the flow velocity v_0 . (b) Longitudinal external vibrations $h\cos\Omega t$ results in an additional pressure difference ΔP_v . (c) Pressure difference as a function of the velocity $h\Omega$. The hysteresis ($\Delta P_2 - \Delta P_1$) due to a small change in velocity $\pm\delta v$ can significantly alter the flow characteristics. (d) Pressure difference as a function of $h\Omega$ for three different fluids with $a=700$, 1000 and 1200 kgm^{-3}	68
Figure 3.17. (a) Both sides of the semipermeable membrane have pure solvent and hence equal chemical potential. Therefore an osmotic equilibrium exists. (b) Osmosis across the semipermeable membrane continues until the chemical potentials equilibrate. (c) The flux of solvent molecules can be reversed by applying a pressure larger than the osmotic pressure. This process is called reverse osmosis.....	70

Figure 3.18. Vibrations can change the permeability of membranes. This may lead to a reverse osmotic flux even when the applied pressure is less than the osmotic pressure.	72
Figure 4.1. Water droplet impacting hydrophobic concrete at room temperature. The droplet is seen to flatten out into a ‘pancake shape’ in the second frame. In the third frame, it retracts and a jet is expelled. The parent droplet however remains partially pinned due to longer contact time with the surface.	84
Figure 4.2. The experimental setups for the droplet impact test. (a) Experiment to measure the height of first bounce of droplet on horizontal hydrophobic concrete sample. The trajectory of the bouncing droplet which is a vertical line, is exaggerated into a parabola to identify h . (b) Experiment to study impact of droplets impinging at 45° and icephobic performance under sub-zero conditions.	88
Figure 4.3. 3D surface topography of the samples. (a) M1 (b) M2 (c) A3 (d) A4 (e) B3 (f) B4. M1 has dense distribution of asperities due to the lack of aggregates in the sample.	89
Figure 4.4. Coefficient of restitution at various Weber numbers (We) for the hydrophobic concrete samples. The curves show a similar trend, with a more negative slope at low We and less negative slope at higher We	90
Figure 4.5. Interaction of distilled and salted water droplets falling from 10 mm, with the samples at 45° inclination, at 20°C and -5°C	92
Figure 4.6. Interaction of distilled and salted water droplets falling from 50 mm, with the samples at 45° inclination, at 20°C and -5°C	93
Figure 4.7. Interaction of distilled and salted water droplets falling from 140 mm, with the samples at 45° inclination, at 20°C and -5°C	94
Figure 4.8. Theoretical Coefficient of restitution (COR) vs. Weber number (We) plot.	96
Figure 5.1. (a) and (b) Corrosion current density as a function of contact angle from published literature. The trend clearly shows a significant decrease in corrosion current densities with increase in contact angle. The lowest corrosion current densities occur in the Cassie-Baxter domain, where contact angle is much greater than 90°	105
Figure 5.2. (a) A typical electrochemical corrosion process in the presence of an electrolyte. Material is removed from anodic sites and then deposited as corrosion products (rust) at cathodic sites. (b) The dynamic equilibrium current is zero.	108
Figure 5.3. (a) A typical i vs η dependency based on the Butler-Volmer equation (b) Red curves show the Tafel plot of the net (anodic and cathodic) current. Corrosion current can be obtained by extrapolating along the tangential lines corresponding to the exponential polarization curves. (c) A typical three electrode set-up for the PPT corrosion measurement. The red arrows show current flow during anodic polarization, and the broken green arrows show current flow during cathodic polarization.	110

Figure 5.4. (a) Variation of the current I with contact angle θ and fractional solid-liquid interfacial area f_{SL} (b) Rate of corrosion reaction r as a function of contact angle θ for different values of roughness factor r_f . The equilibrium contact angle of the surface was assumed to be 50°	112
Figure 5.5. Optical images of surfaces of the samples (a) P1, (b) P2, and (c) P3. The coating on P3 is visibly different with cracks and bubbles on the surface.	118
Figure 5.6. (a) to (i) shows the surface topographies of P1, P2, P3, R1, R2, R3, S1, S2, and S3 respectively. Coating with the liquid repellent spray results in drastic change in surface roughness as seen in the case of P3, R3, and S3. All scales are in μm	119
Figure 5.7. Potentiodynamic polarization curves for the samples. Rendering the surface superhydrophobic is seen to shift decrease the corrosion current density as well as shift the corrosion potential closer to the reference electrode potential.	120
Figure 6.1. Random walk along an ideal polymer chain. The chain attains the most probable configuration.	133
Figure 6.2. (a) Entropic origin of hydrophobic interaction. Aggregation of hydrophobic molecules frees up water molecules to increase the configurational entropy of the system (attaining the most probable configuration). Hydrophobic interaction is manifested as a hydrophobic force which results in (b) clustering of hydrophobic particles in water, and (c) attraction of hydrophobic particles towards a hydrophobic surface in water.	135
Figure 6.3. (a) Intermittent pinning and advancing of the triple line. (b) Energy barriers associated with contact angle hysteresis.	137
Figure 6.4. (a) Folding of protein molecule from a linear primary structure to 3D tertiary (native) structure is similar to the elastic force in a polymer chain. For a polymer chain the force can be attractive or repulsive depending on the end-to-end distance. For a protein molecule the attractive hydrophobic force causes the hydrophobic side chains to retract to the interior of the cluster. (b) Parallelism with snow crystal growth as opposed to the hydrophobic interaction of a particle and a surface. The red vectors denote the entropic force F in each case.....	138
Figure 6.5. (a) Simple snow crystals are either plate-like or columnar. (b) Evolution of intricate shapes in a snow crystal by diffusion-limited aggregation and Mullins-Sekerka growth instability.....	140
Figure 6.6. The Nakaya diagram. The geometry of a snow crystal is dependent on the supersaturation and temperature of the atmosphere in which it grows.....	142
Figure 6.7. Optical images of M1, M5, M6, and M10. The blue broken arrows show the PVA fibers, while the red arrows show the sand grains. The scale bar for M1, M5 and M6 is $100 \mu\text{m}$, and for M10 it is $200 \mu\text{m}$	154

Figure 6.8. The surface topographies of samples M1, M5, M6, and M10. (a) PVA fiber is visible in M1 emerging from the surface; (b) PVA fibers as well as sand grains are observed in M5. The sand creates roughness on the surface (c) M6 has the lowest roughness due to absence of sand and PVA fibers. (d) The presence of sand creates distributed roughness in M10.	155
Figure 6.9. (a) The correlation of water contact angle and ice adhesion strength for the samples (b) The correlation of water contact angle and the roll-off angle for the samples (based on Dr. Kozhukhova's PhD thesis).....	159
Figure 6.10. Stacked images showing the trajectory of water droplets falling from 50 mm impinging on concrete samples inclined at 45° at 0°C and 20 °C. The trajectory of droplets at -5 °C after bouncing is shown in red.....	161
Figure 6.11. Variation of ice adhesion strength with dielectric constant of the icephobic coating.	162
Figure 6.12. (a) Water droplet making a contact angle θ inside a wedge of angle α . (b) Normalized nucleation energy barrier versus contact angle. The energy barrier increases as the wedge angle increases. (c) Surface topography with wide corners will have the highest possible nucleation energy barrier.	165
Figure 7.1. (a) the leaf of skunk cabbage enclosing spathe and spadix, and (b) the spathe. (c) Skunk cabbage as observed in its natural environment in wet land (Schlitz Audubon Nature Center, Milwaukee, WI) in the month of November.	179
Figure 7.2. Water droplets on (a) leaf (b) spathe (c) an adherent water droplet on the vertical surface of leaf.....	182
Figure 7.3. Scanning electron micrographs of skunk cabbage leaf and spathe surfaces. (a) Vapor phase fixed adaxial leaf surface, (b) scarcely distributed wax rodlets on the adaxial leaf surface, (c) adaxial surface of vapor phase fixed spathe showing stomata (d) abaxial surface of vapor phase fixed spathe showing stomata, (e) vapor phase fixed abaxial leaf surface showing pillars covered with wax rodlets, (f) the wax rodlets, and (g) liquid phase fixed abaxial surface of leaf showing the pillars tops void of wax rodlets.	183
Figure 7.4. (a) Heat transfer at composite interface on the leaf surface resulting in melting of ice and an advancing water-ice interface (b) equivalent electrical circuit showing thermal resistances at the composite interface.	186
Figure 7.5. (a) Time for melting of ice layer (thickness, a) at different fractional flat area of the water-air interface (b) time for melting an ice layer 1mm thick at different fractional flat area of the water-air interface (f_{WA}) and roughness factors (r_f).....	187
Figure 7.6. The heat produced by the skunk cabbage plant in tandem with the high adhesion can maintain a slippery layer of water on the leaf surface. Thus the ice slips off the leaf surface. ..	187

LIST OF TABLES

Table 3.1. The range of frequencies where stable levitating droplets were observed.	50
Table 3.2. Summary of recent literature on oil-water separation using selectively wettable membranes.	74
Table 4.1. Composition of the hydrophobic concrete samples.	86
Table 4.2. CA, CAH, equilibrium contact angle from Tadmor equation and S_a for concrete samples.	89
Table 5.1. A brief summary of results from literature. Abbreviations: CRS – cold rolled steel, Cu – copper, SS – stainless steel, Ti – titanium, Al – aluminum, Mg – magnesium. Units for measurements: CA – deg, i_{corr} – $\mu A/cm^2$, E_{corr} – mV.	106
Table 5.2. The contact angles (CA), contact angle hysteresis (CAH), average surface roughness (S_a), corrosion current density (i_{corr}), corrosion potential (E_{corr}), and corrosion rate (in millimeters per year, mmpy) for the samples.	118
Table 6.1. Similarities between the hydrophobicity and the icephobicity.	143
Table 6.2. Ice adhesion strength of some materials from literature.	145
Table 6.3. The composition of concrete/mortar specimen (based on Dr. Kozhukhova’s PhD thesis).	152
Table 6.4. Average surface roughness (S_a) of the samples in μm , and the controlling parameters such as PVA fiber content and sand to cement ratio.	154
Table 6.5. Contact angle (CA), roll-off angle, and ice adhesion strength for concrete and mortar tiles (based on Dr. Kozhukhova’s PhD thesis).	157
Table A1. Chemical and physical properties of portland cement.	199

LIST OF ABBREVIATIONS

CA – contact angle

CAH – contact angle hysteresis

CI – cast iron

COR – coefficient of restitution

deg – degrees

mmpy – millimeters per year

PPT – potentiodynamic polarization test

PVA – polyvinyl alcohol

SOC – self-organized criticality

We – Weber number

ACKNOWLEDGMENTS

I would like to thank my advisor Prof. Michael Nosonovsky for his excellent guidance and support during my PhD. Interactions with him has helped me to become a better researcher. His constructive criticism improved the quality of my research, writing and presentation. For all this I am deeply indebted.

I would like to thank my committee members Prof. Pradeep Rohatgi, Prof. Konstantin Sobolev, Prof. Krishna Pillai and Prof. Woo Jin Chang for their time, support, guidance and valuable comments.

I would like to thank Prof. Sobolev and his group members for the hydrophobic concrete samples. I am grateful to Dr. Marina Kozhukhova for sharing experimental results from her research on the icephobicity. I also would like to thank Dr. Ismael Flores-Vivian for his valuable suggestions on experiments with concrete. The study presented in chapter 4 was supported by the UWM Research Growth Initiative grant 101X245.

I would like to thank Prof. Rohatgi and his group members for the cast iron samples, as well as the chemicals used in making hydrophobic corrosion resistant coatings. I am grateful to Mr. Emad Omrani for training me to use the corrosion test equipment. The study presented in chapter 5 was partially supported by NSF IUCRC FRP award 1331532.

I would like to thank Mr. Matthew Smith of the Schlitz Audubon Nature Center in Milwaukee for helping to harvest the skunk cabbage. I would also like to thank Dr. Steve Hardcastle for permitting me to use the laser scanning microscope in the Advanced Analysis Facility. I am grateful to Dr. Heather Owen from the Department of Biological Sciences for

discussions and guidance on biological sample preparation, and also for scanning electron microscope training. I also thank Prof. Ryoichi S. Amano for the camera used in studying incoming droplets on concrete. I would like to thank the administrative staff at the Mechanical Engineering Department, and the Graduate School for their help during my time at UWM. So many of my friends and family have supported and encouraged me all along. I thank them all.

I would like to thank my parents for all their sacrifices, and for giving me a good education. Finally, I would like to thank my beloved grandmother who spend her life dedicated her family, and has shown unconditional love and support.

CHAPTER 1: INTRODUCTION

Surfaces phenomena are increasingly important for various novel micro/nanodevices and applications, because these devices have small size and, therefore, large surface-to-volume ratios. The intensity of surface forces (for example, adhesion and friction) tends to be proportional to the surface area, and, therefore, they are scaled as the second power of the characteristic length of a device, whereas the volume forces (for example, inertia) tend to scale as the third power of the characteristic length. Therefore, at micro/nanometer scales, the surface effects are predominant, whereas the volume effects are negligible. The common definitions of macro, micro, and nanoscales are as follows. Length scales in the range from 1 mm down to 100 nm are usually called the microscale, while length scales in the range from 100 nm down to 1 nm are called the nanoscale. Length scales larger than 1 mm are the macroscale and length scales smaller than 1 nm are the atomic scale.

Recent advances in micro/nanotechnology have made it possible to design functional micro/nanostructured surfaces with micro/nanotopography providing low adhesion. Surface topography is characterized by the deviations of a surface from a perfectly flat plane as a result of roughness, porosity etc. Some examples of such functional surfaces are superhydrophobic (lotus-effect) surfaces which are extremely water repellent, and gecko-effect surfaces which exhibit controlled adhesion as a result of their surface micro/nanotopography. Many of these surfaces are inspired by materials and surfaces found in living nature and are called biomimetic surfaces. Advances in nanotechnology has enabled to create materials such as engineered cementitious composites and metal matrix composites which have shown higher performance, durability and sustainability than regular concrete and alloys.

The functional surfaces for water and ice-related applications are of special importance in a place like Milwaukee in Wisconsin, which is a hub of the fresh water industry due to its proximity to the Great Lakes, as well as the multitude of water-related industries. Metallic materials (such as steel, brass and cast iron) are common raw materials for the water industry. Milwaukee also receives an annual average snowfall of 133 cm due to the lake effect as well as the Northern latitudes. The salt used for ice and snow removal is corrosive and can affect the durability and performance of metallic components for example, automobile components, metallic reinforcements, or water pipelines.

Concrete is another common material used in the construction of buildings and pavements. Dry concrete is porous and hydrophilic. When the absorbed water freezes in cold weather, it expands and cracks the concrete. This freeze-thaw cycling of the concrete leads to its deterioration and failure. Making the concrete water repellent can reduce or prevent water penetration into the pores. Rendering metallic surfaces hydrophobic can reduce exposure to water as well as corrosive aqueous solutions. Concrete and metallic surfaces with ice-repellant properties make ice removal easy, as well as reduce the need for corrosive salts. Due to the importance of these materials, the present study is concentrated on the interaction of micro/nanostructured metallic materials and concrete with water and ice.

In order to understand the structure-property relationships in these novel materials and surfaces, it is important to study the fundamental aspects of how micro/nanotopography affects surface properties at the macroscale. The surface micro/nanotopography can be viewed as a combination of spatial patterns, while small amplitude fast vibrations constitute periodic temporal patterns. A vibration is said to be fast or slow by comparing it against the natural

oscillations of the physical system it acts on. The frequency of a fast vibration is much greater than the natural frequency of the oscillations of the system.

The method of separation of motions is a mathematical tool used to study dynamics of rigid bodies in rapidly oscillating fields. Using this method, the fast vibrations can be substituted by an effective force. This effective force is obtained by averaging the vibrations over their time period. The simplest mechanical example of vibrations manifesting as an effective force is the vibration-induced stabilization of an inverted pendulum. The method of separation of motions offers a powerful technique to study the effect of small patterns on macroscopic state or properties of a system. This method can be used in the areas of surface engineering, physical chemistry, and material science due to a similarity between the effects of small amplitude patterns and small fast vibrations.

Closely correlated to the superhydrophobicity is the property of the icephobicity. A surface is said to be icephobic if the ice does not form readily on the surface, or if the ice formed on the surface can be easily removed on account of low adhesion. Both the superhydrophobicity and the icephobicity are manifestation of the adhesion. Surface micro/nanotopography affects the adhesion of liquids to solids (in the case of the superhydrophobicity), as well as solids to solids (in the case of the icephobicity). The research on the icephobicity is still in its infancy, having only gained popularity in the 2010s.

1.1 Objectives of the Dissertation

The main goal of this dissertation is to study the effects of surface topography and vibrations on wetting and adhesion properties in application to the novel areas of surface

engineering such as the hydrophobicity, corrosion resistance and the icephobicity. The particular objectives of this work can be listed as follows:

First, to establish a relationship between small amplitude fast vibrations and small amplitude spatially periodic patterns. For example, the method of separation of motions can be employed to demonstrate that small fast vibrations and spatially periodic patterns can be substituted by an effective force or energy, and Kirchhoff's dynamical analogy can be employed to establish an isomorphism between rigid body dynamics and the static bending shape of an elastic flexible beam.

Second, to study the effects of both vibrations and surface topography on the wetting properties including the contact angle and the surface free energy, and also to understand their structure-property relationships. The method of separation of motions will be used to study the structure-property relationships in novel materials and surfaces. Small patterns and vibrations will be averaged using the method of separation of motions and be substituted by an effective force or energy term.

Third, based on the understanding of the structure-property relationships, apply this to novel materials. In particular, I will study how desired surface topography could control the wettability of concrete with the goal of producing hydrophobic concrete. Dry concrete, which is normally a porous hydrophilic material, absorbs water. This is undesirable, especially in cold conditions. Concrete will be hydrophobized by controlling the surface topography as well as the surface free energy using appropriate additives.

Fourth, based on the understanding of the structure-property relationships, apply this to metallic materials to study how producing material with desired surface topography could

control the wettability and thus prevent corrosion of metallic materials. Metals and alloys easily undergo corrosion to return to their stable oxidized native states. Metals and alloys normally have high energy surfaces which are easily wetted by corrosive aqueous solutions. Such surfaces will be hydrophobized by controlling the surface topography as well as the surface free energy to reduce wettability and thereby prevent corrosion.

Fifth, based on the understanding of the structure-property relationships, to study how producing material with desired surface topography could control the icephobicity of the surface. This study will be focused on concrete which is normally hydrophilic. Water absorbed into the pores of dry concrete expands upon freezing. This can lead to crack formation and deterioration. Concrete will be rendered icephobic by controlling the surface topography as well as the surface free energy.

1.2 Organization of the Dissertation

In Chapter 2, the general concepts related to wetting such as the equilibrium contact angle, models of wetting and contact angle hysteresis, and the effect of surface topography on wetting will be reviewed. This will be followed by a review of the general concepts related to vibrational mechanics. This chapter will introduce the method of separation of motions, which is a powerful mathematical tool used to study dynamics of rigid bodies. The method of separation of motions will be used to formulate an effective force that can be substituted for small fast vibration. This force will be obtained by averaging the vibration over its time period.

In Chapter 3, a relationship between small amplitude fast vibrations and small amplitude spatially periodic patterns will be established. The method of separation of motions discussed in Chapter 2 will be used demonstrate that both small fast vibrations and spatially periodic patterns

can be substituted by an effective force or energy. The method of separation of motions will be applied to various examples such as inverted pendulum, multiple pendulums and flexible rope. The latter will be studied by a specially designed experimental setup. The method of separation of motions will be used to understand the structure-property relationships in materials and surfaces, in particular the wetting properties such as contact angle and surface free energy, and fluid flow through membranes. Kirchhoff's analogy will also be used to establish the relationship between vibrations and small spatial patterns. The bending of a tensile-loaded slender elastic flexible beam will be shown to be similar to the dynamics of an inverted pendulum. This analogy will be used to obtain the geometrical conditions for stability (unbuckled state) of such a beam.

In Chapter 4, the understating of the structure-property relationships developed in Chapter 3 will be used to study how desired surface topography could control the wettability of concrete. Hydrophobic concrete samples will be prepared by controlling the surface topography as well as the surface free energy. The ability to repel incoming liquid droplets is an important wetting characteristic of a hydrophobic surface, as well as a desirable property for a ubiquitous construction material such as concrete. Therefore the dynamics of impacting water droplets on the hydrophobic concrete will be studied by a specially designed experiment and also modeled theoretically. The performance of hydrophobic concrete with different droplet impact velocities, as well as in two different environmental conditions will be investigated.

In Chapter 5, the understating of the structure-property relationships developed in Chapter 3 will be used to study how desired surface topography could control the wettability and thus prevent corrosion of metallic materials. The chapter in particular deals with the material ADI90 cast iron which is of interest to the fresh water industry. First, the concepts of electro-chemical corrosion will be briefly discussed. This will be followed by a review of the recent

literature correlating superhydrophobicity and corrosion resistance. The effects of surface roughness and wettability on corrosion will be studied theoretically. Corrosion rate experiments will be carried out on cast iron samples with different surface roughness and wetting properties. The experimental data will be used to validate the theoretical predictions.

In Chapter 6, the understating of the structure-property relationships developed in Chapter 3 will be used to study the effect of surface topography on the icephobicity of materials, in particular the concrete. First, the three aspects of icephobicity and the hydrophobic interactions essential for designing an icephobic surface will be discussed. This will be followed by a brief review of the recent literature in the area of icephobicity. The icephobicity of concrete based on the repulsion of incoming water droplets before freezing, as well as the ice adhesion strength will be investigated. Finally, structure-property relationships as well as the experimental results will be used to study how the three aspects of icephobicity can be optimized by controlling the surface topography and the wetting properties.

In Chapter 7, the potential for biomimetic icephobicity of skunk cabbage, and the effect of surface topography on its icephobicity will be investigated. Skunk cabbage is a plant that is commonly found in the marshes of Wisconsin. The plant is known for its ability to melt snow. The first section of this chapter will review the literature on the heat generating property of the skunk cabbage. Next, the surface micro/nanotopography of the leaf and spathe of the plant will be investigated using scanning electron microscopy. A theoretical model correlating the surface topography with the heat transfer rate will be developed to better understand the effect of surface topography on the icephobicity and the potential for biomimetic icephobicity of skunk cabbage.

The conclusions of this dissertation will be summarized in Chapter 8.

CHAPTER 2: CONCEPTS OF WETTING AND VIBRATIONAL MECHANICS

As discussed in the previous chapter, the goals to this dissertation are to study the effect of surface topography and vibrations on wetting properties, to establish a relationship between small amplitude fast vibrations and small amplitude spatially periodic patterns, to understand the structure-property relationships in materials and surfaces, and to apply this to produce hydrophobic, icephobic and corrosion resistant surfaces. To achieve these, it is important to understand the concept of wetting and vibrational mechanics. In the first part of this chapter, the terms such as the contact angle, contact angle hysteresis, superhydrophobicity are briefly discussed.

The second part of this chapter deals with the vibrational mechanics. Vibrational mechanics is a general approach to study the effect of vibrations on nonlinear mechanical systems. This approach uses the method of separation of motions to study dynamics. The method of separation of motions is a powerful mathematical tool used to solve problems of rigid body dynamics. This method will be discussed in the second part of the chapter.

2.1 Contact Angle and Models of Wetting

Contact angle (CA) is the main parameter characterizing wettability of a solid surface by a liquid, such as water. Hydrophilic surfaces have water CA less than 90° while hydrophobic surfaces have water CA greater than 90° . For an ideally smooth, chemically homogenous surface, the equilibrium contact angle (θ_0) of a liquid droplet (say, of water) is given by the Young equation

$$\cos \theta_0 = \frac{\gamma_{SA} - \gamma_{SW}}{\gamma_{WA}} \quad (2.1)$$

where γ_{SA} , γ_{SW} , and γ_{WA} are the surface free energies (also called as surface or interfacial tensions) of the solid-air, solid-water, and water-air interfaces [1,2].

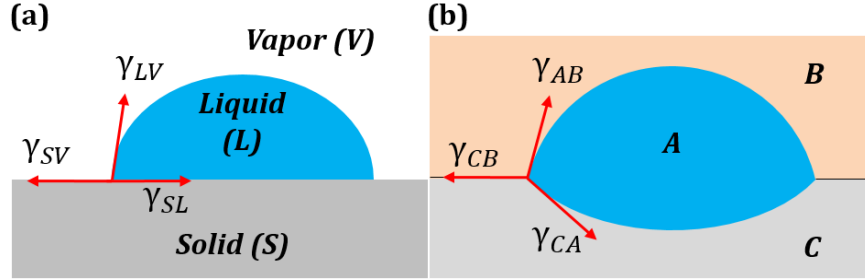


Figure 2.1. (a) Surface tension forces at the three-phase line on a non-deformable solid surface. The vertical components of the forces remain unbalanced. (b) The equilibrium of surface tensions at the three-phase line of liquid phases A, B and C. Note the deformation of the interface between A and C.

Note that Young's equation implies only the equilibrium, at the solid-liquid-vapor three-phase (triple) line, of the horizontal (parallel to the solid surface) components of the surface tension forces, $\gamma_{LV} \cos \theta = \gamma_{SV} - \gamma_{SL}$, whereas the vertical component $\gamma_{LV} \cos \theta$ remains unbalanced. It is however understood that this unbalanced component may result in the deformation of the substrate or even in substrate's dissolution under the droplet. The balance of forces on a liquid substrate (i.e., in a three-phase liquid system) is described by the so-called Neumann's triangle of forces [3]. Figure 2.1a shows the surface tension forces on a solid substrate, while Figure 2.1b shows the equilibrium of surface tension forces in a three-liquid system [4].

On real surfaces with roughness and chemical heterogeneity, the observed contact angles are much different from θ_0 [5,6]. The effect of roughness and chemical heterogeneity on CA is incorporated into two models of wetting, namely the Wenzel [7] and Cassie-Baxter [8] models.

The Wenzel model gives the effective contact angle on a rough, chemically homogenous surface. According to the Wenzel model, the effective contact angle θ_w of a rough surface is given by

$$\cos \theta_w = R_f \cos \theta_0 \quad (2.2)$$

where the so-called roughness factor $R_f \geq 1$ is the ratio of the solid surface area to the projected area. It can be seen from Eq. 2.2 that roughening a hydrophobic surface makes it more hydrophobic (larger CA), while roughening a hydrophilic surface makes it more hydrophilic (lower CA). In the Wenzel wetting state, the surface below the droplet is completely wetted by the liquid, creating a homogenous solid-liquid interface (Figure 2.2a).

The Cassie-Baxter model explains how interfacial heterogeneities affect wetting. For a smooth but chemically heterogeneous surface consisting of n components each with an area fraction f_i and equilibrium CA θ_i , the effective contact angle θ_{CB} is given by[9]

$$\cos \theta_{CB} = \sum_{i=1}^n f_i \cos \theta_i \quad (2.3)$$

If some air is trapped between the rough solid surface and the liquid, then the effective contact angle can be obtained by modifying Eq. 2.3

$$\cos \theta_{CB} = r_f f_{SL} \cos \theta_0 - 1 + f_{SL} \quad (2.4)$$

where r_f is the roughness factor of the wet area, and $0 \leq f_{SL} \leq 1$ is the fractional solid-liquid interfacial area. Note that Eq. 2.4 applies only when cavities on the surface harbor pockets of air and there is no liquid penetration into the cavities [10]. In the Cassie-Baxter state, the interface

below the droplet is non-homogenous involving solid, water, and air pockets (Figure 2.2b). In the so-called “impregnating” Cassie wetting regime, the cavities on the surface are impregnated with water [11]. The effective contact angle is

$$\cos \theta_{CB} = 1 + f_{SL} (\cos \theta_0 - 1) \quad (2.5)$$

The highest possible contact angle on any smooth solid is believed to be 119° [12]. Therefore, only a rough surface may have larger contact angles. Non-homogenous wetting occurs only when the CA is greater than $\cos^{-1} \left(\frac{f_{SL} - 1}{r_f - f_{SL}} \right)$ [11].

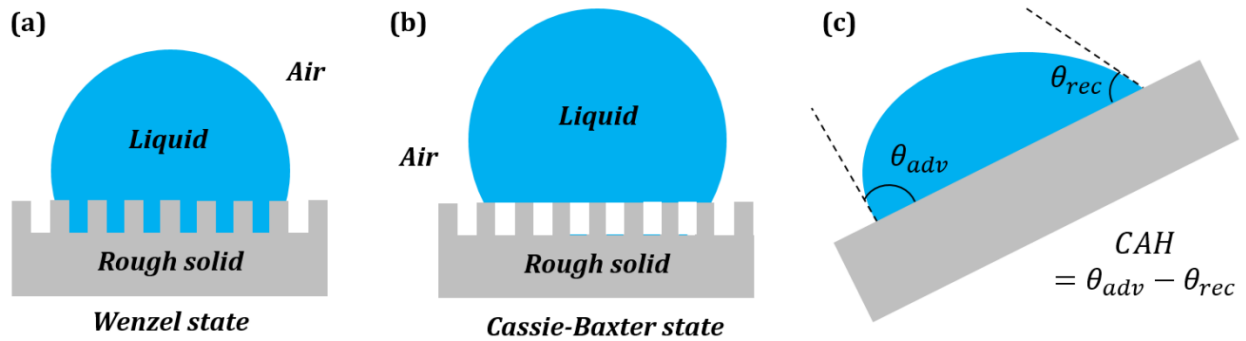


Figure 2.2. (a) A liquid droplet in Wenzel state, with a homogenous solid-liquid interface below the droplet. (b) A liquid droplet in Cassie-Baxter state, with a composite solid-liquid-vapor interface below the droplet. (c) Contact angle hysteresis (CAH) measurement by tilting the droplet. The maximum or advancing (θ_{adv}) and minimum or receding (θ_{rec}) contact angles are measured at the front and rear of a moving droplet respectively.

2.2 Contact Angle Hysteresis

When contact occurs with a rough or chemically heterogeneous surface (and practically all surfaces are rough or heterogeneous to a certain extent), the contact angle can attain a range of values, demonstrating hysteresis: $\theta_{rec} \leq \theta \leq \theta_{adv}$, where θ_{rec} and θ_{adv} denote the receding and advancing contact angles, respectively. Contact angle hysteresis (CAH) is the difference between

the maximum CA (θ_{adv} , for example, in front of a moving droplet) and minimum CA (θ_{rec} , for example, at the rear of a moving droplet).

$$CAH = \theta_{adv} - \theta_{rec} \quad (2.6)$$

The contact angles can be measured also on a tilted surface (Figure 2.2c), although it is recognized that the values measured in this way do not always provide true values of the advancing and receding angles [13]. Contact angle hysteresis is small when the solid-liquid adhesion is small and it is large when the adhesion is large. This makes contact angle hysteresis an important parameter characterizing adhesion, wetting, and energy dissipation during the droplet flow.

When the concept of contact angle hysteresis was originally introduced, the phenomenon was associated with surface contaminants. This phenomenon was described in 1891 in a letter from a German scientist Agness Pockels, who had no formal education and made observations on dishes in a kitchen sink. She observed that water droplets behaved differently on clean and contaminated glass surfaces. She wrote a letter to Lord Rayleigh, who published it in the journal *Nature*: “The surface tension of a strongly contaminated water surface is variable; that is, it varies with the size of the surface. The minimum of the separating weight attained by diminishing the surface is to the maximum, according to my balance, in the ratio of 52:100. If the surface is further extended, after the maximum tension is attained, the separating weight remains *constant*, as with oil, spirits of wine, and other normal liquids. It begins, however, to diminish again, directly the partition is pushed back to the point of the scale at which the increase of tension ceased. The water surface can thus exist in two sharply contrasted conditions; the

normal condition, in which the displacement of the partition makes no impression on the tension, and the *anomalous* condition, in which every increase or decrease alters the tension.” [14]

This phenomenon was later investigated and Adam and Jessop (1925) who wrote: “In the extreme cases, the angle when the liquid is advancing over the solid may be 60° greater than when it is receding. It is not necessary that there should be actual motion, for a force on the liquid tending to move it has the same effect. The phenomenon is obvious on inspection of a drop of water on slightly dirty glass plate; it appears to have been first described in detail by Pockels... The cause of this dragging effect (often called “hysteresis” of the angle of contact) seems to us to lie, not in any absorption of the liquid by the solid, but in a simple friction of the liquid on the surface.” [15]

Adam and Jessop [15] related contact angle hysteresis to the “friction force” per unit length of the three-phase line, F , acting upon the droplet in its motion as $\gamma_{LV} (\cos \theta_{adv} - \cos \theta_{rec}) = F$. Using similar models, Good [16], and Shepard and Bartell [17] investigated later the effect of surface roughness on contact angle hysteresis, which is similar to the effect of surface contamination or chemical heterogeneity.

The contact angle hysteresis is related to the more general phenomenon known as adhesion hysteresis, which is observed also during solid-solid contact. When two solid surfaces come in contact, the energy required to separate them is always greater than the energy gained by bringing them together, and thus the loading-unloading cycle is a thermodynamically irreversible dissipative process. The energy gained for surfaces coming to contact is greater than the energy required for their separation (or the work of adhesion) by the quantity ΔW , which constitutes the adhesion hysteresis. For a smooth surface, the difference between the two values of the interface

energy (measured during loading and unloading) is given by ΔW_0 . These two values are related to the advancing and receding contact angles of the smooth surface, assuming that for a smooth surface, the adhesion hysteresis is the main contributor into the contact angle hysteresis, plus a surface roughness term H_r [18]

$$\cos \theta_{adv} - \cos \theta_{rec} = \frac{\Delta W_0}{\gamma_{LV}} + H_r \quad (2.7)$$

A number of other quantitative theories of contact angle hysteresis have been developed by scientists including an important thermodynamic theory by Tadmor [2] involving the concept of line tension and used by several scientists [5,19-21]. While CA characterizes wetting during normal loading, CAH characterizes wetting during shear loading at the solid-liquid interface. Adhesion under both these types of loadings can be measured separately using the centrifugal adhesion balance.[22,23] The angle of tilt of the substrate at which a droplet deposited on it rolls off, called as the roll-off angle, is also used as a parameter to characterize the adhesion between a liquid and a surface.

2.3 Superhydrophobicity and Biomimetic Self-Cleaning Surfaces

The effect of surface roughness and chemical heterogeneity on CA was discussed in section 2.1, Surfaces that exhibit water CA in the range 120° to 150° are said to be overhydrophobic.[24] Surfaces that exhibit water CA greater than 150° and very low CAH ($<10^\circ$) are said to be superhydrophobic. However there are a number of important exceptions, such as the rose petal. The rose petal has high CA, often in the superhydrophobic region and, at the same time, strong adhesion with water and, therefore, large CAH. This is sometimes called the “petal effect” [25,26]. An alternative term suggested for the petal effect in the literature is the

“parahydrophobic state” [27]. Superhydrophobic surfaces have a non-homogeneous interface below the droplet, with pockets of air trapped on the surface. On superhydrophobic surfaces water beads up into a near-spherical shape. Underwater superhydrophobic surfaces help reduce drag and biofouling. Marmur [28] studied the thermodynamic feasibility of underwater superhydrophobic surfaces. A superhydrophilic (superwetting) surface is one on which water (liquid) spreads completely [29].

If an oil (or organic liquid) droplet makes a $CA > 90^\circ$ on a surface in air, then the surface is oleophobic. Otherwise the surface is oleophilic. If a surface makes oil $CA > 90^\circ$ while being immersed in water instead of air, the surface is said to be underwater oleophobic [30,31]. Liu et al. showed that a hydrophilic surface in air may become oleophobic in water [32]. Superoleophobic surfaces exhibit oil $CA > 150^\circ$. Surfaces that form robust composite interfaces and exhibit CA greater than 150° and low CAH for both polar and nonpolar liquids are said to be omniphobic [33].

An important application of superhydrophobicity is in self-cleaning surfaces. Self-cleaning surfaces are those surfaces which remain clean on account of their low adhesion to water. Water generally beads up and rolls off at the slightest tilt, carry away dirt off the self-cleaning surface. Self-cleaning surfaces were inspired by the remarkable self-cleaning mechanism (the so-called “lotus-effect”) exhibited by the lotus (*Nelumbo nucifera*) leaf. The hierarchical or multiscale roughness on the leaf surface is instrumental in the self-cleaning effect [34,35]. The adaxial surface of the lotus leaf consists of papillose epidermal cells which provide micrometer scale roughness. The leaf surface is also covered with epicuticular wax tubules while provide nanometer scale roughness. Applying the methods and systems found in nature to design

and study artificially engineered systems is called Biomimetics. The term “biomimetics” was coined by Otto Schmitt in 1957 [36].

Surface coatings of a number of superhydrophobic plant leaves are hydrophilic [37]. This is not what one would expect from Eq. 2.2, according to which, roughening a hydrophilic surface makes it more hydrophilic (lower CA). The superhydrophobicity in the above mentioned plant leaves is due to the so-called “re-entrant” surface texture [38,39]. For a re-entrant surface texture, the surface topography cannot be described by a function $z=f(x,y)$, and the vector projected normal to the x - y plane intersects the texture more than once [40]. Tuteja et al. [33] showed that robust omniphobic surfaces can be produced by using the re-entrant surface curvature on low surface energy solids.

Besides water-repellency and self-cleaning, the superhydrophobic surfaces have many emerging applications such as drag reduction in water flow [41], antifouling [42], oleophobicity [32], icephobicity [43-45], water filtering [46] and corrosion inhibition [47].

2.4 Geometric Interpretation of the Surface Tension at Equilibrium

The equilibrium of surface tensions was discussed in section 2.1, with the Young equation (Eq. 2.1) being derived from the balance of forces. The surface tension forces are not forces in the strictly mechanical sense of the word, because they are applied to the imaginary three-phase (triple) line in equilibrium instead of a physical body. Nosonovsky and Ramachandran [4] suggested treating tensions as generalized forces, i.e., the derivative of surface energy by a generalized coordinate, such as the position of a three-phase line. In that case there is no need to perceive surface tensions as applied to a particular object, but as vector quantities in general. It is known that both Young, Wenzel and Cassie equations can be derived from

variational principles [48]. A geometric interpretation of the surface tension balance extending the well-known Neumann's triangle approach was suggested. Phases are represented by points, while tensions are vectors connecting these points. When a three-phase line propagates (Figure 2.3a) for a short distance \vec{dr} , the change of free energy is given by the interfacial area γ times the scalar product of \vec{dr} by the normal to the three-phase line, \vec{n} in the plane of the interface: $dE = \gamma \vec{dr} \vec{n}$. The surface tension vector as a generalized force is a vector given by a derivative

$$\frac{d(\gamma \vec{dr} \vec{n})}{d\vec{r}} = \gamma \vec{n} \quad (2.8)$$

which is not a mechanical force and thus it is not applied to a particular point or a body.

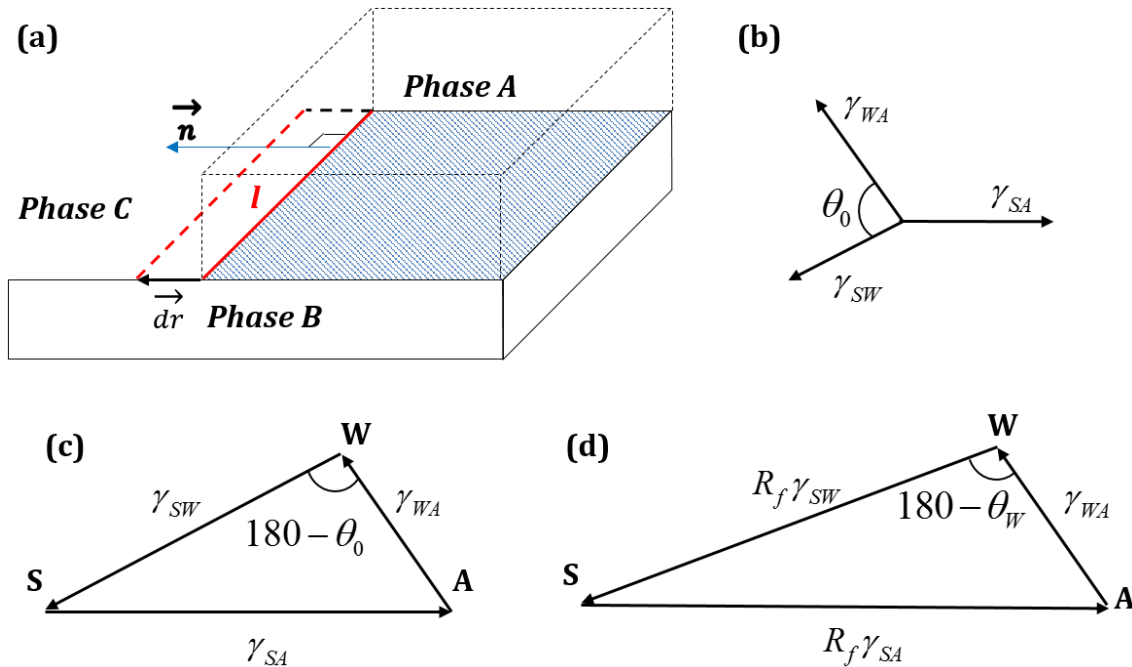


Figure 2.3. (a) When the interface between A and B is displaced along the vector \vec{dr} , the surface tension force acts on the three-phase line l in the direction of the normal \vec{n} . (b) Equilibrium of surface tension vectors at the three-phase line. (c) The Neumann's triangle for a three-phase system. (d) The Neumann's triangle for a three-phase system in the Wenzel state.

Consider a droplet of water placed on a solid surface in air. Let the points S, A and W denote the three phases solid, air and water respectively. The equilibrium of the surface tensions is shown in Figure 2.3b. The surface tensions can be represented as the sides of the triangle with vertices S, A and W (Figure 2.3c). Mechanical equilibrium of the droplet requires that the vector sum of the surface tensions be zero i.e., $\overrightarrow{\gamma_{SA}} + \overrightarrow{\gamma_{WA}} + \overrightarrow{\gamma_{SW}} = 0$ [4].

The Neumann's vector triangle for a droplet in the Wenzel wetting state is shown in Figure 2.3d. The water-air interface which remains unaffected by the roughness and hence its surface tension remains the same. The roughness effectively changes the solid-water and solid-air surface tensions by a factor R_f . For a smooth, chemically heterogeneous solid surface which consists of two different materials S_1 and S_2 , with area fractions f_1 and f_2 (Figure 2.4a,b) the droplet is in the Cassie-Baxter wetting state. The effect of surface heterogeneity can be interpreted as a linear combination of vectors $\overrightarrow{\gamma_{S_1W}}, \overrightarrow{\gamma_{S_1A}}$ and $\overrightarrow{\gamma_{S_2W}}, \overrightarrow{\gamma_{S_2A}}$ which correspond to two components of the interface, with the weight factors of f_1 and f_2 (Figure 2.4c) [4].

A similar approach to the contact angle hysteresis leads to the vector triangle as shown in Figure 2.4d. The change in the solid-air interfacial tension can be obtained as $\overrightarrow{\Delta\gamma_{SA}} = \overrightarrow{\gamma_{SA}^{rec}} - \overrightarrow{\gamma_{SA}^{adv}}$. Similarly the change in the solid-water interfacial tension is $\overrightarrow{\Delta\gamma_{SW}} = \overrightarrow{\gamma_{SW}^{rec}} - \overrightarrow{\gamma_{SW}^{adv}}$. It is visible from the triangle that a range of contact angles are possible under a constraint that $\overrightarrow{\gamma_{WA}}$ remains constant in magnitude. The contact angle hysteresis $\Delta\theta = \theta_{adv} - \theta_{rec}$ can be interpreted as the rotation of the vector $\overrightarrow{\gamma_{WA}}$ in Figure 2.4d [4].

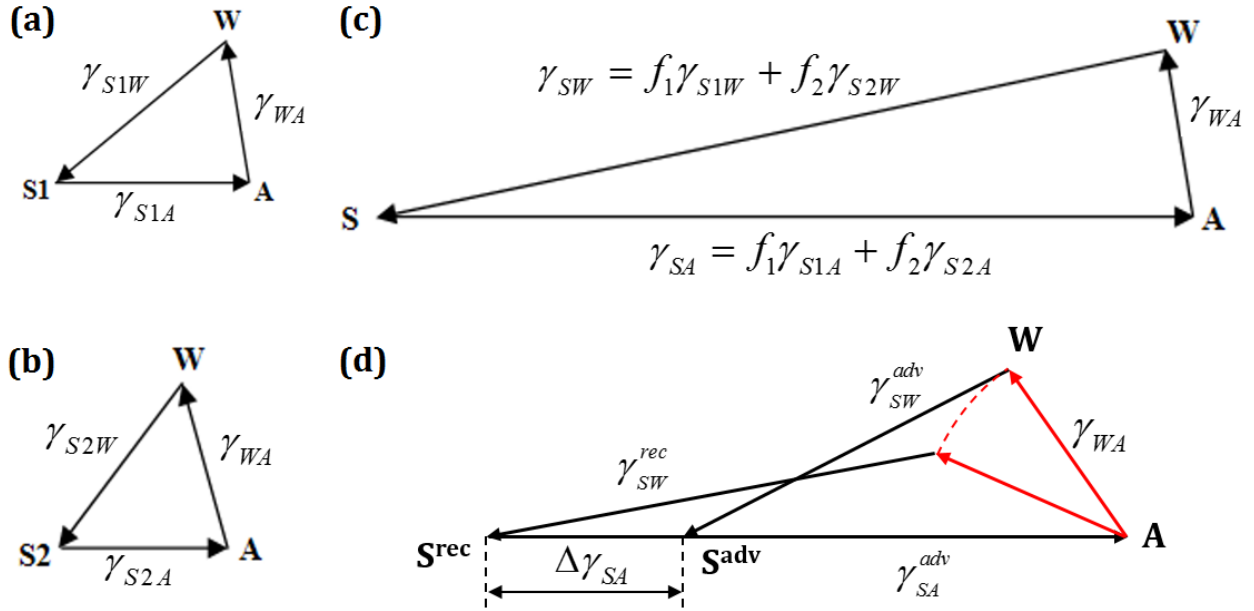


Figure 2.4. The Neumann's triangles for the three-phase systems (a) S1AW, and (b) S2AW respectively. (c) The Neumann's triangle for a three-phase Cassie-Baxter state. (d) Contact angle hysteresis represented using Neumann's triangle as a rotation of the vector $\overrightarrow{\gamma_{wa}}$. A range of contact angles are possible under a constraint that $|\overrightarrow{\gamma_{wa}}|$ remains constant.

The same approach can be used for four phase systems. If the four phases are solid (S), water (W), oil (O) and air (A), the three-phase systems SWO, WOA, SWA and SWA can be represented by four triangles as discussed above. If the four phases exists in mechanical equilibrium (Figure 2.5a), the pyramid (or tetrahedron) SAOW with the vectors representing the interfacial tensions can be drawn as shown in Figure 2.5b. If the vector triangles SWA and SWO are drawn, the surface tension of oil-water interface can be inferred from the magnitude of $\overline{\gamma_{ow}}$ [4].

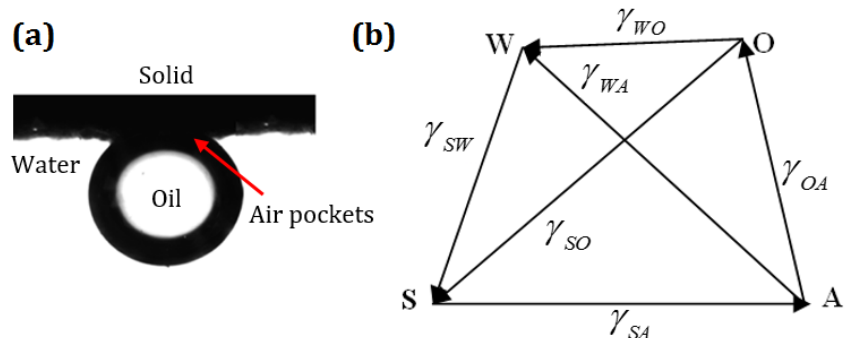


Figure 2.5. (a) A four-phase system. The pockets of air trapped on the solid surface constitutes the fourth phase [31]. (b) Tetrahedron of surface tension vectors in 3D space for a four-phase system.

In the previous sections, the concepts related to wetting were discussed. It was seen that surface patterns (surface roughness and chemical heterogeneity) can affect the wetting state of the surface. The effect of surface patterns is incorporated into the two models of wetting, namely, the Wenzel and the Cassie-Baxter models. In the following section an important mathematical tool from mechanics, namely, the method of separation of motions, is discussed. This method which can be used to substitute the effect of small vibrations with an equivalent force, is not well-known outside the domain of mechanics. The method of separation of motions and idea of averaging the small patterns (temporal or spatial) is central to this dissertation, and is used to substitute small patterns with an effective force or energy.

2.5 Separation of Motions and Effective Forces

In the previous sections, the concepts and terms related to wetting were discussed. To study the relationship between surface topography and vibrations, and their effect on wetting, as well as to study the dynamics of non-wetting droplets over vibrating liquid, it is necessary to understand the method of separation of motions and the concepts of vibrational mechanics.

The method of separation of motions was first suggested by Kapitza [49] to study the stability of a pendulum on a vibrating foundation and then generalized for the case of an arbitrary motion in a rapidly oscillating field by Landau and Lifshitz [50]. Kapitza thought of such systems to be in a state of slow oscillation with a fast vibration superimposed upon it. The effect of fast vibrations can be isolated as a change in the effective potential energy of the system.

Consider a material point with mass m in a potential energy field $\Pi(x)$, where x is the spatial coordinate, with the minimum corresponding to the stable equilibrium. The force acting on the mass is given by $-d\Pi/dx$, therefore, the equation of motion of the particle is $m\ddot{x} = -d\Pi/dx$. In addition to the time-independent potential field $\Pi(x)$, a “fast” external periodic force $f \cos \Omega t$ acts upon the mass with a small amplitude f and high frequency $\Omega \gg \sqrt{(d^2\Pi/dx^2)/m}$. The equation of motion of the particle becomes

$$m\ddot{x} = -(d\Pi/dx) + f \cos \Omega t \quad (2.9)$$

The particle will travel a smooth path due to the slow force $-d\Pi/dx$, and at the same time execute small oscillations $\xi(t)$ of frequency Ω about the smooth path due to the fast force $f \cos \Omega t$. The location of the mass can be expressed as,

$$x(t) = X(t) + \xi(t) \quad (2.10)$$

where $X(t)$ describes the smooth path of the particle averaged over the fast oscillations. The mean value $\bar{\xi}(t)$ of the fast oscillation over its period $2\pi/\Omega$ is zero, whereas $X(t)$ changes only slightly during the same period.

$$\bar{\xi}(t) = \frac{\Omega}{2\pi} \int_0^{2\pi/\Omega} \xi(t) dt = 0 \quad (2.11)$$

$$\bar{X}(t) \approx X(t) \quad (2.12)$$

Therefore the mean location of the mass can be written as

$$\bar{x}(t) = \bar{X}(t) + \bar{\xi}(t) \approx X(t) \quad (2.13)$$

and the second derivative

$$\ddot{\bar{x}}(t) \approx \ddot{X}(t) \quad (2.14)$$

Substituting Eq. 2.10 in Eq. 2.9 and using the Taylor series first-order terms in powers of ξ

$$m\ddot{X} + m\ddot{\xi} = -\frac{d\Pi}{dx} - \xi \frac{d^2\Pi}{dx^2} + f \cos \Omega t + \xi \frac{\partial(f \cos \Omega t)}{\partial X} \quad (2.15)$$

The slow and fast terms in Eq. 2.15 must separately be equal. The second derivative of small fast oscillations $\ddot{\xi}$ is proportional to Ω^2 which is a large term. On the other hand, the terms on the right hand side of Eq. 2.15 containing the small ξ can be neglected. The term $-d\Pi/dx$ is a slow restoring force. The remaining fast terms can be equated, $m\ddot{\xi} = f \cos \Omega t$. Integrating this equation with respect to time t ,

$$\xi = -\frac{f \cos \Omega t}{m\Omega^2} \quad (2.16)$$

Averaging Eq. 2.15 with respect to time, substituting the relation $\frac{\Omega}{2\pi} \int_0^{2\pi/\Omega} f \cos \Omega t dt = 0$,

and combining Eq. 2.11 to 2.14, and Eq. 2.16 gives,

$$m\ddot{X} = -\frac{d\Pi}{dX} + \xi \overline{\frac{\partial(f \cos \Omega t)}{\partial X}} = -\frac{d\Pi}{dX} - \frac{1}{m\Omega^2} \overline{f \cos \Omega t} \frac{\partial(f \cos \Omega t)}{\partial X} \quad (2.17)$$

$$m\ddot{X} = -\frac{d\Pi}{dX} - \frac{1}{2m\Omega^2} \overline{\frac{\partial(f \cos \Omega t)^2}{\partial X}}$$

This can be written as $m\ddot{X} = -\frac{d\Pi_{eff}}{dX}$ where Π_{eff} is an effective potential energy given by

$$\Pi_{eff} = \Pi + \frac{1}{2m\Omega^2} \frac{\Omega}{2\pi} \int_0^{2\pi/\Omega} (f \cos \Omega t)^2 dt = \Pi + \frac{f^2}{4m\Omega^2} = \Pi + \frac{m}{2} \bar{\xi}^2 \quad (2.18)$$

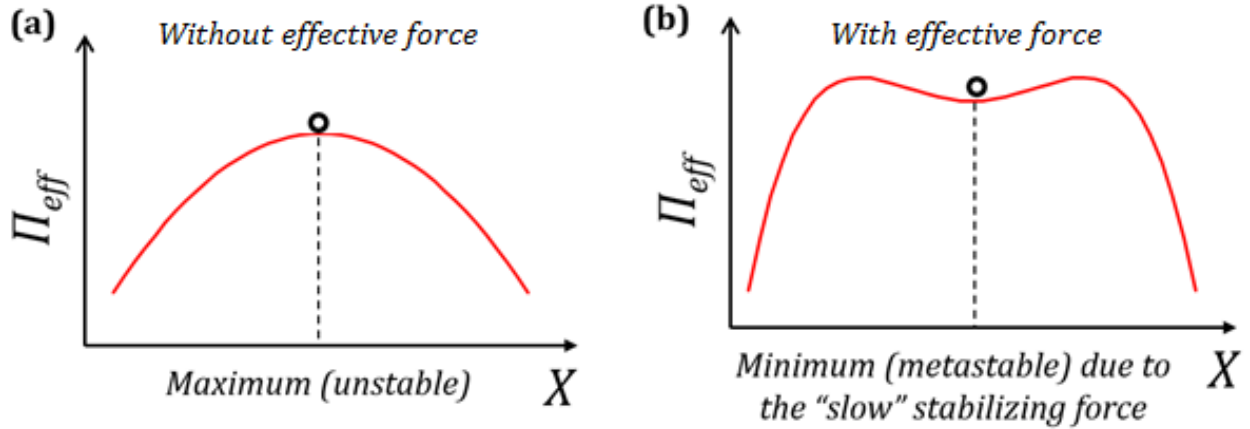


Figure 2.6. (a) Unstable equilibrium corresponding to the maximum potential energy (b) A metastable equilibrium due to the stabilizing effect of the external force.

Thus the effect of fast vibrations ξ when averaged over the time period $2\pi/\Omega$ is equivalent to the additional term $m\bar{\xi}^2/2$ on the right hand side in Eq. 2.18. This term is the mean kinetic energy of the system under fast oscillations. Thus small fast vibrations can be substituted by an

additional term in the potential energy resulting in the same effect oscillations have on the system. The most interesting case is when this term affects the state of the equilibrium of a system. Let us say, in the absence of vibrations a system has an effective potential energy $\Pi_{eff} = \Pi$ with a local maximum of the potential energy (Figure 2.6a). Vibrations can bring this system to a stable equilibrium due to the additional term discussed before, creating a local minimum of the potential energy (Figure 2.6b). In such cases the small fast vibrations have a stabilizing effect on the state of equilibrium.

2.6 Vibrational Mechanics

Blekhman [51] has applied the method of separation of motions to many mechanical systems and suggested what he called the “vibrational mechanics” as a tool to describe diverse range of effects in the mechanics of solid and liquid media, from effective “liquefying” of the granular media which can flow through a hole like a liquid when on a vibrating foundation to the opposite effect of “solidifying” liquid by jamming a hole in a vessel on a vibrating foundation, to vibro-synchronization of the phase of two rotating shafts on a vibrating foundation.

Blekhman [51] has also suggested an elegant interpretation of the separation of motions. According to his interpretation, there two different observers who can look at the vibrating system. One is an ordinary observer in an inertial frame of reference who can see both small, ξ and large, X , oscillations. The other one is a “special” observer in a vibrating frame of reference, who does not see the small-scale motion ξ , possibly, due to a stroboscopic effect or just because his vision is not sensitive enough to see the small scale motion. As a result, what is seen for the ordinary observer as an effect of the fast small vibrations is perceived by the special observer as an effect of some new effective force. This fictitious force is similar to the inertia force which is

observed by observers in a non-inertial frame of reference. Furthermore, when the stabilizing effect occurs, the special observer attributes the change in effective potential energy to fictitious slow stabilizing forces or moments. The additional slow stabilizing force for the system (or torque for rotational systems) V can be written as

$$V = -\frac{\partial}{\partial X} \left(\frac{1}{2m\Omega^2} \frac{\Omega}{2\pi} \int_0^{2\pi/\Omega} (f \cos \Omega t)^2 dt \right) = -\frac{\partial}{\partial X} \left(\frac{f^2}{4m\Omega^2} \right) \quad (2.19)$$

The method of separation of motions is a powerful tool to substitute small scale effects with an equivalent force or energy averaged over temporal or spatial domains. The effective potential energy in Eq. 2.18 and the effective stabilizing force in Eq. 2.19 were obtained as an average over the time period. The method of separation of motions as well as Eq. 2.18 and Eq. 2.19 will be frequently revisited in this dissertation.

2.7 Conclusion

In this chapter, the concepts of wetting and vibration mechanics were reviewed. The method of separation of motions was discussed. Using this method, small fast vibrations can be substituted by an effective force or energy. The equations for effective force and energy were formulated. In the next chapter, the method of separation of motions will be used to study the similarity between small amplitude fast vibrations and surface micro/nanotopography.

2.8 References

- [1] Young, T. An Essay on the Cohesion of Fluids. *Philosophical Transactions of the Royal Society of London (1776-1886)* **1805**, 95, 65-87.
- [2] Tadmor, R. Line Energy and the Relation between Advancing, Receding, and Young Contact Angles. *Langmuir* **2004**, 20, 7659-7664.

- [3] de Gennes, P.; Brochard-Wyart, F.; Quéré, D. *Capillarity and Wetting Phenomena: Drops, Bubbles, Pearls, Waves*; Springer: New York, 2004.
- [4] Nosonovsky, M.; Ramachandran, R. Geometric Interpretation of Surface Tension Equilibrium in Superhydrophobic Systems. *Entropy* **2015**, *17*, 4684-4700.
- [5] Cho, K.L.; Wu, A.H.; Liaw, I.I.; Cookson, D.; Lamb, R.N. Wetting Transitions on Hierarchical Surfaces. *Journal of Physical Chemistry C* **2012**, *116*, 26810-26815.
- [6] Marmur, A. Wetting on Hydrophobic Rough Surfaces: To be Heterogeneous or Not to be? *Langmuir* **2003**, *19*, 8343-8348.
- [7] Wenzel, R.N. Resistance of Solid Surfaces to Wetting by Water. *Ind. Eng. Chem.* **1936**, *28*, 988-994.
- [8] Cassie, A.B.D.; Baxter, S. Wettability of Porous Surfaces. *Trans. Faraday Soc.* **1944**, *40*, 546-551.
- [9] Bormashenko, E. Wetting Transitions on Biomimetic Surfaces. *Philosophical Transactions of the Royal Society A-Mathematical Physical and Engineering Sciences* **2010**, *368*, 4695-4711.
- [10] Milne, A.J.B.; Amirfazli, A. The Cassie Equation: How it is meant to be used. *Adv. Colloid Interface Sci.* **2012**, *170*, 48-55.
- [11] Bico, J.; Thiele, U.; Quere, D. Wetting of Textured Surfaces. *Colloids and Surfaces A-Physicochemical and Engineering Aspects* **2002**, *206*, 41-46.
- [12] Nishino, T.; Meguro, M.; Nakamae, K.; Matsushita, M.; Ueda, Y. The Lowest Surface Free Energy Based on -CF₃ Alignment. *Langmuir* **1999**, *15*, 4321-4323.
- [13] Krasovitski, B.; Marmur, A. Drops Down the Hill: Theoretical Study of Limiting Contact Angles and the Hysteresis Range on a Tilted Plate. *Langmuir* **2005**, *21*, 3881-3885.
- [14] Rayleigh. Surface Tension. *Nature* **1891**, *43*, 437-439.
- [15] Adam, N.K.; Jessop, G. CCL-Angles of Contact and Polarity of Solid Surfaces. *J. Chem. Soc. , Trans.* **1925**, *127*, 1863-1868.
- [16] Good, R.J. A Thermodynamic Derivation of Wenzel's Modification of Young's Equation for Contact Angles; Together with a Theory of Hysteresis. *J. Am. Chem. Soc.* **1952**, *74*, 5041-5042.
- [17] Bartell, F.E.; Shepard, J.W. Surface Roughness as Related to Hysteresis of Contact Angles. II. the Systems Paraffin-3 Molar Calcium Chloride Solution-Air and Paraffin-Glycerol-Air. *J. Phys. Chem.* **1953**, *57*, 455-458.
- [18] Nosonovsky, M. Model for Solid-Liquid and Solid-Solid Friction of Rough Surfaces with Adhesion Hysteresis. *J. Chem. Phys.* **2007**, *126*, 224701.

- [19] Dirany, M.; Dies, L.; Restagno, F.; Leger, L.; Poulard, C.; Miquelard-Garnier, G. Chemical Modification of PDMS Surface without Impacting the Viscoelasticity: Model Systems for a Better Understanding of elastomer/elastomer Adhesion and Friction. *Colloids and Surfaces A-Physicochemical and Engineering Aspects* **2015**, *468*, 174-183.
- [20] Belman, N.; Jin, K.; Golan, Y.; Israelachvili, J.N.; Pesika, N.S. Origin of the Contact Angle Hysteresis of Water on Chemisorbed and Physisorbed Self-Assembled Monolayers. *Langmuir* **2012**, *28*, 14609-14617.
- [21] Ramachandran, R.; Sobolev, K.; Nosonovsky, M. Dynamics of Droplet Impact on Hydrophobic/Icephobic Concrete with the Potential for Superhydrophobicity. *Langmuir* **2015**, *31*, 1437-1444.
- [22] Tadmor, R.; Bahadur, P.; Leh, A.; N'guessan, H.E.; Jaini, R.; Dang, L. Measurement of Lateral Adhesion Forces at the Interface between a Liquid Drop and a Substrate. *Phys. Rev. Lett.* **2009**, *103*, 266101.
- [23] N'guessan, H.E.; Leh, A.; Cox, P.; Bahadur, P.; Tadmor, R.; Patra, P.; Vajtai, R.; Ajayan, P.M.; Wasnik, P. Water Tribology on Graphene. *Nature Communications* **2012**, *3*, 1242.
- [24] Flores-Vivian, I.; Hejazi, V.; Kozhukhova, M.I.; Nosonovsky, M.; Sobolev, K. Self-Assembling Particle-Siloxane Coatings for Superhydrophobic Concrete. *ACS Applied Materials & Interfaces* **2013**, *5*, 13284-13294.
- [25] Feng, L.; Zhang, Y.; Xi, J.; Zhu, Y.; Wang, N.; Xia, F.; Jiang, L. Petal Effect: A Superhydrophobic State with High Adhesive Force. *Langmuir* **2008**, *24*, 4114-4119.
- [26] Bhushan, B.; Nosonovsky, M. The Rose Petal Effect and the Modes of Superhydrophobicity. *Philosophical Transactions of the Royal Society A-Mathematical Physical and Engineering Sciences* **2010**, *368*, 4713-4728.
- [27] Marmur, A. Hydro- Hygro- Oleo- Omni-Phobic? Terminology of Wettability Classification. *Soft Matter* **2012**, *8*, 6867-6870.
- [28] Marmur, A. Underwater Superhydrophobicity: Theoretical Feasibility. *Langmuir* **2006**, *22*, 1400-1402.
- [29] Drelich, J.; Chibowski, E. Superhydrophilic and Superwetting Surfaces: Definition and Mechanisms of Control. *Langmuir* **2010**, *26*, 18621-18623.
- [30] Hejazi, V.; Nyong, A.E.; Rohatgi, P.K.; Nosonovsky, M. Wetting Transitions in Underwater Oleophobic Surface of Brass. *Adv Mater* **2012**, *24*, 5963-+.
- [31] Hejazi, V.; Nosonovsky, M. Wetting Transitions in Two-, Three-, and Four-Phase Systems. *Langmuir* **2012**, *28*, 2173-2180.
- [32] Liu, M.; Wang, S.; Wei, Z.; Song, Y.; Jiang, L. Bioinspired Design of a Superoleophobic and Low Adhesive Water/Solid Interface. *Adv Mater* **2009**, *21*, 665-669.

- [33] Tuteja, A.; Choi, W.; Mabry, J.M.; McKinley, G.H.; Cohen, R.E. Robust Omniphobic Surfaces. *Proc. Natl. Acad. Sci. U. S. A.* **2008**, *105*, 18200-18205.
- [34] Barthlott, W.; Neinhuis, C. Purity of the Sacred Lotus, Or Escape from Contamination in Biological Surfaces. *Planta* **1997**, *202*, 1-8.
- [35] Bhushan, B.; Jung, Y.C.; Koch, K. Micro-, Nano- and Hierarchical Structures for Superhydrophobicity, Self-Cleaning and Low Adhesion. *Philosophical Transactions of the Royal Society A-Mathematical Physical and Engineering Sciences* **2009**, *367*, 1631-1672.
- [36] Vincent, J.F.V.; Bogatyreva, O.A.; Bogatyrev, N.R.; Bowyer, A.; Pahl, A. Biomimetics: Its Practice and Theory. *Journal of the Royal Society Interface* **2006**, *3*, 471-482.
- [37] Herminghaus, S. Roughness-Induced Non-Wetting. *Europhys. Lett.* **2000**, *52*, 165-170.
- [38] Cao, L.; Hu, H.; Gao, D. Design and Fabrication of Micro-Textures for Inducing a Superhydrophobic Behavior on Hydrophilic Materials. *Langmuir* **2007**, *23*, 4310-4314.
- [39] Tuteja, A.; Choi, W.; Ma, M.; Mabry, J.M.; Mazzella, S.A.; Rutledge, G.C.; McKinley, G.H.; Cohen, R.E. Designing Superoleophobic Surfaces. *Science* **2007**, *318*, 1618-1622.
- [40] Tuteja, A.; Choi, W.; McKinley, G.H.; Cohen, R.E.; Rubner, M.F. Design Parameters for Superhydrophobicity and Superoleophobicity. *MRS Bull* **2008**, *33*, 752-758.
- [41] Truesdell, R.; Mammoli, A.; Vorobieff, P.; van Swol, F.; Brinker, C.J. Drag Reduction on a Patterned Superhydrophobic Surface. *Phys. Rev. Lett.* **2006**, *97*, 044504.
- [42] Nosonovsky, M.; Bhushan, B. Superhydrophobic Surfaces and Emerging Applications: Non-Adhesion, Energy, Green Engineering. *Current Opinion in Colloid & Interface Science* **2009**, *14*, 270-280.
- [43] Hejazi, V.; Sobolev, K.; Nosonovsky, M. From Superhydrophobicity to Icephobicity: Forces and Interaction Analysis. *Scientific Reports* **2013**, *3*, 2194.
- [44] Boreyko, J.B.; Collier, C.P. Delayed Frost Growth on Jumping-Drop Superhydrophobic Surfaces. *ACS Nano* **2013**, *7*, 1618-1627.
- [45] Boreyko, J.B.; Srijanto, B.R.; Trung Dac Nguyen; Vega, C.; Fuentes-Cabrera, M.; Collier, C.P. Dynamic Defrosting on Nanostructured Superhydrophobic Surfaces. *Langmuir* **2013**, *29*, 9516-9524.
- [46] Feng, L.; Zhang, Z.Y.; Mai, Z.H.; Ma, Y.M.; Liu, B.Q.; Jiang, L.; Zhu, D.B. A Super-Hydrophobic and Super-Oleophilic Coating Mesh Film for the Separation of Oil and Water. *Angewandte Chemie-International Edition* **2004**, *43*, 2012-2014.
- [47] Ramachandran, R.; Nosonovsky, M. Coupling of Surface Energy with Electric Potential Makes Superhydrophobic Surfaces Corrosion-Resistant. *Physical Chemistry Chemical Physics* **2015**, *17*, 24988-24997.

[48] Bormashenko, E. General Equation Describing Wetting of Rough Surfaces. *J. Colloid Interface Sci.* **2011**, *360*, 317-319.

[49] Kapitza, P.L. Pendulum with a Vibrating Suspension. *Uspekhi Fizicheskikh Nauk* **1951**, *44*, 7-15.

[50] Landau, L.D.; Lifshitz, E.M. *Mechanics Volume 1 of Course of Theoretical Physics*, Second ed.; Pergamon Press, 1969.

[51] Blekhman, I.I. *Vibrational Mechanics*; World Scientific: Singapore, 2000.

CHAPTER 3: EFFECTS OF VIBRATIONS AND SPATIAL MICRO/NANO PATTERNS ON EQUILIBRIUM, WETTING, FLOW AND PHASE TRANSITION

In the previous chapter, the concept of wetting and vibrational mechanics were discussed. The method of separation of motions was introduced, and equations for effective force and energy were formulated. In this chapter, the relationship between small amplitude fast vibrations and small amplitude spatially periodic patterns is investigated. The effects of both vibrations and surface topography on the wetting properties including the contact angle and the surface free energy are studied. Also, the method of separation of motions is used to understand the structure-property relationships in materials and surfaces.

3.1 Effective Force Corresponding to Small Fast Vibrations

This section deals with the study of pure mechanical systems undergoing fast vibrations in a time-independent potential field. Two different approaches have been developed to separate the fast small vibrations from the overall motion of the system; the Mathieu equation approach and Kapitza's method of separation of motions. The latter method was further developed by Blekhman who suggested an interesting interpretation with two observers. One observer can see the small vibrations while the other one who does not see the vibration (for example, due to a specially designed stroboscopic light) however, observes their effect as a fictitious force, similar to the force of inertia.

First the method of separation of motions is applied to the classic example of an inverted pendulum on a vibrating foundation, and a mathematical expression for an effective stabilizing force is derived. This is followed by a review of the Mathieu equation approach to study stability of an inverted pendulum. Then, the stabilization of multiple pendulums, as well as a continuous

system involving a rope are investigated. Replacing fast vibrations with an effective force can not only be applied to systems described above, but also to non-coalescing droplets on a vibrating bath and other liquid systems which will be discussed in later sections.

3.1.1 Inverted pendulum and vibro-levitation

I now consider the classic problem of stability of an inverted pendulum to apply the method of the separation of motions and determine an effective stabilizing force. A simple pendulum is a common example used in mechanics to introduce one to the fundamentals of simple harmonic motion. Consider a pendulum with a point mass m connected to the end of a pivoted link of length L . The angular position of the pendulum about its pivot is described by the angle ψ . It has its stable equilibrium at its vertical lower position $\psi = 0^\circ$ where the potential energy is minimum as shown in Figure 3.1. Any small perturbations from this position results in oscillations about the equilibrium with natural frequency $\omega = \sqrt{g/L}$ where g is the acceleration due to gravity. Eventually the pendulum returns to its equilibrium due to the restoring force

$$-\frac{d(mgL \cos \psi)}{d\psi}.$$

A pendulum also has an unstable equilibrium that corresponds to the point of inflection at $\psi = 180^\circ$ (Figure 3.1). When the foundation of the pendulum is subjected to vertical harmonic oscillations $A \cos \Omega t$, where A is the amplitude and $\Omega \gg \omega$ is the frequency, the equilibrium at $\psi = 180^\circ$ can, under certain conditions, become stable. A pendulum on a vibrating foundation is called “Kapitza’s pendulum” after Peter Kapitza. The equation of motion can be written as,

$$L\ddot{\psi} = g \sin \psi - A\Omega^2 \sin \psi \cos \Omega t \tag{3.1}$$

The form of Eq. 3.1 is similar to that of Eq. 2.9 with $f = -mA\Omega^2 \sin \psi$. Substituting f into Eq. 2.18, the effective potential energy can be obtained as

$$\Pi_{eff} = mgL \left(-\cos \psi + \frac{A^2 \Omega^2}{4gL} \sin^2 \psi \right) \quad (3.2)$$

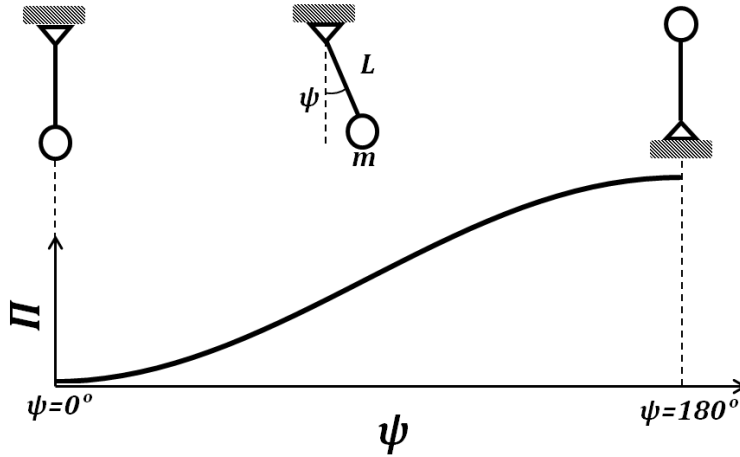


Figure 3.1. The potential energy Π of a pendulum as a function of its angular displacement ψ .

Now the stabilized inverted pendulum appears upright and stationary. By differentiating the effective potential energy in Eq. 3.2 the generalized force (with the dimension of torque) acting upon the pendulum can be obtained. In addition to the term involving $\sin \psi$, this generalized force now involves the term given by Eq. 2.19

$$V = \frac{\partial}{\partial \psi} \left(-\frac{mA^2\Omega^2}{4} \sin^2 \psi \right) = -\frac{mA^2\Omega^2}{4} \sin 2\psi \quad (3.3)$$

Note that V is dimensionally a torque, because the spatial coordinate ψ is angular displacement. This additional effective force can have a stabilizing effect on the unstable equilibrium. The effect of this force is equivalent to that of a spring with the torsional spring constant $k = \frac{mA^2\Omega^2}{2}$

when the angle ψ is close to 180° . This is equivalent to the upright pendulum supported by a spring (Figure 3.2). Since this effective force provides a support to the pendulum as if it is suspended upright, it can be called a “vibro-levitation” force [1]. The vibration-induced levitation is referred to in this study as “vibro-levitation”.

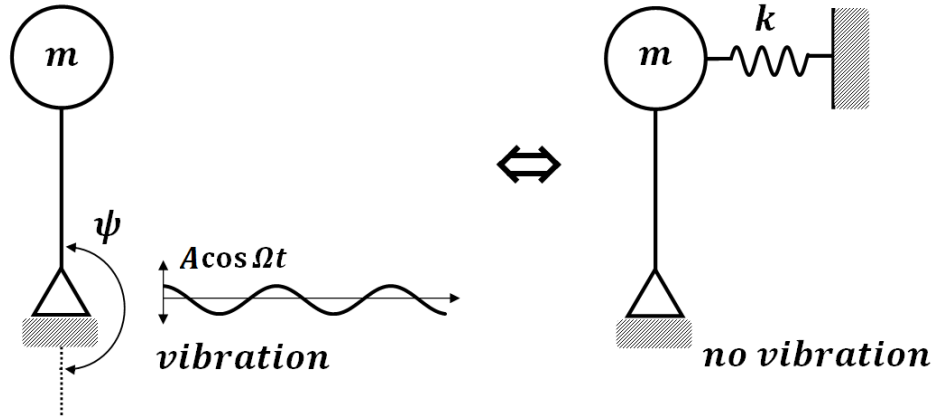


Figure 3.2. The figure on the left shows an inverted pendulum stabilized by a foundation vibrating with a periodic displacement $A \cos \Omega t$. The same system can be represented as shown in the figure on the right with the pendulum being stabilized by a spring of effective spring constant k .

The equilibrium is stable when the effective potential energy in Eq. 3.2 is a positive-definite function near the state of equilibrium, which yields the stability criterion

$$A^2 \Omega^2 > 2gL \tag{3.4}$$

Thus, when the amplitude and frequency of the small fast vibrations of the foundation satisfy Eq. 3.4, the otherwise unstable equilibrium at $\psi = 180^\circ$ can correspond to a local minimum for the effective potential energy, i.e., to become a stable equilibrium. Thus, the expression for the stabilizing force (Eq. 3.3) and a stability criterion for the inverted pendulum (Eq. 3.4) has been derived using the separation of motions method.

3.1.2 Mathieu equation method

The result of Eq. 3.4 has been historically obtained using a different method, namely, the parametric resonance Mathieu equation analysis suggested by A. Stephenson in 1908 [2,3]. The motion of a pendulum on vibration foundation is an example of parametric oscillations. The differential equation of motion of such a pendulum contains time-varying coefficients and is called Mathieu equation. Stephenson found that when the pivot of a pendulum is subjected to a vertical periodic motion at a frequency $2\omega/n$ where n is any integer, then the oscillations of the pendulum are gradually amplified. The pendulum eventually becomes highly unstable. Stephenson used Mathieu equation approach to study the conditions for stability and instability of the pendulum. This section briefly describes the Mathieu equation approach to determining the stability criteria of an inverted pendulum.

The equation of motion of a pendulum on vibrating foundation (Eq. 3.1) can be rewritten as

$$\ddot{\psi} - \left(\frac{g}{L} - \frac{A\Omega^2}{L} \cos \Omega t \right) \sin \psi = 0 \quad (3.5)$$

To study the stability of a solution of Eq. 3.5 using the Lindstedt–Poincaré perturbation method [4,5], the variables $z(\tau) = \psi(t)$, $\delta = 4g/L\Omega^2$, $\epsilon = 4A/L$ where $\epsilon \ll 1$ and $2\tau = \Omega t$, are introduced.

For small values of z , ($\sin z \approx z$) and the equation of motion for a pendulum reduces to the canonical form of the Mathieu equation

$$\ddot{z} - (\delta - \epsilon \cos 2\tau) z = 0 \quad (3.6)$$

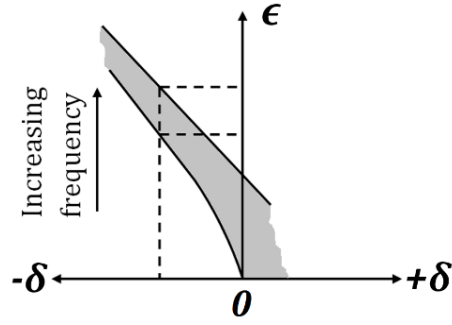


Figure 3.3. The region of stability for an inverted pendulum as seen in the Ince-Strutt diagram.

The stability of a pendulum with vibrating foundation is studied in the parameter plane (δ, ϵ) , with regions of stability and instability, the graphical representation of which is called the Ince-Strutt diagram. For an inverted pendulum the stability criteria is

$$-\frac{1}{8}\epsilon^2 + \dots < \delta < 1 - \frac{1}{2}\epsilon - \frac{1}{32}\epsilon^2 - \dots \quad (3.7)$$

and is represented by the shaded region in Figure 3.3. For stability at any δ , there is an upper and lower bound for ϵ . It follows that for a certain length of the inverted pendulum there exists a stability range of frequencies $\Omega_1 < \Omega < \Omega_2$. From Eq. 3.7, the stability criterion can be obtained as follows. Since this study is concerned with an inverted pendulum, one needs to consider the set of negative values of δ in the vicinity of zero. From Eq. 3.7

$$-\frac{1}{2}\epsilon^2 < -\delta \quad (3.8)$$

Substituting $\delta = 4g/L\Omega^2$ and $\epsilon = 4A/L$ into Eq. 3.8 the same stability criteria in Eq. 3.4 can be obtained. Mathieu equation approach is another way of analyzing the vibro-levitation of an inverted pendulum.

The Mathieu equation approach provides the same stability criterion as the method of separation of motion. However, the latter has a more general application and is not limited to the

parametric excitation of a pendulum. Therefore the method of separation of motions is applied to more complex problems of the multiple pendulum, the continuous pendulum (flexible beam with some stiffness), and liquid systems such as non-coalescing droplets. An analogy is drawn between the mechanical systems undergoing vibration and non-linear behavior in vibrating fluids that lead to phase transition.

3.1.3 Multiple pendulums and the so-called “Indian rope trick”

In the previous sections, I have discussed the stabilization of a single inverted pendulum by small amplitude fast vibration of the pendulum’s foundation. Inverted multiple pendulums consisting of a number of freely jointed links connected end to end can also be stabilized by applying a harmonic oscillation at the foundation as long as the frequency of the oscillation is sufficiently large. The theoretical proof was put forward by Stephenson [6] who derived the stability criteria. Acheson derived the stability criterion for a multiple pendulum using Mathieu equation approach. He showed that the region of stability in the Ince-Strutt diagram diminishes as the number of links in the pendulum increased. As the number of links approached infinity, such as in the case of a perfectly flexible string, the region of stability vanishes [7]. Acheson and Mullin later experimentally demonstrated the stability of double and triple inverted pendulums [8].

An even more complex albeit related case is a continuous system consisting of a flexible beam. Since it has been shown that the limiting case of multiple pendulums i.e., a string, cannot be stabilized in the upside-down position, flexural stiffness should be introduced.

Interestingly, some researchers have suggested that stabilization by a vibrating foundation can explain the so-called “Indian rope trick.” This trick involves a magician (an

Indian fakir) throwing one end of a flexible rope vertically upwards, which under certain conditions levitates like a vertical rod. In certain versions of the trick even a small animal (an ape) could climb the rope leaving the audience in awe. This defies the empirical observation that an upright column exceeding a critical length will buckle under its own weight. While accounts for the trick remain controversial, it has been shown that a rope with bending stiffness can be stabilized with sufficiently high frequencies. A piece of steel curtain wire longer than its critical buckling length was able to stay upright when its pivot was vibrated within a certain range of frequencies $\Omega_1 < \Omega < \Omega_2$. When the frequencies were reduced below Ω_1 , the wire fell over, while increasing the frequencies above Ω_2 resulted in instabilities in the wire [9].

Now the expression for the stabilizing force for multiple pendulums and a flexible stiff rope (i.e. a flexible rope which still possesses some stiffness akin to a stiff beam) are derived. First consider a double pendulum as shown Figure 3.4 with point masses m_1 and m_2 attached to links of lengths L_1 and L_2 respectively. The foundation of the pendulum is subjected to a harmonic oscillation $A \cos \Omega t$. Let the angular displacements of masses m_1 and m_2 be ψ_1 and ψ_2 respectively.

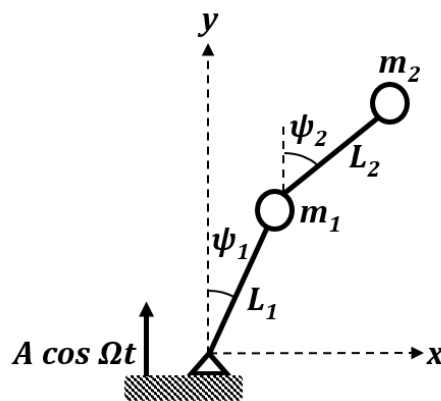


Figure 3.4. An inverted double pendulum whose foundation is subjected to a sinusoidal vibration $A \cos \Omega t$.

For m_1 one can write the horizontal and vertical displacements as $x_1 = L_1 \sin \psi_1$ and $y_1 = L_1 \cos \psi_1 + A \cos \Omega t$ respectively. Similarly for m_2 , the horizontal and vertical displacements are $x_2 = L_1 \sin \psi_1 + L_2 \sin \psi_2$ and $y_2 = L_1 \cos \psi_1 + L_2 \cos \psi_2 + A \cos \Omega t$ respectively. The corresponding x and y components of velocities are $\dot{x}_1 = L_1 \dot{\psi}_1 \cos \psi_1$, $\dot{y}_1 = -L_1 \dot{\psi}_1 \sin \psi_1 - A \Omega \sin \Omega t$, $\dot{x}_2 = L_1 \dot{\psi}_1 \cos \psi_1 + L_2 \dot{\psi}_2 \cos \psi_2$ and $\dot{y}_2 = -L_1 \dot{\psi}_1 \sin \psi_1 - L_2 \dot{\psi}_2 \sin \psi_2 - A \Omega \sin \Omega t$.

The kinetic energy of the system is given by $K = \frac{1}{2} m_1 (\dot{x}_1^2 + \dot{y}_1^2) + \frac{1}{2} m_2 (\dot{x}_2^2 + \dot{y}_2^2)$. The potential energy of the system is given by $\Pi = m_1 g y_1 + m_2 g y_2$. The Lagrangian of the system can be written in terms of the angular displacements and their derivatives as $L = K - \Pi$

$$\begin{aligned}
L = & \frac{1}{2} m_1 (L_1^2 \dot{\psi}_1^2 + A^2 \Omega^2 \sin^2 \Omega t + 2 L_1 \dot{\psi}_1 A \Omega \sin \psi_1 \sin \Omega t) \\
& + \frac{1}{2} m_2 \left(L_1^2 \dot{\psi}_1^2 + L_2^2 \dot{\psi}_2^2 + 2 L_1 L_2 \dot{\psi}_1 \dot{\psi}_2 \cos(\psi_1 - \psi_2) \right. \\
& \left. + 2 A \Omega \sin \Omega t (L_1 \dot{\psi}_1 \sin \psi_1 + L_2 \dot{\psi}_2 \sin \psi_2) + A^2 \Omega^2 \sin^2 \Omega t \right) \\
& - m_1 g (L_1 \cos \psi_1 + A \cos \Omega t) - m_2 g (L_1 \cos \psi_1 + L_2 \cos \psi_2 + A \cos \Omega t)
\end{aligned} \tag{3.9}$$

The equations of motion is then given by the Lagrange equations

$$\frac{d}{dt} \left(\frac{\partial L}{\partial \dot{\psi}_1} \right) - \frac{\partial L}{\partial \psi_1} = 0 \quad \text{and} \quad \frac{d}{dt} \left(\frac{\partial L}{\partial \dot{\psi}_2} \right) - \frac{\partial L}{\partial \psi_2} = 0 \tag{3.10}$$

Substituting for L and simplifying

$$\begin{aligned}
& (m_1 + m_2) L_1 \ddot{\psi}_1 + m_2 L_2 \ddot{\psi}_2 \cos(\psi_1 - \psi_2) + m_2 L_2 \dot{\psi}_2^2 \sin(\psi_1 - \psi_2) - m_1 g L_1 \sin \psi_1 - m_2 g L_1 \sin \psi_1 \\
& + A \Omega^2 \cos \Omega t (m_1 \sin \psi_1 + m_2 \sin \psi_1) = 0
\end{aligned}$$

and

$$m_2 L_2 \ddot{\psi}_2 + m_2 L_1 \ddot{\psi}_1 \cos(\psi_1 - \psi_2) - m_2 L_1 \dot{\psi}_1^2 \sin(\psi_1 - \psi_2) - m_2 g L_2 \sin \psi_2 + m_2 A \Omega^2 \sin \psi_2 \cos \Omega t = 0$$

Rewriting the equations of motion in the form of Eq. 2.9

$$(m_1 + m_2) L_1 \ddot{\psi}_1 + m_2 L_2 \ddot{\psi}_2 \cos(\psi_1 - \psi_2) + m_2 L_2 \dot{\psi}_2^2 \sin(\psi_1 - \psi_2) = m_1 g L_1 \sin \psi_1 + m_2 g L_1 \sin \psi_1 - (m_1 + m_2) A \Omega^2 \sin \psi_1 \cos \Omega t$$

and $m_2 L_2 \ddot{\psi}_2 + m_2 L_1 \ddot{\psi}_1 \cos(\psi_1 - \psi_2) - m_2 L_1 \dot{\psi}_1^2 \sin(\psi_1 - \psi_2) = m_2 g L_2 \sin \psi_2 - m_2 A \Omega^2 \sin \psi_2 \cos \Omega t$

Comparing these with Eq. 2.9

$$f_1 = -(m_1 + m_2) A \Omega^2 \sin \psi_1 \text{ and } f_2 = -m_2 A \Omega^2 \sin \psi_2 \quad (3.11)$$

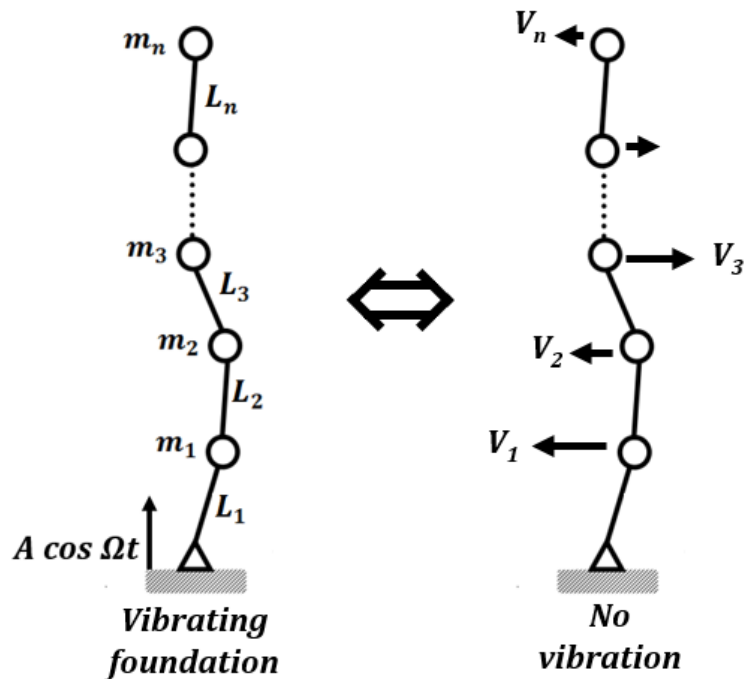


Figure 3.5. A multiple pendulum which is being stabilized by vibrating its foundation is equivalent to a multiple pendulum which is stabilized by a system of generalized vibro-levitation forces $V_1, V_2 \dots V_n$.

Using Eq. 2.19 the effective generalized forces on m_1 and m_2 can be written as

$$\begin{aligned} V_1 &= \frac{\partial}{\partial \psi_1} \left(\frac{f_1^2}{4m_1\Omega^2} \right) = -\frac{(m_1 + m_2)^2}{4m_1} A^2\Omega^2 \sin 2\psi_1 \\ V_2 &= \frac{\partial}{\partial \psi_2} \left(\frac{f_2^2}{4m_2\Omega^2} \right) = -\frac{m_2}{4} A^2\Omega^2 \sin 2\psi_2 \end{aligned} \quad (3.12)$$

For any mass m_i in system of n connected pendulums as shown in Figure 3.5

$$f_i = -A\Omega^2 \left(\sum_{j=i}^n m_j \right) \sin \psi_i \quad (3.13)$$

and the stabilizing effective generalized force is

$$V_i = \frac{\partial}{\partial \psi_i} \left(\frac{f_i^2}{4m_i\Omega^2} \right) = -\frac{A^2\Omega^2}{4m_i} \left(\sum_{j=i}^n m_j \right)^2 \sin 2\psi_i \quad (3.14)$$

The multiple pendulums is stabilized due the system of effective generalized forces $\{V_1, V_2, \dots, V_n\}$ as shown in Figure 3.6. For small angular displacements of the system of n connected pendulums, the equivalent spring constant at the first link is

$$k_1 = \frac{A^2\Omega^2}{2m_1} \left(\sum_{i=1}^n m_i \right)^2 \quad (3.15)$$

In this section, the stabilization of multiple pendulums was studied theoretically using the method of separation of motions. In the following section, the vibration-induced stabilization of a plastic rope is investigated using a specially designed experimental setup.

3.1.4 Experimental

The vibration-induced stabilization of a plastic rope with inherent flexural stiffness was investigated. An experimental setup similar to the one used by Walker [10] was specially designed. A 6.5 inch speaker cone (Pyle Company) formed the vibrating foundation in this study. Sinusoidal waves at a desired frequency ($10 \text{ Hz} < \Omega < 1000 \text{ Hz}$) were generated using a Matlab code, which were then amplified using a 20W amplifier (Lepai) and fed to the speaker (Figure 3.6a). The vibration of the speaker cone was of the form $A \sin \Omega t$. Since the amplitude of the sound wave was not a controlled parameter, the loudness setting was kept constant during the experiment.

A piece of plastic rope 7 mm long, 4 mm wide and 1 mm thick was affixed to the center of the speaker cone using adhesive tape. Then the sound was turned on so that the speaker cone started to vibrate harmonically and the motion of the rope was observed.

3.1.5 Results and discussion

The plastic rope became unstable from its static equilibrium position when the foundation was vibrated at certain frequencies (Figure 3.6b). Instabilities were seen to set in at around 17 Hz. The rope became highly unstable in the range of frequencies 50 Hz to 130 Hz. The instabilities slowly disappeared around 200 Hz and the rope returned to its static equilibrium (buckled) state, which is consistent with the vibration-induced stabilization of inverted and multiple pendulums. The instabilities in the rope are caused by effective forces as given by Eq. 3.14. Flexural stiffness in the rope is essential for its vibration-induced stabilization.

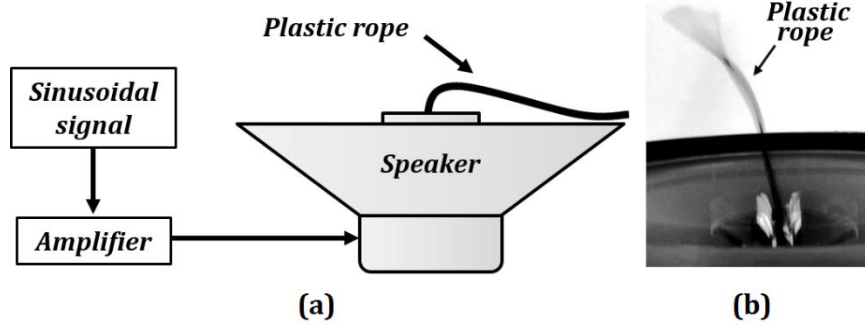


Figure 3.6. (a) Experimental setup (b) Instabilities in the plastic rope with the foundation vibrating at 130 Hz.

Studies on the “Indian rope trick” usually approximate the rope or wire to continuum objects such as rod or column with appreciable stiffness. Champneys and Fraser [11] studied the “Indian rope trick” for a linearly elastic rod. The equation of motion in terms of the lateral displacement u at arc length s is,

$$\eta \frac{\partial^2 u}{\partial t^2} + (1 - \eta \varepsilon \cos t) \frac{\partial}{\partial s} \left((1 - s) \frac{\partial u}{\partial s} \right) + b \frac{\partial^4 u}{\partial s^4} = 0 \quad (3.16)$$

where η , ε and b are the dimensionless acceleration, amplitude and stiffness. Comparing with Eq.

2.9 one can write $f = \eta \varepsilon \frac{\partial}{\partial s} \left((1 - s) \frac{\partial u}{\partial s} \right)$ and formulate the effective vibro-levitation force using

Eq. 2.19.

Shishkina et al. investigated a rope treated as a flexible Euler beam with the stiffness k subjected to the gravity and an axial load oscillating near the constant value of c^2 with the amplitude εa^2 and frequency Ω . The transversal deflection of the beam $u(x,t)$ is governed by

$$\frac{\partial^2 u}{\partial t^2} + k \frac{\partial^4 u}{\partial x^4} + (c^2 + \varepsilon \Omega^2 \sin \Omega t) \frac{\partial u}{\partial x} + (c^2 + \varepsilon \Omega^2 \sin \Omega t) x \frac{\partial^2 u}{\partial x^2} = 0 \quad (3.17)$$

They showed that effect of the oscillating load is equivalent to the increase of the effective flexural stiffness of the rope k , which becomes equal to $k_{eff} = k + \frac{\varepsilon^2 \Omega^2}{2} x^2$, where x is the distance along the rope (Figure 3.7a, b). This increase can be significant to exceed the critical value of the stiffness and prevent buckling of the beam (Figure 3.7c, d) [12].

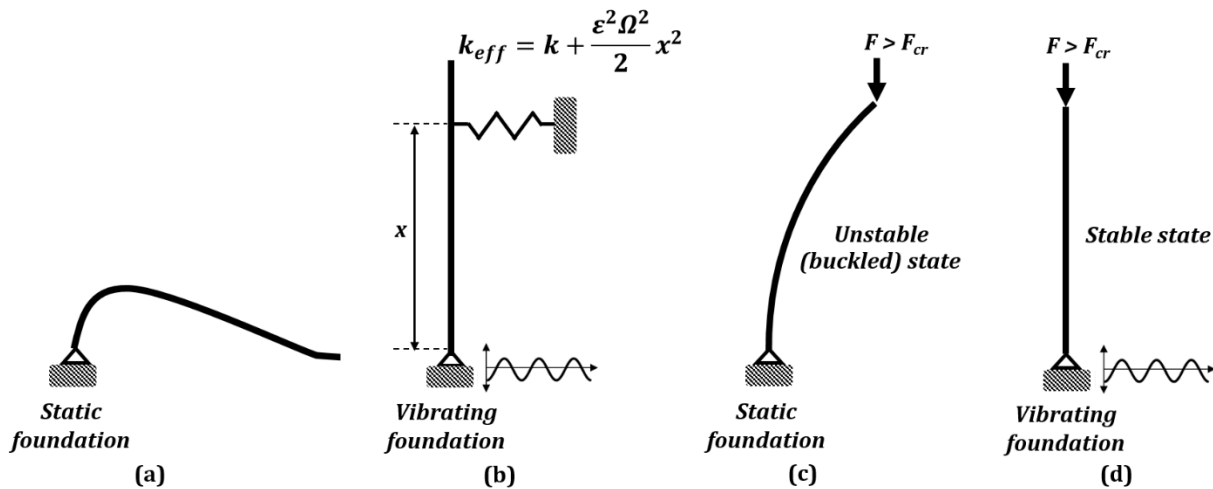


Figure 3.7. (a) A rope which is under no vibration, buckles under its own weight (b) Vertical vibrations results in an increased effective stiffness which prevents buckling (c) For any beam there is a critical force (F_{cr}) that depends on the beam material and geometry. Any load (F) greater than this will cause the beam to buckle (d) Vibrating the foundation leads to an increase in the effective stiffness of the beam, and the beam is able to resist buckling.

For a multiple pendulum of n connected links, as $n \rightarrow \infty$ the system becomes more flexible and its stiffness decreases. Now the system is similar to a limp rope. From Eq. 3.14 the vibro-levitation force is proportional to the mass. Therefore as $n \rightarrow \infty$, the vibro-levitation force becomes infinite. It follows that the “Indian rope trick” cannot be performed if the rope does not have sufficient inherent stiffness.

In the previous section, the method of separation of motions was applied to various mechanical systems undergoing vibration, and in each case an effective stabilizing force was

derived. The next section deals with non-coalescing droplets stabilized by vibrations. The method of separation of motions is once again used to formulate an expression for the effective force that causes their non-coalescing behavior.

3.2 Vibro-Levitation of Droplets

Water droplet is seen to float on surface of water momentarily and then coalesce into the bulk fluid. Sometimes it emits a smaller droplet as a result of coalescence, which then undergoes the same fate as the parent droplet [13]. This phenomenon is called coalescence cascade. Such non-coalescing droplets have been noticed as early as 1881 when Reynolds studied the influence of surface impurities on this peculiar behavior of droplets. He concluded that a pure liquid surface is required for droplets to float over it.[14] Walker demonstrated with a simple experiment that droplets of an aqueous soap solution can levitate in a non-coalescent state above a vibrating bath of the same bulk solution. The droplets could levitate indefinitely if standing waves (Faraday instabilities) were setup on the bulk liquid surface.[10] Recently this phenomenon has attracted the attention of researchers once again. Couder et al.[15] demonstrated that silicone oil droplets could be levitated indefinitely over a sinusoidally vibrating ($A \cos \Omega t$) bath of oil. While Walker noticed indefinitely levitating droplets only in the presence of standing waves on the bulk liquid surface, Couder et al. were able to obtain indefinitely levitating droplets over a stable liquid surface. In both the cases, vibration stabilizes the droplet in a non-coalescing state about the liquid bath. Therefore such a droplet can be referred to as a vibro-levitating droplet [1].

A vibro-levitating droplet is in a repetitive cycle of impact and bounce-off at the liquid surface. If its radius is larger than the capillary length ($\sqrt{\gamma/\rho g}$, where γ and ρ are the liquid

surface tension and density respectively) the droplet undergoes continuous deformation from spherical to oblate and prolate shapes, which may setup oscillations along the droplet surface [16]. When the droplet impacts the liquid surface, the kinetic energy of the droplet is dissipated into surface energy by flattening of the droplet, oscillations of the droplet and viscous damping in the air-film between the droplet and the liquid surface [17]. The droplet does not coalesce with the bulk liquid surface so long as the thin air film is replenished and stabilized due to the applied vibrations.

The vibro-levitating droplets produced weak surface waves every time they bounced off the liquid surface. These surface waves grew larger in amplitude when the amplitude A of the applied vibration was increased. At a critical value of A near the onset of Faraday's instabilities, the levitating droplets started to move in seemingly random horizontal trajectories over the vibrating liquid surface. This motion is due to the interaction between the surface wave and the levitating droplet on each impact. Couder et al. called the system of the droplet and its associated wave as a "walker" [18]. These walkers can interact and orbit with each other, and can also form self-assembled ordered patterns [19-21]. Within certain range of frequencies, the vibro-levitating droplets can roll over the liquid bath due to internal rotation [22].

Vibro-levitating droplets draw parallels with the wave-particle duality from quantum mechanics [23]. But this comes with a caveat that there is a lot of difference between the physics at macro and subatomic domains. The droplets illustrate several quantum mechanical phenomena such as single-particle diffraction, quantized orbits, tunneling etc.[24-26] The discussion on these topics is beyond the scope of this chapter.

There are models which describe the levitation and horizontal motion of these non-coalescent droplets [15,27-29]. The effect of bouncing droplets is thought to be similar to the acoustic levitation due to non-linear viscosity in a thin film which leads to hysteresis. However, a detailed model of such effects remains quite complex. In the following section, an analogy between the vibro-levitating droplets and an inverted pendulum is suggested.

3.2.1 Vibro-levitating droplets and inverted pendulum

The potential energy function of a droplet as it moves from a non-coalescing state to completely coalesced state is similar to that of a pendulum as it swings from an inverted state to stable state. Consider a liquid droplet above a bath of the same liquid. The droplet radius (R_0) is small (compared to the capillary length) so that gravitational effects can be neglected. Assume that the droplet takes the shape of a truncated sphere (Figure 3.8a) as it coalesces into the bath. The droplet can be characterized by the radius R , height h , and the radius of the foundation x (Figure 3.8a, b). The volume, surface area, and the position of the center of mass above the

foundation of the truncated sphere are given by $V = \frac{1}{3}\pi h^2(3R-h) = \frac{1}{3}\pi R^3(2-3\cos\theta + \cos^3\theta)$,

$A_s = 2\pi Rh = \pi(x^2 + h^2)$, $z = \frac{3(2R-h)^2}{4(3R-h)}$ respectively, where θ is the contact angle of the

droplet, $\sin\theta = x/R$ and $x^2 = 2Rh - h^2$.

As the droplet spreads from the initial spherical shape along the flat surface, the total volume of the droplet remains constant. Therefore $R = R_0 \sqrt[3]{4/(2-3\cos\theta + \cos^3\theta)}$. The change in the net surface free energy during spreading is given by the free surface energy (γ) times the area of the droplet minus the foundation area.

$$\Pi = \gamma\pi R^2 (1 - \cos \theta)^2 = \gamma\pi R_0^2 \left(\frac{4}{2 - 3 \cos \theta + \cos^3 \theta} \right)^{\frac{2}{3}} (1 - \cos \theta)^2 \quad (3.18)$$

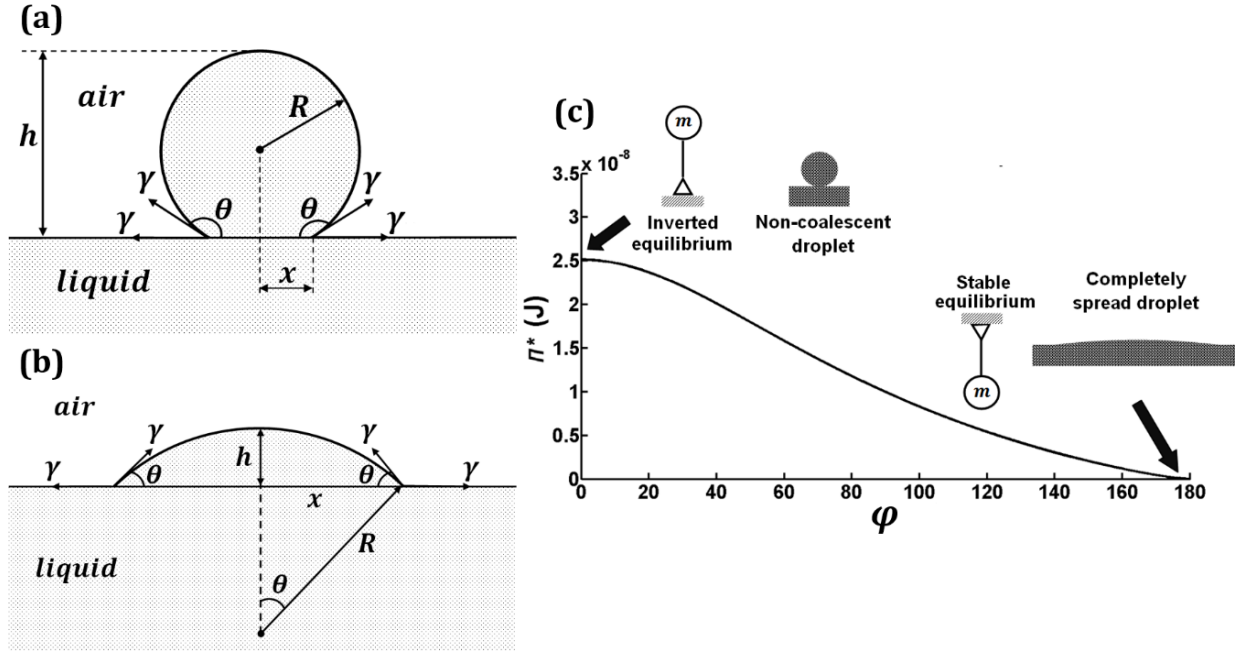


Figure 3.8. (a) and (b) The droplet as it spreads from a full sphere to a spherical cap of radius R , (c) Energy of a droplet (corn oil, $R_0 = 0.25\text{mm}$, $\gamma = 0.032\text{N/m}$) as it coalesces with the bulk liquid, and the similarity of this energy function to that of an inverted pendulum.

The plot of energy as a function of θ for a corn oil droplet of $R_0 = 0.25\text{ mm}$ and $\gamma = 0.032\text{ N/m}$ is shown in (Figure 3.8c), and it is observed that $\theta = 180^\circ$ corresponds to the unstable equilibrium, similar to an inverted pendulum. Therefore, it is convenient to introduce the variable $\phi = 180^\circ - \theta$ to characterize the shape of the droplet so that ϕ is equal to zero at the unstable equilibrium [1].

Now consider a vibro-levitating droplet over the sinusoidally vibrating liquid bath, whose vertical displacement is $u = A \sin \Omega t$. The dynamic equation of motion of the droplet in the vicinity of the unstable equilibrium can be written as

$$\chi\ddot{\varphi} + \beta\dot{\varphi} + \frac{\partial\Pi}{\partial\varphi} = Q_\varphi \quad (3.19)$$

where χ is the inertial coefficient associated with droplet's shape change, β is the viscous coefficient, and Q_φ is the periodic force from the substrate affecting the droplet shape change. The force Q_φ includes a term proportional to the area of contact, and a term proportional to the length of the contact line ($2\pi R_0\varphi$); however, for small φ , the second term prevails. Furthermore, assuming that non-linear viscous force acts in the thin air-film between the droplet and the liquid bath, one can assume that Q_φ includes a term proportional to the velocity (\dot{u}) and squared velocity (\dot{u}^2). The latter term is present due to hysteresis, i.e., the viscous force during the forward motion is different from that during the backward motion. Therefore,

$$Q_\varphi = 2\pi R_0\varphi \left[\alpha_1 A\Omega \sin \Omega t + \alpha_2 (A\Omega \sin \Omega t)^2 \right] \quad (3.20)$$

where α_1 and α_2 are coefficients corresponding to the linear and non-linear components of the force. The values of the parameters χ and β can be estimated using the following considerations. When the droplet is deformed, the work done per unit time is proportional to the momentum of droplet and thus $m \frac{dx}{dt} d\dot{x} = \chi \dot{\varphi} d\dot{\varphi}$, where m is the mass of the droplet. From Figure 3.8a,

$x = R_0 \sin \theta \sqrt{4/(2 - 3\cos \theta + \cos^3 \theta)}$. For $\theta \approx 180^\circ$ (or $\varphi \approx 0^\circ$), $dx/d\varphi = R_0$ which yields

$$\chi = mR_0^2 \quad (3.21)$$

Similarly, one can argue that the viscosity of the liquid, μ is related to β as

$$\beta = \mu R_0 \quad (3.22)$$

Using in Eq. 3.20 $(\sin \Omega t)^2 = (1 - \cos 2\Omega t)/2$ and substituting the amplitudes $f_1 = 2\pi R_0 \phi \alpha_1 A \Omega$ and $f_2 = 2\pi R_0 \phi \alpha_2 A^2 \Omega^2$ into Eq. 2.19 yields an expression for the effective vibro-levitation force [1].

$$V = \frac{4\pi^2 A^2 R_0^2}{\chi} (4\alpha_1^2 + \alpha_2^2 A^2 \Omega^2) \phi \quad (3.23)$$

In the following section a simple experiment to study the vibro-levitation of droplets is described.

3.2.2 Experimental

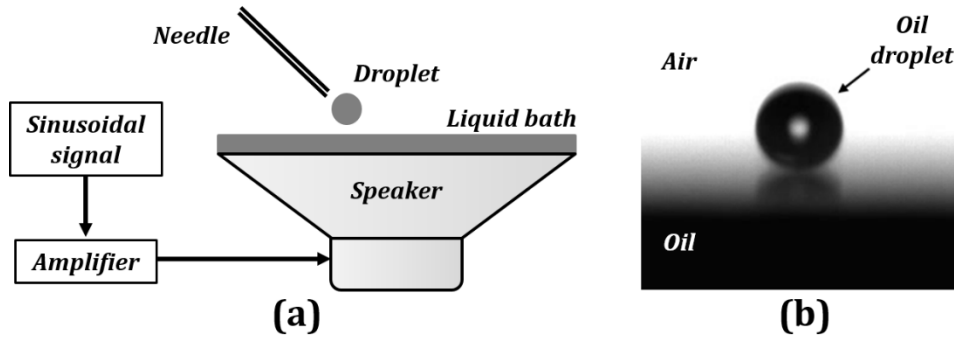


Figure 3.9. (a) Experimental setup (b) A droplet of corn oil levitating on the surface of corn oil vibrating at 150 Hz.

The levitation of oil droplets over a vibrating oil bath was investigated experimentally using the setup discussed in the section 3.1.5. Liquids studied were water, corn oil, SAE 30 engine oil, and 10W40 engine oil. The working liquid was placed at the center of the speaker cone to form a bath. Once the speaker was excited by the sound wave, a small drop of the same liquid was dropped on to the surface of the liquid bath using a syringe. This produced satellite droplets which levitated at certain frequencies of vibration of the speaker cone. Levitating

droplets could also be produced by pinching and lifting off the liquid surface using a pipette tip/needle [1]. The results from this experimental study is discussed in the following section.

3.2.3 Results

It was seen that pure water did not produce levitating droplets in the tested range of frequencies. However, the higher viscosity liquids, corn oil (Figure 3.9b), SAE 30, and 10W40 all produced levitating drops in the range of frequencies listed in Table 3.1. Note, however, that in each case a certain range of frequencies was observed. In other words, besides a lower frequency limit corresponding to the stability onset there was an upper frequency limit above which the droplet was not stable. Using the analogy with the inverted pendulum, this may be due to the fact that for high frequency the assumptions of small vibration may not be valid.

Table 3.1. The range of frequencies where stable levitating droplets were observed.

Liquid	Viscosity (Pa s)	Surface tension (N/m)	Frequency range (Hz)
Water	0.001	0.072	NA
Corn oil	0.052	0.032	35-350
10W40	0.160	0.031	30-400
SAE 30	0.400	0.031	30-400

The droplets were seen to levitate for several minutes. However, the droplets coalesced with the bath as soon as the sound generation stopped. Outside the specified range of frequencies, the levitating droplets were highly unstable, coalescing with the bath after a short while. At low frequencies it was clearly visible that the interaction between the levitating droplet and the bulk liquid surface created a surface wave. It was also possible to have multiple droplets levitating at the same time. The dependence of the stability of multiple levitating droplets on the frequency was not conclusive from the experiments conducted. Increasing the amplitude of

vibration by increasing the loudness resulted in the levitating droplet 'walking' on the surface of the liquid bath. Again, the dependency of horizontal motion of droplets to the amplitude could not be conclusively studied since the loudness could not be precisely regulated [1].

Thus vibro-levitating droplets can remain in a non-coalescent state above a vibrating liquid bath under certain condition. The following section is a discussion on the vibration-induced phase transitions in continuum systems.

3.3 Vibration-Induced Phase Transition and Locomotion

Destabilization of a system with a finite number of degrees of freedom is closely related to a much more complex phenomenon of the phase transition in a continuum system. For example, melting of a solid phase which turns into liquid can be viewed as a destabilization of the solid phase via nucleation of a new phase.

There phase transition of the first kind (with energy released or consumed during the phase transition), such as melting and boiling and phase transitions of the second kind (when no additional energy is released or consumed), such as the transition between the elastic deformation and a plastic flow. The shifting of the stability region in beam can be viewed as a transition from a soft to a hard “quasi-phase” analogous to the elastic-plastic transition in continuous medium. Thus, it has been suggested by K. Lurie [30] that a dynamic composite material with fiber reinforcement can be created using tunable dielectrics, optical pumping with high-energy pulse compression, or electromagnetic stealth technology in such a way that stiffness of the reinforcement fibers can be controlled by an external fast oscillating electric field thus controlling the phase transition in the composite (the parametric stiffness modulation). Blekhman suggested dynamic materials whose flexural rigidity can be controlled by changing

the amplitude and frequency of vibrations. This section covers a discussion of the effective freezing of bouncing droplets and other vibration-induced phenomena which can be interpreted as effective or apparent phase transitions.

3.3.1 *Effective freezing*

In previous section it was shown that liquid droplets can effectively be confined to a spherical shape using vibrations under certain conditions. The vibro-levitating droplets are effectively “frozen” in the spherical shape due to the vibro-levitation force. As soon as the exciting vibration is turned off, the droplet “melts” and coalesces into the bulk liquid. It was also seen that vibration cause an increased stiffness of a rope. A soft rope effectively becomes stiff due to the exciting vibrations, making the “Indian rope trick” possible. Turning off the vibrations once again results in the rope going limp. These vibration-induced stabilizations can be viewed analogous to the latent heat-induced solid-liquid phase transition.

3.3.2 *Cornstarch monsters*

Colloidal suspension of cornstarch in water is a common example of dilatant or shear-thickening fluid. If the cornstarch suspension is taken in hand and squeezed, it can be observed that the suspension turns solid and its surface feels powdery. As soon as the pressure is released, it returns back to its initial flowing state.

Peclet number (Pe) which is the ratio of hydrodynamic to diffusion transport rates governs the behavior of colloids.

$$Pe = r^2 \frac{\partial u}{\partial y} / D \tag{3.24}$$

where r is the particle radius, D is the diffusion coefficient, and $(\partial u/\partial y)$ is the shear rate. At high Pe (high shear rates) the hydrodynamic forces are too strong for the diffusion transport to restore the equilibrium of colloidal particles in the suspension. This non-equilibrium state consists of particles clustering together, called hydroclusters [31]. The hydroclusters are an unstable state, returning to the equilibrium state of randomness and fluidity once the shear stress is removed. It is important to study the effect of vibrations on cornstarch suspension because of the hysteresis observed during its shear loading.

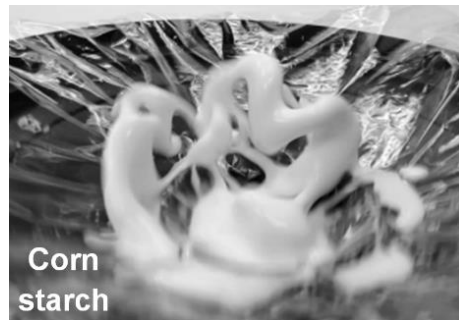


Figure 3.10. Cornstarch monsters in sample A at 30 Hz.

The experimental set-up discussed in the section 3.1.5 was used to study the behavior of cornstarch suspensions under harmonic excitation of the foundation. Two samples of cornstarch suspension in water, with the starch-to-water volume proportions of 1.5:1 (sample A) and 2:1 (sample B) were used. Both the suspensions formed the so-called cornstarch monsters (or “figurines” with long “fingers”) within a certain range of frequencies (Figure 3.10). The typical figurines were visible in both the samples from 15 Hz to around 200 Hz after which they slowly disappeared. The visible difference between the samples was that sample A produced longer cornstarch figurines than sample B.

The “cornstarch monsters” levitate on a vibrating surface like an inverted pendulum or the rope in the “Indian rope trick” within certain range of frequencies. The harmonic vibration of

foundation again is seen to stabilize this system in its otherwise-unstable equilibrium state. The hydroclusters formed in cornstarch on application of stress can be simplified into a system of multiple pendulums as shown in Figure 3.6. High strain rates due to the harmonically vibrating foundation causes formation of hydroclusters of cornstarch particles in water. The hydroclusters of masses m_1, m_2, \dots, m_n (separated by distances l_1, l_2, \dots, l_n) are assumed to be held together by the viscous forces in the surrounding medium. This reduces the phenomenon of “cornstarch monsters” into a problem of stability of a chain of inverted pendulums.[1]

3.3.3 Effective liquid properties and surface tension of granular materials

Small-amplitude fast vibrations have an important effect on the properties of the granular materials. Thus, vibrations can overcome jamming of the granular material due to friction. This is because vibrational acceleration creates an inertia force which can overcome dry Coulomb friction between the grains of the granular medium. As a result, granular medium can flow into a narrow pipe (Figure 3.11), demonstrating an effective liquid-like behavior, which is used for certain industrial applications [32]. Note that from the viewpoint of the rheological models, dry friction represents the key mechanisms of the plasticity. Therefore, the vibration-induced effective “melting” of the granular flow can be interpreted as an elastic-plastic transition rather than a true melting (which is a phase transition of the first kind).

An opposite effect of the “vibrational injection” of gas into liquid and effective locking or jamming of a valve in a vibrating vessel with a liquid (thus preventing leaking of the liquid through the valve) has also been reported in the literature and studied both theoretically and experimentally by Blekhman [33]. This “vibro-jet effect,” when applied at the microscale, can

have broad consequences for such phenomena as the multiphase flow separation and the control of liquid penetration through a semi-permeable membrane (osmosis).

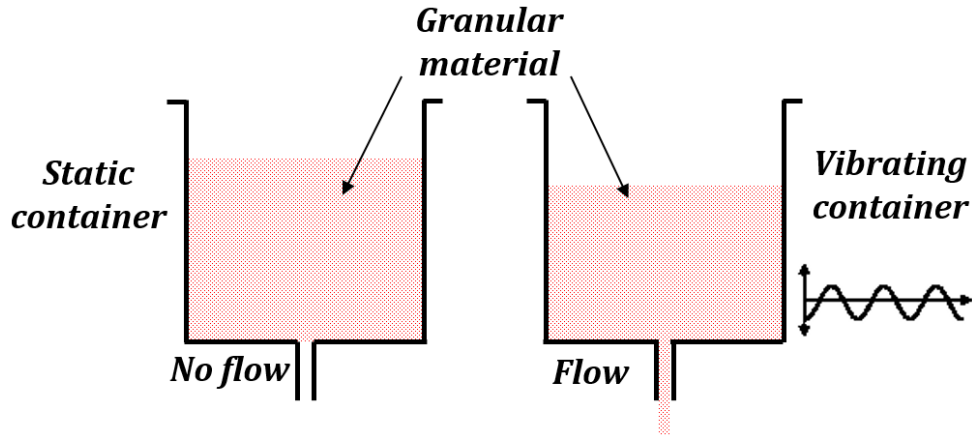


Figure 3.11. Vibrations can result in flow of granular material. This vibration-induced effective liquid-like behavior is similar to melting phase change.

Another effect of vibration on the granular media is the emergence of the apparent surface tension. Clewett et al. [34] studied the vertical vibration of a layer of bronze spheres with the diameter between $150\ \mu\text{m}$ and $180\ \mu\text{m}$ placed between flat glass substrates. The vibrated particles formed 2D clusters demonstrating behavior similar to 3D liquid droplets thus suggesting the presence of an effective surface tension consistent with Laplace's equation, demonstrating the existence of an actual surface tension. The surface tension results predominantly from an anisotropy in the kinetic energy part of the pressure tensor, in contrast to thermodynamic systems where it arises from either the attractive interaction between particles or entropic considerations. The spheres inside the cluster had on average more collisions with neighboring spheres than those at the border of the clusters. Since the collisions are not pure elastic and some energy is dissipated during the collisions, the average energy at the border of the clusters are larger than that inside the clusters, and the trend to minimize energy results in the clusters attaining the circular shape.

Thus small fast vibrations can cause granular media to exhibit fluid-like properties, such as fluidity and surface tension. In the following section the locomotion by vibration in viscous liquids is discussed.

3.3.4 Locomotion in viscous liquid

Another vibrational effect which is worth to mention is the propulsion in a viscous medium due to small-amplitude fast vibrations, which is believed to be a principle of aquatic locomotion of many microorganisms living in water [35]. Due to the small size of these microorganisms, the viscosity prevails over inertia on them, and a regular way of swimming practiced by large organisms would result in the back-and-forth motion rather than in a successful locomotion.

The so-called “scallop theorem” states that to achieve propulsion at low Reynolds number in Newtonian fluids a swimmer must deform in a way that is not invariant under time-reversal. Similarly to what has been observed in the preceding sections, such a motion (fast vibration) results in the effective propulsion force which drags the microorganism forward facilitating aquatic locomotion.

Purcell [35] studied a microscopic swimmer with two hinged paddles in a Newtonian fluid. It swims in a loop by rotating its paddles. Using the approach similar to Eq. 2.19, the propulsion force when averaged during the entire cycle is equal to zero. However, in non-Newtonian fluids reciprocal motions can propel microscopic swimmers [36]. The viscosity depends on the shear rate, and thus the angular velocities of the paddles. As a result, the net propulsion force over a cycle is non-zero. Thus, the hysteresis in the viscosity of a non-Newtonian fluid, coupled with non-reciprocal motion manifests as a net propulsion force.

The effect of vibrational locomotion is not limited to the microorganisms and is widespread among aquatic animals, including the whales [33]. In general, a system should involve an asymmetry to realize this effect. According to Blekhman's classification [33], there are six main types of such asymmetry caused by force, kinematic, structural, gradient, wave, and initial conditions asymmetry which can lead to an effective propulsion force.

3.4 Effect of the Surface Texture on Stability and Phase Transitions

Vibrations are temporal periodic structures, whereas surface micro-structure provides spatial patterns. It is remarkable that, similarly to small fast vibrations, surficial micro/nano patterns can affect bulk properties of a liquid phase and in particular, they result in effective phase transitions of the material. In this section, the so-called "Kirchhoff's dynamical analogy" between the dynamics of motion of a rigid body and static bending of a beam is considered, which establishes parallelism between time and spatial coordinates. This is followed by a review of the recent findings in the area of surface texture-induced phase behavior.

3.4.1 Kirchhoff's analogy between spatial and temporal patterns

Gustav Kirchhoff (1824-1887) was a German physicist who made a significant contribution into mechanics by developing a theory of bending of deformable elastic rods and beams. One particular result of Kirchhoff's theory was establishing an isomorphism between the static bending shape of an elastic flexible beam and the dynamics of motion of a rigid body, such as a pendulum or a hydroscope, in the 3D space [37,38]. This isomorphism, referred to as "Kirchhoff's dynamical analogy," is due to the fact that the differential equations describing bending of an elastic rod are the same as the differential equations describing the dynamics of the

rigid body with the local orientation of the rod corresponding to the position of the pendulum and the length of the rod corresponding to the time variable.

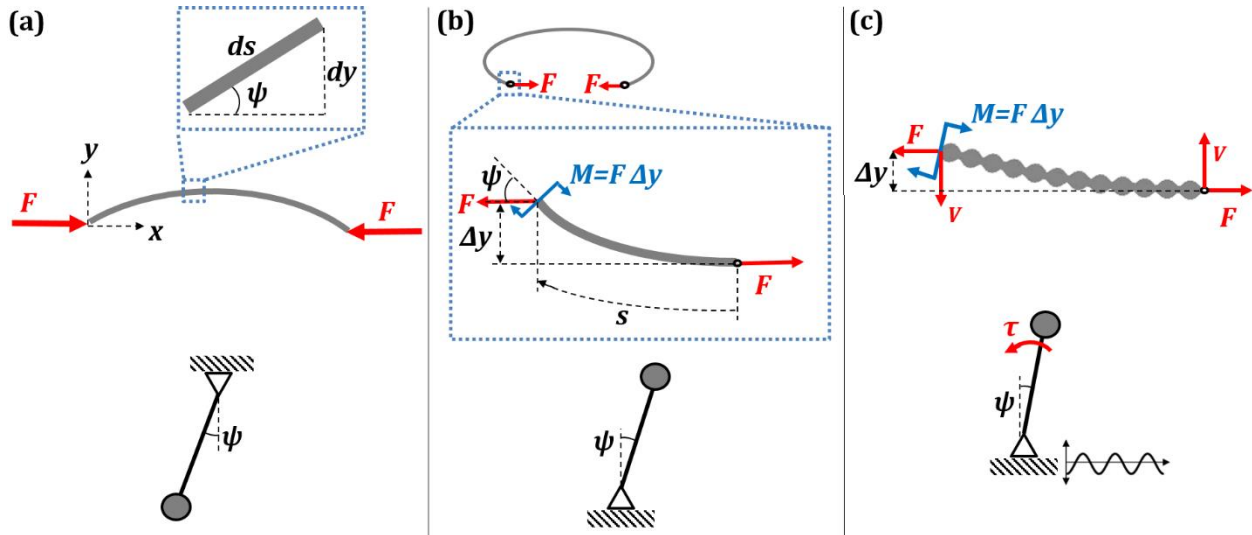


Figure 3.12. Kirchhoff's analogy between a pendulum and a beam. Deflection of the beam due to a (a) compressive load (corresponding to the stable equilibrium of the regular pendulum) and (b) tensile (buckled configuration corresponding to the unstable equilibrium of an inverted pendulum) force F . The waviness in the case (c) would promote stable (unbuckled) equilibrium similarly to the vibrations stabilizing an inverted pendulum.

Consider a slender elastic flexible beam of area moment of inertia I , and modulus of elasticity E , whose end points are loaded by an axial compressive force F as shown in Figure 3.12a. The slope at any point (x,y) is denoted by the angle ψ . For any small element ds on the beam $dy/ds = \sin \psi$. Bending moment at (x,y) is given by $EI \frac{d\psi}{ds} = -Fy$. By combining these equations, a second-order differential equation which describes the spatial bending patterns on the beam can be obtained [39].

$$\frac{d^2\psi}{ds^2} + \frac{F}{EI} \sin \psi = 0 \quad (3.25)$$

This is similar to the differential equation of oscillation of a simple pendulum of length L ,

$$\frac{d^2\psi}{dt^2} + \frac{g}{L} \sin \psi = 0 \quad (3.26)$$

Eq. 3.26 describes the deflection of the pendulum. Note how the spatial variable s in Eq. 3.25 corresponds to time variable t in Eq. 3.26. Static bending of a beam is a boundary value problem, while motion of a pendulum is an initial value problem. However, despite this difference, an analogy exists between the motion of a pendulum and the shape of a buckled elastic rod. Now the analogy of a beam to an inverted pendulum is considered.

Consider the bending of the beam under a tensile load F as shown in Figure 3.12b. The beam is bent 360° making an approximate circle. The inset in Figure 3.12b shows a free-body diagram of a small section of the beam near its end. The equilibrium of the beam corresponds to the value of the bending moment $M = F\Delta y$, which is proportional to the displacement Δy . The expression for the bending moment can be written as $EI \frac{d\psi}{ds} = F\Delta y$. Here we study whether the equilibrium of the beam is stable (straight beam) or unstable (bended beam). Differentiating the expression for the bending moment with respect to s and assuming $\lim_{\Delta s \rightarrow 0} \frac{\Delta y}{\Delta s} = \psi$ one can obtain

$$\frac{d^2\psi}{ds^2} - \frac{F}{EI} \psi = 0 \quad (3.27)$$

which is similar to the equation of motion of an inverted pendulum for small angular

displacement, $\frac{d^2\psi}{dt^2} - \frac{g}{L} \psi = 0$. The equation for the inverted pendulum has a solution of the

exponential form $\psi = c_1 e^{\sqrt{g/L}t} + c_2 e^{-\sqrt{g/L}t}$. The angular displacement grows exponentially with time t implying instability. Eq. 3.27 for the beam has a trivial solution $\psi = 0$, and a nontrivial

solution $\psi = c_1 e^{\sqrt{F/EI}s} + c_2 e^{-\sqrt{F/EI}s}$. The nontrivial solution suggests that the slope of the beam grows exponentially from the point of application of the force.

On the basis of Kirchhoff's analogy, the beam under compressive loading corresponds to the stable regular pendulum (Figure 3.12a), whereas the buckled beam under tensile loading corresponds to the unstable inverted pendulum (Figure 3.12b). An inverted pendulum can be stabilized by harmonically vibrating its foundation. Similarly, a buckled beam can be stabilized by a spatial periodicity in the geometry of the beam (Figure 3.12c).

If the properties of the elastic rod are changed in a periodic manner with small amplitude $h \ll 1$ and frequency Ω about the stationary value EI_0 such that

$$EI = EI_0 (1 + h\Omega \cos \Omega s) \approx \frac{EI_0}{(1 - h\Omega \cos \Omega s)} \quad (3.28)$$

Eq. 3.27 attains the form

$$\frac{d^2 \psi}{ds^2} - \frac{F}{EI_0} (1 - h\Omega \cos \Omega s) \psi = 0 \quad (3.29)$$

which is similar to Eq. 3.1 for an inverted pendulum on a harmonically vibrating foundation. Eq. 3.29 can be converted into the canonical form of the Mathieu equation

$$\frac{d^2 z}{d\kappa^2} - (\delta + \varepsilon \cos 2\kappa) z = 0 \quad (3.30)$$

where $\kappa = \frac{\Omega s}{2}$, $z(\kappa) = \psi(s)$, $\delta = \frac{4F}{EI_0 \Omega^2}$, $\varepsilon = -\frac{4Fh}{EI_0 \Omega}$. The stability and instability of the

Mathieu equation can be studied by Lindstedt–Poincaré perturbation method [4,5]. The stability curves are obtained as

$$\delta = -\frac{1}{8}\varepsilon^2 + \dots, \quad \delta = 1 - \frac{1}{2}\varepsilon - \frac{1}{32}\varepsilon^2 - \dots \quad (3.31)$$

and can be represented on the Ince-Strutt stability diagram (Figure 3.13). The solution of Eq. 3.30 is stable for values of (δ, ε) that lie in the shaded region between the stability curves shown in Figure 3.13. The negative values of δ is of importance in this discussion because of the tensile nature of the force F . For example, $F = -350$ N, flexural rigidity $EI_0 = 14$ Nm², $h = 0.001$ m, $\Omega = 10$ m⁻¹ yields the values $\varepsilon = 0.01$, $\delta = -1$ which lie in shaded region. Thus, in this case the beam is stabilized by the spatial periodicity in its geometry.

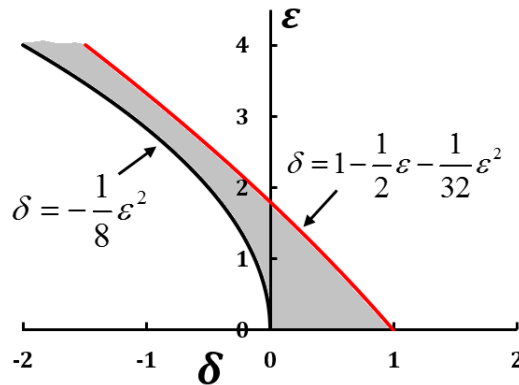


Figure 3.13. Ince-Strutt stability diagram for a beam.

The spatial periodicity of the beam can be interpreted as distributed bending moments along the beam, which can be replaced by an effective stabilizing shear force, V as shown in Figure 3.12c. Therefore, the periodicity in the geometry of the beam manifests as an effective shear force. This shear force can stabilize the beam when the condition

$$-\frac{1}{8}\varepsilon^2 < \delta < 1 - \frac{1}{2}\varepsilon - \frac{1}{32}\varepsilon^2 \quad (3.32)$$

is satisfied. Else, the beam is unstable with an exponentially increasing slope. It can be concluded that a pattern on the surface profile of a rod affects destabilization of the rod just as small fast vibrations affect the stability of an inverted pendulum. In the next section, surface texture-induced superhydrophobicity, phase transitions and propulsion will be discussed.

3.4.2 Surface patterns leading to the superhydrophobicity, phase transition and propulsion

Surface texture (roughness) is an essential parameter in determining the wettability (or non-wettability) of a surface. On a superhydrophobic surface, a water droplet effectively “freezes” into a spherical shape. The roughness features on the superhydrophobic surface also harbor and stabilize pockets of air. On a superhydrophilic surface, a water droplet effectively “melts” into a thin film, similarly to the coalescence of a droplet into a liquid bath.

Consider a solid rough surface of length L along the x -axis and unit width, roughness profile of which is described by the function $F(x)$ and the local surface free energy $\gamma(x)$. The roughness factor of the surface can be written in the integral form as

$$R_f = \frac{1}{L} \int_0^L \sqrt{1 + \left(\frac{dF(x)}{dx} \right)^2} dx \quad (3.33)$$

Similarly to the averaging of small fast vibrations over time in Eq. 2.19, the effect of surface topography and chemical heterogeneity can be incorporated into the effective surface free energies of the interface as an integral over the spatial coordinate x .

$$(\gamma)_{eff} = \frac{1}{L} \int_0^L \gamma(x) \sqrt{1 + \left(\frac{dF(x)}{dx} \right)^2} dx \quad (3.34)$$

For a chemically homogenous rough surface, γ is independent of x , and Eq. 3.34 yields the Wenzel equation in which the surface free energy is augmented by R_f . For a chemically heterogeneous smooth surface, Eq. 3.34 yields the Cassie-Baxter equation. The modification of the surface free energies in Eq. 3.34 using the average of the product of the surface free energy and the surface profile over a length is similar to the augmentation of the effective potential energy in Eq. 2.18 with a term averaged over time. The effective surface energy and thus the contact angle can be modified by controlling the surface texture and chemistry (Figure 3.14).

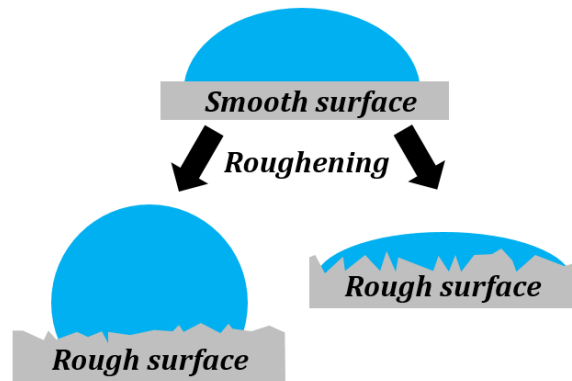


Figure 3.14. A Surface can be made hydrophobic or hydrophilic by controlling the surface texture.

Marmur suggested that appropriate texturing of a surface can lead to stable air films on underwater surfaces resulting in underwater superhydrophobicity [40]. Later on, Patankar and co-workers studied surface texture-induced phase transitions [41-43]. They investigated how surface texture affects the Leidenfrost effect [44] manifested by water droplets levitating over a sufficiently hot skillet due to the presence of an evaporating vapor film (Figure 3.15a). Such a film is formed only when the hot surface is above a critical temperature, whereas at lower temperatures the vapor film collapses. However, the critical temperature can be reduced, and the

vapor film collapse can even be completely suppressed [45] when micro-textured superhydrophobic surfaces are used [41]. Their result demonstrated that the surface texturing can potentially be applied to control other phase transitions, such as ice or frost formation and to the design of low-drag surfaces at which the vapor phase is stabilized in the grooves of textures without heating.

Jones et al. [42] has later demonstrated that rough textured surfaces may be used to manipulate the phase of water since nanoscale roughness pattern stabilizes the vapor phase of water, even when liquid is the thermodynamically favorable phase. Furthermore, the reverse phenomenon exists when patterned hydrophilic surfaces keep a liquid phase layer of water under conditions for boiling. They used molecular dynamics simulations to demonstrate the stability of the vapor and liquid phases of water adjacent to textured surfaces. Patankar [43] has also identified the critical roughness scale below which it is possible to sustain the vapor phase of water and/or trapped gases in roughness valleys, thus keeping the immersed surface dry.

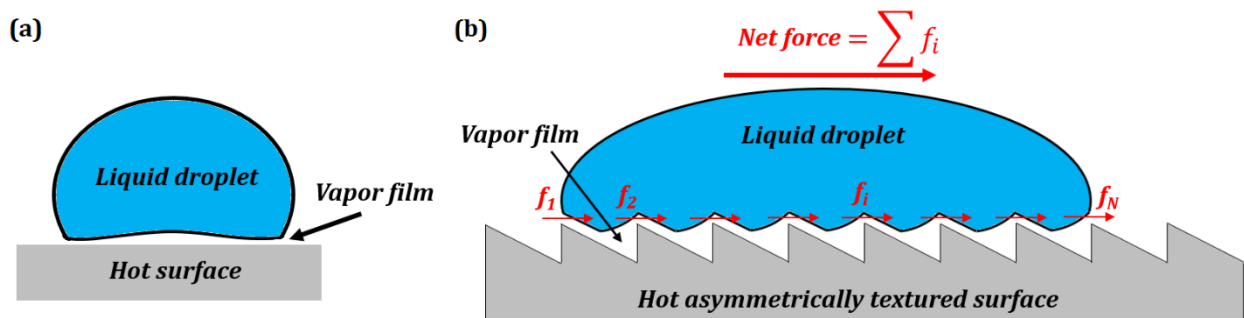


Figure 3.15. (a) Levitating liquid droplet over a sufficiently hot surface due to the Leidenfrost effect. (b) Self-propelled Leidenfrost droplets on an asymmetric saw-tooth surface. The temperature of the surface is usually much greater than the boiling point of the liquid.

Linke et al. [46] demonstrated that hot surfaces with small asymmetric texture (saw-tooth profile) can induce self-propulsion in Leidenfrost droplets, and in the process, the droplets climb

over the steep sides of the surface texture [47]. The temperature of the textured surface has to be much greater than the boiling point of the liquid. A thin film of the vapor phase thus formed at the textured surface supports the Leidenfrost droplets. The vapor phase is expelled from under the droplet due to the pressure gradient in the film between the peaks and the valleys of the surface profile. Due to the inherent asymmetry of the surface texture, the vapor leaks out asymmetrically from under the droplet, causing a net directional flow of vapor. The resultant viscous forces entrain the droplet in the same direction (Figure 3.15b) [48-50]. The self-propulsion effect has potential application such in a sublimation heat engine [51].

Dupeux et al. [48] derived the viscous force generated per tooth of the saw-tooth profile using momentum balance as

$$f_i = \eta \frac{U}{h_f} r_c \lambda \quad (3.35)$$

where η is the viscosity of the vapor, U is velocity of the vapor flow, h_f is the average thickness of the vapor film, r_c is the contact radius of the droplet, and λ is the tooth length. If there are N teeth below the droplet, then the net propulsion force can be obtained as,

$$F = \sum_{i=1}^N \eta \frac{U}{h_f} r_c \lambda = \eta \frac{U}{h_f} r_c N \lambda \quad (3.36)$$

For the values $\eta=1.9 \times 10^{-5}$ Pa s, $U=0.2$ ms⁻¹, $h_f=10$ μ m, $r_c=2.5$ mm, $\lambda=1$ mm, and $N=5$, the force $F=4.75$ μ N. The summation of forces over an area due to surface patterns in Eq. 3.36 is similar to the integration of small fast vibrations in Eq. 2.19. The vibrations can be substituted by an effective stabilizing force. Similarly, the surface topography manifests as a propulsion force.

Thus asymmetric surface patterns on a surface can be substituted by an effective force that spontaneously propels a Leidenfrost droplet over steep inclines. In general, the phenomenon of surface texture-based phase transition can be described as suppressing the boiling point and thus it is similar to superheating or subcooling of water. Similar to the vibration-induced phase transitions, the effect of the small spatial pattern is in changing the phase state of the material.

3.5 Effect of the Patterns on Fluid Flow Through Membranes

In the preceding section it was seen that small fast vibrations or small-amplitude spatial structures can be substituted by an effective energy term, which can lead either to an effective force (such as the vibro-levitation force) or affect mechanical or phase equilibrium. This section deals with the effects of small vibrations and structures on wetting, and specifically, on the filtration.

3.5.1 Water penetration through a hole in a vibrating vessel

In this section deals with the effects of small fast vibrations on the flow through a hole. First consider a macroscopic flow of a fluid through a pipe as shown in Figure 3.16a, with the mean flow velocity v related to the pressure loss ΔP by the nonlinear relation

$$\Delta P = av^2 \tag{3.37}$$

where a is a constant. The quadratic term represents a non-linearity, which may be a consequence of various factors, such as the turbulence, non-linear viscosity, or asymmetric variations in the pipe profile. The non-linearity is essential since it results in hysteresis [32].

Assume a slow velocity v_0 which changes negligibly over a time period $2\pi/\Omega$. If the pipe is subjected to a fast external vibration (Figure 3.16b) of the form $x = h \cos \Omega t$, where h is a small

constant amplitude, then the additional fast component of velocity is $\dot{x} = -h\Omega \sin \Omega t$. The standard assumption of the method of separation of motions is that the flow velocity is small in comparison with the amplitude of the velocity of vibrations, $h\Omega$. The flow velocity can be written as the sum of the slow and fast components.

$$v = v_0 - h\Omega \sin \Omega t \quad (3.38)$$

Substituting Eq. 3.38 in Eq. 3.37,

$$\Delta P = a(v_0 - h\Omega \sin \Omega t)^2 \quad (3.39)$$

$$\Delta P = av_0^2 + a(h\Omega \sin \Omega t)^2 - 2av_0h\Omega \sin \Omega t$$

$$\Delta P = \Delta P_0 + a(h\Omega \sin \Omega t)^2 - 2av_0h\Omega \sin \Omega t \quad (3.40)$$

where ΔP_0 is the pressure loss due to v_0 , which changes negligibly over $2\pi/\Omega$. Averaging Eq. 3.40 over the period $2\pi/\Omega$, similarly to the temporal averaging in Eq. 2.19 gives

$$\overline{\Delta P} = \Delta P_0 + \frac{\Omega}{2\pi} \int_0^{2\pi/\Omega} a(h\Omega \sin \Omega t)^2 dt \quad (3.41)$$

$$\overline{\Delta P} = \Delta P_0 + \frac{a}{2}(h\Omega)^2 \quad (3.42)$$

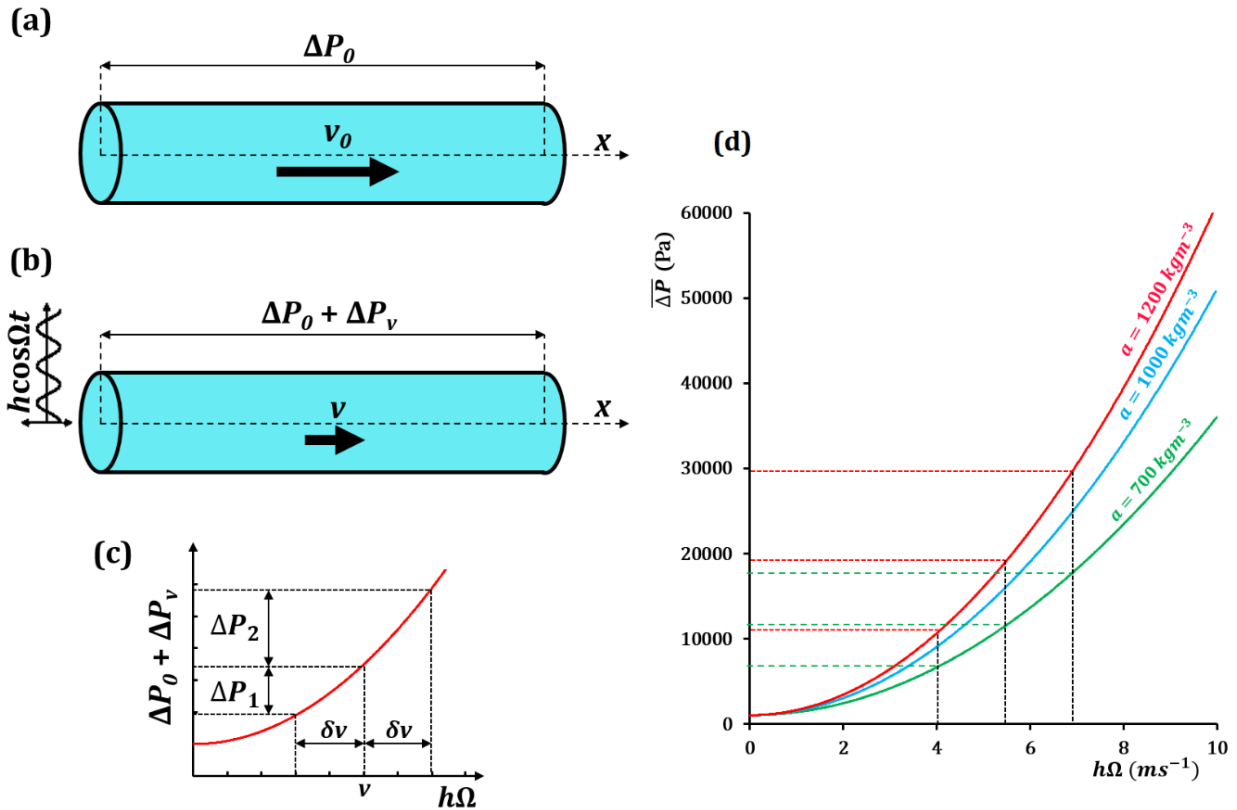


Figure 3.16. (a) Fluid flow through a pipe where the pressure difference ΔP_0 is a nonlinear function of the flow velocity v_0 . (b) Longitudinal external vibrations $h\cos\Omega t$ results in an additional pressure difference ΔP_v . (c) Pressure difference as a function of the velocity $h\Omega$. The hysteresis ($\Delta P_2 - \Delta P_1$) due to a small change in velocity $\pm\delta v$ can significantly alter the flow characteristics. (d) Pressure difference as a function of $h\Omega$ for three different fluids with $a = 700, 1000$ and 1200 kgm^{-3} .

The effect of the fast vibrations is perceived as the additional pressure difference in Eq. 3.42, $\Delta P_v = a(h\Omega)^2/2$, which can intensify or weaken the fluid flow through the pipe. Eq. 3.42 is similar to Eq. 2.18 in which vibrations augment the potential energy of the system. At certain values of $h\Omega$ in Eq. 3.42 the vibrations can effectively stop the fluid flow. A representative plot of Eq. 3.42 is shown in Figure 3.16c. For any small change in velocity $\pm\delta v$ due to the external vibrations, the corresponding change in ΔP are different as shown. The pressure difference ΔP_2 for a small increase in velocity is greater than the pressure difference ΔP_1 for a small decrease in

velocity. This hysteresis can affect the flow in the pipe and under certain conditions even stop the flow. Using values of $\Delta P_0=1$ kPa, and $a=700, 1000, 1200$ kg/m³ (similar to the densities of gasoline, water and glycerin respectively), a plot of Eq. 3.42 is shown in Figure 3.16d. If the hydrostatic pressure driving the flow is ΔP_{in} , the fluid in the vibrating pipe ceases to flow when

$$\frac{a}{2}(h\Omega)^2 > \Delta P_{in} \quad (3.43)$$

If instead of a vibrating pipe, a vibrating fluid container with a hole at the bottom is considered, the velocity of the fluid drainage is related to the static pressure head (H) of the fluid in the container as $v \propto \sqrt{2gH}$. Therefore the non-linearity in Eq. 3.37, and Eq. 3.43 still holds. Thus the drainage of fluid through the hole can be stopped by controlling the amplitude and frequency of the vibrations. Thus small fast vibrations can affect fluid flow through a hole and under certain conditions effectively act as a valve. Next, this result is extended to the case of vibrating membranes on the micro/nano scale.

3.5.2 Liquid penetration through pores in vibrating or patterned membranes

Semipermeable membranes allow solvent molecules (usually water) to diffuse through, but prevent larger molecules such as solutes and ions. Osmosis is the transport of solvent molecules through a semipermeable membrane from a region of higher to lower solvent chemical potential, until the chemical potentials equilibrate. Osmosis is omnipresent in nature at the cellular level. Transport across the semipermeable membrane of living cells is by osmosis. The driving force behind osmosis is the concentration gradient of solute across the membrane or in other words the chemical potential difference of the solvent across the membrane.

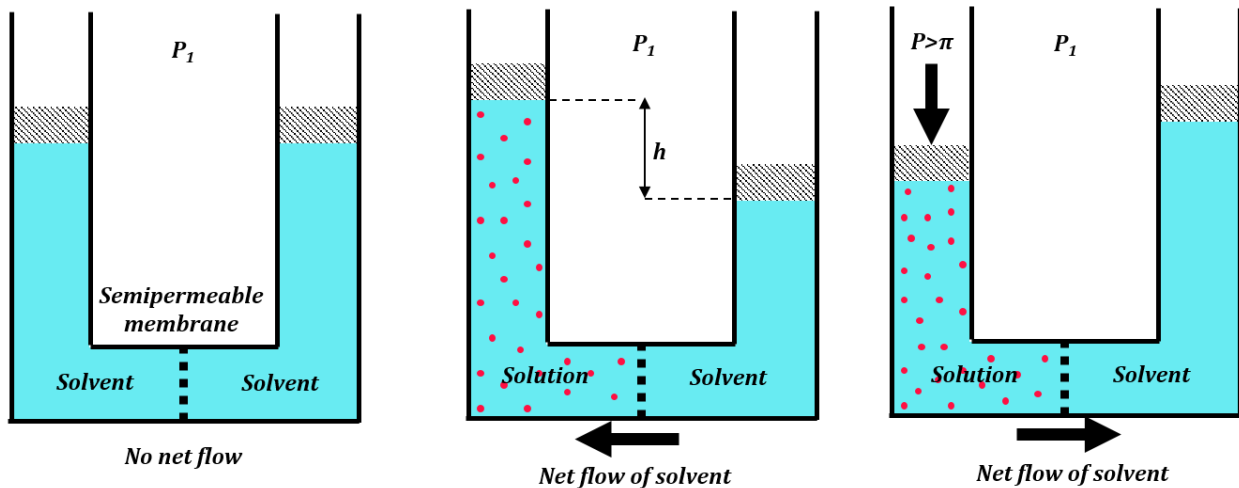


Figure 3.17. (a) Both sides of the semipermeable membrane have pure solvent and hence equal chemical potential. Therefore an osmotic equilibrium exists. (b) Osmosis across the semipermeable membrane continues until the chemical potentials equilibrate. (c) The flux of solvent molecules can be reversed by applying a pressure larger than the osmotic pressure. This process is called reverse osmosis.

Consider two columns of liquid separated by a semipermeable membrane as shown in Figure 3.17. If both columns carry pure solvent at pressure P_1 , osmotic equilibrium exists, i.e., the chemical potentials equate. In such a case the heights of the pistons equilibrate and there is no net flow of solvent molecules across the membrane (Figure 3.17a). Let the chemical potential of pure solvent at P_1 and temperature T be given by $\mu_{solvent}^*$. A small amount of solute is added to the left column to make it a dilute solution (at P_1) (Figure 3.17b). This dilution results in lowering of the chemical potential of the solvent in the solution below that of the pure solvent. There is a net flow of solvent molecules from the pure solvent, across the membrane into the solution. The chemical potential of the solvent $\mu_{solvent}$ in the dilute solution at P_1 is given by the relation

$$\mu_{solvent}^* - \mu_{solvent} = -RT \ln x_{solvent} \quad (3.44)$$

where R is the gas constant, T is the absolute temperature, and $x_{solvent}$ is the mole fraction of the solvent in the solution. The equilibrium can be restored by increasing the pressure on the solution to a value P_2 . This raises the chemical potential of the solvent in the solution to that of pure solvent. The relation for change in chemical potential with pressure can be obtained from the Gibbs free energy relation.

$$\bar{V}_{solvent} \int_{P_1}^{P_2} dP = \mu_{solvent}^* - \mu_{solvent} \quad (3.45)$$

where $\bar{V}_{solvent}$ is the partial molar volume of the solvent. Substituting Eq. 3.45 in Eq. 3.44, and integrating

$$\bar{V}_{solvent} (P_2 - P_1) = -RT \ln x_{solvent} \quad (3.46)$$

The excess external pressure ($P_2 - P_1$) that must be applied to prevent osmotic flow and restore equilibrium is called osmotic pressure, π . Thermodynamically, it is the excess external pressure that must be applied to the solution to raise the vapor pressure of the solvent to that of pure solvent. For a dilute solution, $\ln x_{solvent} = \ln(1 - x_{solute}) = -x_{solute}$, $x_{solute} \approx n_{solute}/n_{solvent}$, and volume of the solution $V \approx n_{solvent} \bar{V}_{solvent}$. Using these relations Eq. 3.46 can be written as

$$\pi = RT \frac{n_{solute}}{V} = c_{solute} RT \quad (3.47)$$

which is the van't Hoff equation, where c_{solute} is the molar concentration of the solute in the solution. Note its similarity to the ideal gas law. When an external pressure P greater than the

osmotic pressure π is applied to reverse the flux of solvent molecules then the process is called reverse osmosis (RO) (Figure 3.17c).

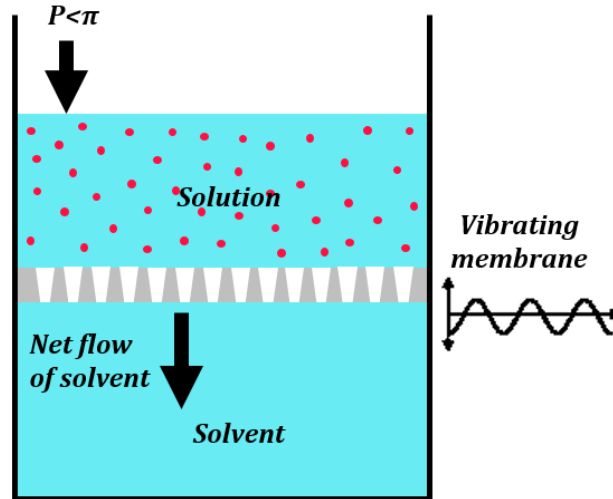


Figure 3.18. Vibrations can change the permeability of membranes. This may lead to a reverse osmotic flux even when the applied pressure is less than the osmotic pressure.

In the previous section, it was shown that vibrations could manifest as pressure affecting the fluid flow. For a vibrating membrane (Figure 3.18) consisting of several holes, the vibrations manifest as an effective pressure $a(h\Omega)^2/2$ as seen in Eq. 3.42. The vibrations can change the effective membrane permeability if

$$\frac{a}{2}(h\Omega)^2 > \pi \quad (3.48)$$

The RO process is used commonly to desalinate water. RO membranes are porous structures used in the RO process. Solvents usually take a tortuous path through the RO membranes. Note that RO is used for separation of a solvent from a solution. However, a completely different principle can be used to separate liquid mixtures using patterned superhydrophobic surfaces.

The RO process is used commonly to desalinate water. RO membranes are porous structures used in the RO process. Solvents usually take a tortuous path through the RO membranes. Note that RO is used for separation of a solvent from a solution. However, a completely different principle can be used to separate liquid mixtures using patterned superhydrophobic surfaces.

One of the recent applications of surfaces with tailored wettability is in separation of oil-water mixtures [52]. Porous media/meshes which are selectively wetted by either water or organic solvents can be used in this process. These porous material are analogous to the RO membranes used in desalination. Surfaces that are superhydrophobic and oleophilic, or hydrophilic and underwater oleophobic can be used to separate out oil from water.

Natural and artificial materials have been used for oil-water separation. Kapok plant fiber which is naturally hydrophobic and oleophilic was seen to separate diesel oil from water. Kapok, which is wetted by diesel due to capillary rise, can be dried and reused [53]. Artificial membranes are made by using porous/meshed structures with specific pore sizes, which may be roughened and coated with a surface agent to tailor the wetting property. The wetting properties depend on the pore size, surface roughness and surface agent used. Stainless steel and copper meshes, and filter paper [54] were commonly used to separate mixtures in which oil is layered over water. If one of the phases in oil-water mixture is dispersed in the other as small droplets (smaller than the pore size) the meshes become ineffective. Hydrophobic porous media has been developed for separation of oil-water emulsions with and without surfactants [55-58]. Table 3.2 summarizes the literature which discusses various types of oil-water filtering membranes.

Table 3.2. Summary of recent literature on oil-water separation using selectively wettable membranes.

Porous material	Surface texturing and treatment	Wetting property	Separates
Kapok plant fiber [53]	None	Hydrophobic, oleophilic	Diesel from water
Stainless steel mesh [59]	Polyacrylamide hydrogel polymerisation	Superhydrophilic, underwater superoleophobic	Vegetable oil, gasoline, diesel, crude oil, hexane, and petroleum ether from water with 99% efficiency
Stainless steel mesh [60]	Vertically-aligned multi-walled carbon nanotubes	Superhydrophobic, superoleophilic	Diesel from water
Copper mesh [61]	Etching followed by immersion in 1-Hexadecanethiol	Superhydrophobic, superoleophilic	Diesel from water
Filter paper [54]	Hydrophobic silica + polystyrene	Superhydrophobic, oleophilic	Diesel from water with 96% efficiency
Stainless steel mesh [62]	Spray coating an emulsion of PTFE, polyvinyl acetate, polyvinyl alcohol and sodium dodecyl benzene sulfonate in water	Superhydrophobic, superoleophilic	Diesel from water
Copper mesh [63]	Copper hydroxide needles grown electrochemically and coated with silane	Superhydrophobic, superoleophilic	n-hexane
Stainless steel mesh [64]	Zinc oxide nano rod coating followed by immersion in stearic acid	Superhydrophobic, superoleophilic	Toluene from water
Stainless steel mesh [65]	Hexagonal ZnO nano rods	Superhydrophobic, superoleophilic	Paraffin oil from water

Consider a mesh with pores of radius w used for oil-water separation. The rough surface of the mesh is wetted partially by oil, water and air. The effective surface free energy of a rough chemically heterogeneous surface is given by Eq. 3.34. The solid-liquid interface area in any

single pore is augmented by the factor $f_{SL}(r_f)_L$. The capillary pressure P_{cap} across the interface of the liquid L is given by the force balance $P_{cap}w^2 = 2wf_{SL}(r_f)_L\gamma_{LV}\cos\theta_0$ which simplifies as

$$(P_{cap})_L = \frac{2f_{SL}(r_f)_L\gamma_{LV}\cos\theta_0}{w} \quad (3.49)$$

where γ_{LV} is the surface free energy of the liquid-vapor interface. Note that the effect of the surface micro/nanotopography is incorporated into Eq. 3.49 via the roughness factor. The roughness factor is the surface profile averaged over an area. This is similar to the effect of vibrations averaged using the temporal integral in Eq. 2.19. The capillary pressure at a solid-oil interface is

$$(P_{cap})_{oil} = \frac{2f_{oil}(r_f)_{oil}\gamma_{oil}\cos\theta_{oil}}{w} \quad (3.50)$$

whereas the capillary pressure at a solid-water interface is

$$(P_{cap})_{water} = \frac{2f_{water}(r_f)_{water}\gamma_{water}\cos\theta_{water}}{w} \quad (3.51)$$

where $\gamma_{oil}, \gamma_{water}, \theta_{oil}, \theta_{water}$ are the surface free energy of the oil-vapor interface, the surface free energy of the water-vapor interface, the equilibrium CA of oil and the equilibrium CA of water respectively.

The capillary pressure (Eq. 3.49) determines if the liquid spontaneously flows through the mesh. For a hydrophobic, oleophilic mesh $(P_{cap})_{water}$ is negative whereas $(P_{cap})_{oil}$ is positive as a result of which oil selectively permeates through the pores; water permeates only if an external

pressure is applied to negate $(P_{cap})_{water}$. For example, the capillary pressures for a mesh of pore size $w=10\ \mu\text{m}$ with the values $r_f=2.0, \gamma_{water}=72\ \text{mNm}^{-1}, \theta_{water}=107^\circ, f_{water}=0.19, \gamma_{diesel}=23\ \text{mNm}^{-1}, \theta_{diesel}=60^\circ, f_{diesel}=1.0$, are $(P_{cap})_{water} = -1.6\ \text{kPa}$ and $(P_{cap})_{diesel} = 4.6\ \text{kPa}$. The mesh will stop the water, while allowing diesel through the pores. In the case of a mesh used for oil-water separation, micro/nano topography augments the capillary pressure and is therefore a critical factor.

Eq. 3.43 is the critical condition for flow through a vibrating pipe or out of a vessel, while Eq. 3.48 is the critical condition for the permeability of a vibrating membrane. The vibrations were averaged over time. In Eq. 3.49 the surface micro/nano topography was averaged over area. In essence micro/nano topography can affect the mesoscale transport through porous media while small fast vibrations can affect the molecular transport through porous media.

Note the similarity between Eq. 3.47 for osmotic pressure and Eq. 3.49 for the capillary pressure. Also note that the osmotic pressure is independent of the membrane properties, whereas the capillary pressure for wetting is dependent on the surface characteristics. The effect discussed in this section is different from the classical osmosis. The osmosis is a molecular scale effect and the expression for the osmotic pressure (Eq. 3.47) is derived from thermodynamics. The pattern-induced liquid separation, or “pseudo-osmosis” is a mesoscale effect with a characteristic length scale, i.e., the superhydro/oleophobic/philic surface pattern, of nanometers.

3.6 Conclusion

In this chapter, the method of separation of motions was used to establish a relationship between surface micro/nanotopography and small fast vibrations. Both small fast vibrations as

well as surface micro/nanopatterns can be substituted by an effective force or energy. This effective force or energy is obtained by averaging the small scale effects over their temporal or spatial domain. Kirchhoff's analogy was also used to study the similarity between surface topography and vibrations. The method of separation of motions was used as a tool to understand the structure-property relationships in materials and surfaces. The effects of vibrations and surface topography on wetting properties were also studied. Surface patterns averaged over the projected area can be incorporated into the effective surface free energy for a textured surface.

The effective stabilizing force was formulated for systems undergoing small fast vibrations such as the inverted pendulum, multiple pendulums connected end to end, and vibro-levitating droplets. Non-coalescing, vibro-levitating oil droplets were observed over a vibrating bath of oil within a range of frequencies of vibrations, similarly to the vibration-induced stabilization of an inverted pendulum. Vibration-induced phase transition was observed in non-Newtonian colloidal suspensions. Using the method of separation of motions, it was shown that vibrations can stop the fluid flow through a hole, effectively acting as a valve. Thus vibrations can affect membrane permeability. An equation for the capillary pressure in an oil-water separating superhydro/oleophobic/philic mesh was formulated using the method of separation of motions.

Using Kirchhoff's analogy it was shown that a slender elastic flexible beam in tension can be stabilized using spatial periodicity in the geometry of the beam. Thus surface topography can manifest as an effective stabilizing shear force on the beam.

It is important to note that in all the cases discussed in this chapter, vibrations or surface patterns leads to some nonlinearity which results in peculiar behavior such as stabilization and

transition. Thus spatial patterns and vibrations can affect material and surface properties. Potential applications include smart materials with tunable properties. The approach developed in this chapter allows estimating system design and performance by knowing the properties of small scale vibrations and patterns. In the following chapters the structure-property relationships are applied to novel materials. In the next chapter, the surface micro/nanotopography is used to control the wetting of concrete.

3.7 References

- [1] Ramachandran, R.; Nosonovsky, M. Vibro-Levitation and Inverted Pendulum: Parametric Resonance in Vibrating Droplets and Soft Materials. *Soft Matter* **2014**, *10*, 4633-4639.
- [2] Stephenson, A. On a New Type of Dynamical Stability. *Memoirs and Proceedings of the Manchester Literary and Philosophical Society* **1908**, *52*, 1-10.
- [3] Stephenson, A. On Induced Stability. *Philosophical Magazine* **1908**, *15*, 233-236.
- [4] Meirovitch, L. *Fundamentals of Vibrations*; McGraw-Hill: Boston, 2001.
- [5] Nayfeh, A.H. *Perturbation Methods*; John Wiley: New York, 1973.
- [6] Stephenson, A. On Induced Stability. *The London, Edinburgh and Dublin philosophical magazine and journal of science* **1909**, *17*, 765-766.
- [7] Acheson, D.J. A Pendulum Theorem. *Proceedings of the Royal Society of London Series A-Mathematical Physical and Engineering Sciences* **1993**, *443*, 239-245.
- [8] Acheson, D.J.; Mullin, T. Upside-Down Pendulums. *Nature* **1993**, *366*, 215-216.
- [9] Mullin, T.; Champneys, A.; Fraser, W.B.; Galan, J.; Acheson, D. The 'Indian Wire Trick' Via Parametric Excitation: A Comparison between Theory and Experiment. *Proceedings of the Royal Society A-Mathematical Physical and Engineering Sciences* **2003**, *459*, 539-546.
- [10] Walker, J. Drops of Liquid can be made to Float on the Liquid. What enables them to do so? *Scientific American* **1978**, *238*, 151-158.
- [11] Champneys, A.R.; Fraser, W.B. The 'Indian Rope Trick' for a Parametrically Excited Flexible Rod: Linearized Analysis. *Proceedings of the Royal Society A-Mathematical Physical and Engineering Sciences* **2000**, *456*, 553-570.

- [12] Shishkina, E.V.; Blekhman, I.I.; Cartmell, M.P.; Gavrilov, S.N. Application of the Method of Direct Separation of Motions to the Parametric Stabilization of an Elastic Wire. *Nonlinear Dyn.* **2008**, *54*, 313-331.
- [13] Blanchette, F.; Bigioni, T.P. Partial Coalescence of Drops at Liquid Interfaces. *Nat Phys* **2006**, *2*, 254-257.
- [14] Reynolds, O. On the Floating of Drops on the Surface of Water Depending Only on the Purity of the Surface. *Proceedings of the Manchester Literary and Philosophical Society* **1881**, *21*, 413-414.
- [15] Couder, Y.; Fort, E.; Gautier, C.H.; Boudaoud, A. From Bouncing to Floating: Noncoalescence of Drops on a Fluid Bath. *Phys. Rev. Lett.* **2005**, *94*, 177801.
- [16] Biance, A.L.; Clanet, C.; Quere, D. Leidenfrost Drops. *Phys. Fluids* **2003**, *15*, 1632-1637.
- [17] Qian, J.; Law, C.K. Regimes of Coalescence and Separation in Droplet Collision. *J. Fluid Mech.* **1997**, *331*, 59-80.
- [18] Couder, Y.; Protiere, S.; Fort, E.; Boudaoud, A. Dynamical Phenomena - Walking and Orbiting Droplets. *Nature* **2005**, *437*, 208-208.
- [19] Vandewalle, N.; Terwagne, D.; Mulleners, K.; Gilet, T.; Dorbolo, S. Dancing Droplets Onto Liquid Surfaces. *Phys. Fluids* **2006**, *18*, 091106.
- [20] Lieber, S.I.; Hendershott, M.C.; Pattanaporkratana, A.; Maclennan, J.E. Self-Organization of Bouncing Oil Drops: Two-Dimensional Lattices and Spinning Clusters. *Physical Review E* **2007**, *75*, 056308.
- [21] Couder, Y.; Boudaoud, A.; Protière, S.; Fort, E. Walking Droplets, a Form of Wave-Particle Duality at Macroscopic Scale? *Europhys. News* **2010**, *41*, 14-18.
- [22] Dorbolo, S.; Terwagne, D.; Vandewalle, N.; Gilet, T. Resonant and Rolling Droplet. *New Journal of Physics* **2008**, *10*, 113021.
- [23] Bush, J.W.M. Quantum Mechanics Writ Large. *Proc. Natl. Acad. Sci. U. S. A.* **2010**, *107*, 17455-17456.
- [24] Couder, Y.; Fort, E. Single-Particle Diffraction and Interference at a Macroscopic Scale. *Phys. Rev. Lett.* **2006**, *97*, 154101.
- [25] Eddi, A.; Fort, E.; Moisy, F.; Couder, Y. Unpredictable Tunneling of a Classical Wave-Particle Association. *Phys. Rev. Lett.* **2009**, *102*, 240401.
- [26] Fort, E.; Eddi, A.; Boudaoud, A.; Moukhtar, J.; Couder, Y. Path-Memory Induced Quantization of Classical Orbits. *Proc. Natl. Acad. Sci. U. S. A.* **2010**, *107*, 17515-17520.

- [27] Protiere, S.; Boudaoud, A.; Couder, Y. Particle-Wave Association on a Fluid Interface. *J. Fluid Mech.* **2006**, *554*, 85-108.
- [28] Molacek, J.; Bush, J.W.M. Drops Walking on a Vibrating Bath: Towards a Hydrodynamic Pilot-Wave Theory. *J. Fluid Mech.* **2013**, *727*, 612-647.
- [29] Oza, A.U.; Rosales, R.R.; Bush, J.W.M. A Trajectory Equation for Walking Droplets: Hydrodynamic Pilot-Wave Theory. *J. Fluid Mech.* **2013**, *737*, 552-570.
- [30] Lurie, K.A. *An Introduction to the Mathematical Theory of Dynamic Materials.*; Springer: Berlin, 2007.
- [31] Wagner, N.J.; Brady, J.F. Shear Thickening in Colloidal Dispersions. *Phys Today* **2009**, *62*, 27-32.
- [32] Blekhman, I.I. *Vibrational Mechanics*; World Scientific: Singapore, 2000.
- [33] Blekhman, I.I. *Selected Topics in Vibrational Mechanics*; World Scientific: New Jersey, 2004.
- [34] Clewett, J.P.D.; Roeller, K.; Bowley, R.M.; Herminghaus, S.; Swift, M.R. Emergent Surface Tension in Vibrated, Noncohesive Granular Media. *Phys. Rev. Lett.* **2012**, *109*, 228002.
- [35] Purcell, E.M. Life at Low Reynolds Number. *American Journal of Physics* **1977**, *45*, 3-11.
- [36] Qiu, T.; Lee, T.; Mark, A.G.; Morozov, K.I.; Muenster, R.; Mierka, O.; Turek, S.; Leshansky, A.M.; Fischer, P. Swimming by Reciprocal Motion at Low Reynolds Number. *Nature Communications* **2014**, *5*.
- [37] Shi, Y.M.; Hearst, J.E. The Kirchhoff Elastic Rod, the Nonlinear Schrodinger-Equation, and Dna Supercoiling. *J. Chem. Phys.* **1994**, *101*, 5186-5200.
- [38] Starostin, E.L. Symmetric Equilibria of a Thin Elastic Rod with Self-Contacts. *Philosophical Transactions of the Royal Society of London Series A-Mathematical Physical and Engineering Sciences* **2004**, *362*, 1317-1334.
- [39] Timoshenko, S.; Gere, J.M. *Theory of Elastic Stability*, 2nd ed.; McGraw-Hill: New York, 1961.
- [40] Marmur, A. Underwater Superhydrophobicity: Theoretical Feasibility. *Langmuir* **2006**, *22*, 1400-1402.
- [41] Vakarelski, I.U.; Patankar, N.A.; Marston, J.O.; Chan, D.Y.C.; Thoroddsen, S.T. Stabilization of Leidenfrost Vapour Layer by Textured Superhydrophobic Surfaces. *Nature* **2012**, *489*, 274-277.

- [42] Jones, P.; Kirn, A.; Rich, D.; Elliot, A.; Patankar, N.A. Controlling Phase Change: Drying-Up Under Water Or Staying Wet during Boiling. In Bulletin of the American Physical Society, San Francisco, California.
- [43] Patankar, N.A. Thermodynamics of Sustaining Gases in the Roughness of Submerged Superhydrophobic Surfaces. arXiv.org, e-Print Arch., Condens. Matter **2015**.
- [44] Leidenfrost, J.G. On the Fixation of Water in Diverse Fire. Int. J. Heat Mass Transfer **1966**, *9*, 1153-1166.
- [45] Wasnik, P.S.; N'guessan, H.E.; Tadmor, R. Controlling Arbitrary Humidity without Convection. J. Colloid Interface Sci. **2015**, *455*, 212-219.
- [46] Linke, H.; Aleman, B.J.; Melling, L.D.; Taormina, M.J.; Francis, M.J.; Dow-Hygelund, C.C.; Narayanan, V.; Taylor, R.P.; Stout, A. Self-Propelled Leidenfrost Droplets. Phys. Rev. Lett. **2006**, *96*, 154502.
- [47] Quere, D. Leidenfrost Dynamics. Annual Review of Fluid Mechanics, Vol 45 **2013**, *45*, 197-215.
- [48] Dupeux, G.; Le Merrer, M.; Lagubeau, G.; Clanet, C.; Hardt, S.; Quere, D. Viscous Mechanism for Leidenfrost Propulsion on a Ratchet. Epl **2011**, *96*, 58001.
- [49] Lagubeau, G.; Le Merrer, M.; Clanet, C.; Quere, D. Leidenfrost on a Ratchet. Nature Physics **2011**, *7*, 395-398.
- [50] Marin, A.G.; del Cerro, D.A.; Romer, G.R.B.E.; Pathiraj, B.; in 't Veld, A.H.; Lohse, D. Capillary Droplets on Leidenfrost Micro-Ratchets. Phys. Fluids **2012**, *24*, 122001.
- [51] Wells, G.G.; Ledesma-Aguilar, R.; McHale, G.; Sefiane, K. A Sublimation Heat Engine. Nature Communications **2015**, *6*, 6390.
- [52] Wang, B.; Liang, W.; Guo, Z.; Liu, W. Biomimetic Super-Lyophobic and Super-Lyophilic Materials Applied for oil/water Separation: A New Strategy Beyond Nature. Chem. Soc. Rev. **2015**, *44*, 336-361.
- [53] Lim, T.; Huang, X. In Situ oil/water Separation using Hydrophobic-Oleophilic Fibrous Wall: A Lab-Scale Feasibility Study for Groundwater Cleanup. J. Hazard. Mater. **2006**, *137*, 820-826.
- [54] Wang, S.; Li, M.; Lu, Q. Filter Paper with Selective Absorption and Separation of Liquids that Differ in Surface Tension. ACS Applied Materials & Interfaces **2010**, *2*, 677-683.
- [55] Zhang, W.; Shi, Z.; Zhang, F.; Liu, X.; Jin, J.; Jiang, L. Superhydrophobic and Superoleophilic PVDF Membranes for Effective Separation of Water-in-Oil Emulsions with High Flux. Adv Mater **2013**, *25*, 2071-2076.

- [56] Wang, Y.; Tao, S.; An, Y. A Reverse Membrane Emulsification Process Based on a Hierarchically Porous Monolith for High Efficiency Water-Oil Separation. *Journal of Materials Chemistry a* **2013**, *1*, 1701-1708.
- [57] Wang, C.; Lin, S. Robust Superhydrophobic/Superoleophilic Sponge for Effective Continuous Absorption and Expulsion of Oil Pollutants from Water. *ACS Applied Materials & Interfaces* **2013**, *5*, 8861-8864.
- [58] Zhu, Y.; Zhang, F.; Wang, D.; Pei, X.F.; Zhang, W.; Jin, J. A Novel Zwitterionic Polyelectrolyte Grafted PVDF Membrane for Thoroughly Separating Oil from Water with Ultrahigh Efficiency. *Journal of Materials Chemistry a* **2013**, *1*, 5758-5765.
- [59] Xue, Z.; Wang, S.; Lin, L.; Chen, L.; Liu, M.; Feng, L.; Jiang, L. A Novel Superhydrophilic and Underwater Superoleophobic Hydrogel-Coated Mesh for Oil/Water Separation. *Adv Mater* **2011**, *23*, 4270-4273.
- [60] Lee, C.; Baik, S. Vertically-Aligned Carbon Nano-Tube Membrane Filters with Superhydrophobicity and Superoleophilicity. *Carbon* **2010**, *48*, 2192-2197.
- [61] Wang, C.; Yao, T.; Wu, J.; Ma, C.; Fan, Z.; Wang, Z.; Cheng, Y.; Lin, Q.; Yang, B. Facile Approach in Fabricating Superhydrophobic and Superoleophilic Surface for Water and Oil Mixture Separation. *ACS Applied Materials & Interfaces* **2009**, *1*, 2613-2617.
- [62] Feng, L.; Zhang, Z.Y.; Mai, Z.H.; Ma, Y.M.; Liu, B.Q.; Jiang, L.; Zhu, D.B. A Super-Hydrophobic and Super-Oleophilic Coating Mesh Film for the Separation of Oil and Water. *Angewandte Chemie-International Edition* **2004**, *43*, 2012-2014.
- [63] La, D.; Tuan Anh Nguyen; Lee, S.; Kim, J.W.; Kim, Y.S. A Stable Superhydrophobic and Superoleophilic Cu Mesh Based on Copper Hydroxide Nanoneedle Arrays. *Appl. Surf. Sci.* **2011**, *257*, 5705-5710.
- [64] Wang, C.; Tzeng, F.; Chen, H.; Chang, C. Ultraviolet-Durable Superhydrophobic Zinc Oxide-Coated Mesh Films for Surface and Underwater-Oil Capture and Transportation. *Langmuir* **2012**, *28*, 10015-10019.
- [65] Tian, D.; Zhang, X.; Wang, X.; Zhai, J.; Jiang, L. Micro/nanoscale Hierarchical Structured ZnO Mesh Film for Separation of Water and Oil. *Physical Chemistry Chemical Physics* **2011**, *13*, 14606-14610.

CHAPTER 4: DYNAMICS OF INCOMING DROPLETS ON TEXTURED HYDROPHOBIC CONCRETE

In the previous chapter, the relationship between surface micro/nanotopography and small fast vibrations was investigated. Vibrations and micro/nanopatterns can be substituted by an effective force or energy obtained by using the method of separation of motions. The structure-property relationships in materials and surfaces were established. Surface topography as well as vibrations can affect wetting properties such as the contact angle and the surface free energy. In this chapter, the surface topography is used to control the wettability of concrete, and thereby produce hydrophobic concrete.

4.1 Introduction

There are two well recognized facets to superhydrophobicity, namely the contact angle (CA) and contact angle hysteresis (CAH). There is another important, although less frequently discussed, facet which is the ability to repel incoming water droplets [1]. Although the ability to repel impinging water droplets is not measured by a single parameter unlike CA or CAH, it can be used to characterize the wetting property of a surface [2]. When a water droplet impinges on a surface, it flattens out into a pancake (lamella) shape with conversion of droplet kinetic energy into surface energy. What happens next depends on the wettability of the surface. On a hydrophilic surface, the droplet continues to flatten out and wet the surface. But on a hydrophobic surface the droplet recedes back from the pancake-like shape to form a spherical cap. In certain cases the droplet has inertia sufficient to bounce off completely or eject a jet depending on the energy dissipation during the whole process (Figure 4.1). If it is desirable that a surface repels incoming droplets, the droplets themselves should be of low viscosity and high

surface tension [3]. If complete bouncing off does not happen, then the droplet is pinned either partially (Figure 4.1) or completely to the surface. This often involves the transition from the Cassie-Baxter to Wenzel state. Pinning has also been shown to be influenced by the contact time with the surface [4,5]. High kinetic energy droplet may also break-up into smaller ones.

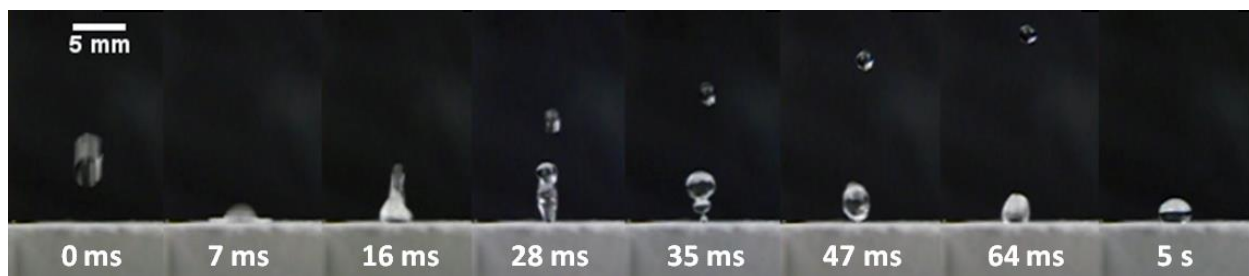


Figure 4.1. Water droplet impacting hydrophobic concrete at room temperature. The droplet is seen to flatten out into a ‘pancake shape’ in the second frame. In the third frame, it retracts and a jet is expelled.

The parent droplet however remains partially pinned due to longer contact time with the surface.

Previous studies have dealt with droplets impacting carbon nanofiber surface [6], electrospun nanofiber membranes [7], carbon nanotube films [8], micro-patterned elastomer [9,10], silicon oil-wetted surface [11], carbon soot[12], polyvinyl chloride, wax and glass [13]. Bird et al. [14] showed that contact time between a drop and a surface can be reduced by using patterns that induce non-axisymmetric recoil. Surface roughness has little impact on the behavior of impacting low velocity droplets, but it can influence the location of transition region between bouncing and pinned states [6,13]. For porous membranes, impacting droplets above a threshold velocity penetrate the pores irrespective of their native wettability [7]. Droplet impact dynamics have been studied in freezing conditions to simulate the icephobicity [8,15]. Water droplets can bounce-off superhydrophobic surface at $-25\text{ }^{\circ}\text{C}$ before ice nucleation can start [15]. A carefully textured surface topography can help resist pinning of water even at $-30\text{ }^{\circ}\text{C}$ [16]. The so called ‘jumping-drop superhydrophobic surfaces’ [17] can slow down frost formation by continuously

ejecting condensate droplets, and thus lead to less ice accretion [18]. In this chapter, impinging water droplets on hydrophobic concrete are studied.

Concrete, which is a mixture of portland cement, water and aggregates, is a versatile construction material. Dry concrete being porous and hydrophilic absorbs water. When such concrete undergoes the freeze-thaw cycling, it can lead to progressive deterioration and failure of concrete. Novel hydrophobic fiber-reinforced concrete was prepared to reduce water penetration, and some samples indicated superhydrophobic behavior (water apparent $CA > 150^\circ$) while others were strongly hydrophobic with CA approaching the superhydrophobicity area [19]. This new material was designed to ensure that beneficial structure is reproduced upon wear. This advanced material can find many applications, especially, in cold regions where there is occurrence of freezing environment combined with deicing agents such as salt. Therefore, the performance of hydrophobic concrete when water and salt solution droplets are impinged upon them both at room temperature and sub-freezing condition is of interest. Ability to repel incoming water droplets can help to prevent ice growth and accretion.

4.2 Experimental

In this section, the ability of concrete to repel incoming water droplets is studied.

4.2.1 Materials

The concept of superhydrophobic concrete was proposed and realized by Professor Konstantin Sobolev from the Department of Civil and Environmental Engineering at the University of Wisconsin-Milwaukee. Some specimens and the coatings used in this study were prepared by Dr. Marina Kozhukhova [20-22].

Mortar specimens were prepared using portland cement type I, standard quartz sand and tap water. The mortar mixes were modified with polyvinyl alcohol (PVA) fibers to induce a certain “self-reproducing” surface structure, important for icephobic properties. The PVA fibers also have a low dielectric constant which may weaken ice adhesion to the surface. An admixture was used to improve the workability of the mortar mixes. The details about the constituents of the mortar mixes are described in the Appendix. Six concrete samples were prepared in the form of mortar tiles. The sample compositions were as given in Table 4.1.

Table 4.1. Composition of the hydrophobic concrete samples.

Mixture ID	M1	M2	A3	A4	B3	B4
Water-cement ratio	0.25	0.3	0.3	0.4	0.3	0.4
Sand-cement ratio	0	1	1	1	0.5	0.5
Super-plasticizer, % solids	0.1	0.1	0.1	0.1	0.1	0.1
PVA fibers, vol %	1	1	1	1	2	2

The surfaces of the samples to be hydrophobized were subjected to mechanical abrasion using 60 grit sand paper for 30 sec. The samples were then coated with hydrophobic emulsions to achieve hydrophobicity. For this purpose, a water-based “shell type” siloxane emulsion was used. Polymethylhydroxysilane (PMHS) and PVA were used as the hydrophobizing agent and surfactant respectively. Silica fume particles were used to stabilize the emulsion, and also to provide micro-roughness when the emulsion is applied to the mortar surface. Two emulsions with different concentrations of hydrophobic agent and silica fume were prepared at proportions of 25% : 5% and 5% : 1%, by weight, respectively. Sample M2 was treated with the emulsion based on 25% and 5% of hydrophobic agent and silica fume respectively, while the other

samples were treated with the emulsion containing 5% and 1% of the components. More information about the components of the emulsion is described in the Appendix. The procedure of emulsion preparation was described in detail in [19,23,24].

4.2.2 Contact angle and surface roughness measurement

A ramé-hart goniometer (model 100-25-M) was used to measure the CA and CAH of the six samples. Distilled water droplets of 10 μl were used and at least five readings were taken for each sample. The samples were observed at 20X with an Olympus Lext OLS4100 laser scanning microscope and average surface roughness (S_a) of an area $0.625\mu\text{m} \times 0.625\mu\text{m}$ was measured.

4.2.3 Droplet impact test

Distilled water droplets of around 14 μl were dropped onto horizontal concrete samples from sixteen different heights ($7 \text{ mm} \leq H \leq 140 \text{ mm}$). Schematic for the experimental setup is shown in Figure 4.2a. The video of droplet impacts on the surfaces were recorded at 420 fps using a camera (Canon EX-FH25). The heights of first rebound (h) were measured from the videos. At least five impacts were measured at each height for each sample. The concrete samples were then kept at 45° incline so that impact is non-axisymmetric. Distilled water droplets (14 μl) as well as droplets of NaCl solution in water (1:4 by weight) were dropped from three different heights (10 mm, 50 mm, and 140 mm). Schematic for the experimental setup is shown in Figure 4.2b. The impact and interaction of the droplets with the surfaces were recorded. The ambient conditions were 20 °C and 38% relative humidity.

Next, the concrete samples were pre-cooled at -20 °C for two hours. Then they were taken to a room at -5 °C and 34% relative humidity, where distilled water droplets (14 μl) as well

as droplets of NaCl solution in water (1:4 by weight) were dropped from three different heights (10 mm, 50 mm, 140 mm) on the concrete samples kept at 45° incline (Figure 4.2b). The impact and interaction of the droplets with the surfaces were recorded.

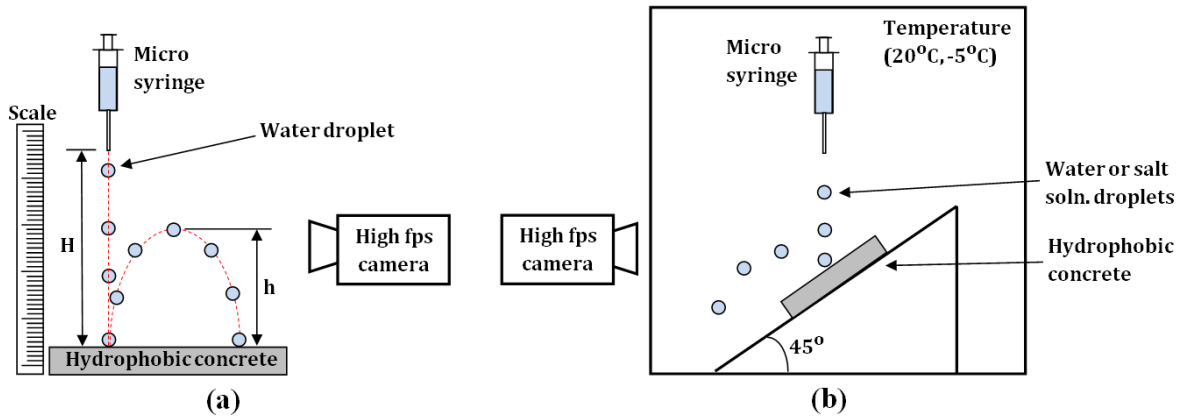


Figure 4.2. The experimental setups for the droplet impact test. (a) Experiment to measure the height of first bounce of droplet on horizontal hydrophobic concrete sample. The trajectory of the bouncing droplet which is a vertical line, is exaggerated into a parabola to identify h. (b) Experiment to study impact of droplets impinging at 45° and icephobic performance under sub-zero conditions.

4.3 Results

4.3.1 Contact angle and surface roughness

The CA, CAH, and S_a measurements for the samples are given in Table 4.2 below. All the samples were over-hydrophobic ($120^\circ < CA < 150^\circ$). All of them also exhibited very high contact angle hysteresis. The droplets remained adherent to the surfaces even when vertical. The equilibrium contact angle based on the equation suggested by Tadmor [25] is also listed in Table 4.2. These values are much different from the observed contact angles. Figure 4.3 shows the 3D surface profiles of the scan area of samples. The surface of M1 (Figure 4.3a) is different from the rest of the samples (Figures 4.3b-f) due to the absence of sand particles. This causes roughness on a different scale as opposed to the case when sand is present.

Table 4.2. CA, CAH, equilibrium contact angle from Tadmor equation and S_a for concrete samples.

Sample ID	CA	CAH	Calculated equilibrium CA	Average roughness S_a (μm)
M1	$140.9^\circ \pm 7.8^\circ$	$67.5^\circ \pm 2.3^\circ$	98.8°	6.09
M2	$132.0^\circ \pm 6.6^\circ$	$51.7^\circ \pm 7.5^\circ$	102.4°	3.82
A3	$121.4^\circ \pm 4.2^\circ$	$55.6^\circ \pm 3.6^\circ$	100.4°	2.72
A4	$129.7^\circ \pm 6.7^\circ$	$66.3^\circ \pm 3.7^\circ$	98.3°	2.53
B3	$139.9^\circ \pm 5.1^\circ$	$55.7^\circ \pm 7.9^\circ$	100.9°	2.49
B4	$139.7^\circ \pm 4.6^\circ$	$60.5^\circ \pm 9.4^\circ$	102.7°	3.57

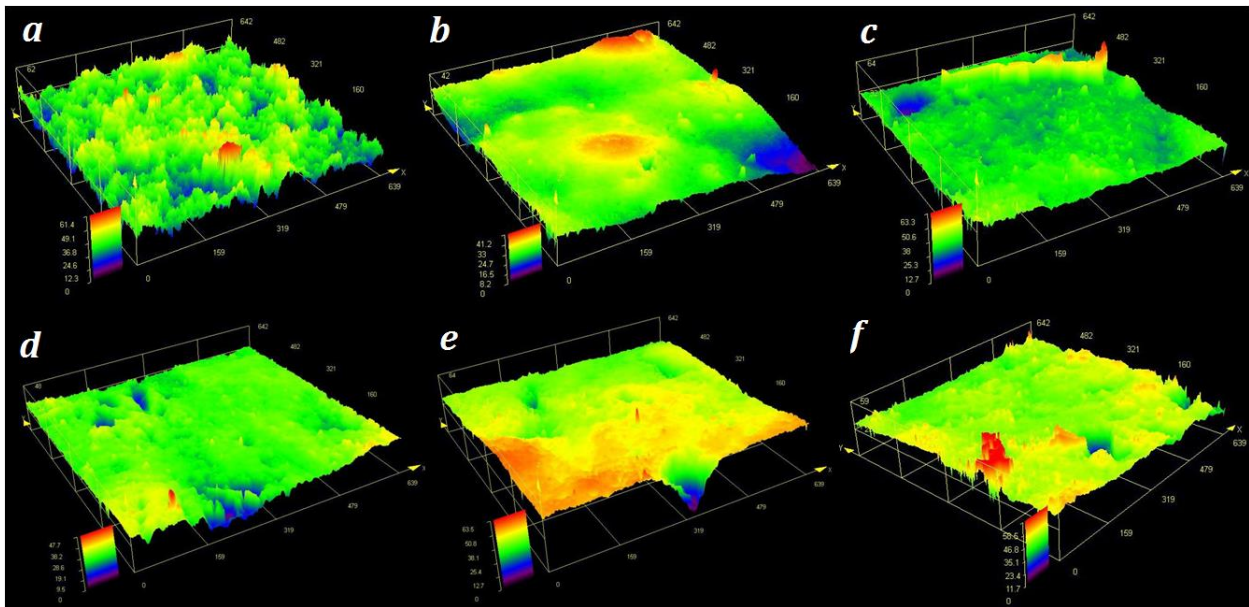


Figure 4.3. 3D surface topography of the samples. (a) M1 (b) M2 (c) A3 (d) A4 (e) B3 (f) B4. M1 has dense distribution of asperities due to the lack of aggregates in the sample.

4.3.2 Analysis of vertical impacts

For experiments as shown in Figure 4.2a, droplets bounced off sample M1 quite easily. Droplets freely falling from a height (H) up to 90 mm were seen to bounce off with very rare instances of pinning. Beyond 90 mm, the droplets got pinned to the surface frequently. Droplets falling from a height of 110 mm and above were seen to break-up into smaller droplets on impact. These smaller droplets adhered strongly to the surface. For M2 the interaction was quite

different. Even some low velocity droplets ($H \sim 10$ mm) got pinned to the surface on impact. Droplets falling from 60 mm broke-up or got pinned on impact. Free falls from 80 mm or higher always resulted in break-up of droplets. For A3, frequent pinning was observed for free-fall from heights up to 60 mm, beyond which the droplets bounced off. At 110 mm and higher the droplets broke-up on impact and the resulting smaller droplets adhered to the surface. For A4, droplets from heights of 110 mm and above broke-up into smaller droplets. The droplets also got pinned frequently on impact from heights up to 100 mm. Sample B3 and B4 resisted pinning for low velocity droplets ($H \sim 15$ mm). For B3, droplets broke-up on free-fall from heights over 100 mm, while for B4 it was 120 mm.

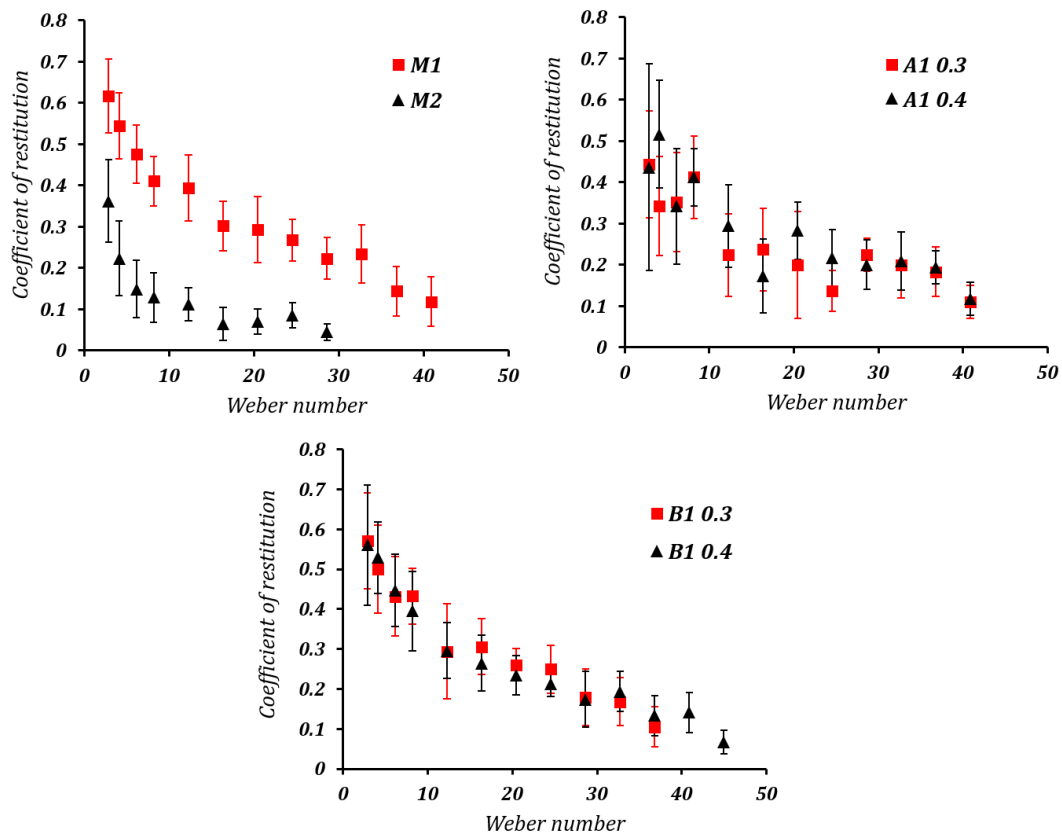


Figure 4.4. Coefficient of restitution at various Weber numbers (We) for the hydrophobic concrete samples. The curves show a similar trend, with a more negative slope at low We and less negative slope at higher We .

The velocities of the droplets in free fall from a height H were calculated as $v \sim \sqrt{2gH}$. Weber number (We) was calculated for distilled water droplets impacting on horizontal concrete surfaces. $We = \frac{\rho r v^2}{\gamma}$, where density $\rho = 1000 \text{ kg/m}$, surface tension $\gamma = 0.072 \text{ N/m}$ and radius of droplet $r = 1.5 \text{ mm}$. Coefficient of restitution was calculated as $COR = \sqrt{h/H}$, where h is the height of first rebound. The variation of COR with We for the concrete samples are shown in Figure 4.4. The curves for each sample apparently has two distinct parts, one that shows a sharp negative slope at low We (0-10), and the other with a gradual negative slope at larger We . Since COR embodies the kinetic energy dissipation, this may mean that two different dissipative mechanisms are at play at low and high impact velocities. This is discussed further in the following section.

4.3.3 Analysis of oblique impacts

Stacked images in Figures 4.5-4.7 show the interaction of droplets with the samples at 45° inclination. The images clearly show the trajectory of the droplet. Whether the droplet wets the surface, or bounces off can also be observed from the Figures. Droplets that bounce off have an apparent parabolic trajectory after impact. For droplets falling from 10 mm (Figure 4.5), sample M1 was seen to repel both water and salt solution droplets at 20 °C and -5 °C. In case of M2, both water and salt solution droplets wetted or stuck to the surface. At -5 °C the wetted area can inhibit ice accretion if more water droplets impinge at the same location subsequently. Water droplets falling from 10 mm was seen to stick to A3, A4, B3 and B4 at -5 °C, while salt solution bounces off. But all four of them repelled both water and salt solution at 20 °C.

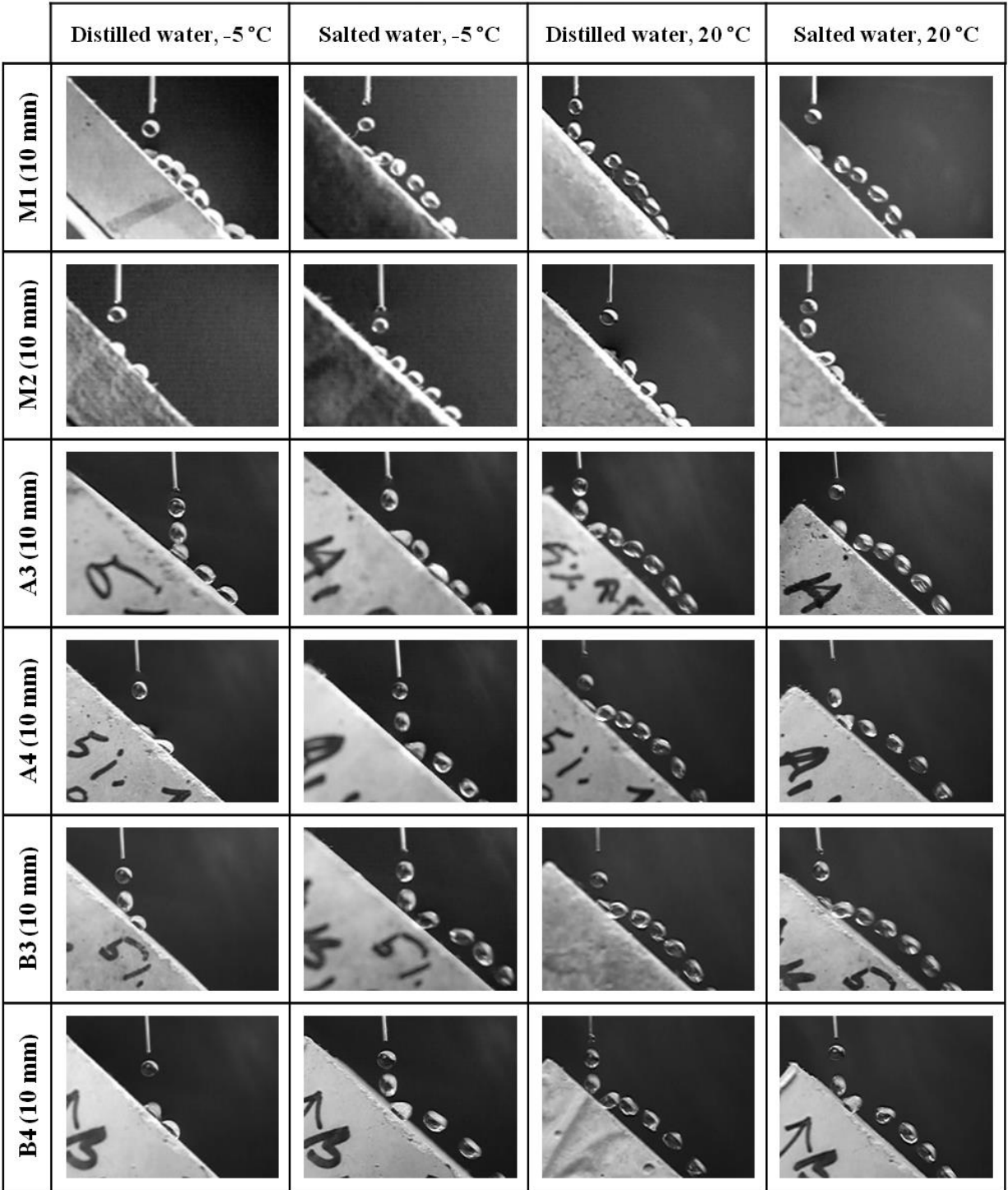


Figure 4.5. Interaction of distilled and salted water droplets falling from 10 mm, with the samples at 45° inclination, at 20 °C and -5 °C.

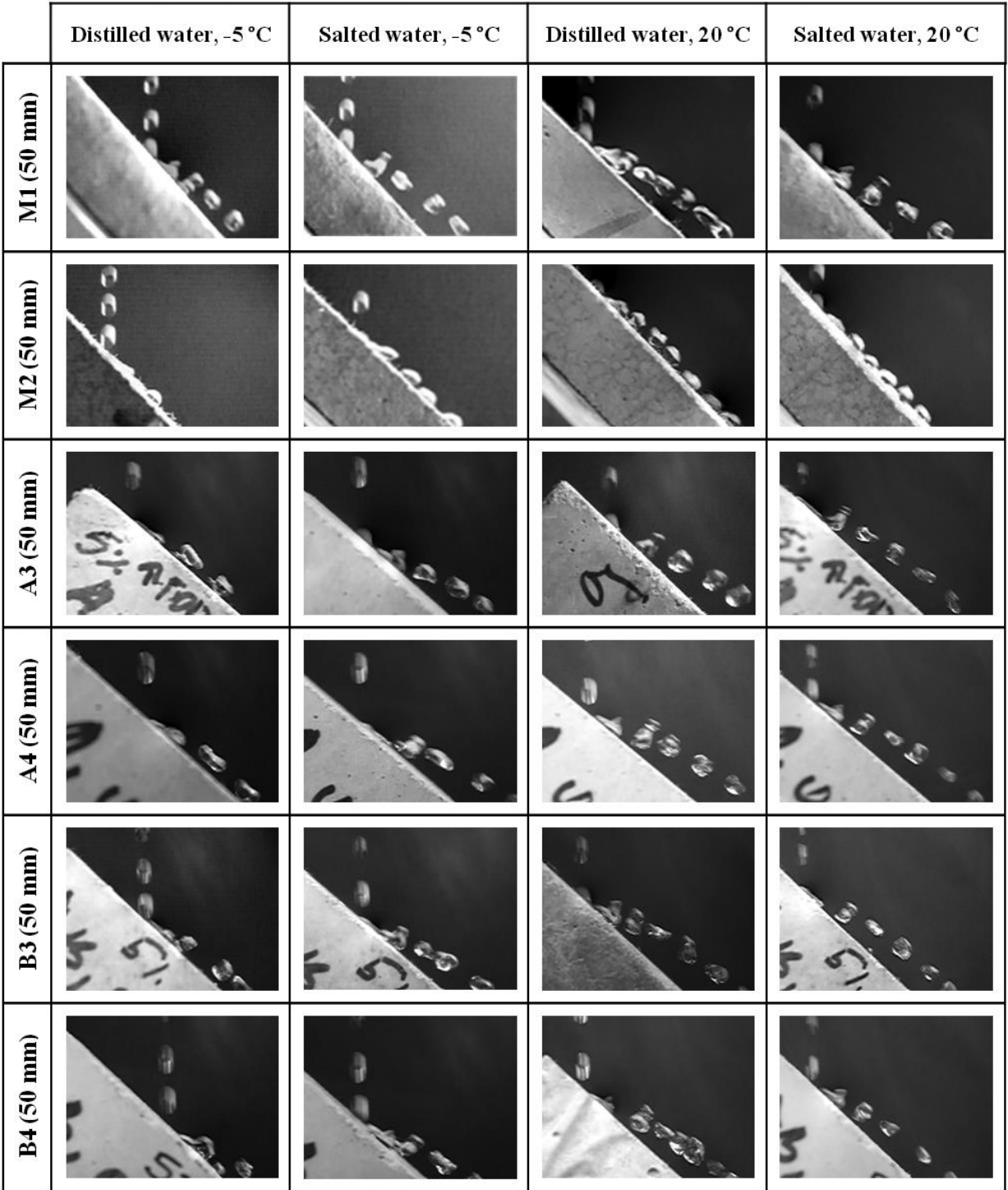


Figure 4.6. Interaction of distilled and salted water droplets falling from 50 mm, with the samples at 45° inclination, at 20 °C and -5 °C.

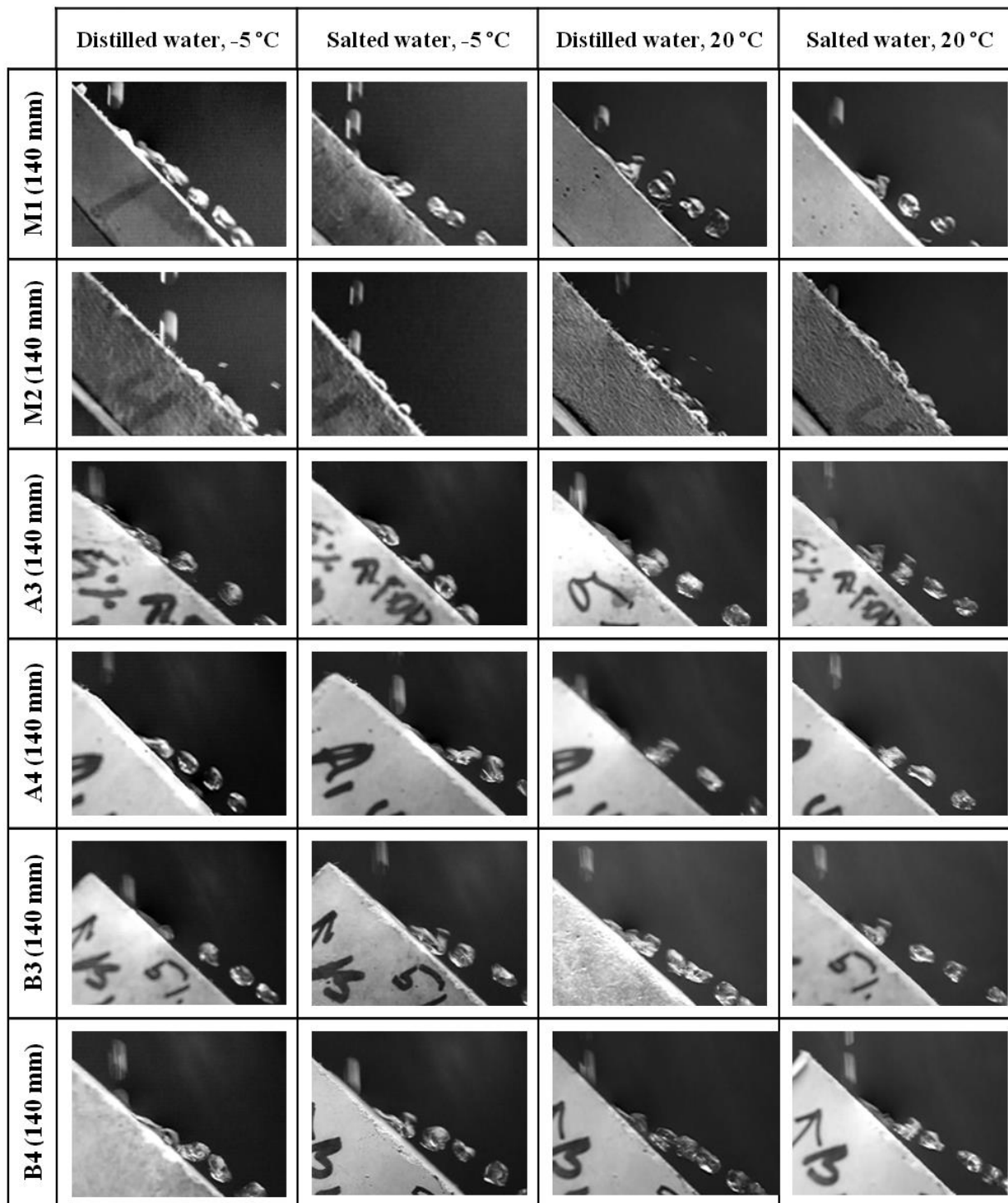


Figure 4.7. Interaction of distilled and salted water droplets falling from 140 mm, with the samples at 45° inclination, at 20 °C and -5 °C.

For droplets falling from 50 mm (Figure 4.6), M1 repelled water and salt solution effectively at -5 °C. At 20 °C, even though the droplets broke-up they still bounced off. Droplets

wetted or stuck to M2 at -5 °C, but at 20 °C both salt solution and water rolled off. A3, A4, B3 and B4 repelled both water and salt solution droplets at -5 °C and 20 °C. At -5 °C, the water droplets just about rolled off the surfaces. But at the same temperature the salt solution droplets bounced off along a longer trajectory. This difference in trajectories can be attributed to change in droplet properties with temperature and salt addition. Similar trajectories were observed at 20 °C for both water and salt solution.

For droplets falling from 140 mm (Figure 4.7), all samples except M2 repelled water and salt solution droplets at both 20 °C and -5 °C. Droplets broke-up on impact, but clearly bounced off. Pinning was not observed. This was unlike what was observed with the droplets impinging horizontal samples. The angle of incoming droplets seemed to affect what happened after impact. For horizontal samples pinning was seen to set in even at low We . In case of M2, the droplets wetted the surface or was pinned.

4.4 Discussion

When a water droplet impinges on a hydrophobic surface, part of its kinetic energy (K) is dissipated. For droplets under consideration, the Reynolds number based on velocity of impact (v) is $553 < Re < 2476$. Viscous damping and pinning are assumed to be the predominant modes of energy dissipation. The damping force $F_{viscous} \propto v$, and the resulting energy dissipation is $\Delta E_{inertial} \propto We^{\frac{1}{2}}$. The energy dissipation of the droplet due to pinning is the result of water hammer-type pressure induced Cassie-Baxter to Wenzel transition [26]. Water hammer-type pressure is given by $P = 0.2\rho Cv$, where ρ is the liquid density, C is the speed of sound in the liquid and v is the impact velocity of the droplet. The force from the water hammer-type pressure acts on the area of contact between the liquid droplet and the surface. Assuming

that there is no rotation of the droplets at impact, then the deformation/flattening of the droplet can be assumed to be proportional to the impact velocity. If X is the deformation of the droplet dimension in unit of length, the energy dissipated due to pinning can be written as $\Delta E_{pinning} \propto VX^2 \propto We^{\frac{3}{2}}$. Kinetic energy of the droplet dissipated on impact, $\Delta K \sim \Delta E_{pinning} + \Delta E_{viscous}$

$$\Delta K \propto We^{0.5} + We^{1.5} \quad (4.1)$$

$$COR = \sqrt{1 - \frac{\Delta K}{K}} = \sqrt{1 - \frac{aWe^{0.5} + bWe^{1.5}}{We}} \quad (4.2)$$

$$COR \sim 1 - \alpha(We)^{-0.5} - \beta(We)^{0.5} \quad (4.3)$$

where the parameters α and β depend on the liquid viscosity and the surface topography respectively.

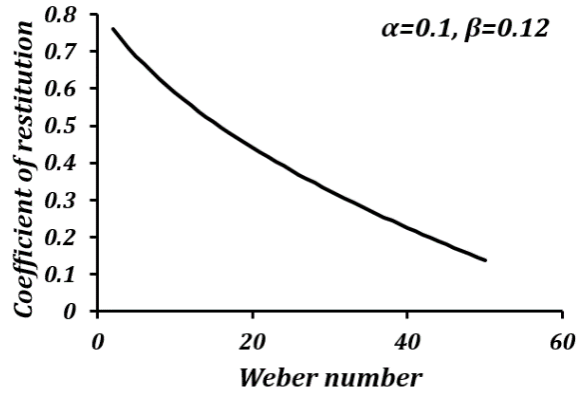


Figure 4.8. Theoretical Coefficient of restitution (COR) vs. Weber number (We) plot.

Assigning nominal values to the parameters α and β , the curve in Figure 4.8 was obtained. The shape of these theoretical curves is much similar to the plot obtained in Figure 4.4. Also, pinning can set in at different We for different surface topographies (based on the value of β). This agrees with experimental observations for the different samples. Thus modifying the surface texture of concrete can produce pinning-resistant hydrophobic concrete.

At an incline of 45°, M1 was seen to repel both water and salt solution droplets at 20 °C and -5 °C. A3, A4, B3 and B4 were seen to repel droplets at 20 °C, and -5 °C except for water droplets falling from 10 mm. The performance of inclined samples at 20 °C was unlike that of horizontal samples. They were seen to better resist pinning. Pinning is caused by water hammer-type pressures which are the result of sudden change in momentum of the droplet. When the samples are horizontal, pinning can also happen at lower We because the velocity vector is normal to the surface of impact. But when the samples are tilted at 45° inclination, the impact is asymmetric and only the component of velocity normal to the surface causes the water hammer-type pressure. The change in momentum associated with this component is lower than the change in momentum associated with the total vertical velocity. Thus the droplets resist pinning on inclined surfaces at similar We . The We range studied in this paper is similar to what is observed for raindrops in light rain ($We \sim 28$) [27]. Heavy rain with large droplets and higher terminal velocities may result in very large We . During rain however, water droplets break up before they reach the critical size of 6mm [28,29].

M2 was seen to be the worst at repelling incoming droplets, with droplets either getting pinned or leaving a wet streak behind in most cases. This wet streak inhibited ice accretion in case of subsequent droplet impacts. Therefore it is important to have surfaces which resist wetting or pinning to reduce chance of ice accretion. Manipulating the composition of concrete can yield samples with specific porosity and roughness. Aggregate (sand) added to concrete results in surface roughness on a scale similar to the size of sand particles. Since sample M1 with no sand content effectively repels incoming droplets at both room and sub-zero temperatures, it is clear that surface roughness on the scale of sand particles is detrimental to the performance. The PVA fiber content does not seem to affect the performance on itself, but the roughness

created by the fibers in tandem with aggregates seems to degrade the performance of hydrophobic concrete as seen with M2. Since incoming angle is a dominant factor in the fate of the impacting droplet, it is apparent that asymmetric impact can reduce water hammer-type pressure. Designing ribs or features of dimension comparable to droplet size can also provide asymmetry needed to prevent pinning.

4.5 Conclusion

In this chapter, surface micro/nanotopography was used to control the wettability of concrete. Micro/nanotextured concrete was produced by controlling the concrete mixture composition. The concrete surface was hydrophobized by coating with a hydrophobic emulsion. The dynamics of droplets impacting the surface of micro/nanotextured hydrophobic concrete was studied. Whether the droplets were pinned, broke-up on impact, or bounced-off depended on the droplet velocity as well as the surface topography. Kinetic energy of the droplet is mostly dissipated due to viscous damping or pinning. At low Weber numbers, the droplet bounces off, but at higher Weber numbers, droplet pinning takes effect. The transition Weber number between bouncing off and pinning was seen to be not well defined and it depended on the surface topography. Also inclined surfaces were seen to resist pinning/break-up of droplets at higher velocities. This is due to the asymmetric impact resulting in lower water hammer pressure. The surfaces which showed a delayed onset of pinning are less susceptible to ice accretion. The ability of hydrophobic concrete to repel incoming rain and corrosive solutions can be optimized by changing the mixture composition.

4.6 References

- [1] Nosonovsky, M.; Bhushan, B. Energy Transitions in Superhydrophobicity: Low Adhesion, Easy Flow and Bouncing. *Journal of Physics-Condensed Matter* **2008**, *20*, 395005.
- [2] Crick, C.R.; Parkin, I.P. Water Droplet Bouncing-a Definition for Superhydrophobic Surfaces. *Chemical Communications* **2011**, *47*, 12059-12061.
- [3] Bergeron, V.; Quere, D. Water Droplets make an Impact. *Physics World* **2001**, *14*, 27-31.
- [4] Tadmor, R.; Chaurasia, K.; Yadav, P.S.; Leh, A.; Bahadur, P.; Dang, L.; Hoffer, W.R. Drop Retention Force as a Function of Resting Time. *Langmuir* **2008**, *24*, 9370-9374.
- [5] Tadmor, R.; Bahadur, P.; Leh, A.; N'guessan, H.E.; Jaini, R.; Dang, L. Measurement of Lateral Adhesion Forces at the Interface between a Liquid Drop and a Substrate. *Phys. Rev. Lett.* **2009**, *103*, 266101.
- [6] Tsai, P.; Pacheco, S.; Pirat, C.; Lefferts, L.; Lohse, D. Drop Impact upon Micro- and Nanostructured Superhydrophobic Surfaces. *Langmuir* **2009**, *25*, 12293-12298.
- [7] Sahu, R.P.; Sinha-Ray, S.; Yarin, A.L.; Pourdeyhimi, B. Drop Impacts on Electrospun Nanofiber Membranes. *Soft Matter* **2012**, *8*, 3957-3970.
- [8] Zheng, L.; Li, Z.; Bourdo, S.; Khedir, K.R.; Asar, M.P.; Ryerson, C.C.; Biris, A.S. Exceptional Superhydrophobicity and Low Velocity Impact Icephobicity of Acetone-Functionalized Carbon Nanotube Films. *Langmuir* **2011**, *27*, 9936-9943.
- [9] Bartolo, D.; Bouamrine, F.; Verneuil, E.; Buguin, A.; Silberzan, P.; Moulinet, S. Bouncing Or Sticky Droplets: Impalement Transitions on Superhydrophobic Micropatterned Surfaces. *Europhys. Lett.* **2006**, *74*, 299-305.
- [10] Tsai, P.; Hendrix, M.H.W.; Dijkstra, R.R.M.; Shui, L.; Lohse, D. Microscopic Structure Influencing Macroscopic Splash at High Weber Number. *Soft Matter* **2011**, *7*, 11325-11333.
- [11] Gilet, T.; Bush, J.W.M. Droplets Bouncing on a Wet, Inclined Surface. *Phys. Fluids* **2012**, *24*, 122103.
- [12] Hejazi, V.; Sobolev, K.; Nosonovsky, M. From Superhydrophobicity to Icephobicity: Forces and Interaction Analysis. *Scientific Reports* **2013**, *3*, 2194.
- [13] Sikalo, S.; Marengo, M.; Tropea, C.; Ganic, E.N. Analysis of Impact of Droplets on Horizontal Surfaces. *Exp. Therm. Fluid Sci.* **2002**, *25*, 503-510.
- [14] Bird, J.C.; Dhiman, R.; Kwon, H.; Varanasi, K.K. Reducing the Contact Time of a Bouncing Drop. *Nature* **2013**, *503*, 385-388.

- [15] Mishchenko, L.; Hatton, B.; Bahadur, V.; Taylor, J.A.; Krupenkin, T.; Aizenberg, J. Design of Ice-Free Nanostructured Surfaces Based on Repulsion of Impacting Water Droplets. *ACS Nano* **2010**, *4*, 7699-7707.
- [16] Maitra, T.; Tiwari, M.K.; Antonini, C.; Schoch, P.; Jung, S.; Eberle, P.; Poulikakos, D. On the Nanoengineering of Superhydrophobic and Impalement Resistant Surface Textures Below the Freezing Temperature. *Nano Letters* **2014**, *14*, 172-182.
- [17] Boreyko, J.B.; Collier, C.P. Delayed Frost Growth on Jumping-Drop Superhydrophobic Surfaces. *ACS Nano* **2013**, *7*, 1618-1627.
- [18] Zhang, Q.; He, M.; Chen, J.; Wang, J.; Song, Y.; Jiang, L. Anti-Icing Surfaces Based on Enhanced Self-Propelled Jumping of Condensed Water Microdroplets. *Chemical Communications* **2013**, *49*, 4516-4518.
- [19] Flores-Vivian, I.; Hejazi, V.; Kozhukhova, M.I.; Nosonovsky, M.; Sobolev, K. Self-Assembling Particle-Siloxane Coatings for Superhydrophobic Concrete. *ACS Applied Materials & Interfaces* **2013**, *5*, 13284-13294.
- [20] Kozhukhova, M.I. 'АНТИОБЛЕДЕНИТЕЛЬНОЕ ПОКРЫТИЕ ДЛЯ МЕЛКОЗЕРНИСТОГО БЕТОНА' / Anti Icing Coating for Concrete. PhD Thesis. **2014**.
- [21] Kozhukhova, M.I.; Strokova, V.V.; Sobolev, K. 'ОСОБЕННОСТИ ГИДРОФОБИЗАЦИИ МЕЛКОЗЕРНИСТЫХ БЕТОННЫХ ПОВЕРХНОСТЕЙ' / Hydrophobization of Concrete. *Bulletin of BSTU* **2014**, *4*, 33-35.
- [22] Kozhukhova, M.I.; Flores-Vivian, I.; Rao, S.; Strokova, V.V.; Sobolev, K. 'Комплексное силиоксановое покрытие для супергидрофобизации бетонных поверхностей' / Complex Siloxane Coating for Superhydrophobization of Concrete Surfaces. *Construction Materials Journal* **2014**, *3*, 26-30.
- [23] Muzenski, S.; Flores-Vivian, I.; Sobolev, K. Freeze-Thaw Resistance of Fiber Reinforced Composites with Superhydrophobic Admixtures. In *Mechanics and Physics of Creep, Shrinkage, and Durability of Concrete*, Cambridge, MA; pp. 269-276.
- [24] Muzenski, S.; Flores-Vivian, I.; Sobolev, K. Hydrophobic Engineered Cementitious Composites for Highway Applications. *Cem. Concr. Compos.* **2015**, *57*, 68-74.
- [25] Tadmor, R. Line Energy and the Relation between Advancing, Receding, and Young Contact Angles. *Langmuir* **2004**, *20*, 7659-7664.
- [26] Kwon, H.; Paxson, A.T.; Varanasi, K.K.; Patankar, N.A. Rapid Deceleration-Driven Wetting Transition during Pendant Drop Deposition on Superhydrophobic Surfaces. *Phys. Rev. Lett.* **2011**, *106*, 036102.
- [27] Foote, G.B.; Du Toit, P.S. Terminal Velocity of Raindrops Aloft. *J. Appl. Meteor.* **1969**, *8*, 249-253.

[28] Villermaux, E.; Bossa, B. Single-Drop Fragmentation Determines Size Distribution of Raindrops. *Nature Physics* **2009**, *5*, 697-702.

[29] Kostinski, A.B.; Shaw, R.A. Raindrops Large and Small. *Nature Physics* **2009**, *5*, 624-625.

CHAPTER 5: CORROSION RESISTANT SUPERHYDROPHOBIC METALLIC SURFACES

In the previous chapter, surface topography was used to control the wettability of concrete. In this chapter surface topography is used to control corrosion of metallic surfaces. When a superhydrophobic surface is immersed in water, it would have less interfacial contact area between water and the solid on account of the solid-water-air non-homogeneous interface at the superhydrophobic surface. Electrolytes which cause electrochemical corrosion are usually aqueous solutions. Corrosion of metallic surfaces can be controlled if the metal-electrolyte contact area is reduced. In this study, the metallic surfaces are modified by changing their surface micro/nanotopography as well as lowering their surface free energy. Electrochemical corrosion tests are conducted on the metallic surfaces to investigate the effect of surface modification.

5.1 Introduction

Corrosion of metals is a highly undesirable process since it damages metallic materials used for various components leading to their gradual destruction. Consequently, various types of anti-corrosive coatings have been developed, including ones which prevent the contact of the material with a corrosive environment, such as aqueous solutions. A relatively new type of coating which repels water and aqueous solutions is the superhydrophobic coating which modifies wetting properties of a material [1]. There are a number of recent experimental studies of how superhydrophobicity can reduce corrosion, although there are few studies of the fundamental physicochemical mechanisms involved or potential applications to fresh water materials. Typically, electrochemical corrosion occurs when a metallic surface is oxidized while in contact

with an electrically conducting solution called electrolyte. A typical electrolyte used in corrosion studies is 3.5 wt. % aqueous solution of sodium chloride in water, with an electrical conductivity of $5.3 \Omega^{-1}\text{m}^{-1}$ due to solvated ions. A hydrophobic/superhydrophobic surface with a non-homogeneous interface would have a reduced interfacial contact area between the electrolyte and the metallic surface.

Making a metallic surface superhydrophobic is a challenging task. Typically, a stable combination of a low-energy surface coating with a hierarchical roughness having roughness details of characteristic length scales from microns down to nanometers is needed. Several attempts to create corrosion-resistant superhydrophobic coatings have been reported in the literature [1]. To operate in an aggressive corrosive environment, a superhydrophobic surface needs to resist chemical etching as well as degradation due to prolonged exposure. Also the surfaces roughness features and coatings need to withstand mechanical wear. Mechanical abrasion [2-4], etching [5,6], oxidation [7,8], galvanic replacement [9], and templating [10-13] are some of the methods used to create roughness on these surfaces. Several methods such as immersion coating [2,4,6-8,14-17], spin coating [18], chemical vapor deposition [9], spray coating [3,19], etc. are used to reduce surface energy. Such surfaces exhibit reduction in corrosion current and maintain superhydrophobicity on prolonged exposure to corrosive environments.

Superhydrophobicity as a means of corrosion inhibition has been studied on several metallic materials such as stainless steel [3], cold rolled steel [10-13] copper,[4,5,19-22], zinc [9,23], aluminum [2,6,14,24], titanium [7,8,17], and magnesium alloys [15,16,25]. The results from literature of corrosion tests on some of the aforementioned materials are summarized in Table 5.1. The general trend observed in these results is that the corrosion current decreases

several folds when the surface is rendered superhydrophobic. Also the corrosion potential tends to become more positive. These two tendencies are interpreted as the signs of reduced corrosion rates for superhydrophobic surfaces. Most of the methods to produce superhydrophobic surfaces involved polymer coatings which might act as diffusion barriers, oxide formation which resulted in passivation of materials, or fillers which reduced the coating permeability. Each of these factors contributed to corrosion inhibition. Therefore, the superior corrosion resistance was not the result of the superhydrophobicity alone, but a synergistic effect of several factors listed above. The influence of the superhydrophobicity alone in reducing corrosion current can be determined by comparing the entries of columns pertaining to flat-coated and rough-coated samples in Table 5.1.

Figure 5.1 shows the corrosion current density as a function of the contact angle based on the same data. In Figure 5.1a this dependency is shown for materials with the tendency of low corrosion in their native state, whereas Figure 5.1b shows the data for materials with high tendency of corrosion in their native state. In all these cases, the corrosion current density decreased significantly as soon as the contact angle became greater than 90° indicating that hydrophobicity leads to corrosion inhibition. Further decrease in corrosion current density is seen as stable air pockets are established in the Cassie-Baxter state. Feng et al.[2] reported superhydrophobic aluminum alloy surfaces with $f_{SL} \sim 0.05$, which showed 87% reduction in corrosion current density compared to uncoated alloy. Similarly, Xu et al.[15] reported superhydrophobic magnesium alloy surfaces with $f_{SL} \sim 0.046$ with a 90% reduction in corrosion current density. Effective corrosion resistant surfaces require not only large contact angles, but also minimal fractional solid-liquid interfacial area. It can be concluded that the mechanisms

which correlate the superhydrophobicity to the corrosion rates, such as the formation of Cassie heterogeneous interface, may explain the experimental data reported in the literature.

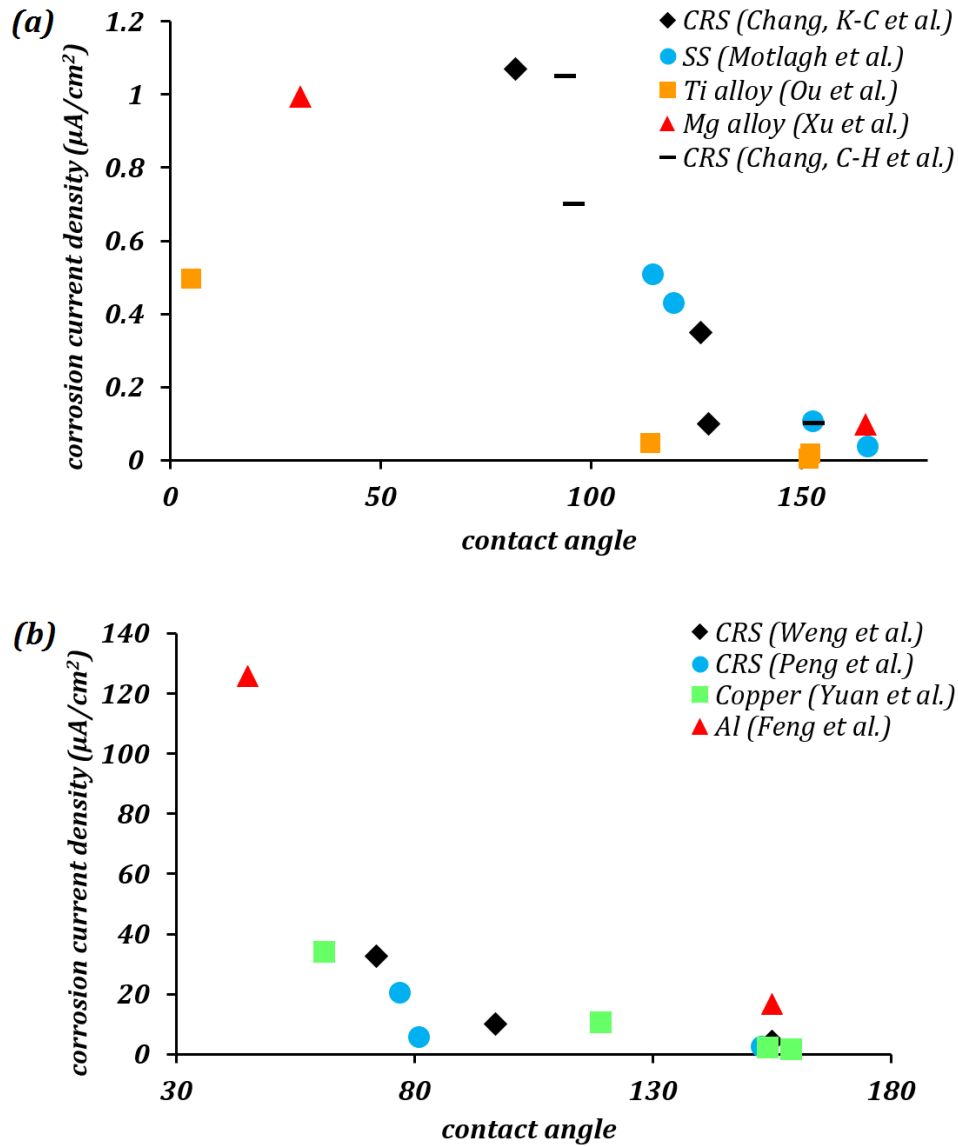


Figure 5.1. (a) and (b) Corrosion current density as a function of contact angle from published literature.

The trend clearly shows a significant decrease in corrosion current densities with increase in contact angle. The lowest corrosion current densities occur in the Cassie-Baxter domain, where contact angle is much greater than 90° .

Table 5.1.1. A brief summary of results from literature. Abbreviations: CRS – cold rolled steel, Cu – copper, SS – stainless steel, Ti – titanium, Al – aluminum, Mg – magnesium. Units for measurements: CA – deg, i_{corr} – $\mu A/cm^2$, E_{corr} – mV.

Ref.	Material	Uncoated samples			Surface texturing	Hydrophobic Coating	Flat, coated samples			Rough, coated samples		
		CA	i_{corr}	E_{corr}			CA	i_{corr}	E_{corr}	CA	i_{corr}	E_{corr}
Weng et al. [10]	CRS	72	32.73	-839	roughness from leaf template	electroactive epoxy	81	10.11	-564	155	4.33	-244
Chang, C-H et al. [11]	CRS	73	4.03	-844	roughness from leaf template	epoxy/organophilic clay	94	1.05	-628	153	0.1	-207
Peng et al. [12]	CRS	77	20.1	-944	roughness from leaf template	UV-curable epoxy acrylate polymer	81	5.44	-730	153	2.3	-394
Chang, K-C et al. [13]	CRS		6.97	-821	roughness from leaf template	epoxy/graphene composite	82	1.07	-678	128	0.1	-411
Yuan et al. [5]	Cu	61	34	-190	etching	2,2,3,4,4,4-hexafluorobutyl acrylate	-	-	-	159	1.61	80
Motlagh et al. [3]	SS	64	-	-	silica particles	perfluorodecyltriethoxysilane	-	-	-	166	0.035	-
Ou et al. [8]	Ti alloy	5	0.497	-325	etching, oxidation	1H, 1H, 2H, 2H-perfluorooctyltrichlorosilane	114.2	0.0464	-151	151.8	0.0039	1
Feng et al. [2]	Al alloy	45	125.9	-1.51	boiling water treatment	stearic acid	-	-	-	155	16.59	-0.88
Xu et al. [15]	Mg alloy	30.9	0.996	-1584.7	electrochemical machining	tridecafluoro octyltriethoxysilane	106.6	-	-	165.2	0.0968	-1422

5.2 Electrochemical Foundations of Corrosion and Wetting

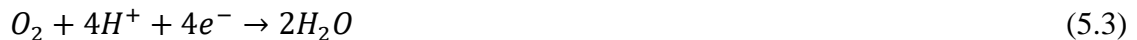
Corrosion current is the main characteristic of the rate of the electrochemical corrosion. This type of corrosion happens when a metal (electrode) comes in contact with an electrolyte. During corrosion, a metal (M) transform from its pure state to more stable oxidized states. This involves an anodic oxidation reaction



where e^{-} denotes electrons, and z is the number of electrons involved in the reaction. These excess electrons in the electrode should be consumed by a reduction reaction to prevent charge accumulation on the metal (Figure 5.2a). The common cathodic reduction reactions are hydrogen evolution



or reduction of dissolved oxygen in the electrolyte



When a metal comes in contact with an electrolyte, an ionic double layer is formed at the electrode surface. Due to that the electrode attains an electrochemical potential referred to as corrosion or open circuit potential, E_{corr} or E_{oc} . This potential is essentially the difference of the potentials between the electrode and electrolyte or a “reference electrode” immersed in the electrolyte next to the working electrode. At the corrosion potential, the anodic and cathodic reactions are in dynamic equilibrium, so that no net charge transfer between the electrode and electrolyte occurs (Figure 5.2b). The anodic current density of oxidation of metal, i_{anode} , is

exactly balanced by the cathodic current density of reduction, $i_{cathode}$, and it is also equal by absolute value to the corrosion current density i_{corr} associated with the transfer of the electrons in the electrode from the anodic to cathodic spots ($|i_{corr}| = |i_{anode}| = |i_{cathode}| \neq 0$).

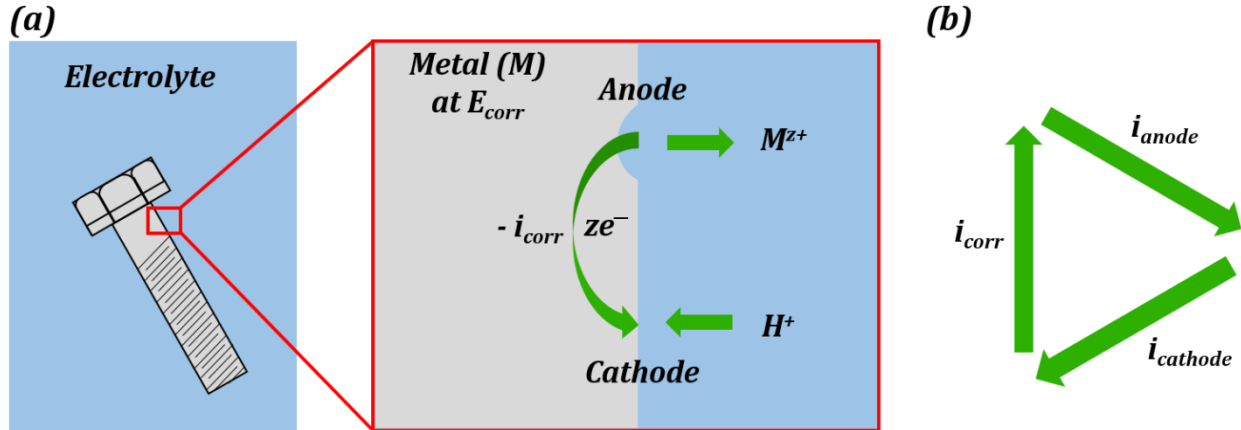


Figure 5.2. (a) A typical electrochemical corrosion process in the presence of an electrolyte. Material is removed from anodic sites and then deposited as corrosion products (rust) at cathodic sites. (b) The dynamic equilibrium current is zero.

While the total current between the electrode and electrolyte is zero, the transfer of ions (such as M^{z+} or H^+) occurs in both directions, and the transfer rate is proportional to the anodic / cathodic / corrosion current. The ion transfer effectively results in corrosion of the metal (for example, rusting). Therefore, the corrosion current can be used as a measure of the corrosion rate. However, the corrosion current cannot be measured directly. Various corrosion tests have been developed to evaluate the corrosion current.

One such corrosion test that is commonly used is the potentiodynamic polarization test (PPT). During the PPT, the potential of the sample electrode is changed above and below E_{oc} , and corresponding changes in the current are measured as a function of the potential. The value of the potential above or below E_{oc} is called the overpotential, overvoltage, or polarization, η . During an anodic polarization, the potential is increased with respect to E_{oc} resulting in oxidation

of the electrode, while during a cathodic polarization the potential is decreased resulting in reduction of the electrode. The electric current density i as a function of the overpotential is given by the Butler-Volmer equation involving both the anodic and cathodic exponential terms.

$$i = i_{corr} \left[\exp\left(\frac{\alpha_a \eta z F}{RT}\right) - \exp\left(-\frac{\alpha_c \eta z F}{RT}\right) \right] \quad (5.4)$$

where α_a and α_c are the anodic and cathodic charge transfer coefficients, $F=96,485 \text{ C mol}^{-1}$ is the Faraday constant, $R=8.31 \text{ J K}^{-1} \text{ mol}^{-1}$ is the universal gas constant, T is the absolute temperature, and z is the number of electrons involved in the reaction per molecule. Note that zero overpotential $\eta = 0$ corresponds to the dynamic equilibrium $|i_{anode}| = |i_{cathode}|$ as it has been explained above. Therefore, in order to find i_{corr} from the experimental data plot of i vs η , one should subtract the exponential term, either anodic or cathodic, from the net dependency and consider the difference at $\eta = 0$ (Figure 5.3a).

Since the current changes over several orders of magnitude during a typical corrosion test, a plot of η vs $\log i$ called the Tafel plot is usually made (Figure 5.3b). The linear regions of the anodic and cathodic plots correspond to the exponential terms of the Butler-Volmer equation, and tangential straight lines can be extrapolated as to intersect at i_{corr} .

The typical set-up used in a PPT test is shown in Figure 5.3c. It employs a three electrode electrochemical cell. In a three electrode system, one electrode is the working electrode which undergoes corrosion, the second is a reference electrode to measure potential difference between the working electrode and the electrolyte, and the third is a counter electrode (usually of an electrochemically inert material, such as gold, platinum, or carbon), which completes the circuit by allowing the current flow. There is negligible current flow through the reference electrode due

to high resistance of the voltmeter. The electrode potential of the reference electrode is known and highly stable (saturated calomel is often used as the reference electrode material). A potentiostat is used to sweep across a range of voltages, and measure the corresponding currents.

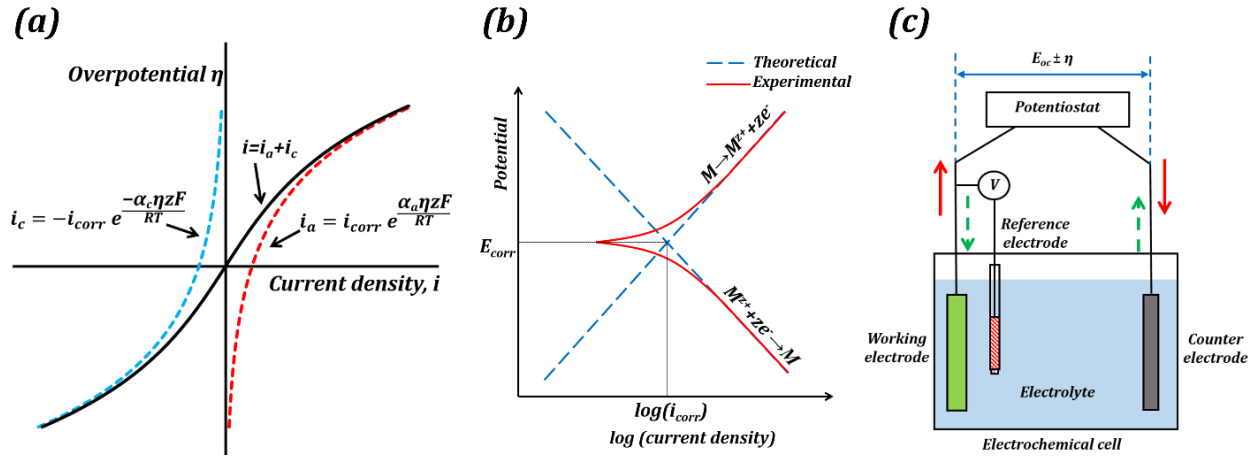


Figure 5.3. (a) A typical i vs η dependency based on the Butler-Volmer equation (b) Red curves show the Tafel plot of the net (anodic and cathodic) current. Corrosion current can be obtained by extrapolating along the tangential lines corresponding to the exponential polarization curves. (c) A typical three electrode set-up for the PPT corrosion measurement. The red arrows show current flow during anodic polarization, and the broken green arrows show current flow during cathodic polarization.

Wetting and electric properties of an interface are related to each other by the so-called Lippmann equation of electrowetting, which states that the contact angle at a solid-liquid interface subjected to the applied voltage η is given by

$$\cos \theta^* = \cos \theta_0 + \frac{C\eta^2}{2\gamma_{WA}} \quad (5.5)$$

where C is the specific capacitance per unit area of the double layer at the interface. A more general form of the Lippmann equation appropriate for a heterogeneous surface has been recently suggested by Bormashenko & Gendelman [26]. While normally changing potential is

used to control wetting properties [27], it has been demonstrated that a reverse process (controlling the electrode potential by changing the wetting properties) is feasible as well [28].

Note that the effect of the electric potential applied to the interface on the surface energy and equilibrium contact angle (Eq. 5.5) is similar to the effects of roughness (Eq. 2.2) and heterogeneity (Eq. 2.4). In accordance with Le Châtelier's principle, one could expect that changing the wetting properties would result in a certain compensatory change of the corrosion potential, which, in turn, could lead to a change of the corrosion current and, finally, of the rate of corrosion.

This chapter correlates wetting and corrosion. Surface wettability is determined by factors such as surface energy, roughness and homogeneity of the interface. The effect of these factors on the corrosion current and the rate of corrosion is studied theoretically in the following section. Experiments are performed to correlate wetting properties with corrosion rate. This is followed by discussion and comparison to theoretical predictions.

5.3 Theoretical Model

The effect of the surface roughness and the wetting state on corrosion rate is discussed in this section. First, I establish how the solid-liquid contact area and surface roughness affect the electric current in the Cassie-Baxter state in accordance with the Ohm's law. Then, the corrosion rate is related to the current using the Faraday's law of electrolysis. Finally, the Nernst equation is used to relate the corrosion rate to the surface energy due to the decrease of the chemical potential.

5.3.1 Ohm's law and the wetting states

Ohm's law $E = IR$ provides the relationship between the interfacial potential E and current I with the interfacial resistance R . The resistance is inversely proportional to the interfacial solid-liquid contact area A_{SL} . One can write,

$$I \propto A_{SL} \propto r_f f_{SL} \quad (5.6)$$

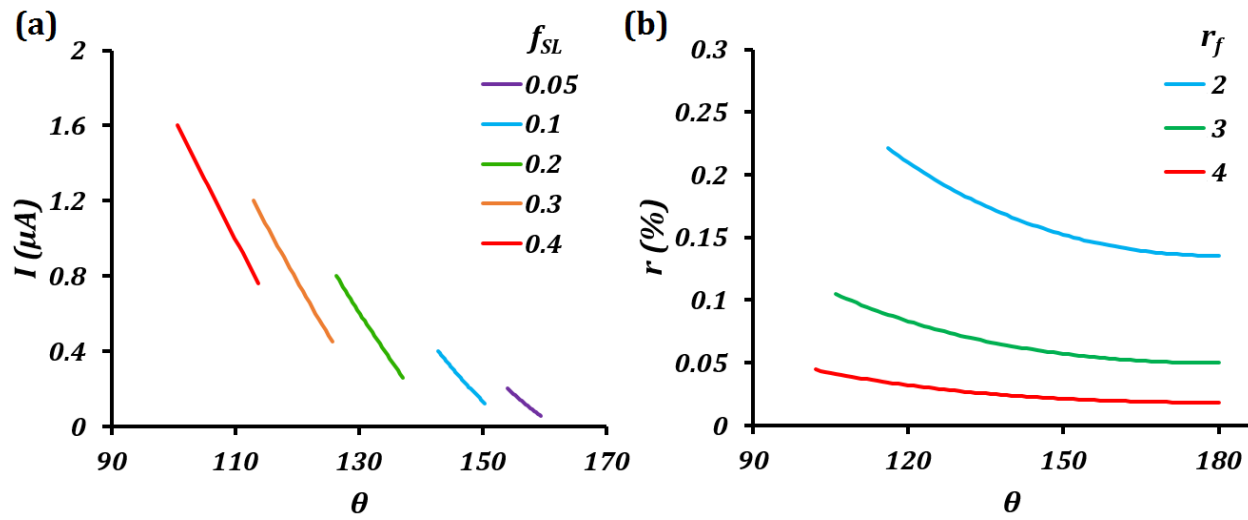


Figure 5.4. (a) Variation of the current I with contact angle θ and fractional solid-liquid interfacial area f_{SL} . (b) Rate of corrosion reaction r as a function of contact angle θ for different values of roughness factor r_f .

The equilibrium contact angle of the surface was assumed to be 50° .

Figure 5.4a shows variation of the current with contact angle (θ) for a substrate whose equilibrium contact angle is 75° . Non-homogeneity (Cassie-Baxter state) created by pockets of trapped air is considered here. The corrosion current decreases with increasing apparent contact angle. As the value of f_{SL} decreases, the current across the interface also decreases. The air pockets serve to increase the interfacial electrical resistance. The theory predicts a large reduction in corrosion current with a decrease in solid-liquid interfacial area. Generating a stable

hydrophobic surface can significantly decrease corrosion. The main factor affecting corrosion current in Cassie-Baxter state is f_{SL} .

5.3.2 Faraday's law of electrolysis and wetting properties

Mass of material removed in corrosion reaction is given by Faraday's law of electrolysis,

$$m = \frac{A i_{corr} t}{zF} \quad (5.7)$$

where A is the atomic (or equivalent) weight of the corroding substance, t is the corrosion time, z is the number of electrons transferred in the corrosion reaction.

5.3.3 Rate of corrosion and the surface free energy

From absolute reaction theory, the rate at which the metal molecules are oxidized can be written as $r = \frac{kT}{h} \exp\left(-\frac{\Delta G}{RT}\right)$, where r is in s^{-1} , k is Boltzmann's constant, h is Planck's constant, and ΔG is the activation energy. The activation energy for a corrosion reaction of a metal can be written as $\Delta G^0 = G_O^0 - G_R^0$, where G_O^0 and G_R^0 are free energies associated with the oxidized state and the metal respectively. If the metal surface is not ideally smooth, but is instead composed of surface asperities, assuming complete oxidation of the surface

$$\Delta G^* = (G_O^0 + \gamma A r_f) - (G_R^0 + \gamma A r_f f_{SL}) \quad (5.8)$$

Then the rate of corrosion reaction is

$$r = r_0 \exp\left(-\frac{\gamma A r_f (1-f_{SL})}{RT}\right) \quad (5.9)$$

where r_0 is the rate of corrosion reaction at ideal surface conditions. Figure 5.4b shows the rate of reaction as a function of apparent contact angle in Cassie-Baxter state. The rate of reaction decreases with increase in contact angle. Increasing the surface roughness decreases the rate of reaction in Cassie-Baxter state.

The main conclusion of this section is that rendering the electrode surface rough and the interface with the electrolyte non-homogeneous provides a coupling mechanism for the wetting and corrosion properties. In other words, both increased surface roughness r_f and decreased solid-liquid (electrode-electrolyte) contact area, f_{SL} , simultaneously affect the effective surface energy and the rate of corrosion.

5.4 Experimental

To further investigate the relationship of the corrosion rate and wetting, several experiments were conducted on metallic materials typically used for fresh water industry applications (for example, water pipes and other similar components) including steel and cast iron. Out of these two, cast iron turned out to be a material of interest which can relatively easily be hydrophobized and also subjected to corrosion at a significant rate. For that end, a procedure was developed which is outlined in this section, and followed by PPT tests on ADI90 cast iron (CI) samples.

5.4.1 Surface roughening

CI samples were cut into 25 mm squares of approximately 6 mm thickness. The sample set identifiers are given in parenthesis, the number 1 denotes uncoated, while 2 and 3 denote two types of hydrophobic coatings. The surfaces were roughened as described below, and then the

samples were ultrasonically cleaned in water, then in ethanol, and then air dried. One set of samples were mechanically abraded by successively using 320, 400, 600, 800, 1200 grit silicon carbide papers, followed by polishing with a soft cloth impregnated with 3 μm alumina particles to obtain a smooth surface (Samples P1). Another set was abraded by using 320 grit silicon carbide paper to obtain a rough surface (Samples R1). A third set was roughened by sandblasting for 30 s to obtain an extremely rough surface (Samples S1).

5.4.2 Hydrophobic coating

Following the procedure of hydrophobization suggested by Yuan[29] with some modifications, the samples (P2, R2, and S2) were immersed in acetic acid (CH_3COOH) solution (36%) for two hours, followed by hydrogen peroxide solution (15%) for three hours. After that, the samples were immersed in a 0.01 M solution of stearic acid ($\text{CH}_3(\text{CH}_2)_{16}\text{COOH}$) in ethanol for 24 hours. Then the samples were taken out of the solution and air dried. Stearic acid coating was used to study if hydrophobization by monolayers can inhibit corrosion.

Another set of samples (P3, R3, and S3) were spray coated with a commercial liquid repelling treatment (Rust-Oleum® NeverWet®). First the samples were spray coated with a base coat and allowed to dry for 30 min. Then four top coats were applied with 2 minutes between each coat. The top coat was allowed to dry for 3 hours.

5.4.3 Contact angle and surface roughness measurements

The as-placed water contact angles (CA) were measured using a ramé-hart goniometer (model 100-25-M) by placing three pure water droplets of 10 μl at different locations on the surface. The contact angle hysteresis (CAH) were calculated by the tilting plate method. The

samples were observed at 20X with an Olympus Lext OLS4100 laser scanning microscope and average surface roughness (S_a) of an area $0.625 \mu\text{m} \times 0.625 \mu\text{m}$ was measured.

5.4.4 Potentiodynamic polarization test

The corrosion behavior of samples was studied using the PPT procedure. A standard three electrode system with the sample as the working electrode, saturated calomel as the reference electrode, and platinum as the counter electrode was used. A potentiostat (Biologic SP-200) with EC-Lab software was used for voltage sweep and data acquisition. The electrolyte was 3.5 wt % NaCl solution. The exposed area of the working electrode was circular with the diameter of 1 cm or approximately 0.79 cm^2 . The samples were kept in contact with the electrolyte for 30 min to reach the open circuit potential. The potential was varied at the rate of 0.116 mV/s during the tests. The results from the experiments are discussed in the following section.

5.5 Results and Discussion

The polished sample P1 had the lowest CA of 50.5° among uncoated samples, while P2 had the lowest CA of 95.4° among stearic acid-coated ones. Roughening of the samples led to increase in CA in uncoated samples. All the uncoated samples showed significant CAH. Once the stearic acid coating was applied, all the samples became hydrophobic with $\text{CA} > 90^\circ$. The sample P2 was only slightly hydrophobic with the CA of 95.4° . The sample R2 had a CA of 110.0° . The sand blasted sample S2 had the highest CA of 124.4° among stearic acid coated ones. The stearic acid-coated samples also showed large CAH values. Water droplet was placed on each of the samples P1, R1, S1, P2, R2, and S2 and then the samples were tilted to a vertical position. The water droplet clung to the surface in all the cases, showing strong adhesion with the

surface. This also suggested that most of the surface cavities were filled with water, than air. CAH of the samples also reveal high adhesion with water. The adhesive forces can be quantified using a centrifugal adhesion balance.[30] All the samples coated with NeverWet were superhydrophobic. It was extremely difficult to place water droplets on the surface for CA measurement. They rolled off at the slightest disturbance, making CAH measurement extremely difficult. Sample P3, R3 and S3 had contact angles of 160.3° , 158.5° , and 150.7° respectively, with negligible CAH. The results of the CA measurements are presented in Table 5.2.

It is difficult to conclude from direct observations whether the wetting state for the samples P2, R2, and S2 were Wenzel or Cassie-Baxter; however, it was found that surfaces immersed in water tended to reflect light indicating possible presence of air pockets. Due to the extreme water repellency observed for P3, R3 and S3, it can be concluded that they were in the Cassie-Baxter state.

The average surface roughness for samples P1 and R1 were 0.042 and $0.144 \mu\text{m}$. For S1 the roughness was on the micron scale with a value of $2.335 \mu\text{m}$. The samples P2, R2 and S2 had average surface roughness values of 0.086 , 0.216 , and $2.843 \mu\text{m}$ respectively. These roughness values are higher than those for corresponding hydrophilic samples. The average surface roughness values for P3, R3, and S3 were substantially higher than those for corresponding hydrophilic and hydrophobic samples. The optical images of samples P1, P2, and P3 are shown Figure 5.5, while the surface topographies of all the samples are shown in Figure 5.6.

Table 5.2. The contact angles (CA), contact angle hysteresis (CAH), average surface roughness (S_a), corrosion current density (i_{corr}), corrosion potential (E_{corr}), and corrosion rate (in millimeters per year, mmpy) for the samples.

Sample ID	CA (deg)	CAH (deg)	S_a (μm)	i_{corr} ($\mu\text{A}/\text{cm}^2$)	E_{corr} (mV)	Corrosion rate (mmpy)
P1	50.5	27.5	0.042	5.81	-646.9	0.144
R1	73.5	24.7	0.144	5.22	-641.2	0.130
S1	69.9	27.5	2.335	18.01	-602.6	0.449
P2	95.4	24.7	0.086	-	-	-
R2	110.0	36.5	0.216	-	-	-
S2	124.4	60.0	2.843	11.98	-608.0	0.299
P3	160.3	-	9.001	6.33×10^{-6}	-315.9	0.158×10^{-6}
R3	158.5	-	8.849	3.16×10^{-8}	-40.3	0.789×10^{-9}
S3	150.7	-	9.884	7.10×10^{-4}	-298.5	0.177×10^{-4}

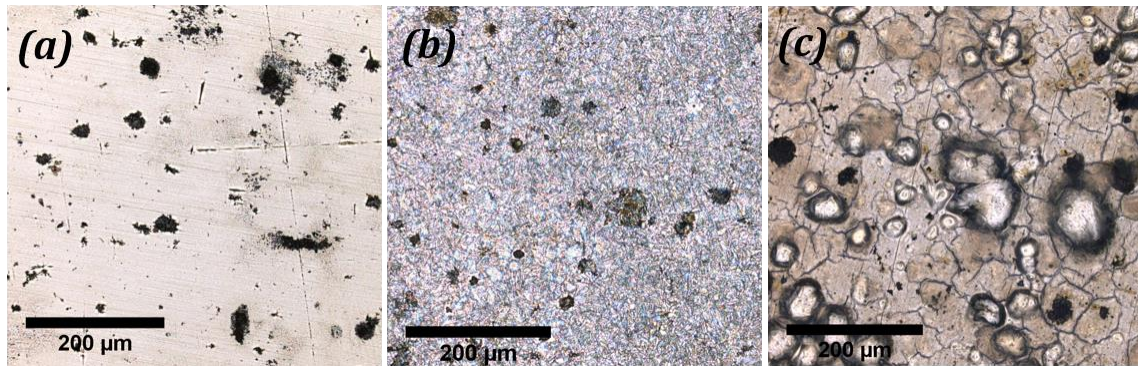


Figure 5.5. Optical images of surfaces of the samples (a) P1, (b) P2, and (c) P3. The coating on P3 is visibly different with cracks and bubbles on the surface.

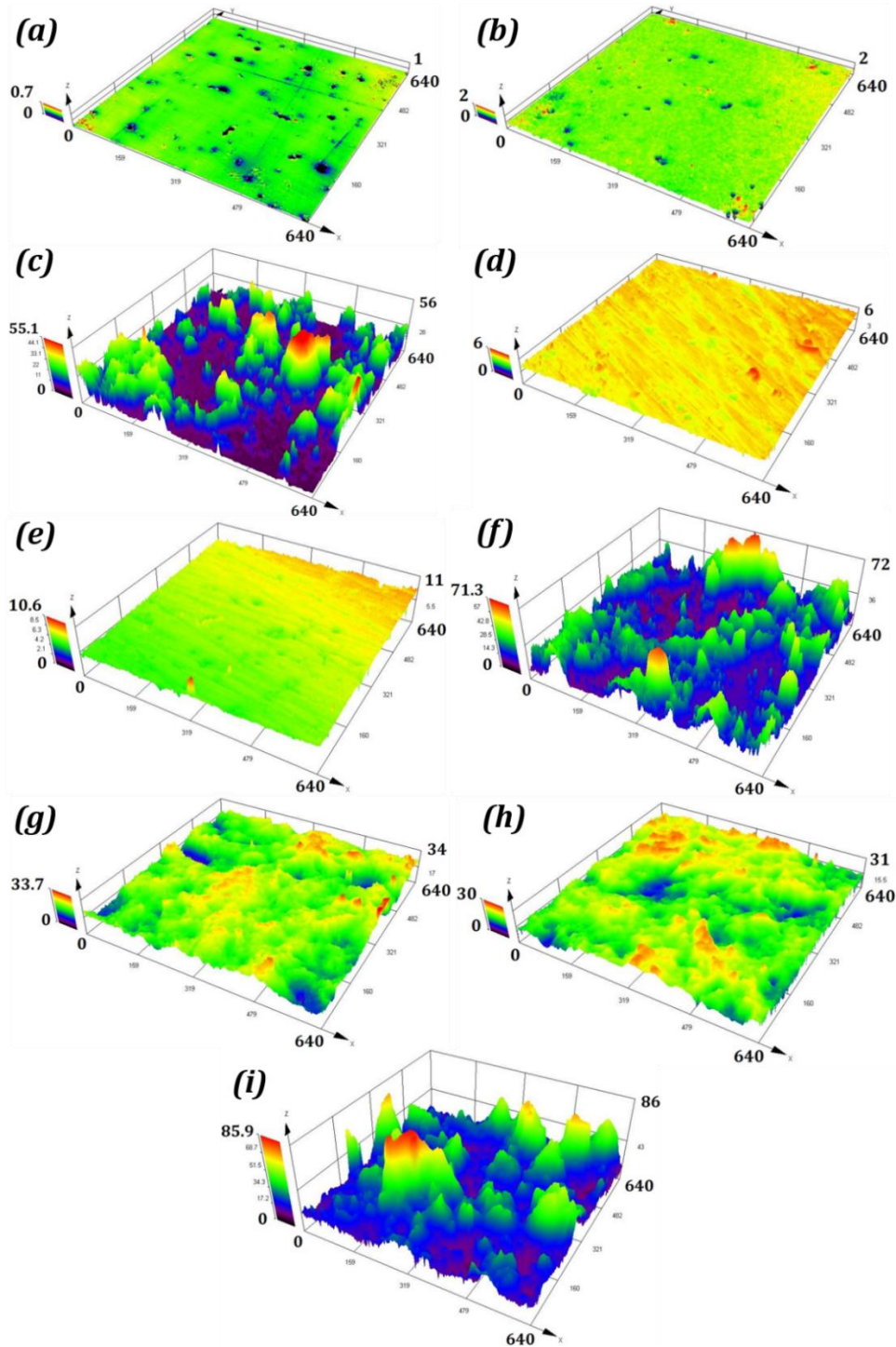


Figure 5.6. (a) to (i) shows the surface topographies of P1, P2, P3, R1, R2, R3, S1, S2, and S3 respectively. Coating with the liquid repellent spray results in drastic change in surface roughness as seen in the case of P3, R3, and S3. All scales are in μm .

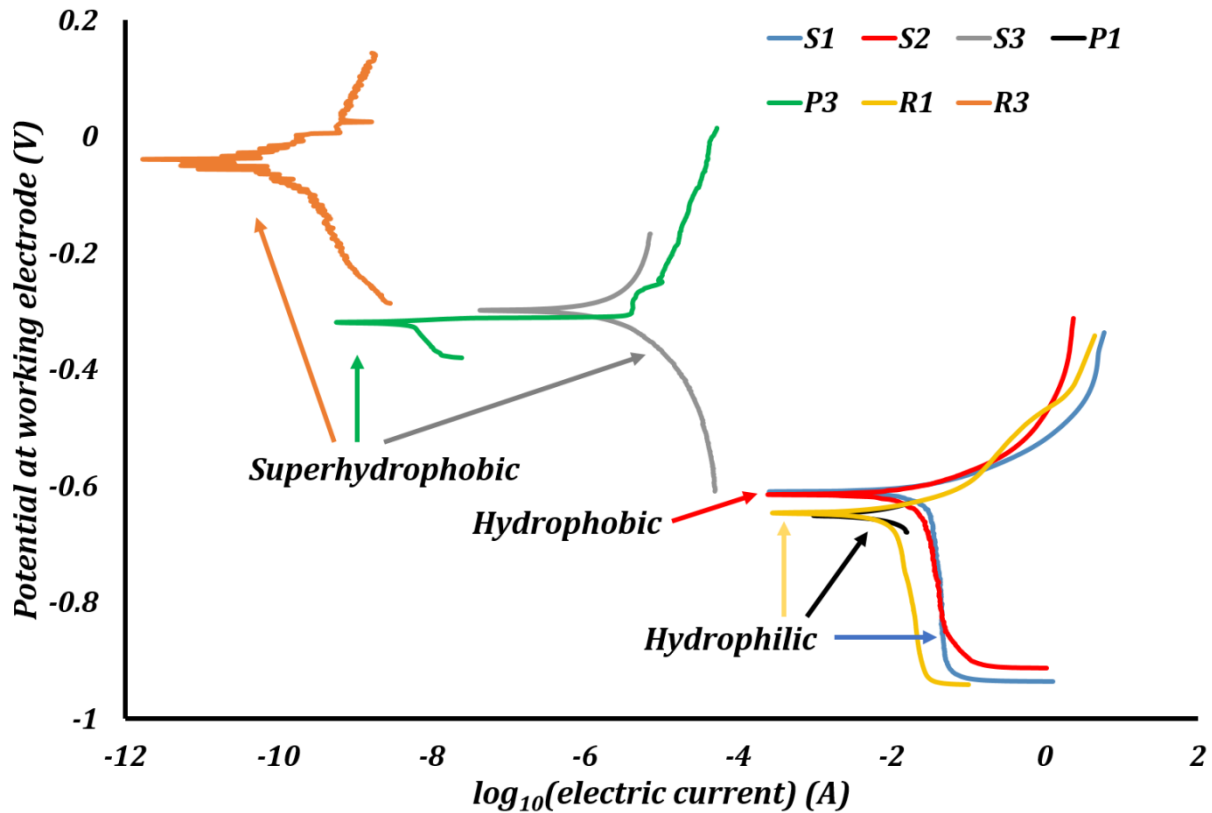


Figure 5.7. Potentiodynamic polarization curves for the samples. Rendering the surface superhydrophobic is seen to shift decrease the corrosion current density as well as shift the corrosion potential closer to the reference electrode potential.

The Tafel plots were obtained from the EC-Lab software (Figure 5.7). For the samples P2 and R2 the PPT did not produce any characteristic Tafel plots, which might be caused by poor stability of the stearic acid coating on the samples with low roughness. Consequently, no corrosion current and potential was measured on these samples.

Corrosion current densities, corrosion potentials, and corrosion rates were obtained from these plots using the software. These values are presented in Table 5.2. The polished sample P1 had an i_{corr} of $5.81 \mu\text{A}/\text{cm}^2$. After rendering it superhydrophobic, the resulting sample P3 had an i_{corr} of $6.33 \times 10^{-6} \mu\text{A}/\text{cm}^2$. The sample R1 had an i_{corr} of $5.22 \mu\text{A}/\text{cm}^2$. Rendering it superhydrophobic resulted in sample R3 with i_{corr} $3.16 \times 10^{-8} \mu\text{A}/\text{cm}^2$. The samples S1, S2 and S3

had an i_{corr} of 18.01, 11.98, and $7.10 \times 10^{-4} \mu\text{A}/\text{cm}^2$ respectively. The corrosion potentials also showed significant change with the wettability of the surface. The absolute values of the corrosion potentials decreased by more than 50% for the superhydrophobic samples. Consequently, the corrosion rates of the superhydrophobic samples were several orders smaller than those of the hydrophilic and hydrophobic samples. Repeated PPT on samples give corrosion current values of similar magnitudes.

The hydrophilic samples P1, R1 and S1 showed significant rusting on their surfaces after PPT. The hydrophobic samples P2, R2 and S2 also showed rusting on their surfaces, with a loss of hydrophobicity after PPT. The loss of hydrophobicity on P2, R2 and S2 is due to the combined effect of corrosion as well as destruction of trapped air pockets under hydrostatic pressure. The superhydrophobic samples P3, R3 and S3 however had no visible rusting on their surfaces following the PPT. These samples were robust, retaining their superhydrophobicity and ability to trap pockets of air at the surface.

The trends observed in the experimental data were that the corrosion current density decreased and the corrosion potential increased as a result of rendering a surface superhydrophobic. The corrosion potentials of most metals and alloys in their native state are negative. Therefore, these metals and alloys have the tendency to get oxidized into corrosion products. The corrosion potential of a hydrophobic surface typically shifts to a value closer to that of the reference electrode. This means a lower thermodynamic tendency to oxidize. Also, the reduction in the solid-liquid interfacial contact area by formation of trapped air pockets results in excellent corrosion resistance.

The experimental results obtained with CI samples showed a similar trend to the results from published literature. Corrosion current densities decreased by several magnitudes and corrosion potentials shifted in the positive direction once the surfaces were made superhydrophobic. These were signs of corrosion inhibition.

The samples P1 and R1 had sub-micron scale surface roughness. As the roughness of the samples increased from P1 to R1, the corrosion current density decreased and the corrosion potential increased, but only slightly. Interestingly, when the roughness increased to the scale of microns for S1, the corrosion current density increased three folds. This can be explained by the formation of homogenous solid-liquid interfacial contact. Roughness at such an interface can amplify the effects of corrosion similar to what is observed in Wenzel model. Increase in surface roughness leads to increase in surface area exposed to the electrolyte. Therefore more reaction sites are available for corrosion to proceed and hence the increased corrosion current density. Having a homogenous solid-liquid interface is detrimental to the metal or alloy.

When the samples were hydrophobized with stearic acid, the surface roughness changed. This is due to the reaction of cast iron with acetic acid, as well as hydrogen peroxide. The stearic acid coating as well as the surface roughness is seen to impart hydrophobicity to the samples. The corrosion current density decreases in the case of S2 when compared with S1. The difference between S1 and S2 is in the type of interface formed when in contact with the electrolyte. The sample S1, as seen before, has an amplified corrosion tendency due to its very rough surface and hydrophilicity. The sample S2 is hydrophobic and can sustain some trapped pockets of air compared to S1 as observed when S2 was dipped in water. These air pockets results in reduced electrode-electrolyte contact. Hence the decrease in corrosion current density

from S1 to S2. But hydrophobic S2 has higher corrosion current densities than hydrophilic P1 and R1. Even though S2 has a non-homogenous interface, its effective solid-liquid contact is more than P1 and R1 due to its high surface roughness. This suggests that as long as the wetting regime on a surface is not purely Cassie-Baxter, the effect of roughness is more pronounced than contact angle on corrosion.

In case of samples P3, R3, and S3, the roughness of the cast iron itself was not of particular importance. After applying the spray coating, the surface roughness of all three samples increased drastically. The coating itself was visible to the naked eye, and felt rough to touch. Under the microscope, the coating was seen to have cracks and bubbles on the surface (Figure 5.5c). These surface features resulted in the extremely high surface roughness values. The surfaces of P3, R3, and S3 looked unaffected to the naked eye after the PPT.

For the samples P2, R2, and S2, the stearic acid coating was not visible to the naked eye. These surfaces showed signs of corrosion after the PPT. Stearic acid usually form a monolayer on the surface that renders the surface hydrophobic. This layer is not robust like the spray coating. Such a fragile layer may also undergo a Cassie-Baxter to Wenzel wetting transition due to the hydrostatic pressure in the corrosion cell. This may be a reason for the relatively feeble performance of S2.

In most of the published literature, epoxy or similar coatings were employed. These coatings themselves act as diffusion barriers to ionic species or are less permeable to air. Such coatings were far superior offering 85% or higher drop in corrosion current densities compared to uncoated metals or alloys. In the experiments described here, both thick coatings as well as monolayers were employed. Therefore, the effects of surface roughness and non-homogenous

hydrophobic interface on corrosion inhibition were isolated in this study. The thickness of coating on P3, R3 and S3 was much larger than the stearic acid monolayer on S2. This suggests that thickness of coating has a significant part to play in corrosion inhibition. Thicker coatings provide a tortuous path for the corrosive agents. In the case of a Cassie-Baxter to Wenzel transition, a relatively thick coating can act as a second line of defense against the corrosive agents.

The general principle of chemical equilibrium (Le Châtelier's principle) states that when many factors affect equilibrium of a system, any change in status quo prompts an opposing reaction in the responding system. Further studies of fundamental mechanisms of corrosion on non-wetting surfaces may be required to understand the underlying mechanisms. However the observed trends are consistent with this principle. In the case of an electrode immersed in electrolyte, the equilibrium surface energy depends both on the inherent surface energy of the material and on the potential of the electrode. By rendering the electrode surface hydrophobic, the inherent surface energy is decreased. This shift in equilibrium of the system is compensated by a change in the potential difference between the surface and the wetting liquid. A positive change in potential was observed in all the cases discussed here. However, the absolute value of the potential decreased, which, in accordance with the electrowetting laws, such as the Lippmann equation (Eq. 5.5) corresponds to increasing surface energy. This change in corrosion potential can lead to a decrease in the corrosion current density for the surface, and thus the rate of corrosion. This trend is also universally observed in the cases discussed here.

5.6 Conclusion

In this chapter the principles of corrosion and electrowetting as well as mechanisms which lead to their correlation with the superhydrophobicity were discussed. The mechanism of electrochemical corrosion was discussed and the technique for measuring corrosion parameters was introduced. Corrosion test data were compiled from recent literature to highlight the trends observed in critical parameters related to corrosion. A facile, scalable hydrophobic coating using stearic acid was developed on cast iron. A commercial liquid repelling spray was used to render cast iron superhydrophobic. Corrosion tests were performed on cast iron in hydrophilic, hydrophobic and superhydrophobic states. Both the compiled data as well as the experimental results of this study showed a decrease up to eight orders of magnitude in corrosion current density and an increase in corrosion potential after superhydrophobization. This can be explained in light of Le Châtelier's principle. A stable non-homogenous solid-electrolyte-air interface was essential for superior corrosion resistance. Surface micro/nanotopography coupled with low surface free energy helps sustain a non-homogeneous interface. However, increasing the surface roughness without hydrophobization led to increase in corrosion current density. A theoretical model was developed and validated with the experimental data. This will provide a fundamental understanding of wetting phenomena in corrosion inhibition.

A relatively new area of corrosion inhibition employing hydrophobic/superhydrophobic surfaces was studied. Existence of a stable non-homogenous interface and the significant reduction in corrosion current density meant that similar coating will find applications in the water industry such as water pipelines, gauges, probes, etc. An ideal superhydrophobic coating for corrosion inhibition should satisfy two requirements: it should be able to withstand Cassie-

Baxter to Wenzel transition under duress, and it should provide a tortuous path for the corrosive agents trying to attack the metallic surface. Therefore corrosion of metallic surfaces can be controlled by changing the surface micro/nanotopography. In the next chapter, the effect of surface micro/nanotopography on the icephobicity of materials will be investigated.

5.7 References

- [1] Montemor, M.F. Functional and Smart Coatings for Corrosion Protection: A Review of Recent Advances. *Surface and Coatings Technology* **2014**, 258, 17-37.
- [2] Feng, L.; Che, Y.; Liu, Y.; Qiang, X.; Wang, Y. Fabrication of Superhydrophobic Aluminium Alloy Surface with Excellent Corrosion Resistance by a Facile and Environment-Friendly Method. *Appl. Surf. Sci.* **2013**, 283, 367-374.
- [3] Motlagh, N.V.; Birjandi, F.C.; Sargolzaei, J.; Shahtahmassebi, N. Durable, Superhydrophobic, Superoleophobic and Corrosion Resistant Coating on the Stainless Steel Surface using a Scalable Method. *Appl. Surf. Sci.* **2013**, 283, 636-647.
- [4] Li, P.; Chen, X.; Yang, G.; Yu, L.; Zhang, P. Preparation of Silver-Cuprous oxide/stearic Acid Composite Coating with Superhydrophobicity on Copper Substrate and Evaluation of its Friction-Reducing and Anticorrosion Abilities. *Appl. Surf. Sci.* **2014**, 289, 21-26.
- [5] Yuan, S.; Pehkonen, S.O.; Liang, B.; Ting, Y.P.; Neoh, K.G.; Kang, E.T. Superhydrophobic Fluoropolymer-Modified Copper Surface Via Surface Graft Polymerisation for Corrosion Protection. *Corros. Sci.* **2011**, 53, 2738-2747.
- [6] Shi, X.; Tuan Anh Nguyen; Suo, Z.; Wu, J.; Gong, J.; Avci, R. Electrochemical and Mechanical Properties of Superhydrophobic Aluminum Substrates Modified with Nano-Silica and Fluorosilane. *Surf. Coat. Technol.* **2012**, 206, 3700-3713.
- [7] Zhang, F.; Chen, S.; Dong, L.; Lei, Y.; Liu, T.; Yin, Y. Preparation of Superhydrophobic Films on Titanium as Effective Corrosion Barriers. *Appl. Surf. Sci.* **2011**, 257, 2587-2591.
- [8] Ou, J.; Liu, M.; Li, W.; Wang, F.; Xue, M.; Li, C. Corrosion Behavior of Superhydrophobic Surfaces of Ti Alloys in NaCl Solutions. *Appl. Surf. Sci.* **2012**, 258, 4724-4728.
- [9] Qiu, R.; Zhang, D.; Wang, P. Superhydrophobic-Carbon Fibre Growth on a Zinc Surface for Corrosion Inhibition. *Corros. Sci.* **2013**, 66, 350-359.
- [10] Weng, C.; Chang, C.; Peng, C.; Chen, S.; Yeh, J.; Hsu, C.; Wei, Y. Advanced Anticorrosive Coatings Prepared from the Mimicked Xanthosoma Sagittifolium-Leaf-Like Electroactive Epoxy with Synergistic Effects of Superhydrophobicity and Redox Catalytic Capability. *Chem. Mat.* **2011**, 23, 2075-2083.

- [11] Chang, C.; Hsu, M.; Weng, C.; Hung, W.; Chuang, T.; Chang, K.; Peng, C.; Yen, Y.; Yeh, J. 3D-Bioprinting Approach to Fabricate Superhydrophobic epoxy/organophilic Clay as an Advanced Anticorrosive Coating with the Synergistic Effect of Superhydrophobicity and Gas Barrier Properties. *Journal of Materials Chemistry A* **2013**, *1*, 13869-13877.
- [12] Peng, C.; Chang, K.; Weng, C.; Lai, M.; Hsu, C.; Hsu, S.; Li, S.; Wei, Y.; Yeh, J. UV-Curable Nanocasting Technique to Prepare Bio-Mimetic Super-Hydrophobic Non-Fluorinated Polymeric Surfaces for Advanced Anticorrosive Coatings. *Polymer Chemistry* **2013**, *4*, 926-932.
- [13] Chang, K.; Hsu, M.; Lu, H.; Lai, M.; Liu, P.; Hsu, C.; Ji, W.; Chuang, T.; Wei, Y.; Yeh, J. *et al.* Room-Temperature Cured Hydrophobic epoxy/graphene Composites as Corrosion Inhibitor for Cold-Rolled Steel. *Carbon* **2014**, *66*, 144-153.
- [14] Zhang, F.; Zhao, L.; Chen, H.; Xu, S.; Evans, D.G.; Duan, X. Corrosion Resistance of Superhydrophobic Layered Double Hydroxide Films on Aluminum. *Angew. Chem. -Int. Edit.* **2008**, *47*, 2466-2469.
- [15] Xu, W.; Song, J.; Sun, J.; Lu, Y.; Yu, Z. Rapid Fabrication of Large-Area, Corrosion-Resistant Superhydrophobic mg Alloy Surfaces. *ACS Appl. Mater. Interfaces* **2011**, *3*, 4404-4414.
- [16] She, Z.; Li, Q.; Wang, Z.; Li, L.; Chen, F.; Zhou, J. Researching the Fabrication of Anticorrosion Superhydrophobic Surface on Magnesium Alloy and its Mechanical Stability and Durability. *Chem. Eng. J.* **2013**, *228*, 415-424.
- [17] Vanithakumari, S.C.; George, R.P.; Mudali, U.K. Enhancement of Corrosion Performance of Titanium by Micro-Nano Texturing. *Corrosion* **2013**, *69*, 804-812.
- [18] Chen, H.; Zhang, X.; Zhang, P.; Zhang, Z. Facile Approach in Fabricating Superhydrophobic SiO₂/polymer Nanocomposite Coating. *Appl. Surf. Sci.* **2012**, *261*, 628-632.
- [19] Xu, X.H.; Zhang, Z.Z.; Yang, J.; Zhu, X. Study of the Corrosion Resistance and Loading Capacity of Superhydrophobic Meshes Fabricated by Spraying Method. *Colloid Surf. A-Physicochem. Eng. Asp.* **2011**, *377*, 70-75.
- [20] Chen, X.; Yang, G.; Kong, L.; Dong, D.; Yu, L.; Chen, J.; Zhang, P. Different Wetting Behavior of Alkyl- and Fluorocarbon-Terminated Films Based on Cupric Hydroxide Nanorod Quasi-Arrays. *Mater. Chem. Phys.* **2010**, *123*, 309-313.
- [21] Fan, Y.; Li, C.; Chen, Z.; Chen, H. Study on Fabrication of the Superhydrophobic Sol-Gel Films Based on Copper Wafer and its Anti-Corrosive Properties. *Appl. Surf. Sci.* **2012**, *258*, 6531-6536.
- [22] Verma, G.; Dhoke, S.K.; Khanna, A.S. Polyester Based-Siloxane Modified Waterborne Anticorrosive Hydrophobic Coating on Copper. *Surf. Coat. Technol.* **2012**, *212*, 101-108.
- [23] Ning, T.; Xu, W.; Lu, S. Fabrication of Superhydrophobic Surfaces on Zinc Substrates and their Application as Effective Corrosion Barriers. *Appl. Surf. Sci.* **2011**, *258*, 1359-1365.

- [24] Pathak, S.S.; Khanna, A.S. Synthesis and Performance Evaluation of Environmentally Compliant Epoxysilane Coatings for Aluminum Alloy. *Progress in Organic Coatings* **2008**, *62*, 409-416.
- [25] Liu, K.; Zhang, M.; Zhai, J.; Wang, J.; Jiang, L. Bioinspired Construction of mg-Li Alloys Surfaces with Stable Superhydrophobicity and Improved Corrosion Resistance. *Appl. Phys. Lett.* **2008**, *92*, 183103.
- [26] Bormashenko, E.; Gendelman, O. A Generalized Electrowetting Equation: Its Derivation and Consequences. *Chemical Physics Letters* **2014**, *599*, 139-141.
- [27] Krupenkin, T.N.; Taylor, J.A.; Wang, E.N.; Kolodner, P.; Hodes, M.; Salamon, T.R. Reversible Wetting-Dewetting Transitions on Electrically Tunable Superhydrophobic Nanostructured Surfaces. *Langmuir* **2007**, *23*, 9128-9133.
- [28] Krupenkin, T.; Taylor, J.A. Reverse Electrowetting as a New Approach to High-Power Energy Harvesting. *Nature Communications* **2011**, *2*, 448.
- [29] Yuan, Z.; Xiao, J.; Wang, C.; Zeng, J.; Xing, S.; Liu, J. Preparation of a Superamphiphobic Surface on a Common Cast Iron Substrate. *Journal of Coatings Technology and Research* **2011**, *8*, 773-777.
- [30] Tadmor, R.; Bahadur, P.; Leh, A.; N'guessan, H.E.; Jaini, R.; Dang, L. Measurement of Lateral Adhesion Forces at the Interface between a Liquid Drop and a Substrate. *Phys. Rev. Lett.* **2009**, *103*, 266101.

CHAPTER 6: ANTI-ICING SUPERHYDROPHOBIC SURFACES

In the previous chapters the effect of surface micro/nanotopography on wetting and corrosion were investigated. It was seen that surface micro/nanotopography can be used to control wetting properties with applications such as hydrophobicity, and corrosion resistance. In this chapter, the effect of surface micro/nanotopography on the icephobicity of materials will be studied. In particular, the icephobicity of concrete is experimentally investigated.

6.1 Introduction

Undesirable ice formation, accretion and adhesion causes various problems ranging from slippery sidewalks and roadways, cracked concrete structures, to icing of airplane wings and windmill propeller blades. Various approaches are used for ice control and removal including active methods, for example, electro-thermal systems or mechanical actuators, and passive methods, for example, adding antifreeze/freezing point depressants (e.g., a salt) or applying surface coatings. However, active ice removal methods consume energy, and freezing point depressants are not environmentally friendly. This is why surface coatings that prevent ice buildup or reduce ice adhesion have become a focus of active research [1]. In cold conditions, a functional icephobic surface should prevent freezing of condensing and incoming water droplets, and upon freezing should result in a weak adhesion with ice when it forms. Surfaces or surface coatings that satisfy one of the above mentioned criteria are often called icephobic. The icephobicity is analogous to the hydrophobicity, although an exact accepted definition of the icephobicity is still missing from the literature.

There are three features required to define an ideal icephobic surface. These three features deal with surface's interaction with the solid, liquid, and vaporous states of water. The

first condition is to have a low adhesive strength of the ice to the surface [2,3]. The second is the ability of the surface to repel incoming supercooled water droplets before these freeze at the surface [4,5]. The third is the ability of expelling water condensate before it undergoes nucleation or delaying the nucleation of ice on the surface from the saturated vapor, thereby delaying the frost formation [6,7]. The first property is analogous to the adhesion of water droplet to a surface. The second is similar to the ability of a superhydrophobic surface to repel incoming water droplets [8]. These three approaches are reviewed and discussed in the following section. An ideal icephobic surface should prevent the condensation of water, delay ice nucleation, and induce a weak bond with ice.

In cold conditions, the precipitation of water can result in sleet, snow, hail, or freezing rain. When the ambient temperature is below the freezing point, there are two ways of how ice can form: by the heterogeneous and homogeneous nucleation. The nucleation occurs when the energy gained in forming the new phase is greater than the energy cost due to creation of a new interface. The rate of nucleation is related to the nucleation energy barrier. The heterogeneous ice nucleation is caused by a seed of the new phase which may be a foreign object (for example, a particle) in liquid water or vapor that acts as a preferential nucleation site. The homogenous ice nucleation occurs spontaneously and randomly for supercooled (metastable) water in the absence of foreign nucleation sites [9]. The heterogeneous ice nucleation in a droplet deposited on a surface starts at the edge of droplets or at surface heterogeneities (chemical or morphological). An important consideration while designing the icephobic surfaces is to delay the heterogeneous ice nucleation so that the supercooled water droplet may be removed by some means (such as the vibration or moving air) before it freezes.

Ice formation is correlated to the hydrophobic/philic properties of a surface. Li et al. [10] showed that at the same temperature, ice nucleation rates on hydrophilic surfaces are about one order higher than those on hydrophobic surfaces. It was also shown that at low relative humidity, superhydrophobic surfaces have higher nucleation barriers for temperatures ≥ -20 °C, thereby considerably slowing down the formation of ice [11]. However, superhydrophobic surfaces rely on the surface roughness. Although surface roughness does not play a significant role in ice nucleation from liquid water [12], the roughness can promote ice formation from vapor since the details of rough profile could serve as seeds for heterogeneous nucleation. Therefore, the hydrophobicity does not always translate into the icephobicity [13]. In addition, the icephobicity of a hydrophobic surface decreases significantly in humid environments [14].

It has been shown that at low humidity, fluorosilicone containing block copolymer can increase the delay in ice formation as well as decrease the adhesion strength of ice on the surface [15,16]. Fluoroalkyl silane coating was seen to reduce ice adhesion compared to just hydrophobic nanoparticle coating [17]. Stainless steel rendered superhydrophobic using nanoparticles and a fluoropolymer was seen to retain its superhydrophobicity after several cycles of icing/deicing [18].

Several new ideas in designing of non-adhesive surfaces were inspired by nature [19]. This includes the “lotus effect” [20] and the so-called “Slippery Liquid-Infused Porous Surfaces (SLIPS)” inspired by the pitcher plant (*Nepenthes*) [21]. The latter showed icephobic properties at 60% relative humidity [7,22]. Bilayer anti-icing coatings inspired by the stimuli-responsive skin of poison dart frogs, have an outer porous superhydrophobic surface over an antifreeze-

infused superhydrophilic surface. These coatings repel incoming water droplets and delay frost formation because ice or water comes into contact with the underlying antifreeze liquid [23].

In this chapter, the fundamental physical interactions related to ice adhesion and nucleation and their similarity to the hydrophobic interactions are discussed. Experimental results on icephobic properties of a superhydrophobic concrete is reported. The effect of surface topography and heterogeneity on the icephobic properties are studied. This is followed by suggestions on how the icephobic properties can be improved and optimized.

6.2 Hydrophobic Interactions Essential for Ice Repulsion

Hydrophobic forces play an important role for both wetting and ice adhesion to solids. These forces are believed to be of entropic nature and they have several important properties including the embedded ability for the self-organization through the effect called “self-organized criticality,” which leads to the formation of fractal structures such as snowflakes and has parallels with such effects as polymer chain folding.

6.2.1 Entropic and hydrophobic forces

The classical example of an entropic force is the elasticity of a polymer chain. Unlike in other materials, the elastic force of a polymer chain is caused by maximizing the configurational entropy (attaining the most probable state). An ideal polymer chain is a simple model with N monomers connected in series with bonds that are linear and free to orient at any angle and also intersect other bonds any number of times. Thus the chain is assumed to be a random walk consisting a succession of random steps. Consider an ideal chain where the bond between any two monomer units is represented by the vector \vec{r}_i (Figure 6.1). The end-to-end displacement

along the chain is given by the vector $\vec{R} = \sum_{i=1}^N \vec{r}_i$. For a freely fluctuating polymer chain with large

N , the mean (over time) end-to-end vector $\langle \vec{R} \rangle = 0$ as the chain is free to fluctuate in any positive

or negative direction with equal probability. The root mean square end-to-end distance (mean

size) of the chain is given by $R = \sqrt{\langle \vec{R}^2 \rangle} = \sqrt{N}r$ where r is the size of the bond between

monomers. For a non-ideal chain (without self-intersections), the effect of the excluded volume

should be considered, which leads to the power exponent of $R \sim N^{3/5}$ [24].

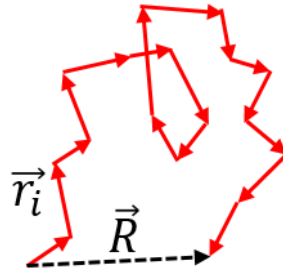


Figure 6.1. Random walk along an ideal polymer chain. The chain attains the most probable configuration.

When an ideal polymer chain is isothermally stretched from its natural state (entropy S_1) to a taut state (entropy S_2), the number of configurations it can take is vastly reduced. The change in entropy is $\Delta S = S_2 - S_1 < 0$. From the Helmholtz free energy relation $\Delta A = \Delta U - T\Delta S$ where A , U and T are the free energy, internal energy, and temperature respectively, $\Delta A > 0$. This implies work done on the system. The force required to do this mechanical work is purely entropic in nature. The force required to isothermally stretch the polymer chain to larger values of \vec{R} is

$$\vec{F} = -\frac{dA}{d\vec{R}} = T \frac{dS}{d\vec{R}} \quad (6.1)$$

The entropy of the chain can be written using the Boltzmann's relation as

$$S = k_B \ln p(R) \quad (6.2)$$

where k_B is the Boltzmann's constant and $p(R)$ is the probability of finding a polymer chain of end-to-end distance R . In three dimensions $p(R)$ is given by the Gaussian distribution function

$$p(R) = \left(\frac{3}{2\pi N r^2} \right)^{\frac{3}{2}} \exp\left(-\frac{3\vec{R} \cdot \vec{R}}{2N r^2} \right) \quad (6.3)$$

Combining Eq. 6.1 to 6.3, the restoring entropic force can be written as

$$\vec{F} = -k_B T \frac{3\vec{R}}{N r^2} \quad (6.4)$$

Thus a change in configurational entropy can manifest as an effective force.

Similarly to the polymer chain elasticity, entropic effects are responsible for the so-called hydrophobic force. When a hydrophobic molecule (for example, a hydrocarbon immiscible with water, such as decane) is added to water, the water molecules arrange themselves around it to form a “clathrate cage”. This arrangement allows a maximum number of hydrogen bonds between neighboring water molecules and thus achieving minimum energy state [25]. However, despite the energetic profitability of such a configuration in terms of the bond energy, the molecules that form the cage are constricted in their motion thus forming an entropically unfavorable ordered (less random) state. At ambient temperatures, the entropic effect overcomes the energy gain. As a result, when two hydrophobic molecules are introduced, the system is forced to spontaneously reduce the size of the cage by pushing the molecules to aggregate together (Figure 6.2a).

The urge for aggregation of hydrophobic molecules or particles in water is called the hydrophobic interaction or hydrophobic force [26]. It should be noted that the hydrophobic force is not a result of attraction between hydrophobic molecules, but the result of increase in configurational entropy of the system, similarly to the elastic force in a polymer chain. Hydrophobic forces increase with increasing temperature [27]. Although there is a general consensus that hydrophobic interactions act over long ranges compared to van der Waals forces, there is still a debate on the exact range of these forces. Hydrophobic forces over distance of several microns between superhydrophobic surfaces have been reported due to formation of cavitation bubbles between the surfaces (Figure 6.2b) [28]. These forces, however, are similar to the capillary force and they may have complex molecular origin. Israelachvili et al. reports the range of hydrophobic forces as 10-20 nm with exponential decay [29]. The hydrophobic force also leads to the preferential attraction of hydrophobic particles towards each other (Figure 6.2c) as well as a hydrophobic surface in water [26].

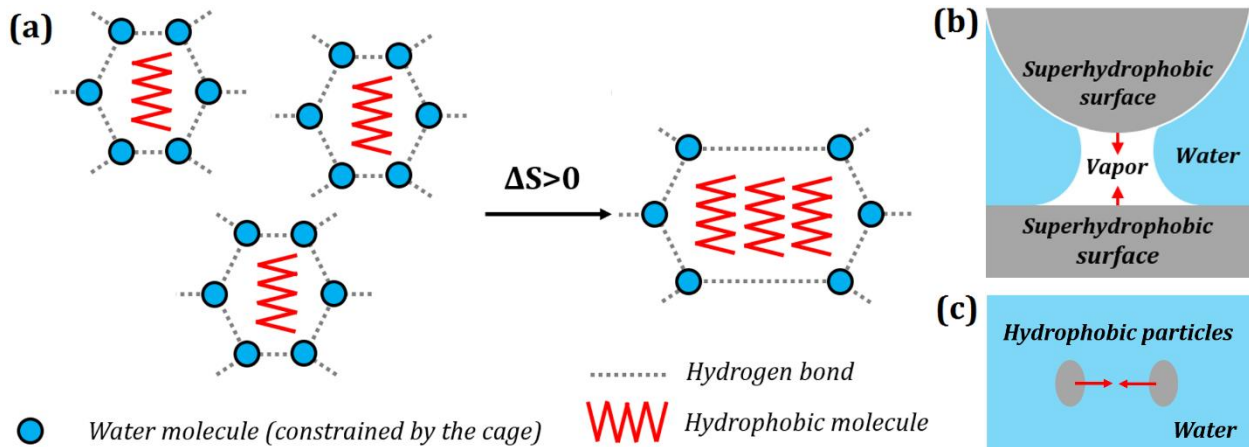


Figure 6.2. (a) Entropic origin of hydrophobic interaction. Aggregation of hydrophobic molecules frees up water molecules to increase the configurational entropy of the system (attaining the most probable configuration). Hydrophobic interaction is manifested as a hydrophobic force which results in (b) clustering of hydrophobic particles in water, and (c) attraction of hydrophobic particles towards a hydrophobic surface in water.

6.2.2 Self-organized criticality and hysteresis of the contact angle

An important effect associated with the hydrophobic force is self-organized criticality (SOC). Bak et. al [30] demonstrated that many dynamical systems can evolve naturally into stable critical points which separate two states of the system. In other words, the system is spontaneously attracted to this critical point irrespective of its starting point. A commonly cited example is SOC in a sand pile. As sand is poured, it falls in a heap. At some point adding a grain of sand, which is a minor event, can trigger an avalanche, a major event, leading to the pile being flattened, and thus the sand pile maintains a certain critical angle dependent on the coefficient of friction between the sand grains. The value of the critical angle is the critical point, separating between the state with the sand flow and a stable pile. Further addition of sand leads to formation of a pile until the next avalanche is triggered. The intensity and the frequency of avalanches follows a power law distribution. SOC has characteristic properties by which it can be detected: the power law distribution of the magnitudes of the avalanche events, the formation of fractal structures, and the “one-over-frequency noise” [30].

Another example of SOC is wetting of a rough or chemically heterogeneous surface and certain types of nanoscale friction [31,32]. If a surface with a sessile droplet on it is tilted, the solid-liquid-vapor triple line advances in intermittent steps (Figure 6.3a). Each of these steps are the result of the energy barriers associated with surface defects (Figure 6.3b). As the surface tilts, gravitational potential energy is added to the droplet which at some point causes triple line to overcome the energy barrier due to surface defects and results in an advance of the triple line (analogous to an avalanche of the sand pile). The advancing triple line then halts at another surface defect until the critical point is reached again [33]. This leads to contact angle hysteresis,

the difference between the larger contact angle at the front and the smaller contact angle at the rear of a moving droplet. There are various thermodynamic theories predicting the values of contact angle hysteresis [34-39].

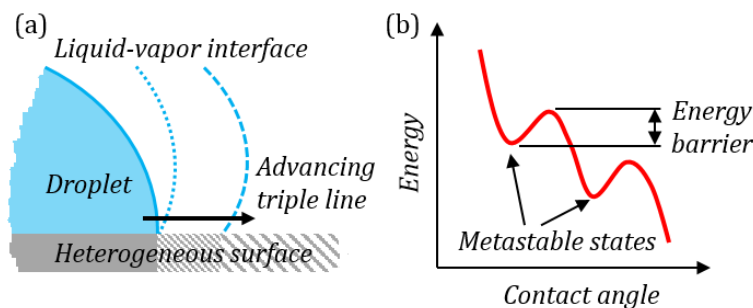


Figure 6.3. (a) Intermittent pinning and advancing of the triple line. (b) Energy barriers associated with contact angle hysteresis.

An important function of hydrophobic forces is in protein folding. Proteins are long chain molecules made of amino acids (AA), and the sequence of the amino acids (the primary structure of the protein) is encoded by genes in the DNA. A protein molecule folds, somewhat similarly to a polymer chain. However, unlike a polymer chain which folds randomly, a protein molecule forms a stable 3D “native configuration” (a so-called “tertiary structure”).

The amino acids can be hydrophobic or hydrophilic. The interaction of these hydrophobic or hydrophilic side chains with each other and the surrounding aqueous medium governs the folded shape of the protein. The folded shape in turn governs function of the protein. The protein chain clusters such that the hydrophobic side chains are attracted to each other and away from water (Figure 6.4a). This behavior is similar to the hydrophobic interaction observed between hydrophobic molecules in water. Thus entropic forces lead to folding of the protein.

According to [40,41], protein folding governed by the hydrophobic forces is controlled by SOC, which is a universal feature of hydrophobic interactions present during both wetting of

hydrophobic surfaces and protein folding. Furthermore, folding of proteins is thought to be the main driving force of the evolution on the gene level [42] which also demonstrates power law and fractal quantitative behavior [43]. The formation of ice (snow) crystals also demonstrates fractal characteristics typical for SOC.

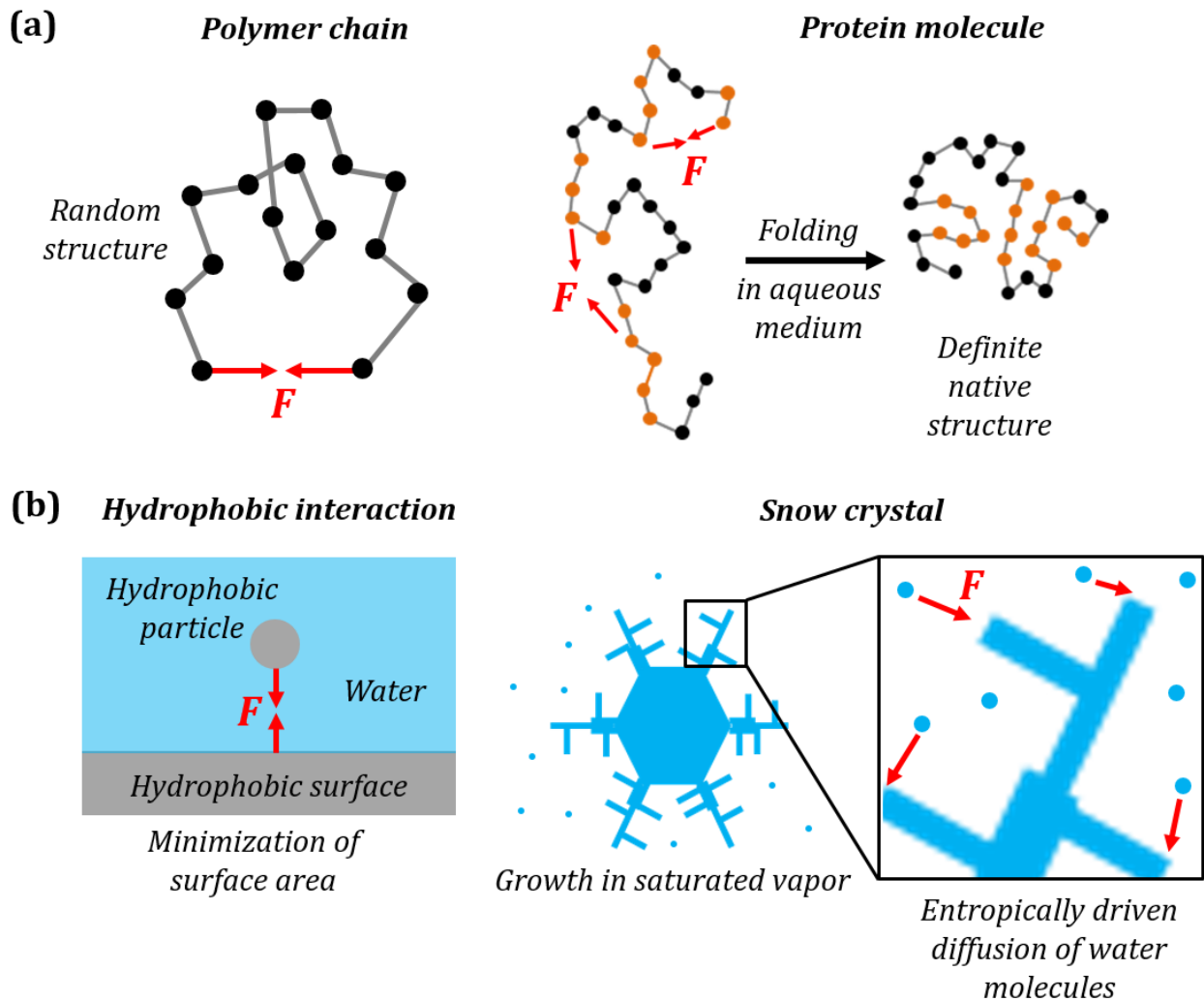


Figure 6.4. (a) Folding of protein molecule from a linear primary structure to 3D tertiary (native) structure is similar to the elastic force in a polymer chain. For a polymer chain the force can be attractive or repulsive depending on the end-to-end distance. For a protein molecule the attractive hydrophobic force causes the hydrophobic side chains to retract to the interior of the cluster. (b) Parallelism with snow crystal growth as opposed to the hydrophobic interaction of a particle and a surface. The red vectors denote the entropic force F in each case.

6.2.3 Ice crystal formation

Ice (snow) crystal formation is another process governed by interactions, which are similar to the hydrophobic forces. It is similar to the hydrophobic interaction between a particle and a surface in water. However, ice crystals can form very complex structures, as opposed to a simple spherical shape formed by a hydrophobic substance in water. This is partially similar to how a protein forms a complex 3D structure as opposed to the random folding of a simple polymer chain (Figure 6.4). For a simple polymer chain, the most probable configuration does not depend on the shape of the polymer chain (but only on the distance between its ends). However, much more complex protein folding depends on the interaction between amino acids, and thus on the 3D shape of the molecule. Similarly, in the case of the hydrophobic attraction of two particles the shape formed by the hydrophobic phase does not matter, since only its surface area is minimized. However, a more complex interaction of a vapor molecule with solid / ice favors certain directions or shapes (Figure 6.4b).

Another parallel between the random polymer versus protein folding and the hydrophobic attraction versus ice crystal formation is in the fractal geometry of both the snow crystals and the protein globules. In a non-ideal polymer chain (using the excluded volume approach) the end-to-end displacement and the radius of gyration are scaled as $R \sim N^{3/5}$ [24]. More accurate estimates using the renormalization group predict the power exponent of 0.588. For the folded polymer chain forming a sphere, the radius of gyration is proportional to the power 1/3 of the volume, $R \sim N^{1/3}$. However, folded proteins tend to show the power exponent of 0.4 rather than 0.333 [44] thus demonstrating scaling of a fractal object. Similarly, hydrophobic liquid droplets in water

would form spheres (with a two dimensional surface), whereas snow crystals, according to the literature, may have a fractal shape with the fractal dimension of about 1.85 [45].

A snow crystal is a single crystal of water molecules arranged in a hexagonal crystal lattice, while many snow crystals clustered together make a snow flake. A snow crystal is formed when water molecules from the vapor attaches to a dust nucleus in a supersaturated atmosphere. The crystal grows as more water molecules from vapor phase hydrogen bond to the water molecules already on the nucleus. The crystal may start out as a spherical particle. Smooth surfaces of a crystal have fewer free sites for incoming water molecules to form hydrogen bonds, while irregular rough surfaces have many. Thus rough surfaces grow relatively fast compared to smooth surfaces. This process leads to evolution of snow crystals into hexagonal prisms with two basal and six prismatic planes or facets. When prismatic facets grow faster than basal facets, plate-like snow crystals are produced. When prismatic facets grow slower than basal facets, columnar snow crystals are produced (Figure 6.5a). Snow crystals formed in very cold and dry conditions are small and have simple geometries due to their slow growth [46].

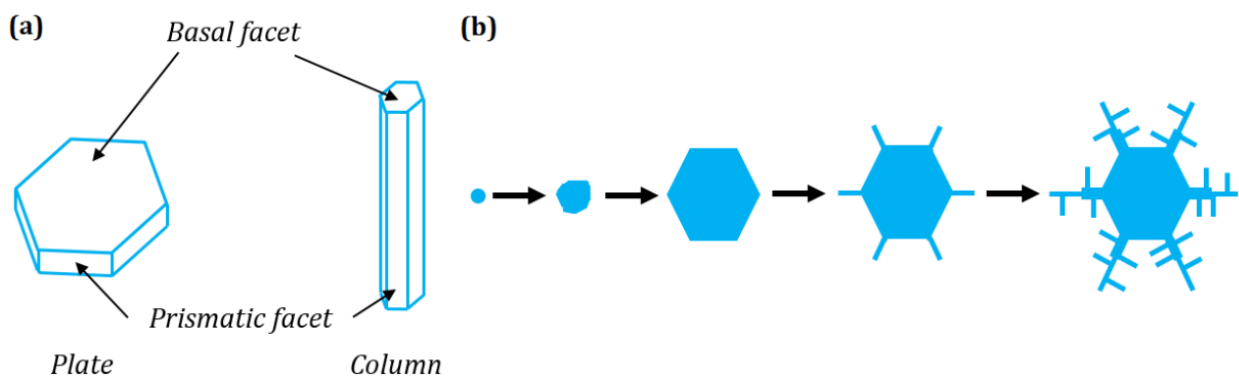


Figure 6.5. (a) Simple snow crystals are either plate-like or columnar. (b) Evolution of intricate shapes in a snow crystal by diffusion-limited aggregation and Mullins-Sekerka growth instability.

It is easier for water molecules from air to diffuse to the corners rather than face centers in a hexagonal prism. Thus corners grow faster (instability) leaving behind irregular steps on the

face centers. This irregularity causes face centers to grow fast and catch up with the corners, thereby minimizing the interfacial energy. This balance between the diffusion and minimization of the interfacial energy helps maintain the hexagonal structure as the crystal grows. Therefore the hexagonal structure acts as a stable critical point in the SOC of a growing snow crystal.

At some limiting value of roughness of the face centers, the corners grow much faster due to the Mullins-Sekerka growth instability. The perturbations at the corners due to diffusion of water molecules (as well as latent heat) can no longer be stabilized by minimizing the interfacial energy of the crystal. This results in hexagonal prisms sprouting digits (instabilities) at the corners. These digits continue to grow until they come under the influence of the growth instability when they start sprouting branches [47]. As a result, fractal geometries are produced in snow crystals. Note that fractal shapes are a characteristic of SOC. Figure 6.5b shows the evolution of an intricate geometry as a result of diffusion and Mullins-Sekerka growth instability.

Ukichiro Nakaya extensively studied the shapes of snow crystals and summarized the relationship between the shapes and atmospheric conditions (temperature, and supersaturation of atmosphere) in the form of the so-called “Nakaya diagram” (Figure 6.6) [48]. He found that the shape of snow crystals change as they pass through regions of different temperature and supersaturation. This is known as “habit change” which can be explained by Kuroda-Lacmann model [49]. The complexity of the crystal structure increases with the supersaturation in atmosphere. Colder and dryer atmosphere promote the growth of simple geometric structures. Natural snow crystals are not always symmetrical. But the intricate shape of a snow crystal suggests an apparent synchronization between the branches of the crystal as it falls through different regions of temperature and supersaturation in the atmosphere. This can perhaps be

explained by an “icephobic interaction” of entropic origin as shown in Figure 6.4b, similar to the hydrophobic interaction.

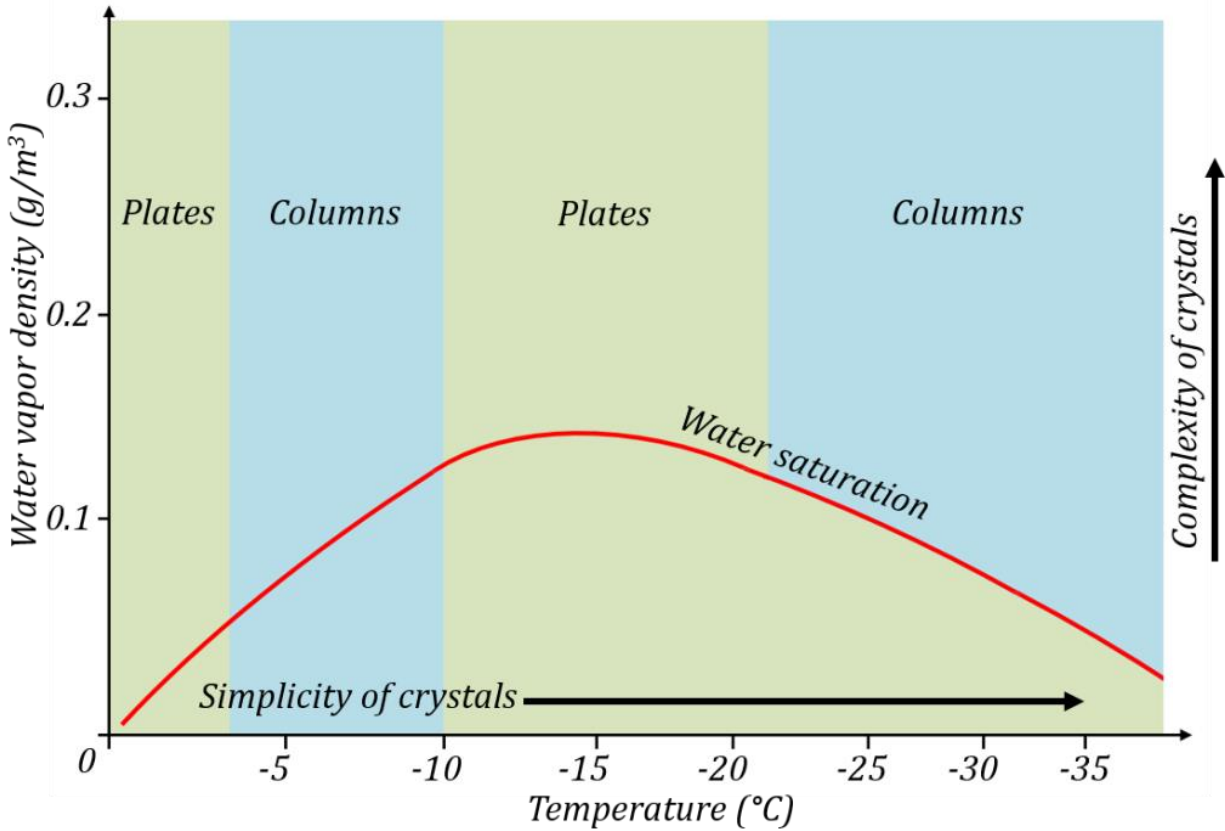


Figure 6.6. The Nakaya diagram. The geometry of a snow crystal is dependent on the supersaturation and temperature of the atmosphere in which it grows.

The shape and direction of snow / ice crystal growth is governed by the roughening transition which happens above a critical roughening temperature. The equilibrium surface configuration depends on the minimization of free energy of the surface. The change of Gibb’s free energy is given by $\Delta G = \Delta H - T\Delta S$ where ΔH is the change in enthalpy. At temperatures above the roughening temperature, the entropic contribution to the free energy dominates, thereby resulting in a rough equilibrium surface configuration. Thus, the growth of snow / ice crystals is governed entropically, similar to the aggregation of hydrophobic molecules in water.

The fundamental physical interaction related to ice nucleation and adhesion were discussed. These interactions are believed to be of entropic nature, and are similar to hydrophobic interactions. There are several similarities between the hydrophobicity and the icephobicity as summarized in Table 6.1. Next, the three aspects of the icephobicity are discussed.

Table 6.1. Similarities between the hydrophobicity and the icephobicity.

Property	Water	Ice
Definition of “phobicity”	Low surface energy / low adhesion High contact angle Low CA hysteresis Bouncing-off incoming droplets Reject condensate droplets	Low adhesion Low normal strength (maximum stress) Low shear strength Bouncing-off incoming supercooled droplets Delay ice nucleation to reject condensate droplets
Interaction	Hydrophobic interaction	Growth of dendritic structures in ice and snow crystals
Thermodynamic relationship	Minimization of free energy $\Delta G = \Delta H - T\Delta S$	Surface roughening transition $\Delta G = \Delta H - T\Delta S$
Typical manifestation of the interaction	Hydrophobic molecules in water	Water vapor molecules in supercooled saturated environment
Effects	Protein folding (including fractal shapes), self-organized criticality, long-range hydrophobic force, wetting transition	Snow crystals (fractal shapes)

6.3 Three Approaches to Synthesizing Icephobic Surfaces

In the preceding section, the superhydrophobicity (very low adhesion of water to a solid) and “icephobic interactions” governing vapor water molecule interaction with a solid surface, such as an ice surface were discussed. This section covers with the three approaches to the icephobicity: low ice adhesion to solid, bouncing off water droplets and suppressing frost formation from vapor can be utilized for anti-icing surfaces.

6.3.1 Ice adhesion to solids

High contact angle does not always yield low ice adhesion. The adhesion of ice to solid surfaces is a result of the synergetic effect of van der Waals forces, chemical bonding, and direct electrostatic interactions. Hydrogen bonding between the surface groups and the water molecules can enhance ice adhesion [1,50]. The electrostatic interactions are the significant factor for metals because charges on the ice surface induce mirror charges thus causing adhesion. Whereas these mirror charges can be reduced by dielectrics [51], the ice adhesion decreases significantly only at low values of the dielectric constant. Thus superhydrophobic surfaces coated with polytetrafluoroethylene with the dielectric constant of about 2 demonstrated negligible ice adhesion [52]. According to Kulinich and Farzaneh, the ice adhesion to a superhydrophobic surface is correlated with contact angle hysteresis, rather than contact angle itself, which can be explained by the reduction of the ice-solid contact area [3]. High valued of the contact angle coupled with low contact angle hysteresis imply the Cassie wetting state with air pockets on the surface [53]. The cavities or voids with air pockets can act as stress concentrators at the ice-solid interface. In this case, the size of the microvoids and cracks at the ice-solid interface becomes a critical parameter controlling the ice adhesion on a surface. According to the analysis of Hejazi

and Nosonovsky, who applied the linear fracture mechanics model, if the cracks are not sufficiently large, the superhydrophobic surface may exhibit strong ice adhesion [13].

Another effect which should be taken into account is the latent heat released during freezing of a droplet. This heat tends to increase the vapor pressure near the solid-ice-vapor contact line resulting in the desublimation of supersaturated water vapor referred to as a “frost halo” surrounding the three phase contact line thus increasing the ice-solid interfacial area and eventually the adhesion force between ice and the solid surface [54].

Table 6.2. Ice adhesion strength of some materials from literature.

No.	Reference	Material	Ice adhesion strength (kPa) at -10 °C
1	Mobarakeh et al. [55]	untreated aluminum	350±25
		plasma polymerized hexamethyldisiloxane coating on aluminum	100±25
2	Farhadi et al. [14]	mirror-polished aluminum	362±26
		superhydrophobic aluminum	55 to 110
3	Fu et al. [17]	glass	820±96
		glass coated with hydrophobic nanoparticles and fluoroalkyl silane	75±19
4	Saleema et al. [52]	bare aluminum	420±27
		polytetrafluoroethylene coated on aluminum	188±12
		polytetrafluoroethylene coated etched aluminum	“Unobtainable”
5	Kim et al. [7]	aluminum	1360±210
		SLIPS coated aluminum	15.6±3.6
6	Hejazi et al. [53]	aluminum	110
		co-polypropylene	71.81

The quantitative parameter characterizing ice adhesion to a solid surface is the adhesion strength. There are several methods for measuring the adhesion strength. One method is the centrifuge adhesion test [56]. Samples with ice are rotated and the adhesion strength is calculated from the speed at which ice detaches from the sample surface [55,57]. Another method is by shear ice adhesion test. A shear stress can be applied to the interface so that the maximum shear strength at which the ice detaches is measured experimentally. Li et al. [15,16] used this method to study the icephobicity of block copolymer coatings. A variation of this method was used by Fu et al. [17], where a piston was used to shear off the ice from the sample surface. Aizenberg and colleagues reported ice adhesion measurement on SLIPS coated aluminum and found that it was two orders of magnitude lower than for aluminum without the coating [7]. Interestingly, a study by Varanasi and colleagues [58] demonstrated that the low ice adhesion force on lubricant-infused surfaces was a result of a thick layer of a lubricant on top of a textured surface. For a surface with a stable lubricant film, the ice adhesion strength decreases with increasing surface texture density increases. Ice adhesion strength of some surfaces and coatings from literature are listed in Table 6.2.

6.3.2 Decreasing contact time for droplets approaching the solid surface

Icephobic surfaces should be able to prevent or delay freezing of incoming water droplets. This can be by bouncing off, breaking up. Minimizing the duration of contact when a droplet interacts with a surface can reduce the heat transfer time and the probability of heterogeneous ice nucleation. Hydrophobic and superhydrophobic self-cleaning surfaces can easily repel incoming water droplets at room temperature. However, the increase in viscosity of supercooled water below 0 °C prevails over the increase in surface forces and increases the

contact time with the surface [59]. High contact angles together with low contact angle hysteresis help minimizing the time of contact and thus maximizing droplet shedding.

Water pressure during the impact can cause the Cassie-Wenzel wetting regime transition, which is usually undesirable because it increases the solid ice contact area and contact time due to pinning of the incoming droplet. This, in turn, increases the rate of heat transfer at the interface [60]. Asymmetric and oblique impacts can reduce chances of this wetting transition as well as droplet pinning [5,61]. Functionalized carbon nanotube superhydrophobic surfaces repel obliquely impacting water droplets at $-8\text{ }^{\circ}\text{C}$ [62]. Mishchenko et al. showed that nanostructured silicon superhydrophobic surface could repel low velocity supercooled water droplets at $-25\text{ }^{\circ}\text{C}$ and thus remain ice free. Despite droplet freezing at temperatures under $-25\text{ }^{\circ}\text{C}$, their removal was easy because the droplets remained in the Cassie-Baxter wetting state before they froze [4]. Hydrophobic fiber-reinforced concrete can repel impacting water droplets (Weber number ~ 55) in an oblique manner at $20\text{ }^{\circ}\text{C}$ and $-5\text{ }^{\circ}\text{C}$ [5].

6.3.3 Suppression of frost formation

Water vapor condenses below the dew point temperature. Humid and supercooled conditions can cause water to condense and freeze on a surface. Therefore, the ability to expel condensing water droplets and delay the process of frost formation and ice nucleation on a surface is important for icephobic surfaces. Water droplets that condense in capillaries of a superhydrophobic surface may undergo the Cassie-Wenzel wetting transition, and adhere strongly to the surface [63]. The energy released during droplet coalescence can eject condensing water droplets spontaneously [64]. Condensation frosting occurs on a surface as a result of formation of inter droplet frost bridges. This makes eventual frost formation on

superhydrophobic surfaces inevitable. However jumping-drop superhydrophobic surfaces can slow down frost formation by ejecting condensate droplets at $-20\text{ }^{\circ}\text{C}$ before they undergo nucleation, and by lowering the chance of frost bridge formation between droplets [65]. Chen et al. reported a hierarchical superhydrophobic surface that can delay ice nucleation and suppress in the inter droplet frost bridge formation [66].

Ice nucleation being a molecular scale phenomenon, is difficult to notice. But the freezing front in a droplet can be observed by change in opacity of the droplet. Water droplets are placed on supercooled test surfaces, and the time taken for a freezing front to appear is noted to quantify the icephobicity [15,57]. Eberle et al. [6] showed that the delay in ice nucleation can constitute up to 25 hours for a droplet at $-21\text{ }^{\circ}\text{C}$ if nanoscale roughness of the surface is carefully controlled. The SLIPS coated surfaces were seen to exhibit delayed ice nucleation for longer time than textured or regular hydrophobic surfaces. This may be because the smooth and chemically heterogeneous surface of the impregnating liquid in SLIPS offers fewer sites for heterogeneous nucleation of ice [22]. Water droplets condensing and coalescing on tilted SLIPS at $-10\text{ }^{\circ}\text{C}$ rolled-off before freezing [7].

The nucleation and formation of frost on a surface is similar to the formation of snow crystals. The entropic force and the growth instability are instrumental in the formation of dendritic structures in snow crystals. Water vapor molecules diffuse from the saturated atmosphere to a supercooled surface due to the entropic (icephobic) forces that minimize the surface energy of the clustered water molecules. This leads to the buildup of ice on surfaces with roughness greater than the critical value for ice nucleation.

Having discussed the theoretical foundations of the icephobicity it was found that the solid-ice interaction is governed by mechanisms similar to the solid-water interactions, in particular, by entropic and hydrophobic forces. It was also found that the superhydrophobicity can be utilized to make icephobic surfaces. In the following section, the icephobic characteristics of rough heterogeneous surfaces are demonstrated. Concrete substrates are used for this purpose. Regular concrete, being porous and hydrophilic, imbibes water. The imbibed water expands upon freezing and initiate the cracks within cementitious matrix. This limits the material's durability required for many civil engineering applications, especially in Northern climates where concrete is exposed to numerous freezing-thawing cycles. Therefore there is the need to make concrete hydrophobic and also icephobic. The icephobic properties of superhydrophobic concrete used in this work is induced using two approaches – by minimization of ice adhesion strength, and by minimizing the contact time for incoming droplets.

6.4 Experimental

In this section, the icephobic characteristics of rough heterogenic surfaces are estimated based on concrete mortars. The icephobicity of concrete is studied using two approaches described previously – by measuring the ice adhesion strength, and studying the interaction of incoming water droplets with the surface.

6.4.1 Materials

The concept of superhydrophobic concrete was proposed and realized by Professor Konstantin Sobolev from the Department of Civil and Environmental Engineering at the University of Wisconsin-Milwaukee. Some specimens and the coatings used in this study were prepared by Dr. Marina Kozhukhova [67-69].

Mortar specimen used in this study were prepared using a commercial Type-I portland cement, standard quartz sand with an average particle size of 425 μm and tap water. Polyvinyl alcohol (PVA) fibers (RECS 15x12 mm Kuralon K-II) with a diameter of 15 μm and length of 12 mm, and high-range water-reducing admixture (polycarboxylate ether super-plasticizer with a 31% solid concentration) were also used while preparing the mix. The PVA fibers induce a certain “self-reproducing” surface structure, important for icephobic properties. Further details about the constituents of the mortar mixes are described in the Appendix.

A water-based “shell type” siloxane emulsion was used in this study for hydrophobizing the mortar surfaces. Polymethylhydroxysilane (PMHS) and PVA were used as the hydrophobizing agent and surfactant respectively. Silica fume particles were used to stabilize the emulsion, and also to provide micro-roughness when the emulsion is applied to the mortar surface. More information about the components of the emulsion is provided in the Appendix. The procedure of emulsion preparation was described in detail in [70-72].

6.4.2 Contact angle and roll-off angle

The hydrophobic characteristics were estimated for samples by measuring the contact angle (CA) and roll-off angles (ROA) of water droplets on the mortar tiles and cubes using Krüss Drop Shape Analysis System DSA100. These tests were conducted by Dr. Marina Kozhukhova [67].

6.4.3 Ice adhesion strength

Ice adhesion strength on mortar samples was measured using the shear test [53]. Contact angle (CA) values, roll-off angle of water droplet as well as concrete mortar formulation were

the main parameters for the icephobicity assessment. Three sets of samples of 10 different formulations were used in the experiment. The first set was used without any treatment as a reference, and two others were differently modified with hydrophobic “shell type” emulsions, as discussed in Flores-Vivian et al.[71] The shear tests were performed by Dr. Marina Kozhukhova [67]. The procedure for the shear tests are described in detail in the Appendix.

6.4.4 Interaction of incoming droplets

In this section the second aspect of the icephobicity of a surface, i.e. minimizing the contact time for incoming droplets, was studied using concrete mortars. The interaction of incoming droplets with the concrete surfaces were studied at -5 °C and 20 °C. Qualitative observations were made if the droplets got pinned, bounced off or froze on the surface. It was observed that droplets bouncing off generally had very low contact time with the surfaces.

The interaction between the incoming droplets and concrete surfaces were studied at -5 °C and 20 °C. Distilled water droplets (14 µl) were dropped using a micro syringe from a height of 50 mm onto the samples set at 45° inclination. The samples were then precooled for two hours at -20 °C. Distilled water droplets (14 µl) stored at 0 °C were dropped from 50 mm height onto the samples inclined at 45°, at an ambient temperature of -5 °C and relative humidity of 34%. The experiments were performed carefully and quickly at -5 °C, so that the water at 0 °C could not freeze in the dispensing syringe. The interactions were video recorded at 420 fps using a Canon EX-FH25 camera in both cases. Stacked images were prepared using the frames captured from the videos to show the trajectories of droplets after impact at -5 °C and 20 °C.

6.4.5 Sample preparation

For studying the ice adhesion strength, 3 sets of 10 different compositions of fiber reinforced concrete (compositions M1-M5)/mortar (compositions M6-M10) rectangular tiles were prepared in laboratory conditions with component proportions presented in Table 6.3.

Table 6.3. The composition of concrete/mortar specimen (based on Dr. Kozhukhova's PhD thesis).

Mixture composition	Water to cement ratio (W/C)	Sand to cement ratio (S/C)	Superplasticizer, % cement	PVA Fibers, % vol
M1	0.25	0	0.14	1.5
M2	0.3	1	0.1	1.5
M3	0.4	2	0.1	1
M4	0.45	2.5	0.1	1
M5	0.5	3	0.1	1
M6	0.25	0	0.042	0
M7	0.3	1	0.045	0
M8	0.4	2	0.04	0
M9	0.45	2.5	0.02	0
M10	0.5	3	0.01	0
M11	0.3	1	0.1	1
M12	0.4	1	0.1	1
M13	0.3	0.5	0.1	2
M14	0.4	0.5	0.1	2

In addition to these specimens, for water droplet bouncing tests, the fiber-reinforced concrete cubes with composition M11-M14 were also used. The compositions of the concrete mortar cubes are also listed in Table 6.3. The sample preparation procedure is described in detail in the Appendix. The difference between these two types of samples (tiles and cubes) was that

for the samples M1-M10 the top side of sample was used as a testing surface and for the samples M11- M14 a newly cut surface was used. Therefore, the direction of imbedded fibers was observed to be different.

6.4.6 Surface roughness

Uncoated mortar samples M1, M5, M6 and M10 were observed at 20x using a Laser Confocal microscope Olympus Lext OLS4100. The average surface roughness (S_a), and average line roughness (R_a) were obtained. The uncoated samples were chosen for microscopy to study the roughness imparted by the sand, and PVA fibers after the abrasion treatment. The samples M1, M5, M6 and M10 were selected to study the effect of PVA fibers and sand on surface roughness.

6.5 Results and Discussion

The controlling parameters of CA and ROA for the tile and cube surfaces were measured before the shear tests and droplet impact tests.

6.5.1 Surface roughness results

The 2D optical images and 3D surface topographies of the mortar surfaces are reported in Figures 6.7 and 6.8 respectively. The average surface roughness (S_a) of the samples are listed in Table 6.4. The PVA fibers are visible in samples M1 (Figures 6.7a, 6.8a) and M5 (Figures 6.7b, 6.8b), emerging from the mortar surface. The surfaces of M5 (Figure 6.8b) and M10 (Figure 6.8d) are wavy due to the presence of sand grains. The sample M6 (Figure 6.8c) which lacks PVA fibers as well as sand has the lowest value of S_a at 2.218 μm . The sample M1 which has

PVA fibers but no sand has S_a of 9.929 μm . This increase in roughness can be attributed to the effect of PVA fibers.

Table 6.4. Average surface roughness (S_a) of the samples in μm , and the controlling parameters such as PVA fiber content and sand to cement ratio.

Composition ID	PVA fibers (%vol)	Sand to cement ratio	S_a (μm)
M1	1.5	0	9.929
M5	1	3	18.054
M6	0	0	2.218
M10	0	3	19.155

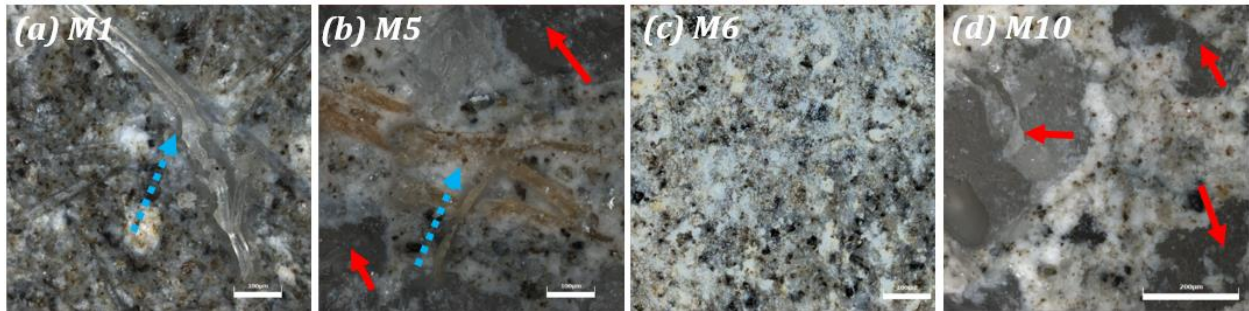


Figure 6.7. Optical images of M1, M5, M6, and M10. The blue broken arrows show the PVA fibers, while the red arrows show the sand grains. The scale bar for M1, M5 and M6 is 100 μm , and for M10 it is 200 μm .

The mortar sample M10 without fibers has the highest S_a of 19.155 μm , whereas M5 which has both sand and fibers has a S_a of 18.054 μm . Thus the presence of sand in the mortar significantly increases the surface roughness. While the surfaces are prepared by abrasion treatment using sand paper, the areas with stronger sand grains exposed wear differently compared to cement matrix zones due to difference in hardness. This explains the approach used to induce required roughness observed on samples containing sand.

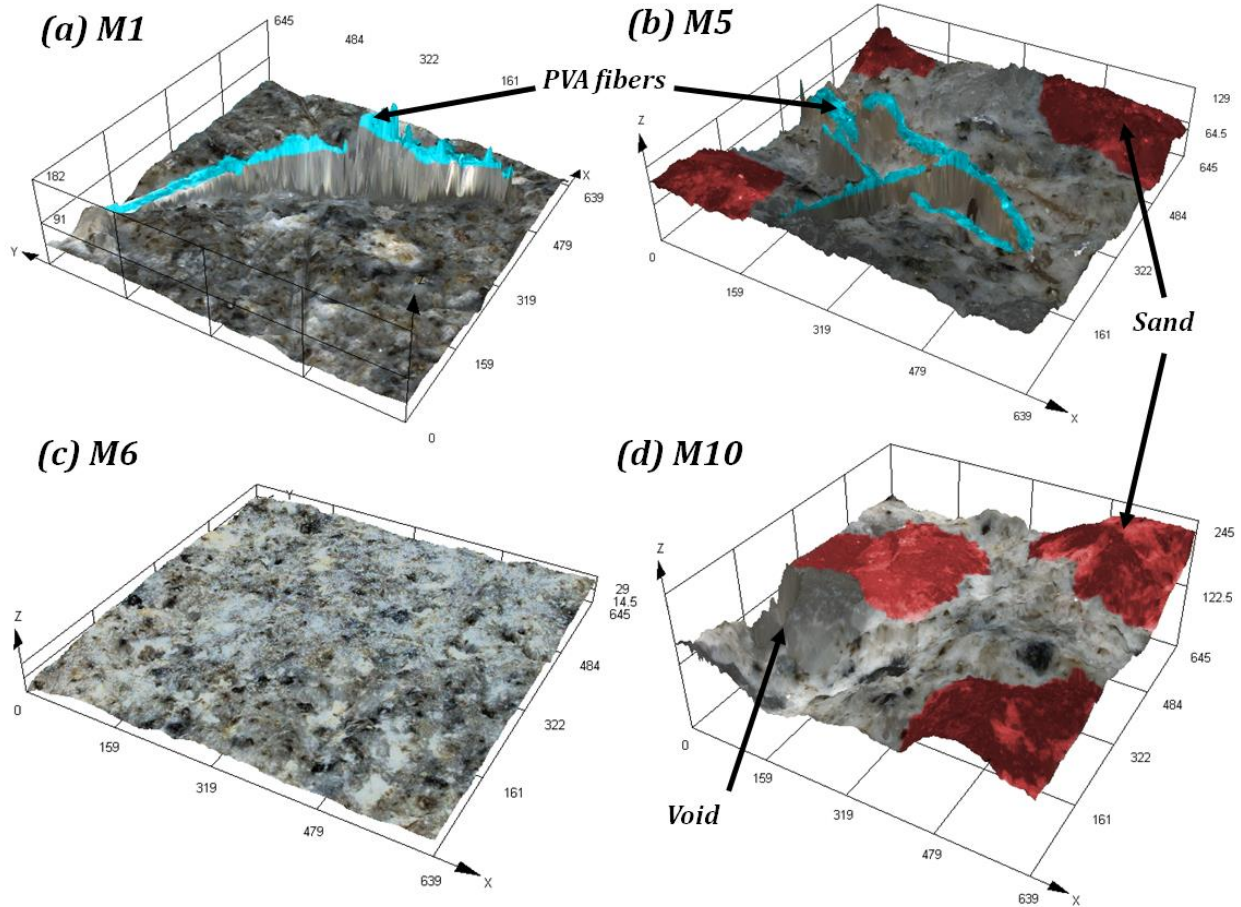


Figure 6.8. The surface topographies of samples M1, M5, M6, and M10. (a) PVA fiber is visible in M1 emerging from the surface; (b) PVA fibers as well as sand grains are observed in M5. The sand creates roughness on the surface (c) M6 has the lowest roughness due to absence of sand and PVA fibers. (d) The presence of sand creates distributed roughness in M10.

Using the surface roughness data, and the mixture composition parameters as two independent variables, namely x_1 - the PVA fiber content and x_2 - the sand to cement ratio, a second degree polynomial model can be derived for the average surface roughness S_a .

$$S_a = 2.218 + 5.141x_1 + 5.646x_2 - 2.081x_1x_2 \quad (6.5)$$

Although the surface roughness is a function of several parameters related to the mortar composition, Eq. 6.5 serves to demonstrate that the surface roughness of mortar can be controlled.

6.5.2 Ice adhesion strength results

In this study the assessment of icephobic characteristics of surfaces with hydrophobic properties was conducted using 3 sets of fiber-reinforced concrete and mortar tiles with different coatings: a) reference tiles without hydrophobic treatment (Set A); b) tiles treated with the emulsion containing 5% and 1% of hydrophobic agent and silica fume, respectively (Set B); c) tiles treated with the emulsion based on 25% and 5% of components (Set C). The test results of CA and ROA values are presented in Table 6.5.

The reference set of samples (A) without hydrophobic treatment has hydrophilic properties with the values of CA barely exceeding 25° ; at the same time, some of the samples demonstrate zero CA, which can be explained by a high absorption capability induced by capillary porous structure of concrete. Because of hydrophilicity, the roll-off angle parameter for those samples cannot be measured.

The set B treated with emulsion containing low concentration of hydrophobic agent and silica fume (5% and 1%, respectively) demonstrated the best results for CA of up to 151° and roll-off angle of less than 1° . The lowest values of roll-off angle $<1^\circ$ within the set belong to the fiber reinforced samples with higher surface roughness, which correlates with the CA data for the same samples. This approach for surface treatment results in over- and superhydrophobic characteristics. Herein, it is important to note that the lowest values of roll-off angle belong to the fiber reinforced samples, produced at low W/C and S/C ratios.

Table 6.5. Contact angle (CA), roll-off angle, and ice adhesion strength for concrete and mortar tiles
(based on Dr. Kozhukhova's PhD thesis).

Set	Composition ID	CA	Roll-off angle	Ice adhesion strength (kPa)	
Tile specimens	A	M1	8.5°	-	310.5±46.5
		M2	9.8°	-	184.5±91.5
		M3	0°	-	240±20
		M4	0°	-	170±75
		M5	25.5°	-	376.5±122.5
		M6	10°	-	182±15
		M7	14.2°	-	266±162
		M8	5.3°	-	305±3
		M9	0°	-	281±36
		M10	0°	-	282.5±56.5
	B PMHS 5% Silica fume 1%	M1	143.7°	2.4°	83±6.5
		M2	145.4°	<1°	33±7
		M3	149.5°	5.9°	29±8
		M4	127.8°	7.9°	51±23
		M5	141.2°	11.7°	48.5±14.5
		M6	141.4°	4.1°	53±6
		M7	141°	7.5°	45.5±4.5
		M8	151°	4.4°	57±10
		M9	140°	14.4°	37±3
		M10	144.1°	9.1°	35±6
	C PMHS 25% Silica fume 5%	M1	122.7°	90°	61±4
		M2	118.6°	81.2°	47±1
		M3	121.7°	66°	53.5±14.5
		M4	128.2°	58.5°	49±0
		M5	128.4°	62.4°	44.5±2.5
		M6	112.8°	56.5°	34.5±13.5
		M7	118.6°	61.3°	56±6
		M8	129.9°	63°	33.5±0.5
		M9	123.8°	57.6°	34±5.5
		M10	127°	52.2°	48±9
Cube samples PMHS 5% Silica fume 1%	M11	138.8°	11°	–	
	M12	138.2°	15.3°	–	
	M13	137.9°	18.5°	–	
	M14	140°	20°	–	

The set C, with tiles treated with high concentration emulsion demonstrated the hydrophobic and over-hydrophobic (water CA between 120° and 150°) characteristics, which can be explained by low surface energy of siloxane hydrophobic agent, covering the hydrophilic surface of the tiles. The best results were demonstrated by the samples with higher water to cement (W/C) 0.4–0.5 and sand to cement (S/C) 2.5–3 ratios which induce beneficial roughness of the surface. High roll-off angle can be observed, however, some of the samples reached the maximum value 90° .

The cube samples M11-M14, which were treated with the emulsion based on 5% and 1% of hydrophobic agent and silica fume, respectively had over-hydrophobic characteristics with pretty equal CA values of average 138.5° and, comparatively, low ROA values for all the cube samples.

Based on the shear strength test, a linear dependence of ice adhesion strength on CA can be observed (Figure 6.9a). Higher the CA, lower the shear force that has to be applied to separate the ice from a sample surface and, thus, the lower the adhesion strength of ice to a surface. Comparing the set A of the samples which are hydrophilic, to the sets B and C which are hydrophobic, the ice adhesion strength is seen to differ by a factor of 10.

At the same time, a slightly weaker ice adhesion to the surfaces of M6-M10 tiles treated with the emulsion containing higher concentration of hydrophobic agent (C set) can be observed. Therefore, lower adhesion strength in the case of C set of specimens is due to thicker hydrophobic layer which over covers the surface roughness and to some extent makes it smooth. This allows ice sliding easier on the surface while applying the shearing force.

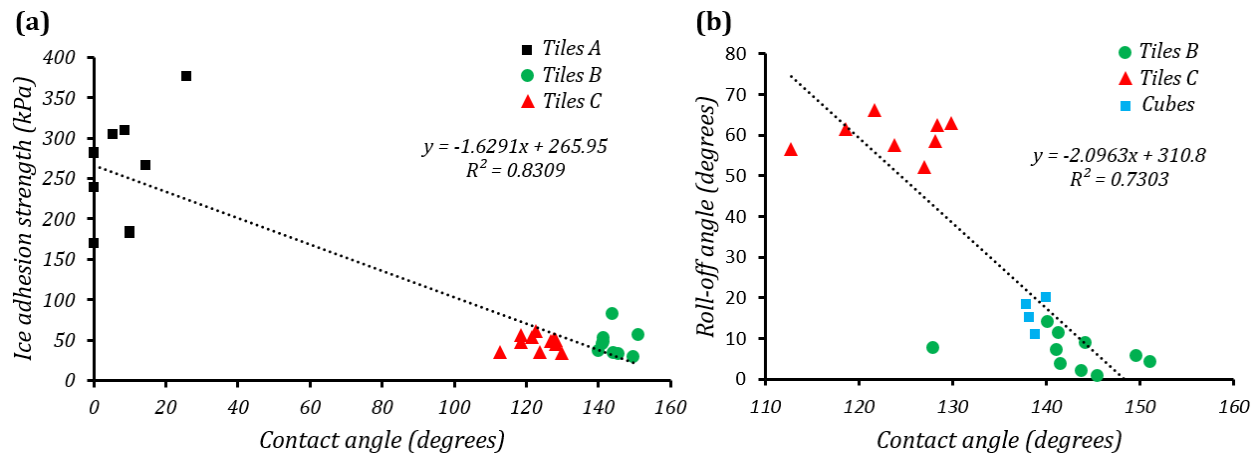


Figure 6.9. (a) The correlation of water contact angle and ice adhesion strength for the samples (b) The correlation of water contact angle and the roll-off angle for the samples (based on Dr. Kozhukhova’s PhD thesis).

There is no correlation between the roll-off angle values and adhesion strength. The correlation between roll-off angles of the samples and their CA is shown in Figure 6.9b. The tile specimen set C show high roll-off angles, whereas the cube specimens and the tile specimen set B which were hydrophobized using low concentration emulsion show both high CA as well as low roll-off angle.

The carried out investigation on the icephobic capability of the concrete tiles with different hydrophobic coatings allows to make a conclusion that the controlling parameters governing the adhesion of ice are the CA values, the thickness of hydrophobic layer, as well as the roughness and structure of a surface. Fine tuning of these parameters can result in the concrete surfaces with adhesion strength of 10 times less than the reference. This finding can lead to the design of ice free roads and runways meeting the extreme durability and extended service life objectives [67-69].

6.5.3 Interaction of incoming droplets

For the bouncing droplet test, the tiles M1 and M2 from set B were chosen, because of the best CA and ROA results. The M11-M14 cube samples, treated with the emulsion containing 5% and 1% of hydrophobic agent and silica fume respectively were also tested in this experiment.

Figure 6.10 shows the stacked images for various samples. The droplets before impact at $-5\text{ }^{\circ}\text{C}$ and the droplets after impact at $20\text{ }^{\circ}\text{C}$ are represented as clear shapes. The droplets after impact at $-5\text{ }^{\circ}\text{C}$ are represented in red. The trajectories of the droplets after impact at $-5\text{ }^{\circ}\text{C}$ and $20\text{ }^{\circ}\text{C}$ are distinct. The droplets bounce further at $20\text{ }^{\circ}\text{C}$. In the case of M1, the droplets at $-5\text{ }^{\circ}\text{C}$ bounce off without freezing, while in the case of M2 the droplets freeze. Droplets either bounce off or roll off after impacting all the samples except M2.

The marked difference in trajectories at $0\text{ }^{\circ}\text{C}$ and $20\text{ }^{\circ}\text{C}$ indicate a higher dissipation of energy of droplet at $-5\text{ }^{\circ}\text{C}$. This can be accounted by the change in density, viscosity, and surface tension of water as well as the change in adhesion with the concrete surface. The surface is sticky at $-5\text{ }^{\circ}\text{C}$ resulting in a longer time of contact with the droplet. This results in heat transfer and heterogeneous nucleation of ice in the droplet, followed by freezing as seen in the case of the sample M2.

The difference in the interaction of water droplets with samples M1 and M2 could be related to extent of surface roughness or relief caused by variation in W/C and S/C ratios of fiber reinforced concrete or mortar formulations. Surface density and porosity are the key parameters the substrate material. At the same time, both of the mentioned parameters significantly affect the height of incorporated PVA fibers, which emerge from the surface after abrasion treatment.

Comparing two samples M1 and M2, the surface roughness of the sample M2 is greater because of higher W/C and S/C ratios, as well as lower surface density and higher porosity.

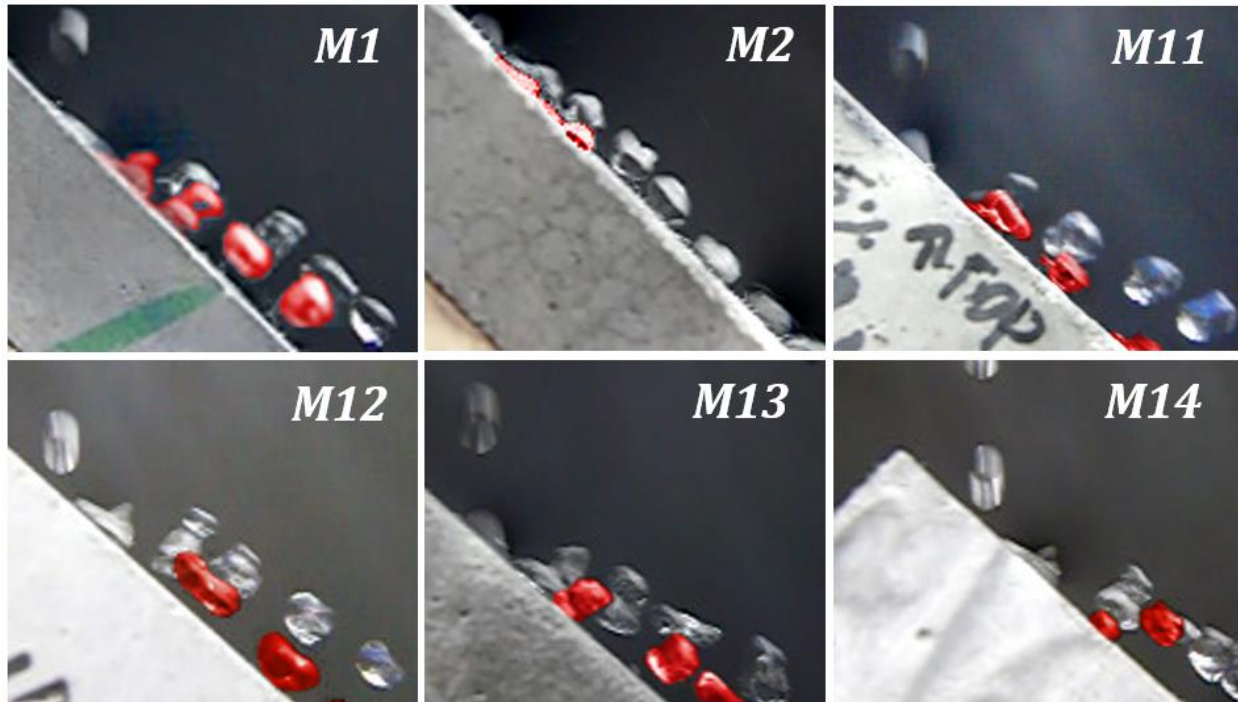


Figure 6.10. Stacked images showing the trajectory of water droplets falling from 50 mm impinging on concrete samples inclined at 45° at 0°C and 20 °C. The trajectory of droplets at -5 °C after bouncing is shown in red.

The trajectory of a droplet after impact depends on the wetting state of the droplet on impact. The roughness of the concrete surface as well as the energy of incoming droplets can influence Cassie-Baxter to Wenzel wetting transition on impact. To prevent the wetting transition and resulting ice formation, the surface roughness and porosity needs to be optimized. This can be achieved by changing the W/C and S/C ratios, and the PVA fiber content.

6.6 Optimization of Icephobic Surfaces

This section covers the optimization of the three aspects of the icephobicity of a surface by controlling surface and material parameters.

6.6.1 Ice adhesion to solids

As discussed in section 6.3.1, dielectric materials can reduce ice adhesion because of the induction of fewer number of mirror charges. Surface charge density of ice is $\sigma = 1.6 \times 10^{-2} \text{ C/m}^2$ [73]. Following Ryzhkin and Petrenko [51], the induced surface charge density on the dielectric coating in contact with the ice can be written as

$$\sigma' = \sigma \frac{\varepsilon - 1}{\varepsilon + 1} \quad (6.6)$$

where $\varepsilon \geq 1$ is dielectric constant of the coating material. The electrostatic interaction force scales as $F_{el} \propto \sigma\sigma'$. The electrostatic interactions are thought to be one of the major causes of ice adhesion, therefore, one can assume that the adhesion strength of the ice-dielectric interface scales similarly to F_{el} . Figure 6.11 shows the variation of the ice adhesion strength with dielectric constant assuming a proportionality constant of the unity. The trend is similar to the experimental results reported by Saleema et al. [52] There is no appreciable decrease in ice adhesion strength when the dielectric constant is larger than 10. However, for $\varepsilon < 10$ the ice adhesion strength decreases considerably.

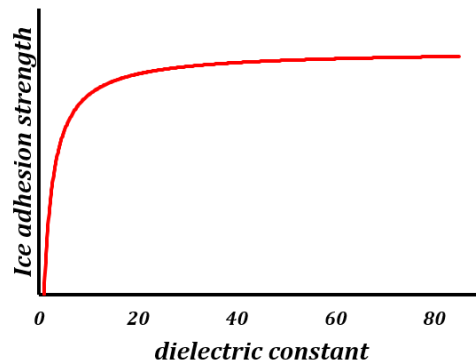


Figure 6.11. Variation of ice adhesion strength with dielectric constant of the icephobic coating.

For water, $\varepsilon \approx 80$, while for air $\varepsilon \approx 1$. Thus having air pockets is favorable to lower the ice adhesion strength. Therefore, the Wenzel state is unfavorable for the icephobicity, whereas the Cassie-Baxter state with air pockets between the solid and water will lead to low ice adhesion strength when water freezes. The PVA fibers, which were used to increase concrete roughness, as described in the preceding sections, have the dielectric constant of about $\varepsilon \approx 2$ [74], which, therefore, helps minimizing the ice adhesion strength.

As discussed in the preceding section, the ice adhesion strength of the hydrophobic concrete is lower than that of the uncoated concrete. This can be attributed, at least partially, to the synergistic effect of the air pockets due to the hydrophobization as well as the exposed PVA fibers. Both these factors minimize the mirrored charges on ice, thereby weakening ice adhesion.

6.6.2 Suppression of frost formation

Nucleation occurs when the energy gained in forming a nucleus is greater than the energy cost due to creation of a new interface. The rate of nucleation is related to the nucleation energy barrier (ΔG^*) as $rate \propto \exp(-\Delta G^*/k_B T)$. The nucleation energy barrier for homogeneous nucleation is

$$\Delta G_{homogeneous}^* = \frac{16\pi}{3} \frac{\gamma^3}{(\rho_n \Delta\mu)^2} \quad (6.7)$$

where $\Delta\mu$ is the difference in chemical potentials between the surrounding phase and the nucleating phase, γ is the interfacial tension of the nucleus, and the number density of the nucleating phase ρ_n is the number of possible nucleation sites per unit volume. Ice nucleation occurs when the critical radius of the nucleus is equal to or greater than [75]

$$R^* = \frac{2\gamma}{\rho_n \Delta\mu} \quad (6.8)$$

The nucleation energy barrier for heterogeneous nucleation at a surface is less than the energy barrier for homogeneous nucleation. The heterogeneous nucleation energy barrier on a flat surface [76] is

$$\Delta G_{flat}^* = \Delta G_{homogeneous}^* \left(\frac{1}{2} - \frac{3}{4} \cos \theta + \frac{1}{4} \cos^3 \theta \right) \quad (6.9)$$

while the heterogeneous nucleation energy barrier in a wedge [77] with a characteristic length greater than the critical radius R^* is

$$\Delta G_{wedge}^* = \Delta G_{homogeneous}^* \frac{1}{4\pi} \left(\cos \theta \sin^2 \theta \sin \varphi - \cos \theta (3 - \cos^2 \theta) \varphi + 4 \sin^{-1} \left(\sin \frac{\varphi}{2} \sin \frac{\alpha}{2} \right) \right) \quad (6.10)$$

where θ is the contact angle of the nucleus at the surface, α is the angle of the wedge, and $\cos \frac{\varphi}{2} = \cot \theta \cot \frac{\alpha}{2}$ (Figure 6.12a). Eq. 6.10 is valid for $(180 - \alpha)/2 \leq \theta \leq (180 + \alpha)/2$ and $0 \leq \alpha \leq 180^\circ$. When $\alpha = 180^\circ$, $\Delta G_{wedge}^* = \Delta G_{flat}^*$.

Nucleation energy barrier for a wedge normalized using the homogeneous nucleation energy barrier varies with contact angle and wedge angle as shown in Figure 6.12b. The narrow wedges lower the energy barrier for nucleation. Thus, ice nucleation occurs readily at concave sites compared to flat or convex sites. For hydrophilic surfaces, the nucleation energy barrier is low whereas for hydrophobic surfaces the nucleation energy barrier is high. Thus, theoretically a smooth superhydrophobic surface should provide the highest energy barrier for heterogeneous

nucleation and frost formation. Molecularly smooth surfaces exhibit delayed ice nucleation in humid conditions compared to rough superhydrophobic surfaces [78].

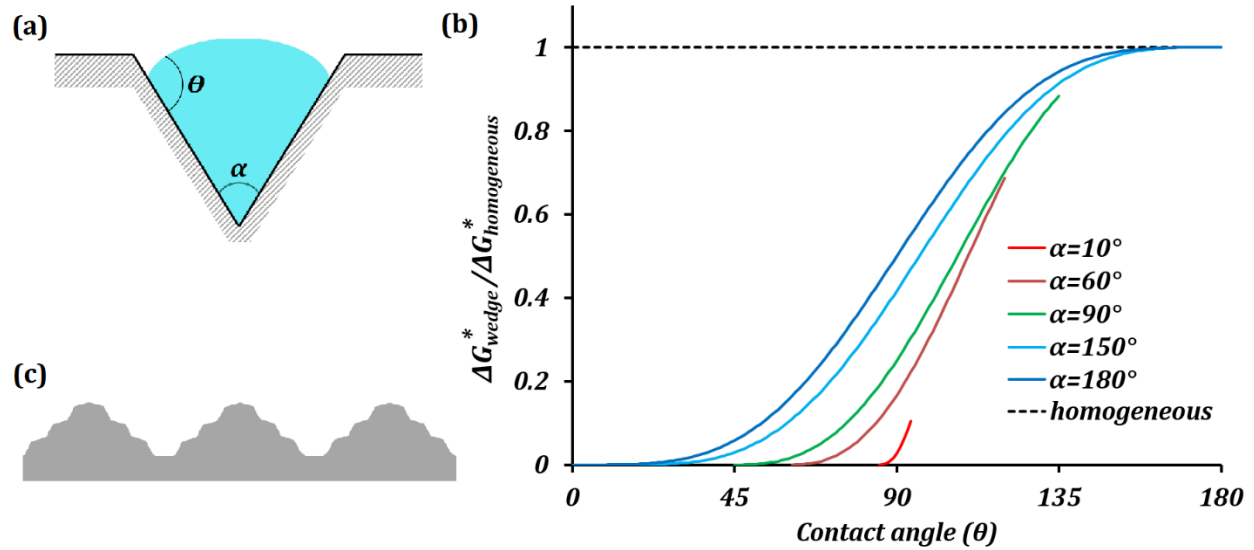


Figure 6.12. (a) Water droplet making a contact angle θ inside a wedge of angle α . (b) Normalized nucleation energy barrier versus contact angle. The energy barrier increases as the wedge angle increases. (c) Surface topography with wide corners will have the highest possible nucleation energy barrier.

The highest possible contact angle on any smooth surface is 119° [79]. Multiscale surface roughness is essential for large values of macroscopic contact angles. The critical radius of the ice nucleus R^* is of the order of a few nanometers. The characteristic length scale of the surface features on a superhydrophobic surface is usually greater than R^* . Therefore, the local contact angle θ of the material is critical for the ice nucleation energy barrier than the macroscopic contact angle.

For rough surfaces, the aim must be to have the wedge angles as large as possible. For a surface topography as shown in Figure 6.12c, both the micro and nano scale features maintain wide angle corners to have high nucleation energy barriers.

For the concrete samples studied here, the surface topography is influenced by the sand to cement ratio and the PVA fiber content. The effect of these parameters on the surface roughness is given by Eq. 6.5. The mechanical abrasion of concrete prior to coating with emulsion also affects the surface topography. An appropriate grit sand paper can be selected so that the prepared surface has a topography resembling Figure 6.12c.

6.6.3 Minimizing contact time for incoming droplets

It was seen in the experiments with impinging droplets that the surface tends to be sticky at -5 °C. The stickiness of the surface can be explained by the spontaneous condensation of water from vapor into the cracks and pores on the concrete surface. The equilibrium curvature of the condensate meniscus is given by the Kelvin equation [25].

$$r_K = \frac{\gamma V_m}{RT \ln(p/p_{sat})} \quad (6.11)$$

where r_K is the Kelvin radius, γ is the surface tension, V_m is the molar volume, p is the vapor pressure and p_{sat} is the saturated vapor pressure at temperature T . For supercooled water at -5 °C, $V_m \approx 18.026 \times 10^{-6} \text{ m}^3/\text{mol}$, $\gamma \approx 0.0764 \text{ N/m}$, and $\gamma V_m / RT \approx 0.62 \text{ nm}$. At saturated conditions ($p/p_{sat} = 1$), $r_K = \infty$. At 34% relative humidity ($p/p_{sat} = 0.34$), $r_K \approx -0.57 \text{ nm}$. The negative value of curvature implies that condensation can occur at undersaturated conditions. The geometry of the surface topographical features plays an important role in the formation of thermodynamically stable interface. Spontaneous condensation can occur in hydrophilic pores of size greater than r_K .

The condensate formed in nano and micro pores of the concrete surface results in the modification of the surface energy of concrete. An incoming liquid droplet encountering a condensate liquid film on the surface will experience an adhesion force [25]

$$F_{ad} = 4\pi R\gamma \cos \theta \quad (6.12)$$

where R is the radius of the undeformed droplet and θ is the contact angle of the condensate film with the surface. The energy required to overcome this adhesion will scale as $4\pi R\gamma X \cos \theta$ where X is the size of the flattened face of the droplet on impact. Consider the concrete surface wetted by the nano scale condensate film ($\theta = 0^\circ$). For a 14 μl water droplet at -5°C impacting the concrete surface at 0.99 m/s the kinetic energy at impact is of the order 10^{-6} J. If the droplet deformation is of the same order as R , the energy required to overcome adhesion and bounce off the surface is of the order 10^{-6} J. The significant energy loss incurred by the droplet results in the droplet wetting the surface followed by freezing.

To minimize the contact time between the incoming droplets and a surface, it is essential to control the surface topography as well as the contact angle. Hydrophobizing the surface pores will result in a reduction of the adhesion force F_{ad} . Sample M1 with no sand content demonstrated the best ability to repel incoming water droplets. The absence of sand resulted in smaller pores which do not sustain a thermodynamically stable continuous condensate film. The hydrophobic coating ensured a low adhesion force. The surface roughness of concrete can be optimized by controlling the parameters in Eq. 6.5.

6.7 Conclusion

In this chapter, the theoretical mechanisms of ice-repellence were discussed. It was found that the interactions involved are similar to hydrophobic interactions. Furthermore, the requirements for an icephobic surface are analogous to the requirements for a superhydrophobic surface, as summarized in Table 6.1. Although it is well known that not all the superhydrophobic surfaces are icephobic, most surface properties needed to design a superhydrophobic surface, such as the surface micro/nanotopography and free energy, affect the icephobic performance. This finding led to development of an icephobic surface using the same approaches which were used for the superhydrophobic modification. For this study, concrete was selected. Concrete is typically hydrophilic and wicks water. Only recently hydrophobic and superhydrophobic types of concrete were synthesized. Concrete is a very common material in civil engineering and construction; therefore, addition of icephobic property can have a significant impact on many applications.

The three aspects of the icephobicity are the reduced ice adhesion, repulsion of incoming droplets prior to freezing, and delayed frost formation. Two aspects of the icephobicity, namely, the ice adhesion to concrete and the repulsion of incoming droplets were studied. The icephobicity of concrete was achieved by hydrophobizing the surface so that it can maintain the Cassie state with air pockets between the solid and water, by using dielectric coatings, and by modifying the surface topography. Uncoated concrete samples were hydrophilic, and showed ice adhesion strength in the range 170-376 kPa. Concrete samples coated with hydrophobic emulsion showed water contact angle as high as 151° and roll-off angle as low as 1° . The ice adhesion strengths of the coated samples were one order lower in the range 29-83 kPa. The PVA

fibers as well as the air pockets on the surface, due to their low dielectric constants can minimize the mirror charges on the ice surface thereby reducing the ice adhesion strength. The addition of PVA fibers and sand to concrete resulted in a significant increase in surface roughness. The coated concrete samples could repel incoming water droplets at 20 °C as well as -5 °C. It was found that icephobic performance of concrete depends on these parameters – the hydrophobic emulsion concentration, the PVA fiber content, the water to cement ratio, and sand to cement ratio.

The surface roughness of concrete can be optimized by controlling the sand and PVA fiber content. An optimally rough surface could prevent wetting transition for incoming droplets and minimize the resulting ice accretion, as well as delay the ice nucleation and frost formation by increasing the ice nucleation energy barrier for the surface. To conclude, surface micro/nanotopography can be used to control the icephobicity of materials. In the next chapter, the biomimetic potential and the effect of surface micro/nanotopography on the icephobicity of skunk cabbage are studied.

6.8 References

- [1] Kreder, M.J.; Alvarenga, J.; Kim, P.; Aizenberg, J. Design of Anti-Icing Surfaces: Smooth, Textured Or Slippery? *Nature Reviews Materials* **2016**, *1*, 15003.
- [2] Blackburn, C.; Laforte, C.; Laforte, J.L. Apparatus for Measuring the Adhesion Force of a Thin Ice Sheet on a Substrate. In *Proceedings of the International Workshop on Atmospheric Icing of Structures (IWAIS)*, Chester, UK.
- [3] Kulinich, S.A.; Farzaneh, M. How Wetting Hysteresis Influences Ice Adhesion Strength on Superhydrophobic Surfaces. *Langmuir* **2009**, *25*, 8854-8856.
- [4] Mishchenko, L.; Hatton, B.; Bahadur, V.; Taylor, J.A.; Krupenkin, T.; Aizenberg, J. Design of Ice-Free Nanostructured Surfaces Based on Repulsion of Impacting Water Droplets. *ACS Nano* **2010**, *4*, 7699-7707.

- [5] Ramachandran, R.; Sobolev, K.; Nosonovsky, M. Dynamics of Droplet Impact on Hydrophobic/Icephobic Concrete with the Potential for Superhydrophobicity. *Langmuir* **2015**, *31*, 1437-1444.
- [6] Eberle, P.; Tiwari, M.K.; Maitra, T.; Poulikakos, D. Rational Nanostructuring of Surfaces for Extraordinary Icephobicity. *Nanoscale* **2014**, *6*, 4874-4881.
- [7] Kim, P.; Wong, T.; Alvarenga, J.; Kreder, M.J.; Adorno-Martinez, W.; Aizenberg, J. Liquid-Infused Nanostructured Surfaces with Extreme Anti-Ice and Anti-Frost Performance. *ACS Nano* **2012**, *6*, 6569-6577.
- [8] Liu, Y.; Whyman, G.; Bormashenko, E.; Hao, C.; Wang, Z. Controlling Drop Bouncing using Surfaces with Gradient Features. *Appl. Phys. Lett.* **2015**, *107*, 051604.
- [9] Pruppacher, H.R.; Klett, J.D. *Microphysics of Clouds and Precipitation*, 1st ed.; Dordrecht : Springer Netherlands, 2010.
- [10] Li, K.; Xu, S.; Shi, W.; He, M.; Li, H.; Li, S.; Zhou, X.; Wang, J.; Song, Y. Investigating the Effects of Solid Surfaces on Ice Nucleation. *Langmuir* **2012**, *28*, 10749-10754.
- [11] Alizadeh, A.; Yamada, M.; Li, R.; Shang, W.; Otta, S.; Zhong, S.; Ge, L.; Dhinojwala, A.; Conway, K.R.; Bahadur, V. *et al.* Dynamics of Ice Nucleation on Water Repellent Surfaces. *Langmuir* **2012**, *28*, 3180-3186.
- [12] Campbell, J.M.; Meldrum, F.C.; Christenson, H.K. Is Ice Nucleation from Supercooled Water Insensitive to Surface Roughness? *Journal of Physical Chemistry C* **2015**, *119*, 1164-1169.
- [13] Nosonovsky, M.; Hejazi, V. Why Superhydrophobic Surfaces are Not always Icephobic. *ACS Nano* **2012**, *6*, 8488-8491.
- [14] Farhadi, S.; Farzaneh, M.; Kulinich, S.A. Anti-Icing Performance of Superhydrophobic Surfaces. *Appl. Surf. Sci.* **2011**, *257*, 6264-6269.
- [15] Li, H.; Li, X.; Luo, C.; Zhao, Y.; Yuan, X. Icephobicity of Polydimethylsiloxane-b-Poly(Fluorinated Acrylate). *Thin Solid Films* **2014**, *573*, 67-73.
- [16] Li, X.; Zhao, Y.; Li, H.; Yuan, X. Preparation and Icephobic Properties of Polymethyltrifluoropropylsiloxane-Polyacrylate Block Copolymers. *Appl. Surf. Sci.* **2014**, *316*, 222-231.
- [17] Fu, Q.; Wu, X.; Kumar, D.; Ho, J.W.C.; Kanhere, P.D.; Srikanth, N.; Liu, E.; Wilson, P.; Chen, Z. Development of Sol-Gel Icephobic Coatings: Effect of Surface Roughness and Surface Energy. *ACS Applied Materials & Interfaces* **2014**, *6*, 20685-20692.

- [18] Boinovich, L.B.; Emelyanenko, A.M.; Ivanov, V.K.; Pashinin, A.S. Durable Icephobic Coating for Stainless Steel. *ACS Applied Materials & Interfaces* **2013**, *5*, 2549-2554.
- [19] Horgnies, M.; Chen, J.J. Superhydrophobic Concrete Surfaces with Integrated Microtexture. *Cem. Concr. Compos.* **2014**, *52*, 81-90.
- [20] Barthlott, W.; Neinhuis, C. Purity of the Sacred Lotus, Or Escape from Contamination in Biological Surfaces. *Planta* **1997**, *202*, 1-8.
- [21] Wong, T.; Kang, S.H.; Tang, S.K.Y.; Smythe, E.J.; Hatton, B.D.; Grinthal, A.; Aizenberg, J. Bioinspired Self-Repairing Slippery Surfaces with Pressure-Stable Omniphobicity. *Nature* **2011**, *477*, 443-447.
- [22] Wilson, P.W.; Lu, W.; Xu, H.; Kim, P.; Kreder, M.J.; Alvarenga, J.; Aizenberg, J. Inhibition of Ice Nucleation by Slippery Liquid-Infused Porous Surfaces (SLIPS). *Physical Chemistry Chemical Physics* **2013**, *15*, 581-585.
- [23] Sun, X.; Damle, V.G.; Liu, S.; Rykaczewski, K. Bioinspired Stimuli-Responsive and Antifreeze-Secreting Anti-Icing Coatings. *Advanced Materials Interfaces* **2015**, *2*.
- [24] Flory, P., J. *Statistical Mechanics of Chain Molecules*. Interscience: New York, 1969.
- [25] Israelachvili, J.N. *Intermolecular and Surface Forces*, 3rd. ed.; Waltham, MA: Academic Press: Waltham, MA, 2011.
- [26] Donaldson, S.H., Jr.; Royne, A.; Kristiansen, K.; Rapp, M.V.; Das, S.; Gebbie, M.A.; Lee, D.W.; Stock, P.; Valtiner, M.; Israelachvili, J. Developing a General Interaction Potential for Hydrophobic and Hydrophilic Interactions. *Langmuir* **2015**, *31*, 2051-2064.
- [27] Chandler, D. Interfaces and the Driving Force of Hydrophobic Assembly. *Nature* **2005**, *437*, 640-647.
- [28] Singh, S.; Houston, J.; van Swol, F.; Brinker, C.J. Superhydrophobicity - Drying Transition of Confined Water. *Nature* **2006**, *442*, 526-526.
- [29] Hammer, M.U.; Anderson, T.H.; Chaimovich, A.; Shell, M.S.; Israelachvili, J. The Search for the Hydrophobic Force Law. *Faraday Discuss.* **2010**, *146*, 299-308.
- [30] Bak, P.; Tang, C.; Wiesenfeld, K. Self-Organized Criticality - an Explanation of 1/f Noise. *Phys. Rev. Lett.* **1987**, *59*, 381-384.
- [31] Zypman, F.R.; Ferrante, J.; Jansen, M.; Scanlon, K.; Abel, P. Evidence of Self-Organized Criticality in Dry Sliding Friction. *Journal of Physics-Condensed Matter* **2003**, *15*, L191-L196.
- [32] Creeger, P.; Zypman, F. Entropy Content during Nanometric Stick-Slip Motion. *Entropy* **2014**, *16*, 3062-3073.

- [33] Nosonovsky, M.; Bhushan, B. Do Hierarchical Mechanisms of Superhydrophobicity Lead to Self-Organized Criticality? *Scr. Mater.* **2008**, *59*, 941-944.
- [34] Tadmor, R. Line Energy and the Relation between Advancing, Receding, and Young Contact Angles. *Langmuir* **2004**, *20*, 7659-7664.
- [35] He, B.; Lee, J.; Patankar, N.A. Contact Angle Hysteresis on Rough Hydrophobic Surfaces. *Colloids and Surfaces A-Physicochemical and Engineering Aspects* **2004**, *248*, 101-104.
- [36] Krasovitski, B.; Marmur, A. Drops Down the Hill: Theoretical Study of Limiting Contact Angles and the Hysteresis Range on a Tilted Plate. *Langmuir* **2005**, *21*, 3881-3885.
- [37] Li, W.; Amirfazli, A. A Thermodynamic Approach for Determining the Contact Angle Hysteresis for Superhydrophobic Surfaces. *J. Colloid Interface Sci.* **2005**, *292*, 195-201.
- [38] Nosonovsky, M. Model for Solid-Liquid and Solid-Solid Friction of Rough Surfaces with Adhesion Hysteresis. *J. Chem. Phys.* **2007**, *126*, 224701.
- [39] Bormashenko, E.Y. *Wetting of Real Surfaces*. De Gruyter: Berlin, Boston, 2013.
- [40] Phillips, J.C. Scaling and Self-Organized Criticality in Proteins I. *Proc. Natl. Acad. Sci. U. S. A.* **2009**, *106*, 3107-3112.
- [41] Phillips, J.C. Hydropathic Self-Organized Criticality: A Magic Wand for Protein Physics. *Protein Peptide Lett.* **2012**, *19*, 1089-1093.
- [42] Lobkovsky, A.E.; Wolf, Y.I.; Koonin, E.V. Universal Distribution of Protein Evolution Rates as a Consequence of Protein Folding Physics. *Proc. Natl. Acad. Sci. U. S. A.* **2010**, *107*, 2983-2988.
- [43] Koonin, E.V. *The Logic of Chance: The Nature and Origin of Biological Evolution* .; FT Press: Upper Saddle River, 2011.
- [44] Hong, L.; Lei, J. Scaling Law for the Radius of Gyration of Proteins and its Dependence on Hydrophobicity. *Journal of Polymer Science Part B-Polymer Physics* **2009**, *47*, 207-214.
- [45] Nittmann, J.; Stanley, H.E. Nondeterministic Approach to Anisotropic Growth-Patterns with Continuously Tunable Morphology - the Fractal Properties of some Real Snowflakes. *Journal of Physics A-Mathematical and General* **1987**, *20*, L1185-L1191.
- [46] Libbrecht, K.G. Morphogenesis on Ice: The Physics of Snow Crystals. *Engineering and Science* **2001**, *64*, 10-19.
- [47] Libbrecht, K.G. The Physics of Snow Crystals. *Reports on Progress in Physics* **2005**, *68*, 855-895.

- [48] Furukawa, Y.; Wettlaufer, J.S. Snow and Ice Crystals. *Phys Today* **2007**, *60*, 70-71.
- [49] Furukawa, Y. Snow and ice crystal growth. In *Handbook of Crystal Growth: Fundamentals: Thermodynamics and Kinetics. Volume 1A*, 2nd ed.; Nishinaga, T., Ed.; Elsevier: Waltham, MA, 2015, pp. 1061.
- [50] Petrenko, V.F.; Peng, S. Reduction of Ice Adhesion to Metal by using Self-Assembling Monolayers (SAMs). *Can. J. Phys.* **2003**, *81*, 387-393.
- [51] Ryzhkin, I.A.; Petrenko, V.F. Physical Mechanisms Responsible for Ice Adhesion. *J Phys Chem B* **1997**, *101*, 6267-6270.
- [52] Saleema, N.; Farzaneh, M.; Paynter, R.W.; Sarkar, D.K. Prevention of Ice Accretion on Aluminum Surfaces by Enhancing their Hydrophobic Properties. *J. Adhes. Sci. Technol.* **2011**, *25*, 27-40.
- [53] Hejazi, V.; Sobolev, K.; Nosonovsky, M. From Superhydrophobicity to Icephobicity: Forces and Interaction Analysis. *Scientific Reports* **2013**, *3*, 2194.
- [54] Boinovich, L.; Emelyanenko, A.M. Role of Water Vapor Desublimation in the Adhesion of an Iced Droplet to a Superhydrophobic Surface. *Langmuir* **2014**, *30*, 12596-12601.
- [55] Mobarakeh, L.F.; Jafari, R.; Farzaneh, M. The Ice Repellency of Plasma Polymerized Hexamethyldisiloxane Coating. *Appl. Surf. Sci.* **2013**, *284*, 459-463.
- [56] Laforte, C.; Beisswenger, A. Icephobic Material Centrifuge Adhesion Test. In Proc. of 11th Int. Workshop on Atmos. Icing of Structures, IWAIS 2005, Montreal, Canada.
- [57] Li, W.; Zhang, X.; Yang, J.; Miao, F. In Situ Growth of Superhydrophobic and Icephobic Films with micro/nanoscale Hierarchical Structures on the Aluminum Substrate. *J. Colloid Interface Sci.* **2013**, *410*, 165-171.
- [58] Subramanyam, S.B.; Rykaczewski, K.; Varanasi, K.K. Ice Adhesion on Lubricant-Impregnated Textured Surfaces. *Langmuir* **2013**, *29*, 13414-13418.
- [59] Maitra, T.; Antonini, C.; Tiwari, M.K.; Mularczyk, A.; Imeri, Z.; Schoch, P.; Poulikakos, D. Supercooled Water Drops Impacting Superhydrophobic Textures. *Langmuir* **2014**, *30*, 10855-10861.
- [60] Kwon, H.; Paxson, A.T.; Varanasi, K.K.; Patankar, N.A. Rapid Deceleration-Driven Wetting Transition during Pendant Drop Deposition on Superhydrophobic Surfaces. *Phys. Rev. Lett.* **2011**, *106*, 036102.
- [61] Bird, J.C.; Dhiman, R.; Kwon, H.; Varanasi, K.K. Reducing the Contact Time of a Bouncing Drop. *Nature* **2013**, *503*, 385-388.

- [62] Zheng, L.; Li, Z.; Bourdo, S.; Khedir, K.R.; Asar, M.P.; Ryerson, C.C.; Biris, A.S. Exceptional Superhydrophobicity and Low Velocity Impact Icephobicity of Acetone-Functionalized Carbon Nanotube Films. *Langmuir* **2011**, *27*, 9936-9943.
- [63] Lafuma, A.; Quere, D. Superhydrophobic States. *Nature Materials* **2003**, *2*, 457-460.
- [64] Boreyko, J.B.; Chen, C. Self-Propelled Dropwise Condensate on Superhydrophobic Surfaces. *Phys. Rev. Lett.* **2009**, *103*, 184501.
- [65] Boreyko, J.B.; Collier, C.P. Delayed Frost Growth on Jumping-Drop Superhydrophobic Surfaces. *ACS Nano* **2013**, *7*, 1618-1627.
- [66] Chen, X.; Ma, R.; Zhou, H.; Zhou, X.; Che, L.; Yao, S.; Wang, Z. Activating the Microscale Edge Effect in a Hierarchical Surface for Frosting Suppression and Defrosting Promotion. *Scientific Reports* **2013**, *3*, 2515.
- [67] Kozhukhova, M.I. 'АНТИОБЛЕДЕНИТЕЛЬНОЕ ПОКРЫТИЕ ДЛЯ МЕЛКОЗЕРНИСТОГО БЕТОНА' / Anti Icing Coating for Concrete. PhD Thesis. **2014**.
- [68] Kozhukhova, M.I.; Flores-Vivian, I.; Rao, S.; Strokova, V.V.; Sobolev, K. 'Комплексное силиконовое покрытие для супергидрофобизации бетонных поверхностей' / Complex Siloxane Coating for Superhydrophobization of Concrete Surfaces. *Construction Materials Journal* **2014**, *3*, 26–30.
- [69] Kozhukhova, M.I.; Strokova, V.V.; Sobolev, K. 'ОСОБЕННОСТИ ГИДРОФОБИЗАЦИИ МЕЛКОЗЕРНИСТЫХ БЕТОННЫХ ПОВЕРХНОСТЕЙ' / Hydrophobization of Concrete. *Bulletin of BSTU* **2014**, *4*, 33–35.
- [70] Muzenski, S.; Flores-Vivian, I.; Sobolev, K. Freeze-Thaw Resistance of Fiber Reinforced Composites with Superhydrophobic Admixtures. In *Mechanics and Physics of Creep, Shrinkage, and Durability of Concrete*, Cambridge, MA; pp. 269-276.
- [71] Flores-Vivian, I.; Hejazi, V.; Kozhukhova, M.I.; Nosonovsky, M.; Sobolev, K. Self-Assembling Particle-Siloxane Coatings for Superhydrophobic Concrete. *ACS Applied Materials & Interfaces* **2013**, *5*, 13284-13294.
- [72] Muzenski, S.; Flores-Vivian, I.; Sobolev, K. Hydrophobic Engineered Cementitious Composites for Highway Applications. *Cem. Concr. Compos.* **2015**, *57*, 68-74.
- [73] Petrenko, V.F. The Surface of Ice. USA CRREL Special Report **1994**, 94-22.
- [74] <http://www.clippercontrols.com/pages/Dielectric-Constant-Values.html>. Accessed January/5 2016.
- [75] Sear, R.P. Nucleation: Theory and Applications to Protein Solutions and Colloidal Suspensions. *Journal of Physics-Condensed Matter* **2007**, *19*, 033101.

[76] Volmer, M. ÜBER KEIMBILDUNG UND KEIMWIRKUNG ALS SPEZIALFÄLLE DER HETEROGENEN KATALYSE. Zeitschrift für Elektrochemie und angewandte physikalische Chemie **1929**, *35*, 555-561.

[77] Sholl, C.A.; Fletcher, N.H. Decoration Criteria for Surface Steps. Acta Metallurgica **1970**, *18*, 1083-1086.

[78] Heydari, G.; Sedighi Moghaddam, M.; Tuominen, M.; Fielden, M.; Haapanen, J.; Mäkelä, J.M.; Claesson, P.M. Wetting Hysteresis Induced by Temperature Changes: Supercooled Water on Hydrophobic Surfaces. J. Colloid Interface Sci. **2016**, *468*, 21-33.

[79] Nishino, T.; Meguro, M.; Nakamae, K.; Matsushita, M.; Ueda, Y. The Lowest Surface Free Energy Based on -CF₃ Alignment. Langmuir **1999**, *15*, 4321-4323.

CHAPTER 7: BIOMIMETIC POTENTIAL OF THE ICEPHOBICITY OF SKUNK

CABBAGE

In the previous chapter, it was seen that surface micro topography as well as surface free energy affect the icephobic performance of a surface. This understanding was used to control the icephobicity of concrete. This chapter will focus on the icephobicity of a plant called skunk cabbage (*Symplocarpus foetidus*) which is a thermogenic plant that emerges through snow. The potential for the biomimetic icephobicity of skunk cabbage, and the effect of surface topography on its icephobicity are investigated.

7.1 Introduction

The lotus (*Nelumbo nucifera*) leaf with its hierarchical structure of papillae covered with rough wax served an initial source of inspiration for the artificial superhydrophobic surfaces. The lotus effect is characterized by high CA and small CAH. However, the petal effect is characterized by high CA (often in the superhydrophobic region) and large CAH. The observation caused a discussion of the very concept of the hydrophobicity and how it is possible for a surface to be “superhydrophobic” (meaning the strong repulsion of water) simultaneously with having strong adhesion to water [1,2]. An alternative term suggested for the rose petal effect in the literature is the “parahydrophobic state” [3]. Among the proposed answers was that water-to-solid adhesion is not characterized by a single number, such as the apparent CA. Instead, the normal and shear loading can be considered separately, presumably, with the CA and CA hysteresis being wetting characteristics during normal and shear loading. Shear and normal loads can be applied and measured independently using the centrifugal adhesion balance [4]. Furthermore, the very concept of static CA is not well defined since the CA may depend on how

water droplet was created and does not necessarily converge with time to a single value [5]. It has also been shown recently that surfaces can exhibit high contact angle coupled with either low or high adhesion by virtue of just surface topography alone [6].

As seen in chapter 6, the icephobicity is closely correlated to the superhydrophobicity. The exact definition of the icephobicity remains the subject of debate, as well as its relationship with the superhydrophobicity [7-12]. However, given that ice will form on any surface, the parameter of practical importance is the work of adhesion between the substrate and ice [7].

Besides the superhydrophobicity, another property which is unusual in lotus is the thermogenesis. Thermogenic plants, including the lotus, can raise their temperature above that of the surrounding air, sometimes exceeding the latter by 20 °C. The role of thermogenesis in plants is still debated by botanists; however, the most popular hypothesis is that heat helps to spread chemicals that attract pollinators to the plant [13,14]. The heat is generated in mitochondria of the plant cells. Besides lotus, only few plants have thermogenic properties including some tropical plants, such as the voodoo lily (*Amorphophalus*), and some plants common in the northern climate including the eastern skunk cabbage (*Symplocarpus foetidus*, also referred to in literature as eastern North American skunk cabbage) and several related plants from the Araceae (arum) family. The skunk cabbage is known for its ability to emerge from under snow.

Apparently, there is no direct correlation between the superhydrophobicity and thermogenesis, since besides lotus there are no examples of plants which possess both properties. However, since these both properties may involve certain common features, such as the ability to repel ice, the issue requires further investigation. In this chapter, the leaves of a thermogenic

plant, *S. foetidus* are studied. A theoretical model correlating the superhydrophobicity, the thermogenesis and the icephobicity is developed.

7.2 *Symplocarpus foetidus* and the Icephobicity

Eastern skunk cabbage (*S. foetidus*) is a member of Araceae family and is of particular interest due to its peculiar thermogenic and thermoregulatory property. The plant is native to North American wetlands. It blooms in late winter or early spring, when there is still a snow cover on the ground. The ability of the plant to survive and melt through thick snow in below-freezing ambient conditions is of interest to us.

The parts of the skunk cabbage shoot are the green leaves (Figure 7.1a) and the purple modified leaves called spathes (Figure 7.1b) which enclose the flowering part of the plant called spadix. It is the spadix which emits the foul smelling odor that gives the plant its name. Spadix also plays an important role in thermogenesis. The plant is able to maintain an average spadix temperature of 15 °C when the ambient temperature is -15 °C [15]. Transpiration plays an important part in regulating the plant temperature. In hot tropical climate, thermogenic plants such as lotus maintain their temperature below that of surroundings by evaporating water. Similarly, plants reduce water loss by evaporation to maintain temperatures above that of surroundings. In plants, the water loss to atmosphere and gaseous exchange occurs through openings on leaf surface called stomata. Usually leaves of terrestrial plants have stomata on their lower (abaxial) surface. Aquatic plants such as lotus have stomata on their upper (adaxial) surface. Many plant leaves are usually covered by a thin wax coating called cuticle whose one of many functions is to prevent excessive water loss. The cuticle is sometimes further covered with epicuticular wax crystals of different geometries such as platelets, tubules, rodlets etc.[16] The

size and geometry of these wax crystals are some of the decisive factors in the wetting state of leaf, for example, lotus leaf.



Figure 7.1. (a) the leaf of skunk cabbage enclosing spathe and spadix, and (b) the spathe. (c) Skunk cabbage as observed in its natural environment in wet land (Schlitz Audubon Nature Center, Milwaukee, WI) in the month of November.

The thermogenesis of skunk cabbage is well documented in literature [15,17,18]. There have been studies on the heat generation at the spadix. But according to the authors' knowledge, there has been no study on regulation of heat loss through the leaves or spathe and of the plant's icephobic properties. The ability of the skunk cabbage to repel ice formation is likely to be related with the elevated temperature of the leaves rather than with the surface structure, however, the surface microstructure should be investigated. In the following section, the surface morphology of the leaves and spathe of skunk cabbage are investigated.

7.3 Experimental

A sample of the plant was collected in early November from a wet land in Milwaukee. The plant had none of its large leaves left at this time of the year. All that remained above ground was the spadix enclosed in a spathe and fresh unsprouted leaves, prepared to weather the long and frigid winter (Figure 7.1c).

7.3.1 Contact angle measurement

Water contact angles (CA) and contact angle hysteresis (CAH) on freshly cut (within three hours after cutting) spathe and leaf surfaces were measured. The as-placed water CA were measured using a ramé-hart goniometer (model 100-25-M) by placing three pure water droplets of 10 μ l at different locations on the surface. CAH were calculated by the tilting plate method.

7.3.2 Surface topography using SEM

The microstructures of the leaf and spathe surfaces were studied using scanning electron microscopy (SEM). Three different sets of samples of leaves and spathe were prepared. Biological specimens, such as cells and tissues or tissue components, must first be fixed to preserve their native structure. Chemical fixation typically uses formalin or glutaraldehyde of varying per cent concentrations in a buffer of a specific pH. The first set (S1) was air dried in a desiccator for over two days at room temperature.[19] The second set (S2) was prepared by chemical fixation in liquid phase. A 10 ml aqueous solution of 2.5% glutaraldehyde, 0.1M HEPES buffer (pH 7.2) and 0.02% triton X-100 was prepared and the samples were left overnight in the solution. The samples were then washed thrice with distilled water and then left overnight in an 8 ml aqueous solution of 1% osmium tetroxide. The samples were then

dehydrated in a series of steps using anhydrous ethanol in 20%, 40%, 60%, 80% and 100% (thrice) solutions. This was followed by critical point drying (Blazers CPD 020) to remove ethanol from the samples.

Since triton X-100 removes all the epicuticular wax, a third set (S3) of samples were prepared using vapor phase fixation [20] to maintain the structure of the cells, while retaining the waxes on the surface. Samples were first exposed to vapor of 2% glutaraldehyde and then 2% osmium tetroxide both at room temperature.

All three sample sets were fixed on aluminum stubs using double sided tape. Then they were sputter coated in an Emitech K575X sputter coater with an Iridium target. The thickness of coating varied based on the fixation procedure- S1 required 4 nm while S2 required 5 nm and S3 required 8 nm. Colloidal carbon paint was applied along the edges of the samples on stubs to further reduce charging. The paint was applied using a fine brush under an optical microscope to ensure that leaf surfaces remained intact. The samples were observed in Hitachi S-4800 FE-SEM.

7.4 Results

The surfaces of both the leaf and spathe were seen to be hydrophobic (Figure 7.2a, b)). The leaf surface showed an average water CA of 92° and the spathe surface showed an average water CA of 97° . The surfaces also showed extremely high adhesion, with the water droplet not rolling off the vertical surface (Figure 7.2c). The advancing and receding CAs on the leaf surface was 110° and 83° respectively with a CA hysteresis of 27° . This is similar to the rose-petal effect where the droplet is usually thought to be in the Cassie-Baxter impregnating wetting state. On the other hand, Marmur showed that the contact area of a drop with the solid in the Wenzel state

can be higher by orders of magnitude compared with the Cassie-Baxter state, for the same contact angle.[21] It is therefore possible that a high contact angle and "adhesive" drop indicate the Wenzel "parahydrophobic" state.[3]

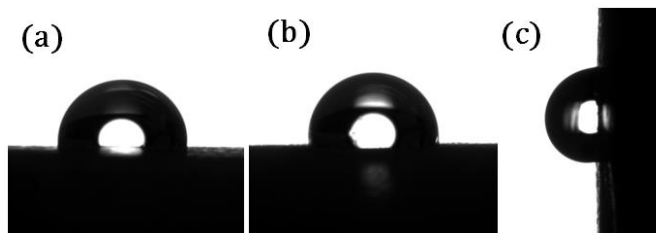


Figure 7.2. Water droplets on (a) leaf (b) spathe (c) an adherent water droplet on the vertical surface of leaf.

It was seen that vapor phase fixation procedure (sample set S3) yielded the best scanning electron micrograph results while preserving the structure of the epicuticular wax crystals. The sample sets S1 and S2 did not preserve the wax crystals. But S2 provided insight into the underlying microstructure. The scanning electron micrographs of the adaxial and abaxial surfaces of both the leaf and the spathe are shown in Figure 7.3. The abaxial surface of the leaf showed pillars (~10 μm diameter) coated with wax rodlets (Figure 7.3e, f, g). The adaxial surface of the leaf displayed a different surface texture with lack of pillar like structures and visibly far less density of wax rodlets (Figure 7.3a, b). The adaxial and abaxial surfaces of the spathe also showed an absence of pillar like structures and dense wax rodlets (Figure 7.3c, d). Interestingly, the adaxial surface of the leaf and the adaxial and abaxial surfaces of the spathe carried stomata, with the spathe showing a denser distribution of stomata. But the stomata on the abaxial surface of the leaf lay beneath the dense canopy of wax rodlets.

Skunk cabbage is known to survive the sub-zero temperatures of winter and bloom in late winter or early spring. The abaxial surface of the leaf is all that covers the spathe and spadix of

the plant during the extremely cold winters. Therefore, from the stand point of conserving heat, it seems logical to have fewer numbers of stomata on the surface exposed to the outside weather. Stomata directly connect the interstitial spaces below the epidermis to the environment for transpiration. Reduced transpiration means, minimal heat loss to the surroundings.

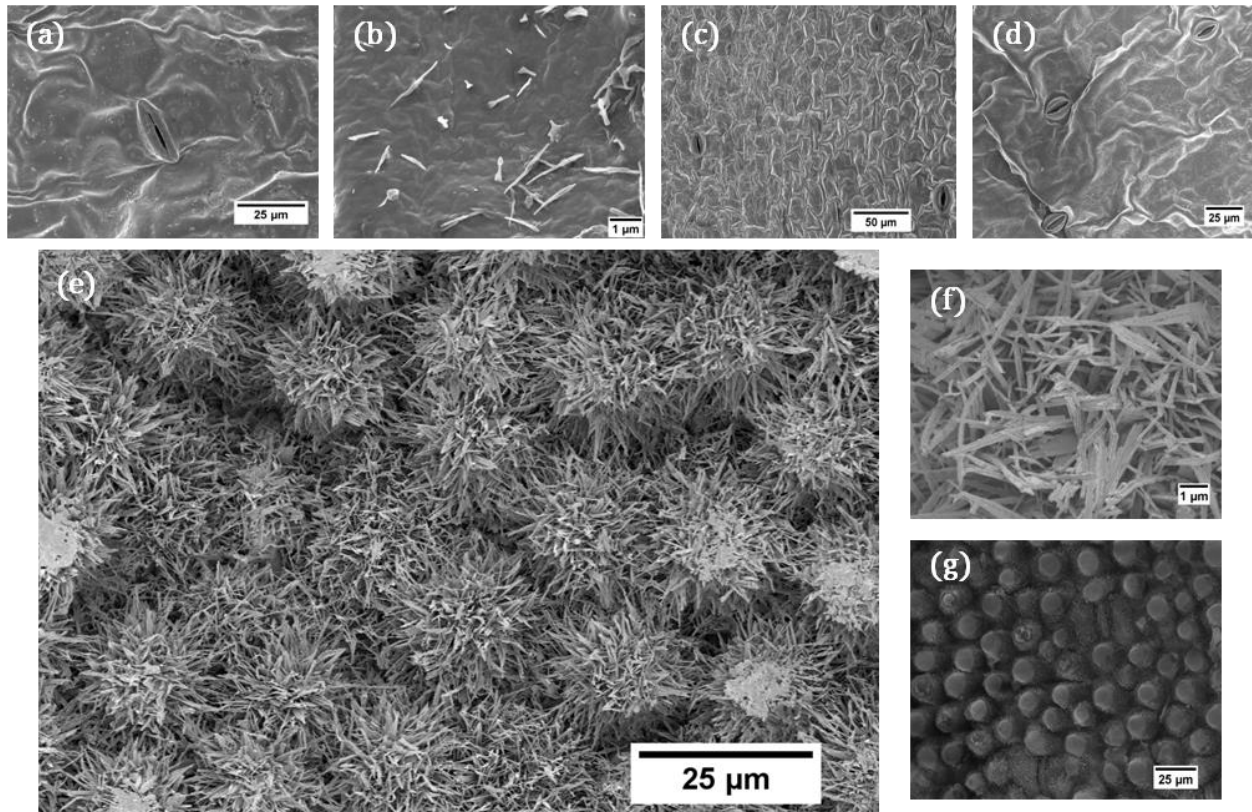


Figure 7.3. Scanning electron micrographs of skunk cabbage leaf and spathe surfaces. (a) Vapor phase fixed adaxial leaf surface, (b) scarcely distributed wax rodlets on the adaxial leaf surface, (c) adaxial surface of vapor phase fixed spathe showing stomata (d) abaxial surface of vapor phase fixed spathe showing stomata, (e) vapor phase fixed abaxial leaf surface showing pillars covered with wax rodlets, (f) the wax rodlets, and (g) liquid phase fixed abaxial surface of leaf showing the pillars tops void of wax rodlets.

The abaxial surface showed hierarchical roughness with high adhesion.[22] This may be similar to high contact angle coupled with high hysteresis seen in leaves of plants such as garlic and scallion of genus *Allium*. Such leaves have a rough surface covered with epicuticular wax

which results in high contact angle. But they also have strong smelling diallyl disulphide, a hydrophobic defect which causes contact line pinning, and thus high contact angle hysteresis.[23] Skunk cabbage is known to have dimethyl disulphide which is known to volatilize and cause the peculiar smell associated with the plant.[24] The dimethyl disulphide might be acting as hydrophobic defects on the skunk cabbage leaf resulting in high adhesion coupled with hydrophobicity.

In addition, a freezing test was performed. A small piece (2 x 2 cm) of skunk cabbage leaf was cut and a water droplet was placed on it. After that, the leaf was placed in a freezer of a kitchen refrigerator (temperature -5 °C). Several hours later, after the water droplet froze, the leaf was removed. The ice droplet was stuck to the leaf surface demonstrating relatively strong adhesion and thus no icephobic property of the cut leaf was found.

7.5 Discussion

The above results show that the leaf has complex micro/nanotopography which affects its wetting properties. The leaf is hydrophobic, however, no superhydrophobic properties were found. A cut leaf demonstrates strong adhesion to ice. This implies that the living leaf repels ice / snow due to its thermogenic properties. Suggested below is a model which relates the heat flow to the surface structure and wetting properties.

Consider a leaf surface at temperature T_1 , initially covered with a layer of ice at temperature T_2 and thickness a . It is assumed that the leaf surface maintains a steady temperature and the heat loss to the surrounding air is neglected. The leaf surface is rough and forms a solid-liquid-vapor composite interface as shown in Figure 7.4a. When $T_1 > T_2$, heat flows from the

plant surface to ice and it melts to form water. At any time t , let the water-ice interface be located at a distance ‘ x ’ from the plant surface. The heat flow from the leaf to ice can be written as

$$Q = LA \frac{dx}{dt} \quad (7.1)$$

where L is the latent heat of fusion of ice, A is the projected area of the leaf surface and $\frac{dx}{dt}$ is the velocity at which the water-ice interface advances. In order to reach the water-ice interface, this heat has to flow through the water, as well as the leaf-water interface. Therefore

$$Q = h_W A (T_i - T_2) \quad (7.2)$$

and

$$Q = \frac{T_1 - T_i}{R_{th}} \quad (7.3)$$

where T_i is the leaf-water interface temperature, h_W is the heat transfer coefficient of water and R_{th} is the thermal resistance of the composite interface. From Eq. 7.2 and Eq. 7.3,

$$Q = \frac{T_1 - T_2}{\frac{1}{h_W} + R_{th}} \quad (7.4)$$

The thermal resistance of the composite interface can be represented as electrical resistors connected in parallel as shown in Figure 7.4b. If h_A is the heat transfer coefficient of air and f_{WA} is the fractional flat area of the water-air interface,

$$1/R_{th} = h_A A f_{WA} + h_W A (1 - f_{WA}) \quad (7.5)$$

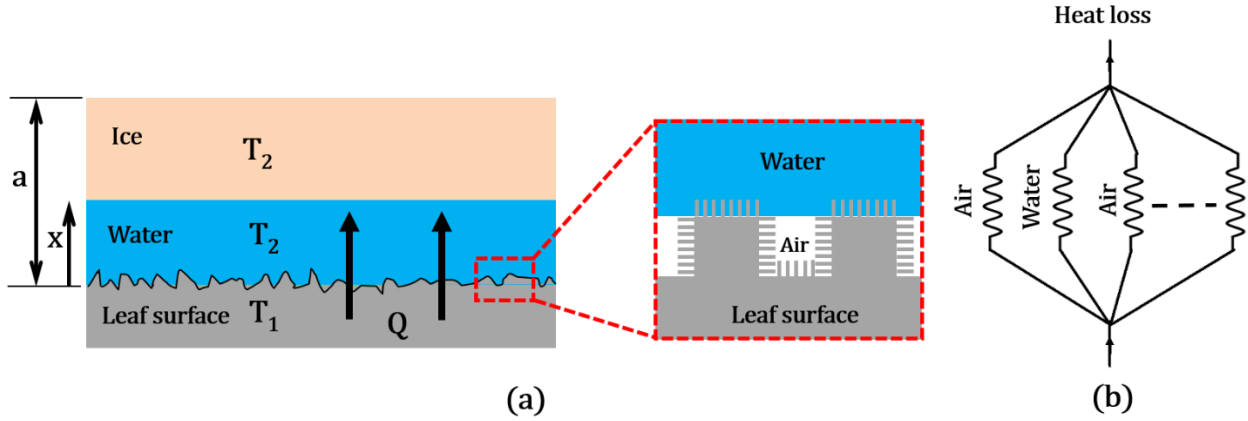


Figure 7.4. (a) Heat transfer at composite interface on the leaf surface resulting in melting of ice and an advancing water-ice interface (b) equivalent electrical circuit showing thermal resistances at the composite interface.

Combining Eq. 7.1, 7.4 and 7.5,

$$\left(\frac{1}{h_W} + \frac{1}{h_A f_{WA} + h_W(1-f_{WA})} \right) dx = (T_1 - T_2) dt \quad (7.6)$$

Integrating, $\frac{L}{(T_1 - T_2)} \left(\frac{1}{h_W} + \frac{1}{h_A f_{WA} + h_W(1-f_{WA})} \right) \int_0^a dx = \int_0^t dt$, the time required to melt an ice layer of thickness 'a' can be obtained

$$t = \frac{La}{(T_1 - T_2)} \left(\frac{1}{h_W} + \frac{1}{h_A f_{WA} + h_W(1-f_{WA})} \right) \quad (7.7)$$

If the leaf-water interface has a roughness factor r_f , then

$$t = \frac{La}{(T_1 - T_2)} \left(\frac{1}{h_W} + \frac{1}{h_A f_{WA} + h_W r_f(1-f_{WA})} \right) \quad (7.8)$$

The plots in Figure 7.5 are obtained using nominal values of $h_A = 10 \text{ W/m}^2\text{K}$, $h_W = 20 \text{ W/m}^2\text{K}$, $L = 334 \text{ kJ/kg}$, $T_1 = 15 \text{ }^\circ\text{C}$ and $T_2 = 0^\circ\text{C}$. As the wetted area of the leaf surface decreases, the longer it takes for the heat transfer to occur (Figure 7.5a). Therefore more the air pockets on leaf surface, the longer the heat is retained. Figure 7.5b shows that as the surface

becomes rougher, the heat loss speeds up. It is also seen that roughness is a predominant factor for heat loss only when the fractional flat area of the water-air interface (f_{WA}) is low. As f_{WA} increases, the effect of r_f on heat loss wanes.

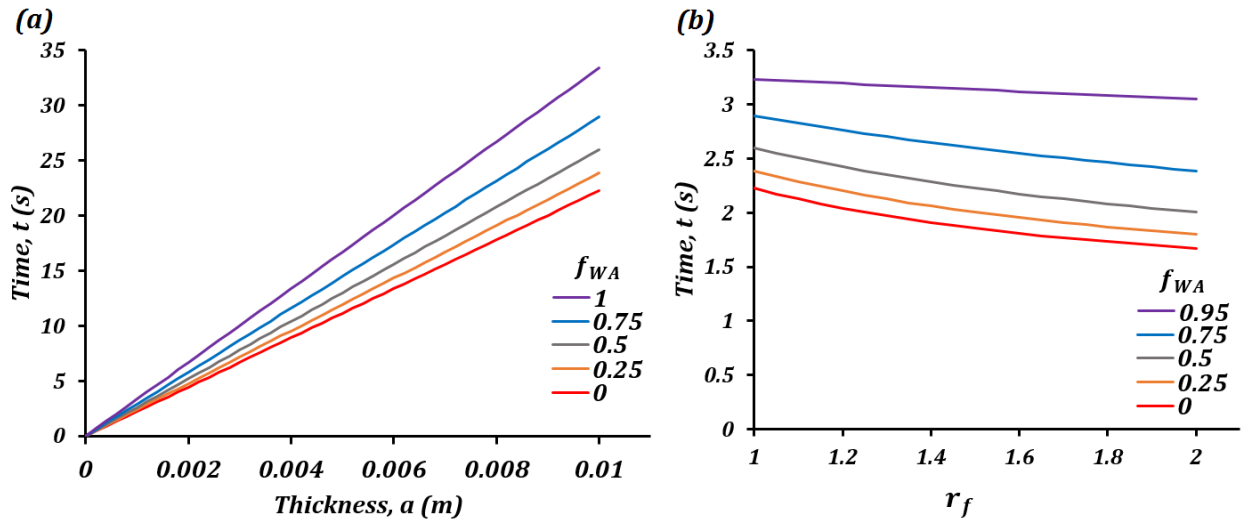


Figure 7.5. (a) Time for melting of ice layer (thickness, a) at different fractional flat area of the water-air interface (b) time for melting an ice layer 1mm thick at different fractional flat area of the water-air interface (f_{WA}) and roughness factors (r_f).

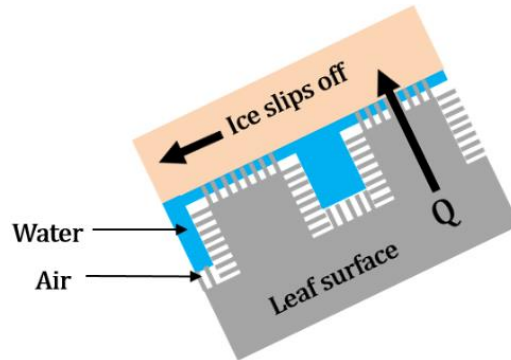


Figure 7.6. The heat produced by the skunk cabbage plant in tandem with the high adhesion can maintain a slippery layer of water on the leaf surface. Thus the ice slips off the leaf surface.

From the above discussion, it is clear that changing the surface texture (r_f and f_{WA}) can either help to conserve heat in extreme cold, or melt the ice cover. In the case of skunk cabbage leaf, water droplets are in a Cassie-Baxter impregnating wetting state with high adhesion possibly due to hydrophobic defects. The heat produced by the plant should be able to maintain a

thin impregnated layer of liquid water and air pockets between the leaf surface and surrounding ice (Figure 7.6). This ensures minimal adhesion between ice and leaf surface, and ice readily slips off under its own weight. This process can be thought of as similar to the *Nepenthes* pitcher plant inspired slippery liquid-infused porous surfaces.[25,26] Also, maintaining a water-air composite interface is conducive to heat conservation because water and air have thermal conductivities of 0.56 W/mK and 0.02 W/mK (at 275 K, 1 atm) respectively, while ice has a thermal conductivity of 2.2 W/mK (at 273 K). Note also that the skunk cabbage plant is able to produce heat with the output up to 1 W.[14] Given the latent heat of melting of ice 334 J/g, such heat output is sufficient to melt one gram of ice in 334 seconds.

Taking inspiration from the skunk cabbage plant, surfaces with Cassie-Baxter impregnating wetting state can be used in tandem with a heat source as functional icephobic surfaces. Such surfaces meet one of the definitions of the icephobicity i.e., low adhesion between the surface and ice. The heat and the surface topography should ensure a slippery water layer on the surface. Also, the Cassie-Baxter impregnating wetting state helps to reduce heat loss compared to Wenzel wetting state. Thus by controlling the wetting state of a surface one can control not only contact angle and contact angle hysteresis, but also other surface properties such as local heat transfer coefficient, ice adhesion and rate of corrosion.

7.6 Conclusion

In this chapter the surface topography and wetting properties of the thermogenic skunk cabbage was investigated. The water contact angle was found to be 92° with very high adhesion displaying rose-petal like or “parahydrophobic” effect. The microstructure of the leaf was bumpy with hair-like wax rodlets, indicating the possibility of Cassie-Baxter impregnated wetting state

with air pockets trapped between the surface and water. Experiment with ice (on a cut leaf) showed strong adhesion of ice to the surface. It is therefore likely that elevated temperature is responsible for ice repellence in the living plant. The leaf's microstructure could maintain a slippery water layer on it, reducing ice adhesion. Also, the composite interface can minimize heat loss. As far as the biomimetic potential of the plant, it can be concluded that the rose-petal effect-like structure can be used to decrease ice contact area for icephobic surfaces.

7.7 References

- [1] Li, W.; Amirfazli, A. Superhydrophobic Surfaces: Adhesive Strongly to Water? *Adv Mater* **2007**, *19*, 3421-3422.
- [2] Wang, S.; Jiang, L. Definition of Superhydrophobic States. *Adv Mater* **2007**, *19*, 3423-3424.
- [3] Marmur, A. Hydro- Hygro- Oleo- Omni-Phobic? Terminology of Wettability Classification. *Soft Matter* **2012**, *8*, 6867-6870.
- [4] N'guessan, H.E.; Leh, A.; Cox, P.; Bahadur, P.; Tadmor, R.; Patra, P.; Vajtai, R.; Ajayan, P.M.; Wasnik, P. Water Tribology on Graphene. *Nature Communications* **2012**, *3*, 1242.
- [5] Bhushan, B.; Nosonovsky, M. The Rose Petal Effect and the Modes of Superhydrophobicity. *Philosophical Transactions of the Royal Society A-Mathematical Physical and Engineering Sciences* **2010**, *368*, 4713-4728.
- [6] Peng, S.; Tian, D.; Miao, X.; Yang, X.; Deng, W. Designing Robust Alumina Nanowires-on-Nanopores Structures: Superhydrophobic Surfaces with Slippery Or Sticky Water Adhesion. *J. Colloid Interface Sci.* **2013**, *409*, 18-24.
- [7] Meuler, A.J.; Smith, J.D.; Varanasi, K.K.; Mabry, J.M.; McKinley, G.H.; Cohen, R.E. Relationships between Water Wettability and Ice Adhesion. *ACS Applied Materials & Interfaces* **2010**, *2*, 3100-3110.
- [8] Kulinich, S.A.; Farhadi, S.; Nose, K.; Du, X.W. Superhydrophobic Surfaces: Are they really Ice-Repellent? *Langmuir* **2011**, *27*, 25-29.
- [9] Bahadur, V.; Mishchenko, L.; Hatton, B.; Taylor, J.A.; Aizenberg, J.; Krupenkin, T. Predictive Model for Ice Formation on Superhydrophobic Surfaces. *Langmuir* **2011**, *27*, 14143-14150.
- [10] Guo, P.; Zheng, Y.; Wen, M.; Song, C.; Lin, Y.; Jiang, L. Icephobic/Anti-Icing Properties of Micro/Nanostructured Surfaces. *Adv Mater* **2012**, *24*, 2642-2648.

- [11] Nosonovsky, M.; Hejazi, V. Why Superhydrophobic Surfaces are Not always Icephobic. *ACS Nano* **2012**, *6*, 8488-8491.
- [12] Boinovich, L.B.; Emelyanenko, A.M. Anti-Icing Potential of Superhydrophobic Coatings. *Mendelev Communications* **2013**, *23*, 3-10.
- [13] Seymour, R.S.; Schultze-Motel, P. Thermoregulating Lotus Flowers. *Nature* **1996**, *383*, 305-305.
- [14] Seymour, R.S.; Schultze-Motel, P. Physiological Temperature Regulation by Flowers of the Sacred Lotus. *Philosophical Transactions of the Royal Society of London Series B-Biological Sciences* **1998**, *353*, 935-943.
- [15] Seymour, R.S.; SchultzeMotel, P. Heat-Producing Flowers. *Endeavour* **1997**, *21*, 125-129.
- [16] Barthlott, W.; Neinhuis, C.; Cutler, D.; Ditsch, F.; Meusel, I.; Theisen, I.; Wilhelmi, H. Classification and Terminology of Plant Epicuticular Waxes. *Bot. J. Linn. Soc.* **1998**, *126*, 237-260.
- [17] Camazine, S.; Niklas, K.J. Aerobiology of *Symplocarpus Foetidus*: Interactions between the Spathe and Spadix. *Am. J. Bot.* **1984**, *71*, 843-850.
- [18] Ito, K.; Ito, T.; Onda, Y.; Uemura, M. Temperature-Triggered Periodical Thermogenic Oscillations in Skunk Cabbage (*Symplocarpus Foetidus*). *Plant and Cell Physiology* **2004**, *45*, 257-264.
- [19] Pathan, A.K.; Bond, J.; Gaskin, R.E. Sample Preparation for Scanning Electron Microscopy of Plant Surfaces-Horses for Courses. *Micron* **2008**, *39*, 1049-1061.
- [20] Kim, K.W. Visualization of Micromorphology of Leaf Epicuticular Waxes of the Rubber Tree *Ficus Elastica* by Electron Microscopy. *Micron* **2008**, *39*, 976-984.
- [21] Marmur, A. The Lotus Effect: Superhydrophobicity and Metastability. *Langmuir* **2004**, *20*, 3517-3519.
- [22] Cho, K.L.; Wu, A.H.-.; Liaw, I.I.; Cookson, D.; Lamb, R.N. Wetting Transitions on Hierarchical Surfaces. *Journal of Physical Chemistry C* **2012**, *116*, 26810-26815.
- [23] Chang, F.; Hong, S.; Sheng, Y.; Tsao, H. High Contact Angle Hysteresis of Superhydrophobic Surfaces: Hydrophobic Defects. *Appl. Phys. Lett.* **2009**, *95*, 064102.
- [24] Kozen, E.N. The Scent of Eastern Skunk Cabbage, *Symplocarpus Foetidus* (Araceae): Qualification of Floral Volatiles and Sex Differences in Floral Scent Composition. **2013**.
- [25] Nosonovsky, M. Slippery when Wetted. *Nature* **2011**, *477*, 412-413.

[26] Wong, T.; Kang, S.H.; Tang, S.K.Y.; Smythe, E.J.; Hatton, B.D.; Grinthal, A.; Aizenberg, J. Bioinspired Self-Repairing Slippery Surfaces with Pressure-Stable Omniphobicity. *Nature* **2011**, *477*, 443-447.

CHAPTER 8: CONCLUSION

The effects of surface micro/nanotopography and small amplitude fast vibrations on wetting properties were studied. Samples of functional surfaces were produced to have hydrophobic, icephobic, and corrosion resistant properties. Surface topography can be used to control the wetting property of hydrophobic concrete, corrosion resistance of hydrophobic metallic surfaces, and the icephobicity of concrete.

In Chapter 1, the motivation and the goals of this dissertation were discussed.

In Chapter 2, the concepts related to wetting and vibrational mechanics were reviewed. Also, the method of separation of motions was discussed. Using the method of separation of motions, small fast vibrations can be substituted by an effective force or energy obtained by averaging the vibrations over their time period. The equations for effective force and energy were also formulated in this chapter.

In Chapter 3, the relationship between surface topography and vibrations was established using the method of separation of motions. Similarly to small fast vibrations, spatially periodic micro/nanopatterns can be substituted by an effective force or energy obtained by averaging the patterns over their spatial domain. The method of separation of motions was used to study and understand the structure-property relationships in materials and surfaces.

Kirchhoff's analogy was also used to study the similarity between surface topography and vibrations. Using the analogy of an inverted pendulum it was shown that a slender elastic flexible beam in tension can be stabilized using spatial periodicity in the geometry of the beam. Thus surface topography manifests as an effective stabilizing shear force on the beam.

The effective force for vibration-induced stabilization of the inverted and the multiple pendulums were formulated using the method of separation of motions. The limiting case of multiple pendulums, a string, cannot be stabilized unless flexural stiffness is introduced. The vibration-induced stabilization of a flexible rope was studied experimentally. The rope was seen to execute whipping motions, due to instabilities, within a range of frequencies of vibration. The rope remained buckled and static at other frequencies of vibration. This is similar to the vibration-induced stabilization of inverted and multiple pendulums.

Several examples of how vibrations affect viscous non-Newtonian liquids with were studied experimentally and theoretically. An analogy was drawn between the mechanical systems undergoing vibration and non-linear behavior in vibrating fluids. Thus, vibro-levitating droplets of oil were observed over a vibrating bath of oil within a certain range of frequency of vibrations, similarly to the vibration-induced stabilization of an inverted pendulum. Then, vibration-induced phase transition of a cornstarch suspension, and granular media was discussed and demonstrated experimentally. In addition, it was theoretically shown that vibrations could stop fluid flow through a hole, thereby affecting membrane permeability. In each case, the method of separation of motions was used to formulate effective forces.

The effect of surface topography can be incorporated into the surface free energy by averaging the surface patterns over the projected area. The effective surface energy can be observed as the macroscopic contact angle. Surface topography can be used to control wetting properties, for applications such as superhydrophobic surfaces. A new application of superhydrophobic surfaces is in separation of oil-water mixtures. Superhydro/oleophobic/philic meshes can be used to separate organic liquids (such as oil) from water. An equation for the

capillary pressure in an oil-water separating superhydro/oleophobic/philic mesh was formulated using the method of separation of motions. Oil-water separation was found to be analogous to the molecular scale phenomenon of reverse osmosis. Surface topography as well as vibrations can affect wetting properties such as the contact angle and the surface free energy. Thus, structure-property relationships in materials and surfaces were established.

In Chapter 4, based on the understanding of the structure-property relationships, the surface topography was used to control the wettability of concrete. Surface topography and wettability of concrete samples were manipulated by changing the concrete mixture composition and using hydrophobic emulsion. The wetting properties of hydrophobic concrete samples such as the contact angle and contact angle hysteresis were experimentally measured using a contact angle goniometer. The surface topographies of the samples were studied and the surface roughness values were measured using a laser scanning microscope. The dynamics of incoming water droplets on hydrophobic concrete surface was studied because repulsion of incoming droplets is a desirable property for any hydrophobic surfaces. An experimental method was developed for that purpose. Whether the droplets were pinned, broke-up on impact, or bounced-off the hydrophobic concrete surface depended on the droplet velocity as well as the surface topography. The ability of the concrete to repel incoming droplets can be optimized by changing the concrete composition.

In Chapter 5, the surface topography was used to control wetting and thus prevent corrosion of metallic materials. Hydrophilic, hydrophobic, and superhydrophobic cast iron samples with different surface roughness values were prepared. The wetting properties of the samples such as the contact angle and contact angle hysteresis were experimentally measured

using a contact angle goniometer. The surface topographies of the samples were studied and the surface roughness values were measured using a laser scanning microscope. Potentiodynamic polarization tests were carried out on the samples.

A decrease of up to eight orders of magnitude in corrosion current density and an increase in corrosion potential was observed after superhydrophobization of the cast iron. However, increasing the roughness without hydrophobization leads to the formation of a homogenous solid-liquid interface thereby increasing the corrosion current density. The trend observed in the experimental results match the theoretical predictions, as well as the data from literature. A stable non-homogeneous solid-electrolyte-air interface is essential for superior corrosion resistance.

In Chapter 6, the effect of surface topography on the icephobicity of materials, particularly concrete, was studied. The essential mechanisms needed for ice repellence are similar to the hydrophobic interactions. In this chapter, two aspects of the icephobicity of hydrophobic concrete, namely, the repulsion of incoming water droplets before freezing as well as the ice adhesion strength were investigated experimentally. An experimental method was designed for that purpose. The icephobicity of concrete samples was achieved by hydrophobization, by using coatings containing dielectric material (such as polyvinyl alcohol fibers), and by controlling the surface topography. The surface topography of the concrete samples were studied using a laser scanning microscope and average surface roughness values were measured. The surface roughness of the concrete depends on the polyvinyl alcohol content and the sand to cement ratio of the concrete mixture.

Ice accretion on the concrete surface is reduced if the incoming droplets do not undergo wetting transition. Wetting transition can be prevented by optimizing the surface roughness of the concrete. The ice adhesion strength of hydrophobized concrete samples were one order in magnitude less than that of regular concrete samples. It was found that icephobic performance of concrete depends on these parameters – the hydrophobic emulsion concentration, the PVA fiber content, the water to cement ratio, and the sand to cement ratio. Optimizing the roughness of a surface and hydrophobizing it will minimize ice accretion from incoming droplets, as well as delay ice nucleation at the surface.

In Chapter 7, the potential for biomimetic icephobicity of skunk cabbage, and the effect of surface topography on its icephobicity were investigated experimentally and theoretically. The ability of the plant to melt ice is related to the heat generated by thermogenesis. The wetting properties such as the contact angle and contact angle hysteresis of the plant leaves were measured using a contact angle goniometer. Although the skunk cabbage leaves are slightly hydrophobic, they exhibit high adhesion to water. The surface topography of the plant leaves were investigated using a scanning electron microscope. The abaxial surface of the leaves have a hierarchical microstructure which consists of pillars covered with hair-like wax rodlets. The surface micro/nanotopography of the leaf coupled with its high adhesion to water suggested an impregnated wetting state.

A theoretical model correlating the heat transfer from the leaf with its micro/nanotopography was developed. The surface topography of the leaf could maintain a layer of liquid water on it, thereby reducing ice adhesion. Also, a composite interface at the leaf surface can minimize heat loss. As far as the biomimetic potential of the plant, it can be

concluded that the rose-petal effect-like structure can be used to decrease ice contact area for icephobic surfaces.

This study established that the method of separation of motions can be used to study the effect of small patterns on macroscopic properties of a system. Small patterns can be substituted by an effective force or energy similarly to small amplitude fast vibrations. The method of separation of motions is suited not only for the study of rigid body dynamics, but also the areas of surface science, physical chemistry and material science.

Surface micro/nanotopography and small amplitude fast vibrations affect wetting and adhesion properties of various surfaces studied experimentally and theoretically in this dissertation. Functional materials and surfaces such as hydrophobic and icephobic engineered cementitious composites, and corrosion resistant metallic surfaces can be produced by controlling the surface micro/nanotopography. Such materials can find many environmentally friendly applications in fresh water industry, as well as in cold regions.

APPENDIX

In the experimental study for chapters 4 and 6, the concrete samples used were obtained from Prof. Konstantin Sobolev's laboratory at the Department of Civil and Environmental Engineering at the University Wisconsin-Milwaukee. Some specimens and the coatings used in this study were prepared by Dr. Marina Kozhukhova.

Materials

Portland cement Type I (PC) supplied by Lafarge (Alpena, MI, USA) was used to prepare the mortar specimens. All the required characteristics of the cement, according to the ASTM150, are presented in Table A1. Standard quartz sand with an average particle size of 425 μm , according to the ASTM C778 and a regular tap water were used to produce the mortar samples. Kuralon K-II RECS15x12 polyvinyl alcohol (PVA) fibers (supplied by Kuraray Co. Osaka, Japan) were used to modify mortar mixes and induce a certain "self-reproducing" surface structure. The fibers had diameter of 45 μm with the length of 12 mm. In order to improve the workability of fiber reinforced mortars, polycarboxylate ether (PCE) high-range water-reducing admixture supplied by Handy Chemicals (Montreal, Canada) was used.

"Shell type" water-based siloxane emulsion was used in this study for hydrophobic modification of the mortars surfaces. Polymethylhydroxysilane (PMHS) was used for emulsion preparation as a hydrophobic agent and polyvinyl alcohol (PVA) with molecular weight of 16000 (supplied by Across Chemicals) was used as a surfactant. Silica fume particles were incorporated in order to stabilize the emulsion and also to serve as micro-roughness forming elements when attached to the rough mortar surface coated by the emulsion. For the experiment two emulsions with different concentrations of hydrophobic agent and silica fume were prepared

at proportions of 25% : 5% and 5% : 1%, by weight, respectively. The concentration of the PVA surfactant in water was kept constant at 5% for both types of emulsions.

Table A1. Chemical and physical properties of portland cement.

Chemical	Spec	Test	Physical	Spec	Test
Composition	Limit, %	Result, %	Properties	Limit	Result
SiO ₂	-	20.6	Air content, %	-	3.2
Al ₂ O ₃	-	4.7	Time of setting, min		
Fe ₂ O ₃	-	2.7	Initial	45 min	110
CaO	-	63.9	Final	375 max	225
MgO	6.0 max	2.3	Compressive strength, MPa		
SO ₃	3.0 max	2.4	1 day	-	12.4
Ignition Loss	3.0 max	2.1	3 days	12.0 min	21.7
Free Lime	-	1.1	7 days	19.0 min	27.6
Limestone	-	3.4	28 days	28.0 min	37.9
CO ₂	-	1.3	Blaine fineness, m ² /kg	260 min	380
C ₃ S	-	54.5	Autoclave expansion, %	0.8 max	0.02
C ₂ S	-	17.9	Heat of hydration at 7 days, kJ/kg	-	411
C ₃ A	-	7.9	Passing 325 mesh, %	-	95.4
C ₄ AF	-	8.2			
C ₄ AF+2(C ₃ A)	-	24.2			
C ₃ S+4.75(C ₃ A)	-	93			
Na ₂ O _{eq}	0.6 max	0.55			
CaCO ₃ in LS		93			

Preparation of Concrete Tiles

Small rectangular tile specimens of 10x10x5 mm were cast, compacted using shaking table and placed in a curing room for 24 hours. These were then demolded and placed into the

moist room (RH= 90 ±5%) for total of 28 days of curing. Later, the tiles were dried in an oven for 2 days at 70 °C. The dried samples were sealed in ziplock bags filled with paper to adsorb extra water (if any), and stored at laboratory conditions (22±3 °C and RH= 55%) before further testing.

Before coating with hydrophobic emulsions tile surfaces were subjected to mechanical abrasion using 60 grit sand paper for 30 sec. Thus prepared samples were treated with two hydrophobic emulsions, with different concentration of hydrophobic agent and silica fume. Upon coating, the samples were cured for 48 hours at a room temperature of 22±3 °C and relative humidity of 55%.

Preparation of Concrete Cubes

The fiber-reinforced concrete cubes were prepared as follows. The procedure involved the production of 40x40x160 mm beams using the same approach as described above. These beams were cut into cubes of 40x40x40 with diamond saw.

Ice Adhesion Strength Measurement

In order to estimate the icephobicity, which was defined by the adhesion strength between the ice and concrete samples, PASCO CI-6746 stress-strain apparatus was employed to test the adhesion strength by measuring the shear force, applied to a cylindrical mold filled with ice and attached to the surface of a tile.

All mortar tiles and cylindrical molds were placed into freezing room and stored at -18 °C for 24 hours. After that, molds were placed on the top on the tiles and filled with cool water (0 °C). The samples with attached cylinders were cooled for an additional 5 hours at -18 °C to

achieve the complete crystallization of ice. Three sets of the specimens with different hydrophobic surfaces were tested for icephobic characteristics. Two specimens of each composition were prepared and tested and the average value of the shear strength was calculated and reported. The shear test, including settling of a sample and applying force, was conducted at a temperature of 0 ± 2 °C for 2 minutes in order to avoid melting of ice.

CURRICULUM VITAE

EDUCATION

Ph.D., University of Wisconsin-Milwaukee, WI

May 2016, Mechanical Engineering, GPA: 3.9/4.0

Thesis: Effects of Surface Topography and Vibrations on Wetting: Superhydrophobicity, Icephobicity, and Corrosion resistance

M.E., Birla Institute of Technology and Science (BITS)-Pilani, India

June 2011, Mechanical Engineering, CGPA: 8.5/10.0

Thesis: Development and Characterization of a Novel Superhydrophobic Surface

B.Tech., Cochin University of Science and Technology, Cochin, India

April 2008, Mechanical Engineering

AWARDS

2015-16 UW-Milwaukee Distinguished Dissertation Fellowship Award

2012-16 Chancellor's Graduate Student Award, UW-Milwaukee

PUBLICATIONS

Journal Articles

- Ramachandran R, Maani N, Rayz V L, Nosonovsky M. Vibrations and Spatial Patterns in Biomimetic Surfaces: Using the Shark-skin Effect to Control Blood Clotting. *Philos. Trans. R. Soc. , A* **2016** (In Press).
- Ramachandran R, Kozhukhova M, Sobolev K, Nosonovsky M. Anti-icing Superhydrophobic Surfaces: Controlling Entropic Molecular Interactions to Design Novel Icephobic Concrete. *Entropy* **2016**, *18*, 132.
- Ramachandran R, Nosonovsky M. Coupling of Surface Energy with Electric Potential Makes Superhydrophobic Surfaces Corrosion-Resistant. *Phys. Chem. Chem. Phys.* **2015**, *17*, 24988-24997.
- Ramachandran R, Sobolev K, Nosonovsky M. Dynamics of Droplet Impact on Hydrophobic/Icephobic Concrete with the Potential for Superhydrophobicity. *Langmuir* **2015**, *31*, 1437-1444.
- Nosonovsky M, Ramachandran R. Geometric Interpretation of Surface Tension Equilibrium in Superhydrophobic Systems. *Entropy* **2015**, *17*, 4684-4700.

- Ramachandran R, Nosonovsky M. Surface Micro/Nanotopography, Wetting Properties and the Potential for Biomimetic Icephobicity of Skunk Cabbage *Symplocarpus Foetidus*. *Soft Matter* **2014**, *10*, 7797-7803.
- Ramachandran R, Nosonovsky M. Vibro-levitation and Inverted Pendulum: Parametric Resonance in Vibrating Droplets and Soft Materials. *Soft Matter* **2014**, *10*, 4633-4639.
- Ramachandran R, Seetharaman M, Sharma N N. Investigations Into Superhydrophobicity of a Soot Surface Attributed to Nano-Asperities. *J. Micro Nano-Manuf.* **2013**, *1*, 014502.

Book Chapter in Press

- Ramachandran R, Nosonovsky M. Non-wetting, Stabilization, and Phase Transitions Induced by Vibrations and Spatial Patterns. In: Ras R, Marmur A, editors. *Non-wettable Surfaces: Theory, Preparation and Applications*: Royal Soc. Chemistry, 2016.

Manuscripts in Preparation

- Ramachandran R, Nosonovsky M. Vibrations and Spatial Patterns Change Effective Wetting Properties of Superhydrophobic and Regular Membranes.

Conference Proceedings

- Ramachandran R, Nosonovsky M. Superhydrophobic and Icephobic Materials for Energy Applications. *Materials and Technologies for Energy Efficiency*, 2015, pp. 243-247.
- Ramachandran R, Nosonovsky M. Inverted-Pendulum Model for the Stability of Bouncing Droplets on Vibrating Foundation. *The Eighth International Conference on Materials Technologies and Modeling (MMT-2014)*, Ariel, Israel, pp. 112-121.
- Ramachandran R, Sharma N N. Miniaturized Wire Guided Droplet Manipulation System for Lab-on-a-Chip with a Low Cost Superhydrophobic Surface. *In the proceedings of the 6th International ISSS conference*, 2012, Bangalore, India.

Posters

- Maani N, Ramachandran R, Rayz V L, Nosonovsky M. Vibrations and Spatial Patterns in Biomimetic Surfaces: From the Lotus Effect to Blood Clotting Control. *UWM Graduate Student Poster Competition*, April 2016.
- Ramachandran R, Kozhukhova M, Sobolev K, Nosonovsky M. Nano-Engineered Pinning Resistant Hydrophobic Concrete. *The Fifth International Symposium on Nanotechnology in Construction*, 2015, Chicago, Illinois.
- Ramachandran R, Nosonovsky M. Superhydrophobic and Icephobic Materials for Energy Applications. *The Energy and Materials Research Conference (EMR2015)*, Madrid, Spain, 25-27 February 2015.

- Ramachandran R, Nosonovsky M. Superhydrophobic/Oleophilic and Hydrophilic/Oleophobic Porous Media. *The Sixth International Conference on Porous Media*, 2014, Milwaukee, Wisconsin.
- Ramachandran R, Nosonovsky M. Biomimetics in Icephobic Surfaces and Non-wetting Systems: from bouncing droplets to smart materials. *UWM Graduate Student Poster Competition*, April 2012.